

# **Preparation of monodisperse microbubbles in a capillary embedded T-Junction device and the influence of process control parameters on bubble size and stability**

A thesis submitted in partial fulfilment of the requirements for the degree of

**Doctor of Philosophy**

By

**Maryam Parhizkar**

Department of Mechanical Engineering

University College London

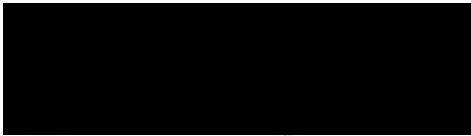
Torrington Place, London WC1E 7JE

**U.K**

**March, 2014**

## **Declaration**

I, Maryam Parhizkar, confirm that the work presented in this thesis is my own. Where information has been derived from other sources, I confirm that this has been indicated in the thesis.



.....

Maryam Parhizkar

## Abstract

The main goal for this work was to produce microbubbles for a wide range of applications with sizes ranging between 10 to 300  $\mu\text{m}$  in a capillary embedded T-junction device. Initially the bubble formation process was characterized and the factors that affected the bubble size; in particular the parameters that reduce it were determined. In this work, a polydimethylsiloxane (PDMS) block (100 x 100 x 10  $\text{mm}^3$ ) was used, in which the T-shaped junction was created by embedded capillaries of fixed outer diameter. The effect of the inner diameter was investigated by varying all the inlet and outlet capillaries' inner diameter at different stages. In addition, the effect of changes in the continuous phase viscosity and flow rate ( $Q_l$ ) as well as the gas pressure ( $P_g$ ) on the resulting bubble size was studied. Aqueous glycerol solutions were chosen for the liquid phase, as they are widely used in experimental studies of flow phenomena and provide a simple method of varying properties through dilution. In addition, the viscosity could be varied without significantly changing the surface tension and density of the solutions. The experimental data were then compared with empirical data derived from scaling models proposed in literature, which is widely used and accepted as a basis of comparison among investigators. While the role of liquid viscosity was investigated by these authors, it was not directly incorporated in the scaling models proposed and therefore the effect of viscosity was also studied experimentally. It was found that bubble formation was influenced by both the ratio of liquid to gas flow rate and the capillary number. Furthermore, the effect of various surfactant types and concentrations on the bubble formation and stability were investigated. Preliminary studies with the current T-junction set-up indicated that producing microbubbles with size ranging from 50-300  $\mu\text{m}$  was achievable. Subsequently, the study progressed to optimise the junction to produce smaller bubbles ( $\sim 20 \mu\text{m}$ ) by directly introducing an electric field to the T-junction set-up and assisting the bubble breakup with the combination of microfluidic and electrohydrodynamic focusing techniques. Finally, in this thesis, a novel method that combines microfluidics with electrohydrodynamic (EHD) processing to produce porous BSA scaffolds from microbubble templates with functional particles and/or fibres incorporated into the scaffolds' structure is presented.

## Publications

### Refereed Journal Papers

- M. Parhizkar, M. Edirisinghe and E. Stride, “*Effect of Operating Conditions and Liquid Physical Properties on the Size of Monodisperse Microbubbles Produced in a Capillary Embedded T-junction Device*” *Microfluidics & Nanofluidics*, 14(2013)797-808.
- M. Parhizkar, E. Stride and M. Edirisinghe, “*Preparation of Monodisperse Microbubbles using an Integrated Embedded Capillary T-Junction with Electrohydrodynamic Focusing*” *Lab on a Chip* (accepted in press)
- M. Parhizkar, P. Sofokleous, E. Stride and M. Edirisinghe, “*Novel preparation of controlled porosity particle/ fibre loaded scaffolds using a hybrid microfluidic and electrohydrodynamic technique*” (in preparation)
- M. Parhizkar, M. Edirisinghe and E. Stride, “*The Effect of Surfactant Type and Concentration on the Size and Stability of Microbubbles Produced in a Capillary Embedded T-Junction Device*” (in preparation)

### Conference Presentations

- M. Parhizkar, E. Stride and M. Edirisinghe, “*Effect of Geometry on Microbubble Formation and Size in an Embedded Capillary T-Junction Microfluidic device*”, *Advances in Microfluidics & Nanofluidics* May 2013. University of Notre Dame, Indiana, USA.
- M. Parhizkar, E. Stride, M. Edirisinghe. *Effect of Operating Conditions and Liquid Physical Properties on the Size of Monodisperse Microbubbles Produced in a Capillary Embedded T-junction Device*, PhD Forum, Department of Mechanical Engineering, UCL, London, UK, (2012).

- M. Parhizkar, E. Stride, M. Edirisinghe, (2011), *The effect of viscosity on size of microbubbles prepared using a T-Junction Microfluidic device*, PhD forum, Department of Mechanical engineering, UCL, London,UK.

### **Participating in symposia**

- Bubbles and Encapsulation, University College London, UK, April 2010.

## **Acknowledgements**

I would like to express my wholehearted thanks to my supervisor Professor Mohan Edirisinghe for accepting me under his wings as a research student at UCL. I am very grateful for his continuous guidance, patience and valuable support during the period of my study. I am honoured to have been able to do this research under his mentorship.

My thanks are equally due to my second supervisor Dr. Eleanor Stride for her trust, guidance, advice and great support throughout this research work. She is extremely patient, and always enthusiastic to teach, and listen to my views. I feel extremely privileged to be jointly supervised by Prof. Edirisinghe and Dr. Stride.

I would also like to thank the Engineering and Physical Science Research Council and Instrument Loan Pool, UK for providing the high speed cameras for this work.

Continuous and invaluable support provided by my friends and colleagues, Mr. Panayiotis Sofokleous, Dr. Bhairav. Patel, Mr. Hanif Ghanbar, Mr. Dimitris Tsaoulidis, Dr. Marjan Enayati and Dr. Chaojie Luo, is unforgettable. My dream of doing this research study wouldn't have been possible if not for the unparalleled understanding, love and support extended to me and my family.

Last but not least, I would like to give my special thanks to my father, Mr. Alireza Parhizkar, and my sister, Ms Minou Parhizkar as well as my brother Mr Ehsan Parhizkar for their love, belief, support and help in the past years, without them I would not be brave enough to face this challenge in my life.

I cannot imagine to be able to have this achievement without these important people.

Thank you all.

## **DEDICATION**

**To**

**My Father;**

**Alireza Parhizkar**

**for his sacrifices and supports throughout my life and mostly during the time of  
this research**

**And to the loving memory of my Mother;**

**Farkhondeh Khazaie Nejad**

**Who taught me to be strong and I wish she was here with us to celebrate this  
achievement**

## Nomenclature

Symbol	Definition	Units
$A_{interface}$	Projected area of liquid-gas interface	$m^2$
$B$	Universal gas constant	Dimensionless
$Bo$	Bond number	Dimensionless
$Ca$	Capillary number	Dimensionless
$C_i$	Initial concentration of dissolved gas in liquid	g/ml
$C_{sat}$	Saturation concentration of dissolved gas in liquid	g/ml
$d$	Characteristic dimension of the system	m
$D_b$	Bubble diameter	$\mu m$
$D_{ch}$	Microchannel diameter	$\mu m$
$E$	Electric field strength	N/C
$\epsilon_g$	Gas dielectric constant	Dimensionless
$\epsilon_l$	Liquid dielectric constant	Dimensionless
$K$	Electrical conductivity	$\mu S/m$
$L$	Length of the slug	m
$L_{gap}$	Gap between the coaxial capillaries	m
$M$	Molecular weight	g/mol
$M$	Mach number	Dimensionless
$\mu_g$	Gas viscosity	mPa s
$\mu_l$	Liquid viscosity	mPa s
$P_g$	Gas inlet pressure	kPa
$P_{gmax}$	Maximum gas pressure	kPa
$P_{gmin}$	Minimum gas pressure	kPa
$P_{lg}$	Gas outlet pressure downstream of junction	kPa
$\Delta P_c$	Characteristic pressure from lubrication analysis	kPa

$Q_g$	Gas flow rate	ml/min
$Q_l$	Liquid flow rate	ml/min
$R_a$	Principle radii of curvature in horizontal plane	m
$R_r$	Principle radii of curvature in vertical plane	m
$Re_g$	Gas Reynolds number	Dimensionless
$Re_l$	Liquid Reynolds number	Dimensionless
$\rho_e$	Volume charge density	C/m <sup>3</sup>
$\rho_g$	Gas density	kg/m <sup>3</sup>
$\rho_l$	Liquid density	kg/m <sup>3</sup>
$\sigma_l$	Liquid surface tension	mN/m
$T$	Temperature	K or (°C)
$t$	Time	s
$\theta$	Contact angle	°
$u_g$	Gas flow velocity	m/s
$u_l$	Liquid velocity	m/s
$V$	Voltage	kV
$w$	Width of the channel	m
$w_c$	width of the continuous phase capillary	m
$We$	Weber number	Dimensionless

## **Glossary of abbreviations**

<b>BSA</b>	Bovine serum albumin
<b>BSS</b>	Balanced salt solution
<b>CEHDA</b>	Co-axial electrohydrodynamic atomization
<b>CMC</b>	Critical micelle concentration
<b>CTAB</b>	Cetyltrimethyl ammonium bromide
<b>DEP</b>	Dielectrophoresis
<b>EHDA</b>	Electrohydrodynamic atomization
<b>FC</b>	Fluorocarbon
<b>FDA</b>	Food and Drug Administration
<b>FEP</b>	Fluorinated ethylene propylene
<b>HIFU</b>	High intensity focused ultrasound
<b>HPLC</b>	High performance liquid chromatography
<b>MRI</b>	Magnetic resonance imaging
<b>MEMS</b>	Microelectromechanical systems
<b>O/W</b>	Oil-in-water
<b>PBS</b>	phosphate buffered saline
<b>PDMS</b>	Polydimethylsioxane
<b>PEG</b>	Poly ethylene glycol
<b>PET</b>	Polyethylene terephthalate
<b>PI</b>	Polydispersivity index
<b>PLGA</b>	Poly (lactic acid-co-glycolid acid)
<b>PMMA</b>	Poly(methyl methacrylate)
<b>PMSQ</b>	Polymethylsilsesquioxane
<b>PTFE</b>	Polytetrafluoroethylene
<b>PVA</b>	Poly vinyl alcohol
<b>SEM</b>	Scanning electron microscopy

<b>SDS</b>	sodium dodecyl sulfate
<b>SLS</b>	sodium lauryl sulfate
<b>W/O/W</b>	water-in-oil-in-water
<b>W/O</b>	water-in-oil

### **Subscripts**

<i>b</i>	bubble
<i>c</i>	continuous phase
<i>ch</i>	channel
<i>d</i>	dispersed phase
<i>g</i>	gas
<i>i</i>	initial
<i>l</i>	liquid
<i>lv</i>	liquid-vapour
<i>sat</i>	saturation
<i>sl</i>	solid-liquid
<i>sv</i>	solid-vapour

Contents	Page
Declaration.....	1
Abstract.....	2
Publications.....	3
Refereed Journal Papers.....	3
Conference Presentations.....	3
Participating in symposia.....	4
Acknowledgements.....	5
DEDICATION.....	6
Nomenclature.....	7
Glossary of abbreviations.....	9
Subscripts.....	10
List of Figure.....	17
List of Tables.....	22
<b>Chapter 1</b> .....	<b>23</b>
Introduction and Background.....	23
1.1 Background.....	23
1.2 Objectives of the research.....	26
1.2.1 Production of Microbubbles using the capillary embedded T-junction device.....	26
1.2.1.1 Microbubble size and distribution study.....	27
1.2.1.2 Effect of surfactant properties on microbubble formation, size and stability.....	27
1.2.1.3 Optimising the setup to reduce the bubble size by introducing Electrohydrodynamic flow focusing.....	28
1.2.2 Production of scaffolds and foams from microbubbles.....	28
1.2.2.1 BSA Foams and scaffolds from microbubbles.....	28
1.2.2.2 Production of novel BSA scaffolds loaded with nanoparticles/fibres.....	29
1.3 The structure of the thesis.....	29
<b>Chapter 2</b> .....	<b>32</b>
Literature review.....	32
2.1 Introduction.....	32
2.2 The applications of microbubbles.....	33

2.2.1	Ultrasound contrast imaging .....	33
2.2.2	Targeted drug delivery .....	33
2.2.3	Water and wastewater treatment .....	35
2.2.4	Food engineering.....	36
2.2.5	Scaffolds from microbubbles for tissue engineering.....	36
2.2.5.1	Scaffold fabrication techniques.....	37
2.2.5.1.1	Particle leaching .....	38
2.2.5.1.2	Emulsion freeze drying.....	38
2.2.5.1.3	Foaming via pressure quenching method.....	39
2.2.5.2	Polymeric scaffolds .....	40
2.2.5.3	Protein scaffolds .....	41
2.3	Stability of microbubbles and foams .....	42
2.3.1	Stabilisation by low diffusivity gases.....	43
2.3.2	Role of surfactants in microbubble stability .....	44
2.3.2.1	Surfactant effect on microbubble stability .....	46
2.3.2.2	Surfactant types .....	47
2.4	Current preparation methods.....	49
2.4.1	Sonication.....	49
2.4.2	Coaxial Electrohydrodynamic Atomization (CEHDA) .....	50
2.4.2.1	Electrospraying of nanoparticles.....	51
2.4.2.2	Electrospinning of nanofibres .....	52
2.4.3	Microfluidic devices.....	52
2.4.3.1	Co flowing devices.....	54
2.4.3.2	Flow focusing devices.....	55
2.4.3.3	Cross flowing (T Junction) devices.....	56
2.5	Mechanism of bubble/droplet formation .....	58
2.5.1	Formation of droplets or bubbles in microfluidic devices .....	58
2.5.1.1	Capillary instability .....	59
2.5.2	Type of flow in microfluidic devices .....	60
2.5.2.1	Pressure driven flows .....	62
2.5.2.1.1	Type of flow pattern and bubble shape .....	62
2.5.2.2	Electroosmotic flows.....	63
2.6	Scaling models for bubble breakup and size prediction in T-junction Devices.....	64

2.6.1	Governing forces in the presence of electric field.....	67
2.6.2	Role of channel geometry .....	69
2.6.3	Role of flow parameters on bubble size .....	70
2.6.4	Role of liquid properties on bubble formation .....	71
2.6.4.1	Interfacial tension.....	71
2.6.4.2	Surfactant effect .....	72
2.6.4.3	Viscosity.....	73
2.6.5	Microchannel surface characteristics and wetting .....	73
2.7	Microfluidic device material and fabrication methods .....	74
2.8	Summary of the literature .....	75
<b>Chapter 3</b>	.....	<b>76</b>
Experimental details.....		76
3.1	Introduction.....	76
3.2	Materials .....	76
3.2.1	Glycerol.....	77
3.2.2	Surfactants.....	77
3.2.3	Phospholipid.....	78
3.2.4	Bovine serum albumin (BSA).....	79
3.2.5	Polymethylsilsesquioxane (PMSQ).....	79
3.2.6	Poly (lactic-co-glycolic acid) (PLGA) .....	80
3.2.7	Collagen .....	80
3.2.8	Phosphate buffered saline (PBS).....	80
3.2.9	Ethanol .....	81
3.2.10	Acetone.....	81
3.3	Characterisation of the solutions.....	81
3.3.1	Density .....	81
3.3.2	Viscosity.....	82
3.3.3	Surface tension and contact angle .....	82
3.3.3.1	Wilhely's plate method .....	82
3.3.3.2	Drop shape analysis method.....	83
3.3.4	Electrical Conductivity and pH .....	84
3.4	Preparation of solutions .....	85
3.4.1	For the study of the influence of liquid physical parameters on microbubble size study.....	85

3.4.2	For the study of the T-junction setup with electrohydrodynamic focusing ..	86
3.4.3	For the study of the effect of surfactant properties on bubble size and stability .....	87
3.4.4	For the generation of BSA scaffolds loaded with polymer and collagen nanoparticle/fibres .....	88
3.5	Characterisation of generated microbubbles and scaffolds .....	90
3.5.1	Optical microscopy .....	90
3.5.2	High speed camera images .....	90
3.5.3	Scanning electron microscopy (SEM).....	91
3.6	Experimental Setup.....	92
3.6.1	Standard capillary embedded T-junction device.....	92
3.6.1.1	Specific experimental details for the effect of parameters on bubble size .....	95
3.6.1.2	Specific details of experiments for the effect of surfactants on bubbles .....	95
3.6.2	Capillary embedded T-junction device with electrohydrodynamic focusing	97
3.6.3	Combined T-junction and single needle EHD setup.....	99
<b>Chapter 4</b> .....		100
Results and Discussion .....		100
4	Production of Microbubbles using a capillary embedded T-junction device ....	100
4.1	Overview.....	100
4.2	Effect of operating conditions and liquid physical properties on the size of microbubbles in the T-junction device .....	101
4.2.1	Introduction .....	101
4.2.2	Bubble formation.....	102
4.2.3	Effect of gas inlet pressure on bubble size .....	103
4.2.4	Effect of flow ratio and liquid viscosity on bubble size.....	105
4.2.5	Effect of capillary size on bubble diameter.....	107
4.2.6	Comparison of experimental data with scaling model .....	110
4.2.7	Effect of the vertical gap size (Cavity) on bubble size .....	112
4.2.8	Bubble entrapment inside channels.....	115
Summary .....		115
4.3	Preparation of microbubbles with T-junction integrated with electrohydrodynamic focusing.....	117
4.3.1	Introduction .....	117

4.3.2	Influence of electric field on bubble formation.....	117
4.3.3	Effect of voltage increment on microbubble size.....	119
4.3.4	Mapping of the dimensionless bubble diameter with applied voltage and liquid physical parameters.....	123
4.3.5	Influence of electric field on bubble uniformity and production yield .....	126
4.3.6	Comparison with other bubble formation techniques .....	126
4.3.7	Applications impacted on by the reduction of microbubble size using electric field.....	127
	Summary.....	128
4.4	The effect of surfactant type and concentration on the Size and stability of microbubbles in the T-junction device .....	129
4.4.1	Introduction.....	129
4.4.2	Effect of surfactant concentration on the properties of the liquid phase.....	129
4.4.3	Effect of surfactant concentration on bubble size .....	132
4.4.4	Influence of surfactant type on the bubble formation time .....	132
4.4.5	Effect of surfactant type on bubble size .....	134
4.4.6	Stability of microbubbles .....	137
	Summary.....	141
	<b>Chapter 5</b> .....	142
5	Production of scaffolds and foams from microbubbles .....	142
5.1	Overview.....	142
5.2	BSA Foams and scaffolds from microbubbles .....	143
5.2.1	Introduction.....	143
5.2.2	Formation of foams from bubbles.....	143
5.2.3	Effect of concentration of BSA on foam stability and scaffold structure ...	144
5.3	Preparation of controlled porosity particle/ fibre loaded scaffolds using a hybrid micro-fluidic and electrohydrodynamic technique.....	148
5.3.1	Introduction.....	148
5.3.2	Formation of Bio-products .....	148
5.3.2.1	Bubbles.....	148
5.3.2.2	Particles .....	149
5.3.2.3	Collagen beaded Nanofibres .....	149
5.3.2.4	Combination of bio-products .....	149
5.3.3	Bubble formation.....	150

5.3.4	Scaffold structure .....	153
5.3.5	Particles sprayed on bubbles .....	156
5.3.6	Spraying of collagen beaded fibres .....	160
5.3.7	Possible applications .....	160
	Summary .....	163
	<b>Chapter 6</b> .....	164
	Conclusions and Future Work .....	164
6.1	Conclusions.....	164
6.1.1	T-junction and parameters influencing bubble formation and size.....	165
6.1.2	Surfactant type and concentration on microbubble formation and stability	166
6.1.3	Optimization of T-junction with electrohydrodynamic focusing and reduction of bubble size .....	167
6.1.4	Production of foams and scaffolds from bubbles and loading with nanoparticle/fibres.....	168
6.2	Future Work.....	169
6.2.1	Commercial viability.....	172
	References.....	174
	Appendix .....	190

<b>List of Figures</b>	<b>Page</b>
<b>Figure 1. 1:</b> Objectives of the research presented in this thesis.	26
<b>Figure 2. 1:</b> Different types of microbubble agent used for ultrasound imaging and therapy. a) Coated microbubble. b) Phase shift emulsion. c) Echogenic liposome. d) Multilayered microbubble (Stride 2009).	34
<b>Figure 2. 2:</b> SEM images of scaffolds fabricated with different techniques of a) gas foaming, b) electrospinning, c) phase separation and d) freeze drying.	39
<b>Figure 2. 3:</b> Schematic of microbubble shell and coating.	43
<b>Figure 2. 4:</b> Surfactant classification according to their head group composition and schematic of adsorption monolayer of a gas bubble coated with surfactants.	48
<b>Figure 2. 5:</b> Schematic representation of the CEHDA setup.	51
<b>Figure 2. 6:</b> Illustrations of the three main microfluidic geometries used for bubble formation. (a) Co-flowing, (b) flow focusing geometry, and (c) cross flowing streams in a T-shaped junction.	53
<b>Figure 2.7:</b> Types of flow in T-junction a) Cross-flowing and b) Perpendicular flow (Xu et al. 2006)	57
<b>Figure 2. 8:</b> Illustration of the most common flow patterns are bubbly flow, segmented flow and annular flow (Serizawa et al. 2002).	63
<b>Figure 2. 9:</b> Inertial, viscous and gravitational body forces, relative to interfacial forces, as a function of the channel size and characteristic velocity in microfluidic multiphase systems (Gunther and Jenson 2006).	70
<b>Figure 3. 1:</b> Submersion of platinum plate for the Wilhelmy balance measurement.	83
<b>Figure 3. 2:</b> Illustration of contact angles formed by sessile liquid drops on a smooth homogeneous solid surface.	84
<b>Figure 3. 3:</b> Schematic of the T-junction device (system apparatus)	93
<b>Figure 3. 4:</b> (a) 3D and (b) 2D representation of junction diagram, where $P_g$ and $Q_l$ are gas pressure and liquid flow rate, respectively, and $L$ gap is the distance between the capillaries in the junction.	94
<b>Figure 3. 5:</b> (a) 3D and (b) 2D illustration of the junction geometry for 3 cases of 1. Gap size < Capillary inner diameter ( $50\ \mu\text{m}$ ), 2. Gap size = Capillary inner diameter ( $200\ \mu\text{m}$ ) and 3. Gap size > Capillary inner diameter ( $220\ \mu\text{m}$ ).	94

<b>Figure 3. 6:</b> T- Junction setup a) and schematic of the T-junction setup and bubble formation with b) and without c) an applied electric field.	98
<b>Figure 3. 7:</b> Schematic illustration of the T-junction/EHD setup used for the experiments.	99
<b>Figure 4. 1:</b> Bubble formation process as a function of time for liquid solution viscosity of 10.8 mPa s and flow rate of 0.01 ml/min at (a) $t=0$ ms, (b) $t=1.62$ ms, (c) $t=3.82$ ms, (d) $t=4.95$ ms, (e) $t=6.62$ ms, (f) $t=7.45$ ms, (g) $t=8.28$ ms.	102
<b>Figure 4. 2:</b> The variation of bubble size with gas inlet pressure for liquid with different viscosities at a constant liquid flow rate of 0.1 ml/min.	104
<b>Figure 4. 3:</b> High speed camera images of bubble formation for liquid solution viscosity of 10.8 mPa s at constant flow rate of 0.01ml/min varying gas inlet pressure a) 150 kPa, b) 170 kPa.	104
<b>Figure 4. 4:</b> Microscopic images of bubbles with constant liquid flow rate of 0.1 ml/min and viscosities of: a) $\mu = 1.76$ mPa s @ $P_{gmin} = 52$ kPa, b) $\mu = 10.8$ mPa s @ $P_{gmin} = 81$ kPa c) $\mu = 22.5$ mPa s @ $P_{gmin} = 190$ kPa d) $\mu = 60$ mPa s @ $P_{gmin} = 246$ kPa.	105
<b>Figure 4. 5:</b> The variation of bubble size with viscosity and flow ratio.	106
<b>Figure 4. 6:</b> Comparison between the experimental data and predictive values.	107
<b>Figure 4. 7:</b> Dependence of capillary diameter on the flow ratio for different capillary diameters at liquid viscosity of a) 15.2 mPa s and b) 60 mPa s.	109
<b>Figure 4. 8:</b> Diameter of bubbles produced in the T junction as a function of liquid capillary number for three different viscosities (see legend in the figure) and constant gas pressure of 60 kPa.	112
<b>Figure 4. 9:</b> Micrograph images of bubbles produced with two different junction gap sizes of a) 50 $\mu$ m and b) 220 $\mu$ m.	113
<b>Figure 4. 10:</b> Graph representing variation of bubble size with gas inlet pressure at three different gap sizes of 50, 200 and 220 $\mu$ m.	114

- Figure 4. 11:** High speed camera images of time evolution of the bubble formation in the capillary embedded T-junction, for two different junction gap sizes of a) 50 and b) 220  $\mu\text{m}$  at constant liquid flow rate (0.04 ml/min) and viscosity(60 mPa s). 114
- Figure 4. 12:** Existence of trapped bubbles in the junction cavity. 115
- Figure 4. 13:** High speed camera images of microbubbles at the tip of the outlet at applied voltages of 0, 6 and 12kV. Scale bar is 1.6mm. 118
- Figure 4. 14:** Optical micrographs of bubbles formed in aqueous glycerol with 5, 50 and 75 % concentration at applied voltages of 0, 6,9 to 12 kV and a constant liquid flow rate of 0.01ml/min. Scale bar is 200  $\mu\text{m}$ . 119
- Figure 4. 15:** Optical micrographs of microbubbles from a solution with 75% glycerol concentration at constant liquid flow rate of 0.01 ml/min at applied voltages of a) 12, b) 15 and c) 21 kV. 120
- Figure 4. 16:** a) Graph showing variation of bubble diameter with applied voltage for solution viscosities of 1.3, 6, 15 and 36 mPa s, and b) 3D plot of dimensionless bubble diameter with respect to voltage and capillary number increment. 121
- Figure 4. 17:** Graph showing variation of bubble diameter with applied voltage for solution with constant viscosity of 6 mPa s with and without NaCl solution added. (PDI < 1% , Error bars indicating the experimental errors.) 122
- Fig. 4. 18:** Experimental results versus correlations and predictive model for bubble dimensionless diameter for solution with viscosity of a) 1.3, b) 6, c) 15 and d) 36 mPa s. (PDI < 1% , Error bars indicating the experimental errors.) 124
- Figure 4. 19:** Graph representing experimental data for dimensionless bubble diameter against predictive values. 125
- Figure 4. 20:** Graph showing variation in the number of bubbles generated with applied voltage for three different solution viscosities of 1.3, 6 and 36 mPa s over a fixed time period of 5 seconds and collection area of 1.5  $\text{mm}^2$ . 125
- Figure 4. 21:** The effect of surfactant concentration on bubble size and gas pressure range where bubble formation is achievable for a) PEG 40 and b) Tween 40, all of the microbubbles produced with this setup were highly monodispersed with polydispersity index < 2 %. 131

- Figure 4. 22:** High speed camera images of the bubble formation time for a) CTAB, b) SDS, c) Tween 40 and d) PEG 40, scale bar is 200  $\mu\text{m}$ . 135
- Figure 4. 23:** The effect of surfactant type on microbubble size for a) 2wt % concentration and b) 5wt % concentration, all bubbles were monodispersed with polydispersity index < 2 % . 136
- Figure 4. 24:** Micrographic images showing the stability of 5 wt % concentration of a) Tween 40, b) PEG 40, c) SDS and d) CTAB. 137
- Figure 4. 25:** Bubble dimensionless diameter stability profile for a) PEG 40 b) Tween 40. 139
- Figure 4. 26:** Micrograph images of microbubbles with 2 wt % Tween 40 surfactant from a) centre of the collection sample b) edge of the collected sample at i) time of collection ii) 2.5 hours and iii) 5 hours after collection. 140
- Figure 5. 1:** Preparation of BSA scaffolds through a) microbubble formation, b) and c) foams from bubbles and d) dried BSA scaffolds. 144
- Figure 5.2:** Micrograph images showing the diffusion and change in bubble size in a multi-layer bubble structure of the solution containing 25 wt % BSA at a)  $t = 0$  s, b) 10 mins, c) 15 mins and d) 20 mins, and e) SEM image of scaffold with both small and large shrinkage voids. 146
- Figure 5. 3:** BSA bubbles produced from the T-junction. 150
- Figure 5. 4:** Optical microscope images of BSA bubbles after: a) 1min, b) 10min, c) 15min and d) 20min after generation. 152
- Figure 5. 5:** SEM images of a single layer of dried BSA bubbles formed on a glass slide with [(a,b)i] showing structures with two different windows controlled by changing the T-junction parameters and [(a,b)ii] showing the images in [(a,b)i] at higher magnification. 153
- Figure 5. 6:** Double layer dried BSA scaffold structure (a) optical and (b) SEM micrographs. 154

**Figure 5. 7:** Scanning electron micrographs of multi-layer scaffold made using dried BSA bubbles showing the different diameter window sizes obtained by changing the T-junction processing parameters (a) having the biggest gap diameter ( $543\pm 33\ \mu\text{m}$ ) and (d) the smallest one ( $162\pm 17\ \mu\text{m}$ ). 156

**Figure 5. 8:** Images showing (a) dried BSA bubbles, (b) dried BSA bubbles with PLGA nanoparticles, (c) a single layer BSA scaffold with PLGA nanoparticles in its cavities after spraying for 1min (see arrows), (d) PLGA nanoparticles aggregating into different shapes in a BSA scaffold cavity after spraying for 5min (e) a two layer BSA scaffold with PLGA nanoparticles and (f) a multilayer BSA scaffold with PLGA nanoparticles. 158

**Figure 5. 9:** SEM images at different magnifications showing the same multilayered BSA scaffold after sprayed with PMSQ micro-particles with images (a) and (d) having the lowest and the highest magnification, respectively. 159

**Figure 5. 10:** SEM images at different magnifications showing the same multilayered BSA scaffold after spraying with collagen micro-particles with images (a) and (f) having the lowest and the highest magnification, respectively. 161

**Figure 5. 11:** Scanning electron micrographs of multilayered BSA scaffolds sprayed with collagen beaded nanofibres for (a) 5min and (b) 15min at different magnifications. 162

**Figure 6. 1:** T-junction device with different angles. 170

<b>List of Tables</b>	<b>Page</b>
<i>Table 3. 1: Physico-chemical characteristics of surfactants (data for CMC and Molecular weight were obtained from Prakesh (Prakesh 2010), and Sigma Aldrich, UK)</i>	78
<i>Table 3. 2: Measured values of viscosity and surface tension.</i>	85
<i>Table 3. 3: Characteristic properties of solutions used in the experiments.</i>	86
<i>Table 3. 4: Physical properties of the solutions used in the experiment.</i>	88
<i>Table 3. 5: Physical properties of liquids used in experiments. All % refer to weight unless stated otherwise.</i>	89
<i>Table 3. 6: Conditions tested in the experiments (at 22 ° C)</i>	96
<i>Table 5. 1: Properties of BSA foams and scaffolds produced via T-Junction microfluidics.</i>	145
<i>Table 5. 2: Parameters used to generate bubbles and their stability. The bubbles diameter value is the mean diameter of 50 bubbles.</i>	151

## **Chapter 1**

### **Introduction and Background**

#### **1.1 Background**

Microbubbles are used in a very wide range of applications ranging from biomedical to food, cosmetics and agricultural science and technologies (Gordillo et al., 2004, Park et al., 2010). Microbubbles are used in ultrasound medical imaging as contrast agents to enhance the acoustic contrast between blood and surrounding tissues and therefore improve the quality of ultrasonic images (Zheng, 2012, Taverna et al., 2012, Kiessling et al., 2012, Blomley et al., 2001). Microbubbles are also employed in therapeutic applications as vehicles for targeted drug and gene delivery (Stride et al., 2009, Unger et al., 2001, Stride and Edirisinghe, 2008). In order for microbubbles to be used as ultrasound contrast agents or in drug delivery platform, their size and distribution are critical parameters (Chen et al., 2009). The technology to use microbubbles in the food industry in a controlled manner has also recently emerged as an important breakthrough (Campbell and Mougeot, 1999). Microbubbles have great potential to be used in a number of processes, including aquaculture and hydroponic cultivation, food preservation and quality control, and water and wastewater treatment (Cassell et al., 1975). The requirements on the properties of microbubbles such as size, monodispersity, surface property, and stability vary amongst different applications (Xu et al., 2008).

Microbubbles are typically referred to as gas in liquid emulsions with diameters ranging from 1 to 200  $\mu\text{m}$ . Over the last century, the existence of naturally occurring

## Chapter 1: Introduction and Background

microbubbles in fresh water, sea water and blood and other body fluids has been studied by many investigators (Johnson and Cooke 1981; Cassell et al. 1975). These suspensions have been the topic of intense investigation by scientists and engineers in many practical fields. For instance, in wastewater treatment, small microbubbles are applied to efficiently separate colloidal pollutants from water during microflotation (Cassell et al., 1975). The presence of bubbles near the surface of the ocean has profound significance in marine biology over a number of oceanographic processes, such as converting organic carbon to particulate formed by dissolving small bubbles in seawater (Johnson and Cooke, 1980). In meteorology, air bubbles produced by breaking waves affect the local air quality and rain formation while carrying surface active organic materials upon rising to the ocean surface and ejecting them into the air in the form of aerosols upon breaking (Blanchard, 1975). Due to the high surface area to volume ratio, microbubbles are ideal tools for mass and energy transfer. In bioprocessing, yeast biomass production largely depends on the oxygen transfer efficiency of the aeration system performed by microbubbles (Ago et al., 2005). In the pharmaceutical industry, microbubble aeration systems are used in bioreactors to carry out similar air/oxygen mass transfer (Zimmerman et al., 2008).

An important topic for scientists and engineers to study is the origin of the microbubbles' long lasting stability. Currently microbubbles are applied in a large scope of industrial and technological applications. In the more recent years, microbubbles have received increasing attention for biomedical applications. In the next section, a detailed developmental history of microbubbles as ultrasound contrast agents for diagnostic imaging is reviewed.

There are several methods to produce microbubbles. The microfluidic method has many advantages over conventional methods, which are discussed below:

- It is a method capable of producing fine and highly monodisperse microbubbles. Monodisperse bubbles have the advantage in many applications, for instance in ultrasound imaging, using uniform microbubbles enables similar attenuation and scatter characteristics.

## Chapter 1: Introduction and Background

- It is a technique that can be scaled up easily for mass production with multiple microchannels being used in parallel.
- This method is very flexible and different surfactants and stabilizers can be added to adjust the stability of microbubbles produces.
- The capillary embedded T-junction device described in this work is different from the conventional microfluidic chips manufactured through much more expensive methods (i. e. lithography).
- This device provides a simple but yet robust production of highly monodisperse microbubbles without the need of continuous cleaning and replacement due to the blockage of channels caused by the material residue.
- Another advantage of this setup is that the channel diameter is generally larger and therefore pressure drop in the channel is much lower than smaller diameter channels.
- The T-junction device is optimized by introducing the electric field directly into the bubble breakup region, the flow of the continuous phase is assisted with electrohydrodynamic flow and bubbles with almost an order of magnitude smaller than the channel diameter were generated.

The above-mentioned advantages make the capillary embedded T-junction an attractive method for the production of monodisperse microbubbles.

## 1.2 Objectives of the research

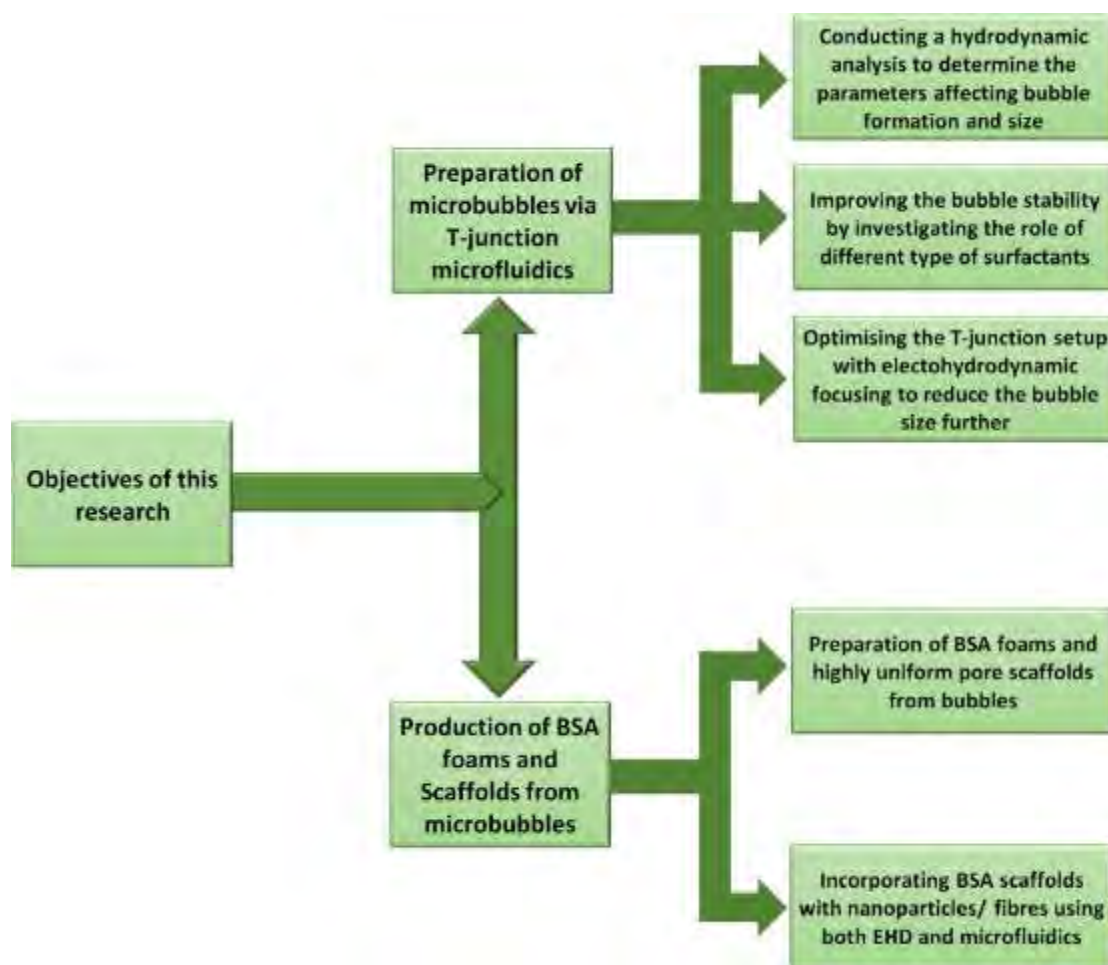


*Figure 1.1: Objectives of the research presented in this thesis.*

The flow chart in **Figure 1.1** sets out the key objectives of this study. The detail of each objective is discussed below.

### 1.2.1 Production of Microbubbles using the capillary embedded T-junction device

The **primary objective** of this work was to investigate the parameters affecting the formation of bubbles in a simple capillary embedded T-junction device. In addition, the aim was to demonstrate that this device could successfully produce microbubbles with control over size and size distribution under ambient conditions. Furthermore, the focus was on the optimisation of the device by including an external electric field and further

reduction in bubble size due to the addition of the external field. To meet these objectives, several studies were necessary which were arranged into different stages as follows:

### **1.2.1.1 Microbubble size and distribution study**

Initially, the aim of this study was to investigate the fundamentals of the T-junction microfluidic processing for the preparation of microbubbles. The main goal for this part of the work was to determine how the size and size distribution of the microbubbles generated can be systematically controlled through the range of operating parameters: solution and gas flow rates, channel diameter and the inherent properties of the solution such as viscosity and surface tension during microbubble generation. Finally, to complete this part of the study, the intention was to validate the experimental data with the scaling models previously studied to assess the role of the capillary number has on bubble size.

### **1.2.1.2 Effect of surfactant properties on microbubble formation, size and stability**

The purpose of this part of the work was to conduct an experimental study to determine the effect of surfactant type and concentrations on bubble formation and size. The study was aimed at four differently charged surfactants: an anionic surfactant, sodium dodecyl sulfate (SDS), two non-ionic surfactants, polyoxyethylene sorbitan monopalmitate (Tween 40) and polyoxyethylene glycol 40 stearate (PEG 40), and a cationic surfactant, cetyltrimethyl ammonium bromide (CTAB). The intention of this part of the research was also to achieve stable bubbles by altering the surfactant type and concentration.

### **1.2.1.3 Optimising the setup to reduce the bubble size by introducing Electrohydrodynamic flow focusing**

This aspect of the study was aimed at the optimisation of the standard T-junction by introducing an external electric field to produce bubbles with a versatile range of applications. The objectives in this section were to modify the basic T-junction microfluidic device by applying an electrical potential difference across the outlet channel to reduce the bubble size, as well as exploring the effect of applied voltage in conjunction with the capillary number. It was intended further in this work to produce a model to predict the bubble size for the range of experimental conditions tested in this study.

## **1.2.2 Production of scaffolds and foams from microbubbles**

In this work, the main goal was to provide an understanding of the concepts of microfluidics and electrohydrodynamic (EHD) techniques and the combination of two simple but highly reliable methods in order to construct advanced multi-dimensional structures. This part of the work was focused on production of highly uniform protein scaffolds from microbubbles generated with the state of the art capillary embedded T-junction device with a high level of control over the size of microbubbles. In addition, the intention was to demonstrate that the attachment of nanoparticles/fibres on the multi-layered structures through the EHD method is viable and can improve the functionality of the scaffolds for possible future applications.

### **1.2.2.1 BSA Foams and scaffolds from microbubbles**

The objective in this section was to generate foams from protein coated microbubbles produced via the T-junction set-up. The study was aimed at bovine serum albumin (BSA) solutions with different concentrations to produce stable foams and fine 3D scaffold structures. The fabrication of scaffolds and foams for applications such as tissue engineering and food and cosmetics industries in a scaled up and cost effective manner was intended in this part of the research.

### **1.2.2.2 Production of novel BSA scaffolds loaded with nanoparticles/fibres**

The purpose of this research was to produce multi-dimensional scaffolds containing biocompatible particles and fibres using a combination of two techniques of T-junction microfluidics and electrohydrodynamic (EHD) processing. The aim was to form porous scaffolds by drying the layers of monodisperse bovine serum albumin (BSA) bubbles generated from the T-junction method and further spraying or spinning poly (lactic-co-glycolic) (PLGA), polymethylsilsesquioxane (PMSQ) and collagen particles/fibres onto the scaffolds during their production and after drying by using the EHD processing. The key motivation for conducting this study was to produce multifunctional BSA scaffolds with controlled porosity that have bio-products such as PLGA, PMSQ and collagen particles/fibres attached on them, which can provide these structures with the potential to be used in many biomedical and cosmetics applications.

## **1.3 The structure of the thesis**

This dissertation describes the way in which the research is proceeded by surveying literature, assembling the experimental setup, selecting materials and methods, and conducting experiments etc., in order to exploit the potential available in T-junction microfluidic device as a viable technique to prepare microbubbles primarily for medical and secondarily for other industrial applications. The organisation of this thesis is given in this section. This **Chapter 1** provides background information about the research project and gives an overview about the basics of microbubble formation in T-junction microfluidics and parameters influencing the size and stability of bubbles. The objectives of the research are stated and the organisation of this thesis and scope of the research outlined.

**Chapter 2** presents a detailed literature survey. Since the aim of the research is to prepare microbubbles through T-junction microfluidics, optimisation of the microfluidic device with electrohydrodynamic focusing and finally generation of scaffolds from microbubbles, an extensive collection of literature has been surveyed to understand the principles of microfluidics and electrohydrodynamic atomization, the procedures and their uses, as well as the materials and the methods used for the

## Chapter 1: Introduction and Background

preparation of microbubbles and scaffolds. A literature survey has been presented on the uses and properties of microbubbles that are used in medical, food and agricultural applications and the investigations carried out previously using microfluidic systems and the theory behind the microbubble formation in different microfluidic devices.

**Chapter 3** describes the experimental setup, materials used, experiments and characterisation procedures carried out, and a detailed description of the experimental tools employed.

In **Chapter 4**, results obtained during the experiment using a capillary embedded T-junction device are discussed in conjunction with existing literature. This chapter is split into three sections; in **Section 4.1**, aqueous glycerol solutions with different concentrations were used to show the effect of different parameters such as; flow rate ratios, viscosity and channel geometry were studied on size, size distribution and polydispersity index of microbubbles.

In **Section 4.2**; surfactants with different charge type and chain lengths were used to investigate the effect of various surfactants on the formation and stability of microbubbles. The effect of surfactant wetting characteristics on the surface of channels walls were studied. The stability profile of microbubbles were measured to select an ideal surfactant for applications requiring stable microbubbles such as ultrasound imaging and drug delivery.

**Section 4.3** discusses a novel method of integrating the T-junction microfluidics with electrohydrodynamic focusing to reduce the microbubbles size further. Parameters such as viscosity, electric conductivity and applied voltage were varied and an empirical model was suggested for the range of capillary numbers studied in this study.

## Chapter 1: Introduction and Background

**Chapter 5** studies the role of microbubbles in production of protein foams and scaffolds. This chapter has two sections. **Section 5.1** focuses on the production of BSA foams and scaffolds from microbubbles produced in a T-junction microfluidic device. A detailed description is given in **Section 5.2** on the formation of BSA scaffolds loaded with nanoparticles/fibres using a combination of two well established techniques. Scaffolds with uniform pore size were developed from protein microbubbles formed via capillary embedded T-junction microfluidic cross flowing device. Polymer nanoparticles were electrosprayed on the structure; while Collagen beaded nanofibres were electrospun via the EHD setup.

**Chapter 6** is divided into two sections. **Section 6.1** summarizes the experimental results and presents the conclusions of the work. **Section 6.2** discusses some recommendations for future work, employing microfluidics processing of microbubbles and beyond, to continue the research presented in this thesis in new directions. Finally, the literature referred to throughout the thesis is listed in the **References** section

## **Chapter 2**

### **Literature review**

#### **2.1 Introduction**

The motivation and the objective behind this literature survey is to provide an overview of techniques to prepare microbubbles that can satisfy the requirements of primarily in medical engineering, particularly in biomedical applications such as scaffolds from bubbles for tissue engineering and microbubbles as contrast agents for ultrasound imaging and targeted drug delivery. In order to fulfil this objective, the literature connected to the usages, properties, requirements and preparation methods of microbubbles that are used in ultrasound imaging and targeted drug delivery, food engineering, water and wastewater management and finally their role as platforms for generation of scaffolds for tissue engineering has been surveyed in the first instance. Secondly, the work carried out by previous authors on microfluidic systems have been reviewed in order to understand how these techniques offer opportunities for further research in fulfilling the objectives of the work.

## **2.2 The applications of microbubbles**

Microbubbles play an important role in a highly diverse range of applications ranging from biomedical to food, cosmetic and agricultural science and technologies (Gordillo et al., 2004, Park et al., 2010, Kiessling et al., 2012, Blomley et al., 2001, Xu et al., 2008). The requirements in terms of the properties of microbubbles such as size, monodispersity, surface functionalization and stability for these applications similarly vary widely (Unger et al., 2001, Stride and Edirisinghe, 2008, Stride et al., 2009).

### **2.2.1 Ultrasound contrast imaging**

Compared with other imaging modalities such as computed tomography and magnetic resonance imaging (MRI), ultrasound imaging is one of the most popular medical diagnostic techniques due to its safety, low cost, and easy accessibility (Kang and Yeh, 2012). However, due to the relatively poor quality of the images obtained using this technique, methods to improve this problem are considered amongst researchers (Stride and Saffari, 2003). The application of encapsulated microbubbles, in particular in the area of ultrasound contrast imaging, is rapidly expanding in the field of medical engineering. Microbubbles are highly compressible and therefore they are found to be practical as contrast agents in ultrasound imaging (Lindner, 2004). Since their discovery in the late 1960's (Kremkau et al., 1970), it is established that surfactant or polymer shell stabilized microbubbles are the most effective means of contrast enhancement in ultrasound imaging and various current commercially available contrast agents (Dijkmans et al., 2004). Microbubbles scatter ultrasound much more efficiently than red blood cells due to their high compressibility. By introducing a suspension of microbubbles into the blood stream, the contrast between blood vessels and the surrounding tissue in an ultrasound image is improved by several orders of magnitude (Cui et al., 2005).

### **2.2.2 Targeted drug delivery**

As well as their use in diagnostic imaging, microbubbles have been the subject of intensive research in therapeutic applications. Microbubbles in intravascular ultrasound

treatment can improve drug penetration into tissues, such as through the blood-brain barrier (Hernot and Klibanov, 2008). In drug delivery and gene therapy, the required therapeutic agent is loaded in microbubbles, where they can be traced to the target by using low-intensity ultrasound and further the material is released locally by destroying the microbubbles with a high intensity burst and therefore avoiding systemic administration such as toxic chemotherapy. The risk of harmful side effects can be substantially reduced by localizing the treatment using this method. In order to increase the speed and efficacy of the treatment in high-intensity focused ultrasound (HIFU) surgery, microbubbles have been used as means of nucleating cavitation in the target volume (Stride, 2009). Microbubbles are used as theranostic agents as they provide simultaneous and co-localised contrast for diagnostics imaging and drug carrying and delivering capacity for targeted therapy. In this case, the imaging modality and therapeutic trigger is ultrasound (Sirsi and Borden, 2009). Improvements in both microbubble design and ultrasound devices and methodology have made this technology clinically relevant.

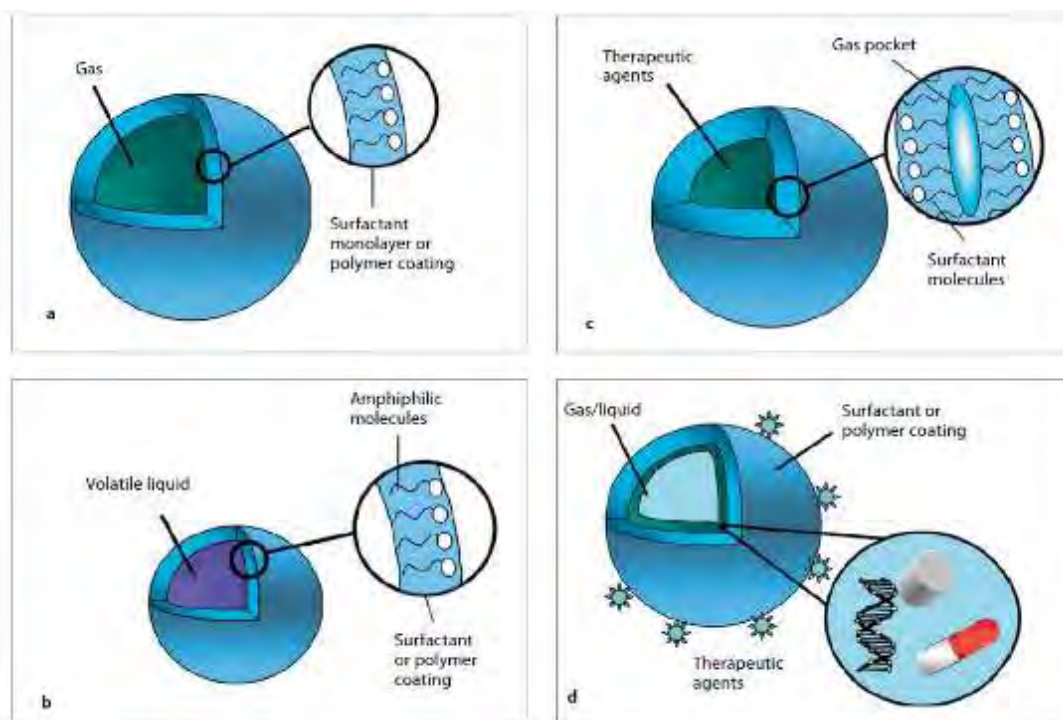


**Figure 2. 1:** Different types of microbubble agent used for ultrasound imaging and therapy. a) Coated microbubble. b) Phase shift emulsion. c) Echogenic liposome. d) Multilayered microbubble (Stride, 2009).

**Figure 2.1** illustrates different types of microbubbles for specific biomedical applications. These include coated gas microbubbles, phase shift emulsions, echogenic liposomes and multi-layered structures for therapeutic applications. Phase shift emulsion consists of a stabilised emulsion of volatile liquid droplets (**Figure 2.1 b**) which vaporise to form microbubbles either upon injection or following exposure to ultrasound of sufficient intensity. Echogenic liposomes are similar in terms of their chemical composition to phospholipid-coated microbubbles but consist of phospholipid bi-layers encapsulating a mixture of liquid and gas. Compared with gas microbubbles, this type of agents provide enhanced stability and therefore they are particularly attractive in drug delivery applications.

### **2.2.3 Water and wastewater treatment**

Small gas bubbles are known to be extensively used in many environmental and industrial separation processes. Bubbles generated for these applications are used in the treatment of potable water and wastewaters for the removal of volatile contaminants in the aqueous phase as well as the separation of particulate materials from the aqueous phase (Ahmed and Jameson, 1985, Ketkar et al., 1991, Chu et al., 2007). Many different methods are used to generate bubbles depending on the treatment application. Since smaller bubbles act as more efficient collectors and optimize mass transfer rates, it is important to control the diameter and size distribution of the bubbles produced by these different methods (Burns et al., 1997). Microbubbles are used in microflotation for wastewater treatment because of their large surface area and relatively slow rise velocities (Cassell et al., 1975, Rodrigues and Rubio, 2007). As microbubbles rise in wastewater, they come into contact with organic pollutants and other low-density particulates and carry them to the surface to form a collective foam layer for subsequent separation and purification processes. In the mineral industry, fine particles are separated from solutions using microbubbles in a similar fashion called electroflotation (Jimenez et al., 2010). Electroflotation is a simple process that floats particles to the surface of a water body by microbubbles of hydrogen and oxygen gases generated from water electrolysis (Chen, 2004).

#### **2.2.4 Food engineering**

Bubbles play a significant role in the manufacturing of many food products such as cakes, ice creams and soft drinks. Introducing microbubbles in food has many advantages such as lowering the cost and forming novel structures (Campbell and Mougeot, 1999). There are a number of positive benefits from aeration of food including texture change, digestibility modification or flavour intensity (Lau and Dickinson, 2005). Replacement of the carbonated drinks, enrichment of the nutrition value of the food and reduction of price per volume in products such as candy bars are potential novel applications of microbubbles compared to traditionally aerated food. Microbubbles effectively adsorb oppositely charged molecules, tiny particles, and/or fine oil droplets due to their charged surface and large surface area. Microbubbles dispersed in food products can not only modify the texture, but also have several very interesting and value-added benefits. Previous studies have reported the use of microbubbles for enzyme extraction, protein recovery, bacteria harvest and oil removal or recovery (Xu et al., 2008). The appearance and shelf-life of food incorporated with microbubbles can be influenced by the physical stability and amount of air. By sufficiently adding small amounts of such bubbles per unit mass without significantly altering the macroscopic rheological properties, healthier (reduced calorie) food with a similar taste can be produced. In addition, microbubbles coated with nutritional ingredients or drugs could help to improve the nutrition or act as a medicinal aid in food (Shen et al., 2008). Methods of making coated microbubbles suitable for food applications is a challenging area for manufacturers.

#### **2.2.5 Scaffolds from microbubbles for tissue engineering**

Scaffolds play an important role in tissue engineering by acting as porous biodegradable structures containing various bio-products (cells, genes, drugs and proteins) (Dhandayuthapani et al. 2011, Cutroneo, 2003, Haynesworth et al., 1998). They serve as surrogate matrices, e. g. extra cellular (ECM) and can be produced from natural or synthetic material or a combination of both (Pereira et al. 2013, Carletti et al., 2011). In order for scaffolds to mimic the function of the natural ECM available in the human body, they must balance mechanical function with transport of bioactive agents (Chan and Leong, 2008, Hollister, 2005). While a denser scaffold offers a better function and

mechanical strength, a more porous scaffold provides greater diffusion of gas/liquid components and provides cell growth (Carletti et al., 2011).

Scaffolds developed for tissue engineering are to assist with the growth of cells migrating from the surrounding tissue in to the porous structure of the scaffold. As the primary function of the scaffolds is to support the growing tissue, they are required to allow cell migration, attachment and proliferation (Hollister, 2005). In order to satisfy these requirements they must have high porosity, high surface area and uniform three-dimensional shape, which can be tailored to suit the requirements of different types of tissue (Vats et al., 2003). There has been many studies into the morphological design of scaffolds to stimulate cellular growth. Several factors are important including the pore shape and size, as well as their interconnectivity and spatial distribution through the scaffold. Generally, scaffolds with high porosity have relative lower mechanical property while the honeycomb structure of a scaffold is attributed to the well compressive strength (Wang et al., 2009). Foam and honeycomb like structures with interconnecting and large pores are ideal templates for tissue engineering scaffolds.

Recently microbubbles have been used as pore generators in the biomedical field. Wang et al. (Wang et al., 2009) showed that a sponge-type, multiple-layer alginate scaffold could be formed by collecting bubbles over a period of time, with uniform pore sizes of 250  $\mu\text{m}$  promoted more cell migration and distribution in the scaffold with an increased cell (chondrocyte) proliferation over 7 day period. Scaffolds prepared by Nair et al. (Nair et al., 2009) using protein microbubbles as porogens have shown to be an excellent candidate to be used as tissue engineering scaffolds as well as drug / growth factor delivery vehicles.

### **2.2.5.1 Scaffold fabrication techniques**

A great variety of well-known fabrication techniques are used in scaffold design for tissue engineering applications. Particle leaching (Mikos et al., 1994), polymer casting and phase separation (Liu et al., 2011), solvent casting, emulsion freeze

drying, electrospraying (Sullivan and Jayasinghe, 2007), electrospinning (Li et al., 2005) and foaming (Ekemen et al., 2011) are amongst the main fabrications methods. Some of the widely used techniques are described here. Examples of scaffolds generated with various techniques are shown in **Figure 2.2**.

Scaffolds produced by these methods have pores with a wide size and shape distribution leading to insufficient transport of nutrition, migration and attachment of cells. Moreover, the use of organic solvents and particulate leaching in most of these techniques reduce the biocompatibility of the structure which hinders the growth of cells (Lee et al., 2011).

#### **2.2.5.1.1 Particle leaching**

Particle leaching incorporates particles, e.g. salt, sugar or specifically prepared the spheres, dissolved in a polymer sample and further washed out after processing the polymer sample into the final form creating additional porosity in the structure of the scaffold (Mikos et al., 1994). One of the advantages of this method is the creation of large pores with high control over the pore morphology. However, this method is not suitable for materials such as soluble protein scaffolds as well as the risks of remaining material residue after processing that is harmful for the tissue.

#### **2.2.5.1.2 Emulsion freeze drying**

In emulsion freeze-drying, an emulsion is formed by homogenization of a polymer-solvent system and water. The emulsion is then cooled down quickly resulting in solidification of the polymer and the creation of a polymeric porous structure. Later the solvent and water content are removed by freeze drying (Ma and Zhang, 1999). Creation of relatively thick scaffolds with large pores is one of the highlights of this method, as well as enabling the incorporation of proteins during the fabrication. The permeability of the pores in the obtained morphology is however very poor and therefore this limits the growth of cell and transport of nutrients through the scaffold.

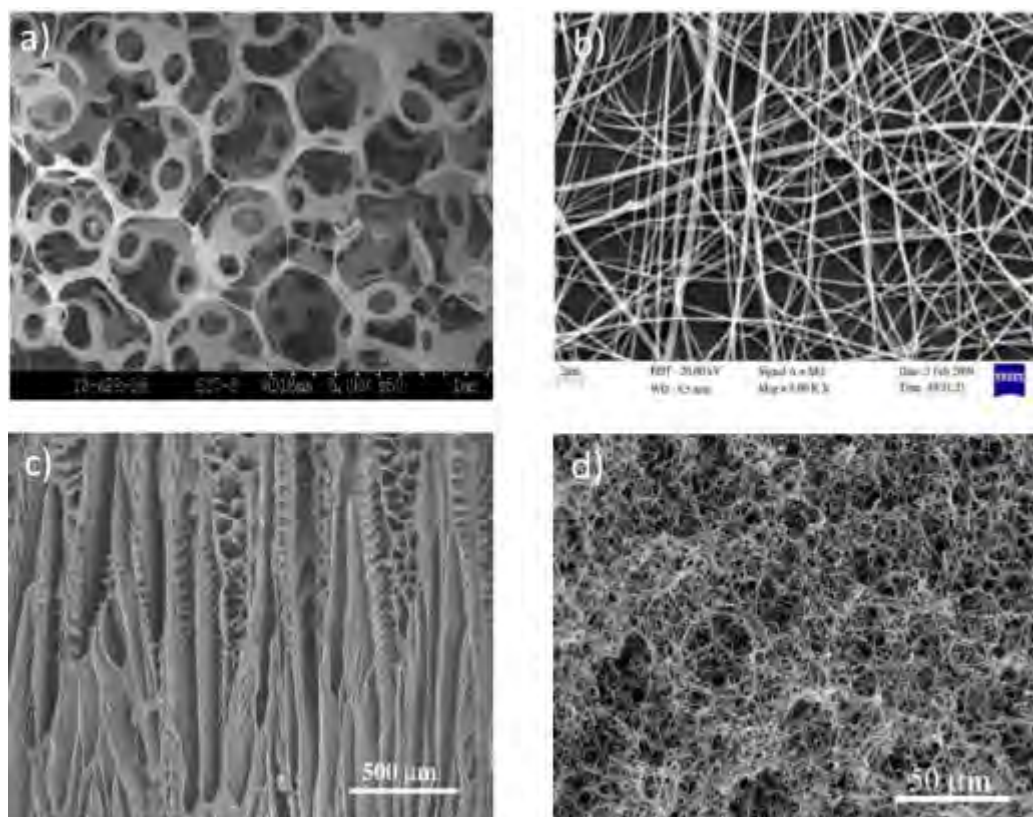


**Figure 2. 2:** SEM images of scaffolds fabricated with different techniques of a) gas foaming (Ma and Choi, 2001), b) electrospinning (Bhardwaj and Kundu, 2010), c) phase separation (Ma and Zhang, 2001) and d) freeze drying (Ma and Zhang, 1999).

### 2.2.5.1.3 Foaming via pressure quenching method

Generally, in the foaming process, a soluble inert gas such as CO<sub>2</sub> or N<sub>2</sub> is used as a blowing agent to create porosity in polymers via pressure quenching method. The properties of the scaffold is adjusted by variation of the process conditions. This method is also applicable for composites of polymer and ceramics (Ma and Choi, 2001). The advantage that this method has over the other processes is the lack of solvents, eliminating the risk of remaining residue. However, one of the drawbacks of this method is the pores are not percolated. Nonetheless, there are additional post processing steps such as plasma treatment or pulsated ultrasound to obtain porous morphologies.

### **2.2.5.2 Polymeric scaffolds**

In order to fabricate scaffolds suitable for tissue engineering, biocompatible polymers that do not have the potential to elicit an immunological or foreign body reaction should be used. The selected polymers should degrade with a controlled rate in conjunction with tissue regeneration. There are many types of polymeric materials that have been used for bone tissue engineering that can be categorized as naturally derived materials (e.g. collagen and fibrin) and synthetic polymers (e.g. poly(lactic acid) (PLA), poly(glycolic acid) (PGA), and their copolymers (PLGA) (Hollister, 2005). One of the potential advantages of naturally derived polymers is that they positively support cell adhesion and function, however they may exhibit immunogenicity and contain pathogenic impurities. Another disadvantage of the naturally derived materials is the lack of control over their mechanical properties and biodegradability as well as limitation in supply and being costly. On the other hand synthetic polymers have the advantage of being reproducible in large scale production with controlled properties of strength, degradation rate and microstructure. Although there is a variety of biodegradable polymers available for tissue engineering, no single polymer meets all the requirements for the design of scaffolds. As a result, composite materials that often have an excellent balance between mechanical properties and cell adhesion are introduced to mimic the natural bone or tissue matrix, for instance natural bone matrix is a composite material of collagen and apatites (Liu and Ma, 2004).

In order to create favourable scaffold environment the base material should have a suitable decomposition rate, good biocompatibility, surface characteristics and favourable plasticity (Wang et al., 2013). Biodegradable materials from natural polymers such as hyaluronic acid, alginate and chitosan to synthetic polymers such as poly (L-lactic acid) (PLA) and poly (L-lactic-co-glycolic acid) (PLGA), are commonly used for the fabrication of scaffolds and have been extensively researched (Kim et al., 2005). However, most polymeric scaffolds are hydrophobic and this discourages cell attachment and growth. In order to address this problem many methods have been suggested such as coating the scaffold with proteins or soaking it in various growth factors via spontaneous adsorption or covalent linking (Nair et al., 2007). While these additional treatment methods assist with cell attachment and growth in polymeric

matrices, they may also alter the morphological and physical properties of the scaffolds (Nair et al., 2010).

### **2.2.5.3 Protein scaffolds**

The technique of using protein bubbles as porogens provides two distinct advantages. Firstly, the coating material is a biological polymer without any toxicity and secondly preparing scaffolds from microbubbles has a potential to function as a drug delivery mechanism in the matrix by incorporating biological molecules within the bubble shell or inside the core. The importance of proteins as biomaterials is mainly due their inherent tendency to deposit on surfaces as tightly bound adsorbents and the influence these deposits have on cell-surface interactions (Ekemen et al., 2011). In addition, their excellent biocompatibility and biodegradability, availability on large scale and low cost has brought about a great effort in developing applications for proteins as biomaterials.

Recently bovine serum albumin (BSA) microbubbles have been used as porogens with low toxicity and high biocompatibility to fabricate scaffolds (Lima et al., 2012). In addition to improvement in the porosity of scaffolds, albumin microbubbles can shield encapsulated growth factors from solvent denaturation. Nair et al. (2007) used a sonication technique to produce the BSA microbubbles and fabricated scaffolds by phase separation of a polymer solution mixed with microbubbles. Microbubbles produced using the sonication technique generally have a wide size distribution and therefore the scaffolds produced with this methods were not homogeneous. An alternative to this method is to use a microfluidic technique, whereby emulsions and foams characterized by monodisperse droplet/bubble sizes can be readily prepared. These systems could be used to generate porous materials with a highly consistent pore size (Wang et al., 2011, Chung et al., 2009).

In addition to microbubbles, particles containing growth factors have been incorporated into porous scaffolds (Hu et al., 2001). Encapsulation of drugs into polymeric microparticles, and subsequent injection, is a proven method of controlled delivery for bioactive agents (Enayati et al., 2009). Electrohydrodynamic (EHD) processing can produce uniform solid and encapsulated particles and fibres with diameters ranging

from a few nanometres to several micrometers in a single step, under ambient conditions, at low cost and without the need of high concentrations of additives or surfactants (Sofokleous et al., 2013b, Yoon and Kim, 2011). Moreover, multifunctional products (particles/fibres) loaded with therapeutic compounds (drugs, growth factors, DNA etc.) can be generated via co-axial electrohydrodynamic processing (CEHD) (Sofokleous et al., 2013a). However, there are limitations to incorporating polymeric particles/fibres into polymeric scaffolds due to the simultaneous equivalent solubility of the particles and scaffolds. Alternatively, protein-engineered biomaterials have the advantage of being able to combine desirable biocompatibility properties of natural ingredients to which tuning in with those of synthetic structures (Sengupta and Heilshorn, 2010). Proteins are complex organic macromolecules with inhomogeneous charge distribution that results in amphiphilicity, structural flexibility and bioactivity, and therefore play a significant role in reinforcement, structuring and functionalization of ceramics and tissue engineering scaffolds (Maas et al., 2013, Ekemen et al., 2011).

### **2.3 Stability of microbubbles and foams**

The generation and the breaking of liquid films cause the formation and collapse of foams and bubbles. In the absence of thermal or mechanical perturbation, the stability of the foam as an isolated system depends on its resistance to factors such as the gravitational drainage, drainage by capillary suction between regions with different radii of curvature (Laplace equation will be described in detail in (**chapter 4**) and finally gas diffusion through the liquid film induced by the pressure gradient between two bubbles (Laplace equation) (Beneventi et al., 2001).

Microbubbles can be stabilized by the effect of surface tension and can provide resistance to gas permeation. Microbubble shell used for biomedical applications is comprised of different materials including lipid, protein and polymer (**Figure 2.3**). The lipid molecules are held together through physical force fields, such as van der Waals interactions. The protein is cross-linked by covalent disulphide (structural unit composed of a linked pair of sulfur atoms) bonds. The polymer chains are covalently cross-linked and/or entangled to form a bulk-like material (Sirsi and Borden, 2009).

Diverse hard shells (made of gelatin, alginate, poly (ter-butyloxycarbonylmethyl) - glutamate, the biodegradable block copolymer poly (D,L-lactide-co-glycolide), polyelectrolyte multilayers, etc.) have been investigated (Gerber et al., 2006). Phospholipids are also being used as shell components. In biomedical applications, air bubbles dissolve rapidly in the blood under the combined action of Laplace pressure, arterial pressure, and oxygen metabolism. It has been demonstrated that the resistance of the phospholipid monolayer shell to gas permeation was a significant contributor to the stability of air-filled microbubbles. This contribution is particularly effective when the phospholipid is in the condensed state and increases with the phospholipid's chain length. However, the half-lives of these bubbles in partially degassed water do not exceed a few minutes. Alternately, bubbles can be stabilized using a perfluorocarbon (PFC) gas. PFCs, when used as part of the filling gas, retard bubble dissolution very effectively, due to very low water solubility.

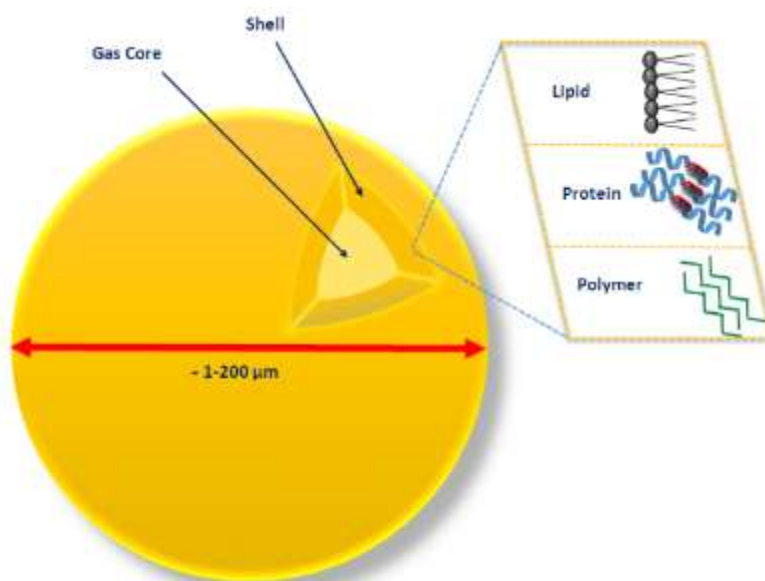


*Figure 2. 3: Schematic of microbubble shell and coating.*

### **2.3.1 Stabilisation by low diffusivity gases**

First generation microbubbles used in biomedical applications are microspheres with ordinary air. However, a few seconds after intravenous administration, air microbubbles disappear due to the high solubility of air in blood and the lungs filtering microbubbles, especially those with larger diameters. Microbubbles' stability and

survival was reached by coating them with a thin shell, like albumin, polymer or lipid. These microbubbles are capable of passing the pulmonary capillary bed, but cannot resist arterial pressure gradients. In order to increase the stability of microbubbles further, second generation contrast agents are filled with a high molecular weight gas such as sulphur hexafluoride or perfluoropropane with lower solubility. This therefore improves the survival and stability of bubbles under higher pressure (Dijkmans et al., 2004, Cui et al., 2005). Microbubbles stabilized by gases that have low Ostwald coefficients, yet relatively high saturated vapour pressures have recently been the centre of many biomedical applications. Researchers are investigating fluorocarbons (FCs) for a range of biomedical uses, including intravascular oxygen transport, ophthalmology, drug delivery, treatment of lung diseases, lung surfactant replacement preparations due to their biological inertness and extremely low solubility in water (Szijjár et al., 2012). Essentially all the commercially available or under development injectable soft-shell microbubble contrast agents for diagnosis are stabilized by fluorocompound gases, including sulphur hexafluoride, perfluoropropane, perfluorobutane, perfluoropentane, and perfluorohexane (Rossi et al., 2009). In addition, phospholipids are used in most of these agents as the main bubble wall component. The mechanism of bubble stabilization by FC-driven compounds has been assigned to retarding bubble dissolution in the blood due to osmotic counteraction of the blood pressure and Laplace pressure. It was predicted that bubble stability increases with decreasing Ostwald coefficient of the gas. Compounds with low vapour pressure usually have low Ostwald coefficients and vice versa.

### **2.3.2 Role of surfactants in microbubble stability**

The main phenomenon governing surfactant solutions foaming properties is the ability of surfactant adsorption at the air/liquid interface. In order for an aqueous solution to form a stable foam, three conditions must be fulfilled: firstly the solute must be surface active; secondly, the liquid film at the interface of the foam must have a low surface free energy; and finally the liquid film must have good elastic properties. In principle, the large variety of available surfactants lends great flexibility to the production of surfactant stabilized microbubbles.

If molecules are dissolved in the bulk liquid that are at least partially hydrophobic, then these molecules will be attracted to the gas liquid interface. These surface active molecules are generally named surfactants. Because surfactants are attracted to the gas-liquid interface, where the hydrophobic portion of the molecule can be expelled from the liquid phase, they displace water molecules from the interface, reducing the number of interfacial water molecules, in turn reducing the surface tension of the interface. This process of migration toward the interface and displacing of water molecules is called adsorption, and is generally explained by the hydrophobic effect. If a surfactant molecule is highly surface active, and the interface is already packed with surfactants, then the surfactant molecules sometimes self-assemble into structures called micelles, which effectively sequester the hydrophobic portions of the micelle-member surfactants from the water. The concentration at which one can expect the self-assembly of micelles is called the critical micelle concentration (CMC). If the bulk concentration of the surfactant solution is above the critical micelle concentration, then adsorption becomes more complicated. The adsorption kinetics will be coupled to the association and dissociation kinetics of the micelles in solution.

The molecular composition at the interface dominates the interactions between the interface and its surroundings. In the case of a gas bubble, the composition of the interface will determine mechanical properties, such as surface tension, which will affect the motion and deformation of the bubble in the blood stream (Eckmann and Diamond, 2004).

A rather delicate balance between the respective roles of surface tension, surface activity and adsorption kinetics guarantee stability of foams and bubbles. Therefore, for a surfactant molecule with a particularly short hydrophobic chain, a sufficient decrease in surface tension may not necessarily lead to the fast adsorption of the surfactant molecule. On the other hand, an exceedingly large hydrophobic chain might be too slow in reaching the fresh surface and again the foam stability cannot be maintained by decrease in surface tension. The interplay between these two opposite parameters in intermediate situations can favour or disfavour foam stability which depends on more specific factors (Beneventi et al., 2001).

### 2.3.2.1 Surfactant effect on microbubble stability

Due to the action of interfacial tension, microbubbles are naturally unstable. The effect of capillary pressure acting on a spherical microbubble surface can be expressed by the Laplace equation:

$$R_{Laplace} = 2\sigma/R \quad \text{Eq (2.1)}$$

where  $R$  is the instantaneous radius of the microbubble and  $\sigma$  is the surface tension. The diameter of microbubble in an unsaturated liquid will decrease exponentially as the gas diffuses into the surrounding under constant ambient conditions. The rate of dissolution of the gas depends on the magnitude of the surface tension, the concentration and diffusivity of the gas in the liquid, the ambient temperature and pressure, and the size of the microbubble (Epstein and Plesset, 1950, Reddy and Copper Jr, 1966). Epstein and Plesset (Epstein and Plesset, 1950) presented an equation for the rate of change of bubble size ( $\frac{dR}{dt}$ ) under constant surface tension ( $\sigma$ ), while they considered the effect of convection negligible:

$$\frac{dR}{dt} = \frac{D(C_i - C_{sat}(R))}{\rho(\infty) + \frac{2M}{3BT} \frac{2\sigma}{R}} \left[ \frac{1}{R} + \frac{1}{(\pi Dt)^{1/2}} \right] \quad \text{Eq (2.2)}$$

Where  $C_i$  and  $C_{sat}$  are the initial and saturation concentrations of the dissolved gas in the liquid, respectively,  $M$  is the molecular weight of the gas,  $B$  is the universal gas constant,  $T$  is the gas temperature,  $t$  is time and  $\rho(\infty)$  is the density of the gas at a zero curvature interface with a constant coefficient of dissolution,  $D$ . **Eq (2.2)** is for an uncoated bubble, hence the effects of surfactant coating is not considered. These can be included either by making diffusivity and surface tension functions of surfactant concentration at the gas-liquid interface as previously described by Mohamedi et al. (2012) or by introducing a “shell” term similar to the model proposed by Borden and Longo (2002). By introducing a surfactant layer on the microbubble surface the dissolution of the bubble is affected due to the decrease in interfacial tension as well as the restriction to the mass transfer of the gas in and out of the bubble surface by the surfactant film. The concentration of the surfactant on the bubble surface is an important subject to consider with respect to both phenomena (Mohamedi et al., 2012).

### 2.3.2.2 Surfactant types

Surfactants also known as surface active agents have amphipathic structures. The characteristic molecular structure of surfactants consists of a structural group that has very little attraction for the solvent, known as a lyophobic group, together with a group that has strong attraction for the solvent, called the lyophilic group (**Figure 2.4**).

Usually, the hydrophobic group is a long-chain hydrocarbon residue, and less often a halogenated or oxygenated hydrocarbon chain while the hydrophilic group is an ionic or highly polar group (Rosen and Kunjappu, 2012). Surfactants are classified in four groups depending on the nature of the hydrophilic group as:

- **Anionic:** The surface-active portion (hydrophilic group) of the molecule bears a negative charge. Examples of this type of surfactant include: alkylbenzene sulfonates (detergents), (fatty acid) soaps, lauryl sulfate (foaming agent), dialkyl sulfosuccinate (wetting agent) and lignosulfonates (dispersants) (Salagar, 2002). About 50 % of the world production of surfactants comprises of anionic type.
- **Cationic:** The hydrophilic head group bears a positive charge. A very large proportion of this type contains nitrogen compounds such as fatty amine salts and quaternary ammoniums, with one or several long chain of the alkyl type, often coming from natural fatty acids. Generally, this type of surfactants are more expensive compared to anionics, due to the high pressure hydrogenation reaction required during their synthesis. Therefore, when there is no cheaper substitute they are only used either as bactericide, or as positively charged substance. This enables them to adsorb on negatively charged substrates that provides antistatic and hydrophobant effect, often of great commercial importance such as in corrosion inhibition (Salager, 2002).
- **Zwitterionic:** This class contains both positive and negative charges in the surface-active hydrophilic head group. As a result, these can adsorb onto both negatively charged and positively charged surfaces without significantly changing the charge of the surface.

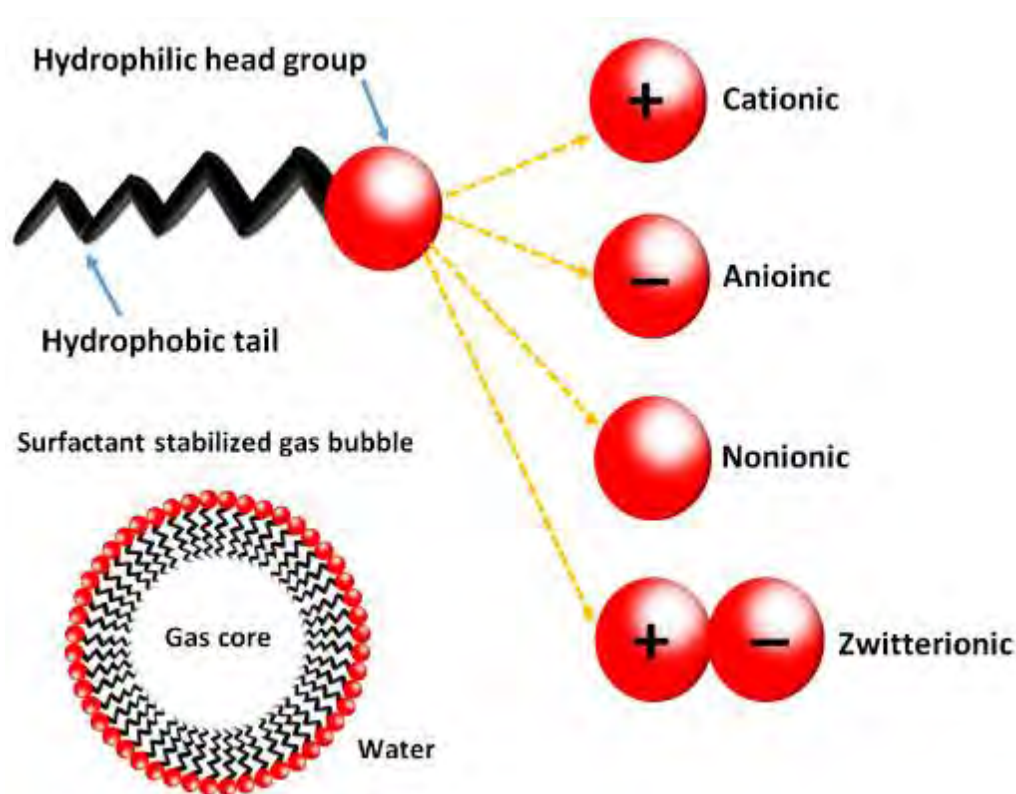


*Figure 2. 4: Surfactant classification according to their head group composition and schematic of adsorption monolayer of a gas bubble coated with surfactants.*

- **Nonionic:** These surfactants the hydrophilic head group contain are no apparent ionic charge. Around 45% of the overall industrial production of surfactants are nonionics, making them the second largest category. Due to their hydrophilic group being a non dissociable type (i.e. alcohol, phenol, ether, ester, or amide), nonionic surfactants do not ionize in aqueous solution. The presence of a polyethylene glycol chain makes a large proportion of these nonionic surfactants hydrophilic, which is achieved by the polycondensation of ethylene oxide. These are called polyethoxylated nonionics (Salager, 2002). On the other hand, the lipophilic group is often of the alkyl coming from fatty acids of natural origin or alkylbenzene type. The polycondensation of propylene oxide produces a polyether which (in opposition to polyethylene oxide) is slightly hydrophobic. This polyether chain is used as the lipophilic group in the so-called polyEO-polyPO block copolymers, which are most often included in a different class, e.g. polymeric surfactants.

## 2.4 Current preparation methods

In order to meet the demand for improved control over the characteristics of microbubbles a number of new preparation technologies have been developed. Over the past decade several techniques have been developed to generate microbubbles. Amongst these techniques, sonication and fractionation (Stride and Edirisinghe, 2008), electrohydrodynamic atomization (Cui et al., 2008, Farook et al., 2007) and microfluidic devices (Garstecki et al., 2004, Hettiarachchi et al., 2007) are the most commonly used methods. Generation of microbubbles with diameters smaller than 10  $\mu\text{m}$  from electrified cone jets using the electrohydrodynamic atomization (EHDA) technique was reported by Farook et al. (Farook et al., 2007), where the jet breakup and microbubbling zones were thoroughly investigated. Whilst much narrower than those obtained by sonication, the microbubble size distributions obtained with this method were not perfectly monodisperse. Microfluidic devices on the other hand offer an unparalleled level of control over microbubble size and size distribution (Chen et al., 2009, De Menech et al., 2008, Teh et al., 2008), facilitating the formation of microbubbles suitable for a diverse range of applications, including in the biomedical field (Ferrara et al., 2007, Hernot and Klibanov, 2008, Farook et al., 2009). One disadvantage of using microfluidics for preparing bubbles in the  $< 10 \mu\text{m}$  range, however, is the tendency for microchannels to become clogged.

A detailed review and comparison between the conventional bubble preparation technique, sonication, with two more recent methods, Electrohydrodynamic atomisation (EHDA) and microfluidic processing is described in this section. These methods vary in terms of their ability to produce bubbles, which are sufficiently small and stable for *in vivo* use in biomedical applications, microbubble uniformity, relative production rates and other practical and economic considerations.

### 2.4.1 Sonication

This method uses high intensity ultrasound to produce a suspension of gas microbubbles in a liquid containing either surfactant or polymer solution which forms a stabilising coating on the surfaces of the microbubbles (Suslick et al., 1999). This is

normally achieved either with the assistance of a sonicator or a high-shear mixer. Sonication can be accomplished via a number of methods. For instance, a vial containing a surfactant solution and gas in headspace of the vial can be sonicated through a thin membrane. Sonication can be performed by contacting the membrane with an ultrasonic probe or with a focused ultrasound “beam” (Prajapati and Agrawal, 2012). This method produces bubbles with a broad size distribution and it is necessary to filter out microbubbles having diameters  $> 10\mu\text{m}$  (Klibanov, 1999). This disadvantage of broad size distribution results in a wide range of microbubble resonance frequencies. The size distribution of the microbubbles produced depends upon the frequency, power and pulse regime of the ultrasound. Moreover, there is a wide variation in the properties of individual microbubble coatings which has a significant effect upon their dynamic and acoustic response (Wang et al., 1996). Whilst sonication is the most commonly used method for preparation of microbubbles, the relatively broad size distributions of suspensions need to be fractionated and/or filtered to remove any large bubbles (for intravenous use) and excess surfactant (Stride and Edirisinghe, 2009).

### 2.4.2 Coaxial Electrohydrodynamic Atomization (CEHDA)

Electrohydrodynamic atomization is a process where a liquid is passed through a capillary needle at a controlled flow rate and maintained at several kilovolts relative to a ground electrode few centimetres away. The liquid at the outlet of the capillary takes various shapes under the influence of the electric field (Tang and Gomez, 1994). One of the methods that produce microbubbles by this phenomenon is Coaxial Electrohydrodynamic Atomization (Farook et al., 2007, Stride and Edirisinghe, 2008). In this process, the simultaneous coaxial flow of a liquid medium (such as a lipid suspension) and a gas (in this case compressed air or nitrogen) under the influence of an external electric field allows the liquid to encapsulate the gas phase, and hence form bubbles. **Figure 2.5** illustrates a schematic of a CEHDA setup, where two needles are coaxially aligned and each supplied with fluid from a separate syringe pump.

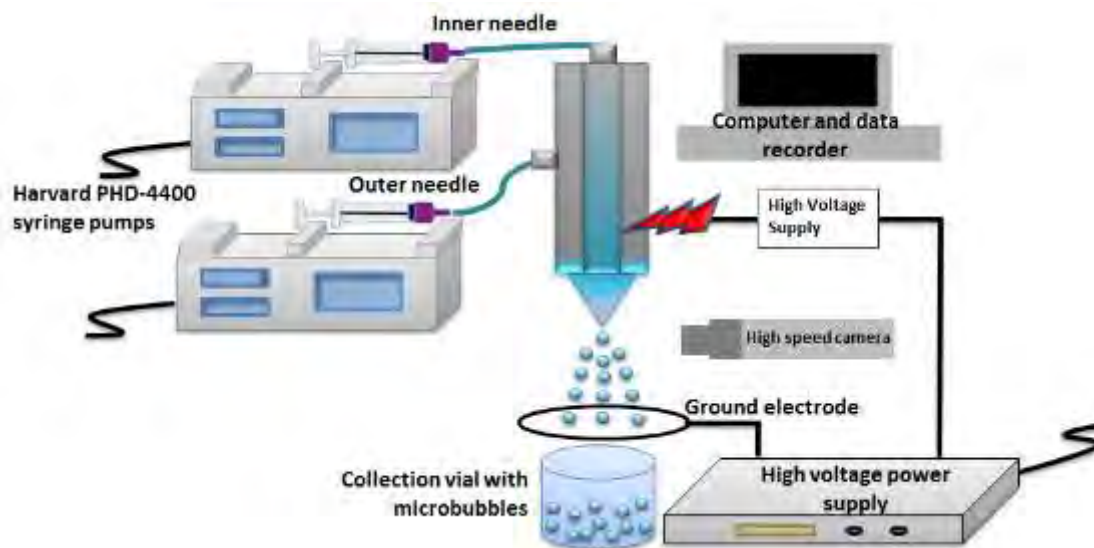


*Figure 2. 5: Schematic representation of the CEHDA setup.*

In order to form microbubble, the gas is supplied through the inner needle, whilst the outer needle is filled with a suspension of the coating material. An electrical potential difference of several kilovolts is applied between the needles and an earthed ring electrode positioned a short distance below the end tip of the needles. It has been shown that the uniformity and size of microbubbles are dependent on both the applied voltage and the gas and liquid flow rates (Farook et al. 2007; Stride and Edirisinghe, 2009). Although this method produces microbubbles with diameter in range of 1-10  $\mu\text{m}$  (suitable for medical applications), but the uniformity of the bubbles still remain a challenge to scientists.

#### **2.4.2.1 Electro spraying of nanoparticles**

One of the procedures that has been widely used in both industrial processes and scientific instrumentation is electro spraying. In this method, droplets are generated and charged simultaneously by means of an electric field. With regards to pharmaceutical applications, electro spraying is an acknowledged technique to produce nanoparticles. Electro spraying is an effective and reproducible method to enable micro and nano thin film deposition, micro/nanoparticle production, and micro/nanocapsule formation with high scalability (Jaworek, 2007).

### **2.4.2.2 Electrospinning of nanofibres**

Electrospinning has been recognized as a broadly used technique for the fabrication of electrostatic fibres which utilizes electric force to produce fibres with diameters ranging from micrometres (10-100  $\mu\text{m}$ ) to nanometres ( $\sim 100$  nm) from a wide range of materials such as polymers, composites, semiconductors and ceramics (Huang et al., 2003, Cooley, 1902, Bhardwaj and Kundu, 2010) Several characteristics appear at this level such as very large surface area to volume ratio, flexibility in surface functionalities, and superior mechanical properties (e.g. stiffness and tensile strength) (Huang et al., 2003).

Electrospun fibres are used in many applications including tissue scaffolds, protective clothing, filtration and nano-electronics (Ramakrishna et al., 2005) and food-grade films (Wongsasulak et al., 2013). Recent studies on electrospun fibres have been on the usage, characterisation and finding new applications of various materials that are electrospinnable (Ramakrishna et al., 2005). From the derivatives of the EHDA, electrospinning has been the process preferred for making scaffolds and films.

### **2.4.3 Microfluidic devices**

Microfluidic devices and methods that produce monodisperse liquid droplets and microbubble suspensions by means of controlling and manipulating fluids with the length scale on the order of a micrometre, has drawn considerable attention in the last decade (Zhao and Middelberg, 2011). The microbubble formation process in microfluidic devices occurs at an orifice at which a column of gas impinges upon a liquid flow. Subsequently, at a certain distance from the orifice, the gas–liquid interface becomes unstable and bubbles are formed by a “pinch-off” process (Stride and Edirisinghe, 2009).

The size and uniformity of bubble depend upon the physical properties of the liquid, the gas and liquid flow rates and the dimensions and profile of the orifice and channels. Microfluidic devices facilitate the formation of monodisperse microbubbles as they can be fabricated with internal dimensions on the micrometre scale.

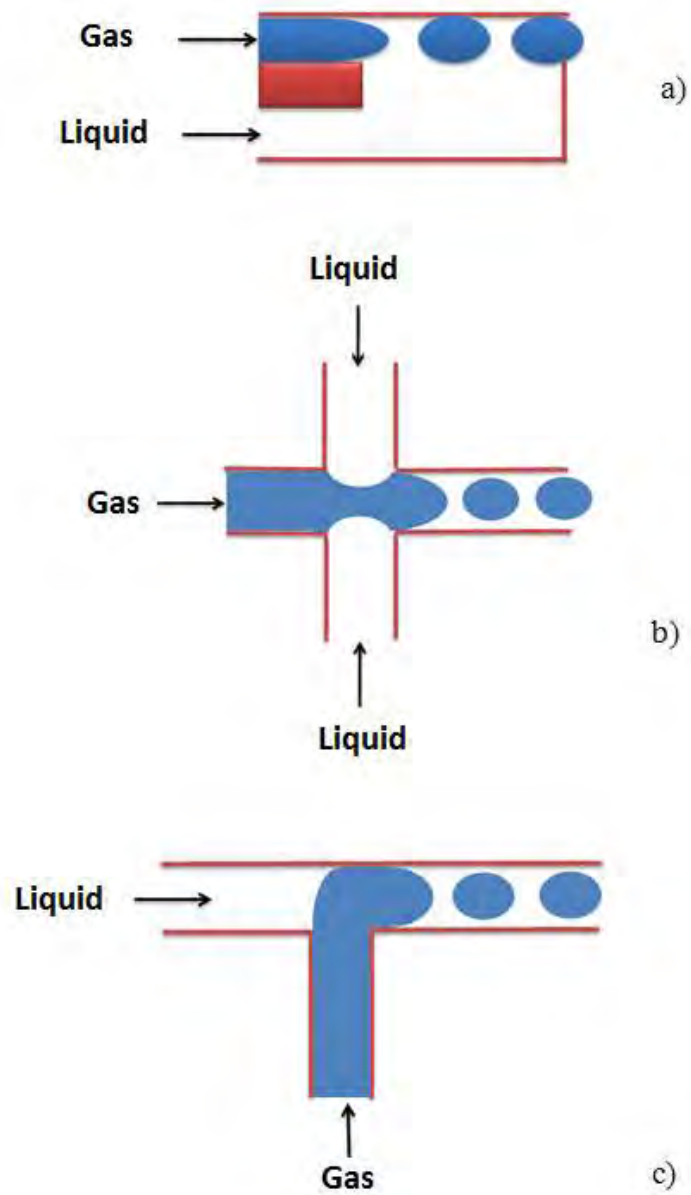


**Figure 2. 6:** Illustrations of the three main microfluidic geometries used for bubble formation. (a) Co-flowing, (b) flow focusing geometry, and (c) cross flowing streams in a T-shaped junction.

Recently there have been several methods investigated to build microfluidic structures to prepare monodisperse microbubbles using gas and liquid streams and microdroplets with two immiscible liquid streams, which include cross flowing devices (i.e. T-shaped junctions) (Zhang and Wang, 2009, Garstecki et al., 2006, Xu et al., 2006b), flow focusing devices (Fu et al., 2009, Nie et al., 2008) and others based on co-flowing rupturing method (Xiong et al., 2007, Castro-Hernandez et al., 2011), and the geometry dominated break up technique (Yasuno et al., 2004). The bubble/droplet formation process in a microfluidic device over the scale of the liquid flow at various rates and viscosities is dominated by viscous forces as well as the capillary forces and interfacial tension (Zhao and Middelberg, 2011). Bubble formation mechanisms vary between different microfluidic devices.

Microbubble and droplet formation are achieved by three main types of devices depending on the geometry of the device and the nature of the flow field near pinch off: 1) co flowing 2) flow focusing and 3) Cross flow technique (T-junction). **Figure 2.6** illustrates the geometry of these devices. Each of these methods uses a specific flow field to promote the uniform generation of microbubbles.

The geometry of the microfluidic device can be divided into two main groups. Firstly, those based on flow focusing generators and secondly, those that rely on the shearing of bubbles/droplets against a channel wall or edge (Martinez 2009). A complete description of these devices is provided in this section. The structure of the microfluidic device plays an important role in the control of liquid-liquid and liquid-gas flows. The most frequently used microfluidic geometries and the resulting flow patterns, particularly the three main structures: T-junction, flow focusing, and co-flowing, are described in this section.

### **2.4.3.1 Co flowing devices**

The co-flowing microfluidic system is one of the techniques used to produce monodisperse droplets/ bubbles (**Figure 2.6a**). In this device, droplets and microbubbles are formed when the dispersed phase (gas for microbubbles and liquid for droplets) is fed through a capillary or needle into the co-flowing continuous phase (Zhang and Wang, 2009, Hua et al., 2007). In order to form microbubbles, a gas column initially enters the mixing channel that is parallel to the liquid flow, consequently a bubble starts to grow and move downstream where the velocity component of the liquid

flow pushes the bubble surface against the channel wall and breaks up. The whole process is repeated when the gas thread returns to the mixing channel (Martinez, 2009).

#### **2.4.3.2 Flow focusing devices**

Flow focusing is another frequently used structure (Stone et al., 2004) (**Figure 2.6b**). This method has been widely used for producing spherical monodisperse droplets (Xu and Nakajima, 2004, Yobas et al., 2006) and microbubbles (Fu et al., 2009). Generally the continuous phase flows through two side channels and the dispersed phase is fed through a middle channel. The dispersed phase is squeezed and breaks up into spherical droplets or microbubbles at a mixing channel where the two phases meet (**Figure 2.6b**). Due to the confinement of the dispersed phase in the central region of the main channel, the flow-focusing device compared with T-junction microchannels usually generates spherical bubbles rather than slugs (Zhao and Middelberg, 2011). As a result, the bubbles can be protected from shear, and contact with the channel walls, that can cause adhesion or damage of the bubbles. The flow regime in microfluidic flow-focusing is divided into two different modes of dripping and jetting (Zhou et al., 2006). While jetting occurs at higher flow rates, the dripping regime occurs at low flow rates. Monodispersed microbubbles are formed at the outlet of the mixing channel in the dripping regime. By increasing the flow rate, the dispersed phase (gas column) infiltrates into the downstream channel, where the bubbles break up at the orifice where a neck forms. The flow focusing generators are categorised in to two axisymmetric and asymmetric geometries. A detailed description of these two geometries is presented here.

- *Axisymmetric Flow focusing devices*

Axisymmetric flow focusing devices are typically made by inserting capillaries inside square channels forming a coaxial arrangement where the liquid channel surrounds the gas channel and both merge into a single stream near a narrow exit where bubble breakup takes place (Martinez, 2009). This geometry is highly effective in flow focusing the gas phase, leading to the breakup of monodispersed bubbles with a narrow size distribution (<1%) at a high generation frequency. The liquid flow focuses the gas through a small orifice and a thin gas thread is formed. Contrary to liquid–liquid

systems, in which flow focusing leads to the formation of a thin liquid thread that increases in length with increasing flow rates, the length of the gas thread is very short and it breaks up at a constant frequency. Higher gas/liquid flow ratios lead to smaller monodisperse bubbles. In fact, the thread size becomes independent of the capillary tube diameter.

- *Asymmetric Flow focusing devices*

Asymmetric devices are generally manufactured either by etching or machining channels on a rigid substrate such as glass or by forming channels on PDMS rectangular blocks (Zhang and Wang, 2009, Garstecki et al., 2005a). Polydimethylsiloxane (PDMS) devices are fabricated using soft lithography to form a relieved channel pattern on the surface of a silicon wafer. These geometries are composed of a central channel that merges with two side channels into an exit opening in which the bubble/droplet breakup take place.

### **2.4.3.3 Cross flowing (T Junction) devices**

T-junction geometry is the most common method to form microbubbles and droplets in which the two phases are injected perpendicularly into the main flow channel. One of the most frequently used microfluidic geometries used to produce bubbles/droplets is the T-junction microchannel (**Figure 2.6c**) (Van der Graaf et al., 2006)( Garstecki et al. 2006; Xu et al. 2006a). Bubbles and droplets formation in these devices is remarkably different than that in the flow-focusing devices. Initially the dispersed phase (gas or liquid) enters the main fluid channel and a bubble/droplet starts to grow until it obstructs the channel. Due to the obstruction of the channel and the gradient in pressure the fluid flow distorts the bubble/droplet and the breakup occurs when the bubble/droplet in the upstream side touches the downstream side of the inlet channel. The diameter of bubble/droplet can be controlled by varying the ratio of the gas pressure, liquid flow rate and physical parameters, and the channel dimensions. Generally, flows in T-junction geometries occur in one of two modes:

- I. Cross-flowing (**Figure 2.7a**): In this geometry the dispersed phase is introduced from the perpendicular channel and the continuous phase flows through the horizontal channel, therefore the droplets/bubbles breakup is influenced by the cross-flowing shear force (Thorsen et al., 2001).
- II. Perpendicular flowing (**Figure 2.7b**) (Xu et al., 2006b, Pancholi et al., 2008): In this method contrary to cross-flowing, the continuous phase flow is fed through the perpendicular channel and the dispersed flow from the horizontal channel. Compared with the perpendicular flowing technique, the cross-flowing rupture technique produces droplets/bubbles with a narrower range of size.

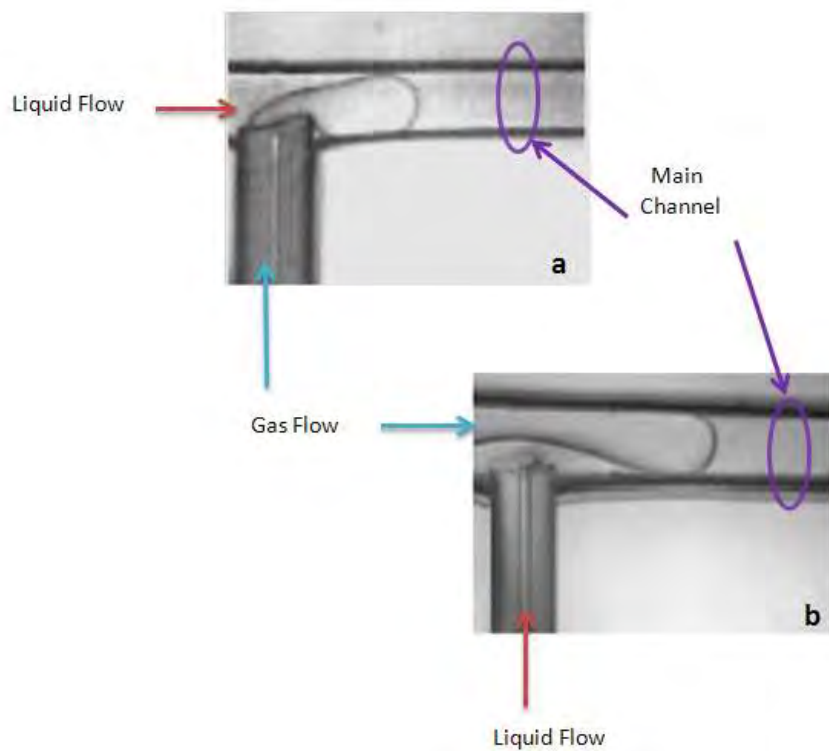


**Figure 2.7:** Types of flow in T-junction a) Cross-flowing and b) Perpendicular flow (Xu et al. 2006a)

## **2.5 Mechanism of bubble/droplet formation**

### **2.5.1 Formation of droplets or bubbles in microfluidic devices**

There have been various studies on the formation of bubbles and droplets to control size and uniformity in microfluidic devices (Xiong et al., 2007, Yasuno et al., 2004, Xu et al., 2006a, Garstecki et al., 2006). Bubble size is affected by the ratio of the gas/liquid flow rates as well as the physical properties of the continuous phase. Generally bubbles or droplets produced in microfluidic devices rarely coalesce with each other inside the capillaries prior to collection and therefore the studies are mainly focused on the area where the interface of the two phases occur and the bubbles or droplets form (Fu et al., 2009). It is fair to compare the behaviour of bubble formation in gas–liquid flows to droplet formation in liquid–liquid flows in a similar manner. In general, in microfluidic devices gas flows are much more unstable and difficult-to-control than their liquid counterparts and therefore bubble formation mechanisms have been widely investigated.

Xiong et al. (2002) performed experimental and numerical investigations on bubble generation in co-flowing devices and found that the bubble size is proportional to the ratio of the gas/liquid flow rates. The variation of liquid viscosity and surface tension produced different bubble shapes from slugs to spherical bubbles. Yasuno et al. (2004) proposed that the bubble size in the geometry dominated breakup technique increases with increasing viscosity of the continuous phase, but surface tension and flow rates do not affect the size. For the cross flowing rupture technique, Garstecki et al. (2006) reported that the bubble size is mainly determined by the ratio of the gas/liquid flow rates and the dominant effect in the break-up of either liquid or gaseous streams in the continuous fluid is the balance of hydrostatic pressures in the two immiscible fluids. Moreover, Xu et al. (2006) produced microbubbles with average diameters of 160 to 300  $\mu\text{m}$  using a cross flowing microfluidic device and suggested that the bubble size is also influenced by the viscosity of the continuous phase, while independent of the surface tension in T-junction microfluidic devices. Similarly, (Zhang and Wang, 2009) used a confined T-junction with rectangular cross section of the microchannel and investigated a range of bubble formation regimes applying the Young-Laplace equation and bubble volume as a function of gas inlet pressure, liquid flow rate, viscosity and

surface tension. Microbubble formation mechanisms vary between different microfluidic devices and are mainly provided by three aforementioned methods (**Figure 2.6**) depending on the geometry of the device and the nature of the flow field near pinch off. Each of these methods utilizes a specific flow field to promote the uniform breakup of microbubbles.

### 2.5.1.1 Capillary instability

Many researchers studied droplet and bubble formation in microfluidic devices and they related the process to the classical treatment of a capillary instability at a sheared, cylindrical interface in an unbounded flow (Rallison, 1984, Sherwood, 1984, Stone, 1994). The formation of monodisperse bubbles or droplets is associated with such instabilities in microfluidic devices. Ganan-Calvo et al. (Gañán-Calvo and Gordillo, 2001) were the first group of investigators to generate microbubbles at relatively high Reynolds numbers,  $Re$ , between  $10^2$  and  $10^3$ . The groups led by Stone (2004) were pioneers in experimenting the flow-focusing microfluidic devices, where  $Re$  was much smaller (typically between 0.01 and 1). They demonstrated that the interfacial forces dominate the breakup and the influence of inertia is often small compared with viscous effects. Contrary to the classical treatment of unbounded flows, the breakup of a cylindrical liquid or gas core into droplets or bubbles is influenced by the fluid confinement between microchannel walls (Garstecki et al., 2005a, Garstecki et al., 2006). Capillary instability is expected to generate liquid–liquid (Stone 2004) or gas–liquid (Cubaud and Ho, 2004, Garstecki et al., 2004) segmented flows with uniform droplet or bubble sizes in many applications.

There have been several attempts to characterize the dynamic behaviour of segmented flows in microfluidic devices as well as very irregular flow behaviour. Kraus et al. (Kraus et al., 2004) measured statistical properties (distribution of liquid slug and gas bubble lengths) in segmented gas–liquid flow and studied the sensitivity to external disturbances e.g. fluctuations of the pressure in syringe pump. Garstecki et al. (Garstecki et al., 2005b) investigated the dynamics of a single-channel microfluidic bubble generator by analysing the phase distribution and produced a model system for

studying complex systems in space and time. Garstecki et al. (2006) demonstrated that drops or bubbles breakup at a microfluidic T-junction at low capillary numbers ( $Ca$ ) occur due to the pressure drop across the emerging bubble or droplet and is irrelevant of the shear stress. Depending on the value of  $Ca$ , three different regimes of squeezing, dripping and jetting for the formation of droplets and bubbles were identified. Garstecki et al. (2006) demonstrated that in the squeezing regime the pressure fluctuations during breakup determines the droplet/bubble formation and breakup is independent of  $Ca$ .

### 2.5.2 Type of flow in microfluidic devices

Fluid actuation through microchannels can be achieved through two common methods. These two manners of fluid transport in most microfluidic systems are: pressure-driven or electrokinetically-driven flows. Fluid flow in the channels of microfluidic devices has most commonly been controlled using high precision mechanical pumps (Chakraborty et al., 2012). However the other type of flow in microchannels, broadly referred to as electroosmotic flow (Bayraktar and Pidugu, 2006), initiated by the application of an electric field, has also been studied extensively (Glasgow et al., 2004). This method of driving and controlling the operating fluid, has some distinct advantages in terms of the degree to which electrical forces can be localized in miniaturized devices and the relative ease with which high electric fields can be obtained (Zeng, 2011). Thus, in order to alleviate the difficulties of excessive pressure gradients associated with microfluidic pumps in microchannels, pressure driven flows are often replaced by electroosmotic flows (Lee and Li, 2006). The combination of electroosmotic and electrophoretic transport are referred as electrokinetic transport. (Molho et al., 1998) Electro-osmosis occurs when an aqueous solution moves in bulk past a stationary solid surface which is triggered by applying an external electric field. Electrophoresis describes the motion of a charged surface submerged in a fluid under the action of an applied electric field.

In order to manipulate microfluidic flows many kinds of external fields (pressure, electric, magnetic, capillary, and so on) are readily used. By decreasing the dimensions of the channels, the surface to volume forces become relatively more important. These flow manipulations can be achieved either by applying forces in macroscopic scale,

(e.g., at appropriate inlets and outlets), or can be generated locally within the microchannel by integrated components. For instance, at either a gas-liquid or liquid-liquid interface, it is possible to generate fluid motion by controlling spatial variations of surface tension (so-called Marangoni stresses)(Stone et al., 2004). Surface tension gradients can be created with thermal, chemical, electrical, or light gradients. Another possible way for fluid motion in channels is to partially wet the surfaces by using capillary pressure gradients. Young-Laplace law (described in detail in **Section 2. 6**) states that the latter can be created by varying either wetting properties (contact angle, surface tension) along the channel through one of the above mentioned methods, or changing the geometrical features (i.e. channel diameter).

Electrokinetics is an alternative method for controlling microflows that is now studied in a variety of forms. Electro-osmosis causing the fluid movement against the stationary charged solid surface; dielectrophoresis, which moves an interface (often a particle) due to electric field gradients; and electrowetting, modifying the wetting properties by applied electric field have all been studied previously.

There are many advantages that both capillary-driven and electrically driven flows can offer compared to the more familiar pressure-driven flows as dimensions shrink. However, surface contamination or heterogeneities can cause both to be hindered, or potentially even eliminated.

There are other means, in particular external fields, which can be used to control the motion of particles in the fluid, or by systematically distorting the channel walls. Amongst these external forces is magnetic fields that can influence flows directly or manipulate dispersed magnetic particles, as well as sound fields that can generate acoustic streaming motions, and cyclic deformation of a wall induced by peristaltic pumping. In order to provide additional control the surface characteristics of the device can also be varied for each manner of driving a fluid motion. This includes altering the geometrical, chemical, and mechanical features of the channel and network of channels. Additionally, the rheology of the fluid has a significant effect on the flow type, therefore it is important to consider both Newtonian and non-Newtonian fluids. Therefore, by considering the best way to mix, react, detect, analyse and separate in microflows, the combination of the driving forces and the surface characteristics is possible.

### 2.5.2.1 Pressure driven flows

Pressure driven flow occurs when the fluid is displaced within the device via positive displacement pumps, such as syringe pumps (Chakraborty et al., 2012). By being quite reproducible in pumping fluids through microdevices, pressure driven flows are relatively inexpensive and reliable compared to electrically driven flows. There have been increasing numbers of efforts to develop functional micropumps because pressure driven flow is more favourable to miniaturization. According to one of the basic laws of fluid mechanics (so-called no-slip boundary condition) for pressure driven laminar flow, the fluid velocity at the walls must be zero.

#### 2.5.2.1.1 Type of flow pattern and bubble shape

The type of flow pattern in a given microchannel is influenced by the properties of the fluid, the wetting characteristics of the channel surface, the diameter of channels and their cross-sectional shape. Dimensional analysis is used to reduce the number of parameters. However, the number of dimensionless groups remains large and mapping the flow studied in most literature (Serizawa et al., 2002) is only applied to the conditions under which the models were obtained. In order to obtain a better understanding of the flow regime behaviour, it is important to characterize multiphase micro-flows over significant ranges of parameters and provide meaningful dimensionless representation of the results in a systematic manner (Kim et al., 2011). Types of flows studied previously are categorised as following:

1. *Bubbly flow*: In this type of flow, droplets/bubbles with diameters that are smaller than the microchannel size are formed since the flow rate of the dispersed phase is much lower than that of one of the continuous phase.
2. *Segmented flow*: When the ratio of flow rates of the continuous to the dispersed phases reaches unity, droplets or bubbles are formed whilst they span most of the cross-section of the channel. The continuous liquid phase is confined between two consecutive droplets/bubbles.
3. *Annular flow*: This type of flow occurs when the ratio of flow rates for the continuous phase to the dispersed phase is very small and therefore the continuous phase is confined to the wall, flowing as an annular film. In channels

with non-circular cross-section the film thickness varies considerably along the perimeter, with a significant liquid volume confined to the microchannel corners. The film may become wavy as a result of the interaction with the non-wetting phase at higher velocities.

4. *Churn flow*: when the velocities are very high, regular flow patterns are replaced by chaotic flows, thus the droplets/bubbles sizes and shapes vary widely.

Depending on the wetting properties of the microchannel walls, the lubricating films of the continuous phase, that are found in segmented and annular flow, may break into droplets/bubbles of a characteristic size. The type of flow patterns explained above are shown in **Figure 2.8**.

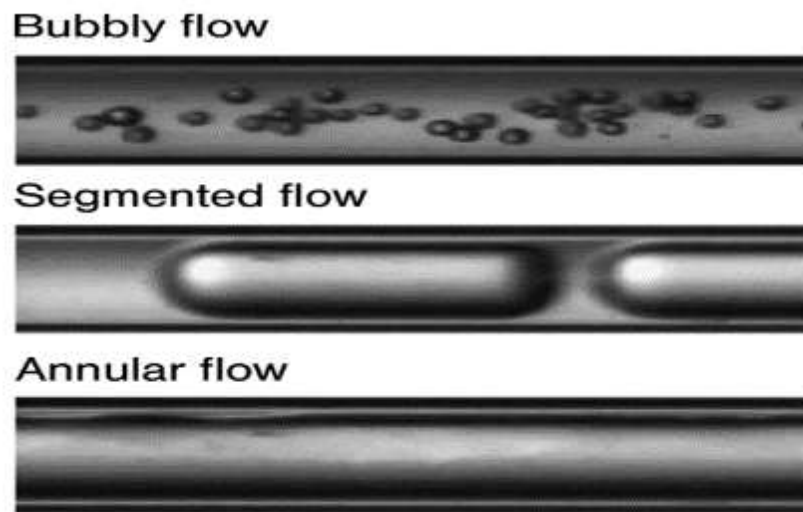


**Figure 2. 8:** *Illustration of the most common flow patterns are bubbly flow, segmented flow and annular flow (Serizawa et al., 2002)*

### 2.5.2.2 Electroosmotic flows

Electroosmotic pumping is another common technique for the control of fluids in microchannels (Reddy et al., 2005). The surface of a microchannel wall contains electric charge, where an electric double layer of counter ions is formed. By applying an electric field across the channel, the ions in the double layer move towards the

electrode of opposite polarity. Consequently, the fluid moves near the walls and transfers via viscous forces into convective motion in fluid bulk.

Electrically driven microfluidic devices have previously been used in many studies for mixing of two phase flows (Reddy et al., 2005), and generation of monodisperse droplets (Kim et al., 2006, Ahmadi et al., 2011, Sen et al., 2011), fibres (Ahmad et al., 2012, Srivastava et al., 2008) and microbubbles (Pancholi et al., 2008). Kim et al. (Kim et al., 2006) developed a microchip droplet generator using an electrohydrodynamic actuation method. Droplet formation was controlled by the application of an electric field between the charged liquid sample and a ground electrode without the need for an external pneumatic pump. Srivastava and coworkers (Srivastava et al., 2008) described a microfluidic based electrospinning method to fabricate hollow and core/sheath nanofibers. Of particular relevance to this study, Pancholi et al. (Pancholi et al., 2008) produced phospholipid coated microbubbles with diameters smaller than 8  $\mu\text{m}$  using a device consisting of a combined T-junction microfluidic and electrospraying device. However, size distribution of microbubbles produced in this study was still relatively broad.

A T-junction microfluidic device is one of the easiest methods of producing highly monodisperse microbubbles. However, to generate bubbles with diameters smaller than the geometrical diameter of the channels, using mechanically assembled devices is challenging due to constraints on capillary size, especially at higher viscosities (Parhizkar et al., 2013). As indicated above, the use of electric field can offer significant advantages for liquid manipulation in microchannels. The small channel cross sectional area presents high electrical resistance to ionic currents, which allows high electric fields to be maintained with low currents and hence control over the liquid velocity (Kim et al., 2011b). This in turn provides control over the breakup of the gas column formation of bubbles.

### **2.6 Scaling models for bubble breakup and size prediction in T-junction Devices**

Because of the flow complexity in T-shaped microchannels, there is no exact analytical expression for the prediction of droplet and bubble size. However, there have been several scaling models proposed to estimate the bubble size produced in a T-junction.

Thorsen et al. (Thorsen et al., 2001) suggested that the dynamics of droplet formation is dominated by the balance of tangential shear stresses and interfacial tension (i.e. the capillary number, as anticipated in unconfined shear flows. On the other hand Garstecki et al. (2006) proposed a mechanism they referred to as the squeezing process that is directly connected to the confined geometry where the bubble/ droplet forms. Based on the previous work carried out by Garstecki et al. (2006), when the capillary number ( $Ca_l = \mu_l u_l / \sigma_l$ ) is small, the dynamics of bubble formation is dominated by the pressure balance of continuous phase ( $P_l$ ) and dispersed phase ( $P_g$ ) at the junction. When the gas pressure in the capillary becomes higher than the sum of Laplace pressure and flowing resistance ( $R$ ), the bubble begins to grow. Laplace pressure decreases during the bubble growth process and the bubble size enlarges quickly as the pressure releases.

$$\Delta P_L = \sigma \left( \frac{1}{R_a} + \frac{1}{R_r} \right) \quad \text{Eq (2.3)}$$

$R_a$  and  $R_r$  are the principle radii of curvature in the horizontal and vertical plane respectively. The scaling model proposed by Garstecki et al. (2006) based on the mechanism of breakup can be expressed by **Eq (2.4)**.

$$L = d \left( \frac{Q_g}{Q_l} \right) + w \quad \text{Eq (2.4)}$$

Where  $L$  is the length of the slug,  $w$  is the width of the channel,  $Q_g/Q_l$  is the ratio of volume flow rates of gas and liquid phase respectively, and  $d$  is the characteristic width of the bubble, for which the value depends on the geometry of the junction.

$$Q_g = \frac{P_g - P_{lg}}{R} \quad \text{Eq (2.5)}$$

In **Eq (2.5)**,  $R$  is the resistance to flow in the channel and  $P_g - P_{lg}$  is the pressure difference between the gas inlet and outlet of the downstream channel from the junction. Based on the assumption that  $R$  would scale in a similar way as in a channel filled with continuous liquid, then:

$$R \propto \frac{\mu_l L_{gap}}{A^2} \quad \text{Eq (2.6)}$$

Therefore  $R$  is directly proportional to  $\mu$ . The model based on the scaling law proposed by Garstecki et al. (2006) is independent of the value of the capillary number and includes only the ratio of the rates of the flow. The proportionality constants for this scaling model which are independent of fluid properties, vary with several aspect ratios of the T-junction. Because  $Ca \leq 1$ , the interface of the forming bubble maintains the shape that minimizes the surface area, independent of  $Ca$ . Geometry plays a major role, in particular, in non-round channels. Van Steijn et al. (van Steijn et al., 2007) suggested that longer droplets or bubbles are formed in channels of near-square cross-section due to significant leakage past the forming droplet in the gutters, which reduces the speed with which the interface is squeezed. De Menech et al. (2008) presented numerical results that included both the squeezing (Garstecki et al. 2006) and shear-driven (Thorsen et al. 2001) types of breakup in dynamics of droplet formation in T-junction geometries. De Menech et al. (2008) identified a critical value of capillary number ( $Ca < 0.015$ ) below which the squeezing (rate of flow controlled) breakup mechanism occurs and for any values of capillary number above the critical value the shear dominated (dripping) mechanism is dominant.

The complex interplay between interfacial, gravitational, viscous and inertial forces is responsible for a variety of phase distributions and flow patterns. One of the characteristics of multiphase microflows is the combination of dominant interfacial forces with the laminar nature of the flow that create regularly shaped gas–liquid and liquid–liquid interfaces (Gunther and Jenson 2006). Multiphase microflows are influenced by the ratio of viscous to surface forces, the capillary number ( $Ca$ ) and by the ratio of fluid viscosities:

$$Ca_c = \frac{\mu_c u_c}{\sigma} \quad \text{and} \quad Ca_d = \frac{\mu_d u_d}{\sigma} \quad \text{Eq (2.7)}$$

Where,  $\mu_c$  and  $\mu_d$  are the viscosities of the continuous and the dispersed phases, respectively.

The dimensionless Bond number describes the ratio of interfacial forces with respect to gravity:

$$Bo = (\Delta\rho)gd_h^2\sigma^{-1} \quad \text{Eq (2.8)}$$

Where  $\Delta\rho$  is the density difference between the two immiscible fluids (gas–liquid, liquid–liquid) and  $d_h$  the characteristic channel dimension, the hydraulic diameter ( $d_h = 4A/\Gamma$ , where  $A$  is the channel cross-sectional area and  $\Gamma$  is the wetted perimeter).

The ratio of inertia to surface forces is expressed by the Weber number:

$$We = \frac{\rho u_d^2 d_h}{\sigma} \quad \text{Eq (2.9)}$$

Regarding the single-phase flows, the Reynolds number,  $Re = We/Ca$ , relates viscous and inertial forces and is fixed for given  $We$  and  $Ca$ . **Figure 2.9** (Gunther and Jensen, 2006) demonstrates the relevance of Bond, capillary and Weber numbers, i.e. the relevant forces with respect to the interfacial force, by altering the channel hydraulic diameter,  $d_h$ , and the velocity,  $u_d$ . The practical range of fluid properties for organic–gaseous, organic–aqueous and aqueous–gaseous systems are represented by the thickness of the planes obtained. The interfacial forces dominate over gravity, inertial and viscous forces at low velocities and small microchannel sizes. However, inertial forces dominate over gravity and viscous forces when  $u_d$  is on the order of several meters per second or in the presence of very large accelerations of liquids at the initial stage of rapid expansion of a vapour bubble. Bubbles and droplets much smaller than  $d_h$  can be formed under these conditions, where microbubbles/droplets can be entrained, potentially resulting in fluid interfaces with complex shapes or interfacial instabilities.

### 2.6.1 Governing forces in the presence of electric field

According to electrohydrodynamic theory (Chen et al., 2007, Quan et al., 2011), electric Korteweg-Helmholtz force density exerted on the fluid can be written as:

$$f_e = \rho_e E - \frac{1}{2} E^2 \nabla \epsilon + \frac{1}{2} \nabla (E^2 \frac{d\epsilon}{d\rho} \rho) \quad \text{Eq (2.10)}$$

Where  $\rho_e$  is the volume charge density,  $\rho$  is the liquid density,  $\epsilon$  is the dielectric constant for the liquid and  $E$  is the electric field strength. The first term in **Eq (2.10)** represents the Coulomb force acting on the free charge and can be neglected when the current is small. The second term is the dielectrophoresis force (DEP) exerted on the liquid due to the spatial gradient in the permittivity (Oh and Kwak, 2000), which is classified as the main force acting on the liquid-gas interface.

$$F_{DEP} = \frac{2\pi D_b^3 \varepsilon_l (\varepsilon_g - \varepsilon_l)}{\varepsilon_g + 2\varepsilon_l} \nabla E^2 \quad \text{Eq (2.11)}$$

Where  $D_b$  is the bubble diameter and as shown in **Eq (2.11)**, the diameter of the bubble is inversely proportional to the electric field strength, i.e. the voltage supply through a fixed distance. Since the dielectric constant of a gas is smaller than that of a liquid, the DEP force at the liquid-gas interface will act towards the centre of the bubble. In the presence of the electric field, an emerging bubble into the outlet channel becomes polarized and similar to an electric dipole an excess of positive charge at one end and an excess of negative charge at the other accumulate on the interface between the two phases. When the electric field is applied, a growing bubble with a relative permittivity lower than its surrounding medium will be driven towards the place of lower field intensity since the forces acting on the two ends are not equal, i.e. the bubble moves away from the contact area due to the much lower relative permittivity of the bubble compared with the liquid.

Finally, the third term in **Eq (2.10)** refers to the electrostriction force caused by a non uniform electric field. By varying the pressure distribution in the liquid phase, this force increases the elongation of the gas column into the outlet channel.

In the absence of an electric field, the competition between liquid and gas pressure, viscous forces and interfacial tension controls the breakup of the gas column into bubbles. Once the sum of viscous stress and pressure difference due to the obstruction of channel by the emerging gas column exceeds the capillary pressure, detachment begins. The capillary force  $F_\sigma$  is given by the difference between the Laplace pressures at the upstream and downstream ends of the emerging bubble multiplied by the projected area of the emerging interface (where  $R_1$  and  $R_2$  are the radii of curvature and  $A_{interface}$  is the projected area).

$$F_\sigma \approx \sigma \left( \frac{1}{R_1} + \frac{1}{R_2} \right) A_{interface} \quad \text{Eq (2.12)}$$

Viscous shear force  $F_\tau$  is given by the product of viscous stress acting on the emerging interface and the projected area of the emerging interface.

$$F_\tau \approx \mu_l Q_l A_{interface} \quad \text{Eq (2.13)}$$

And finally similar to Garstecki et al. (Garstecki et al., 2006) the squeezing pressure force  $F_p$  as a product of characteristic pressure ( $\Delta P_c$ ) arising from lubrication analysis for pressure-driven flow and emerging interface area:

$$F_p \approx \Delta P_c A_{interface} \quad \text{Eq (2.14)}$$

The dielectrophoresis force predominates capillary pressure force that is resisting the bubble breakup just after bubbles are detached. When an electric field is applied, electrical charge accumulates at the gas liquid interface which behaves as a capacitor. As the voltage increases, the charge build up at the interface increases resulting in a higher attraction of the gas stream downstream. The resulting elongation of the gas column in the axial direction and radial compression accelerates the breakup process and therefore leads to smaller bubbles.

### 2.6.2 Role of channel geometry

The layout of many microfluidic channel networks is created in a 2D plane lithographically and then extruded into the third dimension, either by etching the bulk material (e.g. dry etching in silicon, glass and quartz) (Zhang and Wang 2009; Garstecki et al. 2005) or by patterning the channel into a layer of negative resist, resulting in (near) rectangular cross-section microchannels with close to vertical side-wall profiles. Most university based or commercial microfabrication facilities use dry etching tools as standard equipment for manufacturing microelectromechanical systems (MEMS). By looking closer it is revealed that many of the underlying theories were originally developed either for an unbounded system (no channel walls) or for circular cross-section channels.

Computational and theoretical studies prefer round channels where only two-dimensional, i.e. axisymmetric flows occur. In multiphase microfluidics, in order to extrapolate theoretical predictions for axisymmetric studies to non-round channels considerable care must be taken. The shape of the channel in bubbly flows is less effective than for droplet systems where the effect is considerable due to the dispersed phase having dimensions comparable to the channel size. However in both flows, the dominance of surface tension ensures that fluid–fluid interfaces maintain smooth curvatures and conform poorly to the sharp microchannel corners.

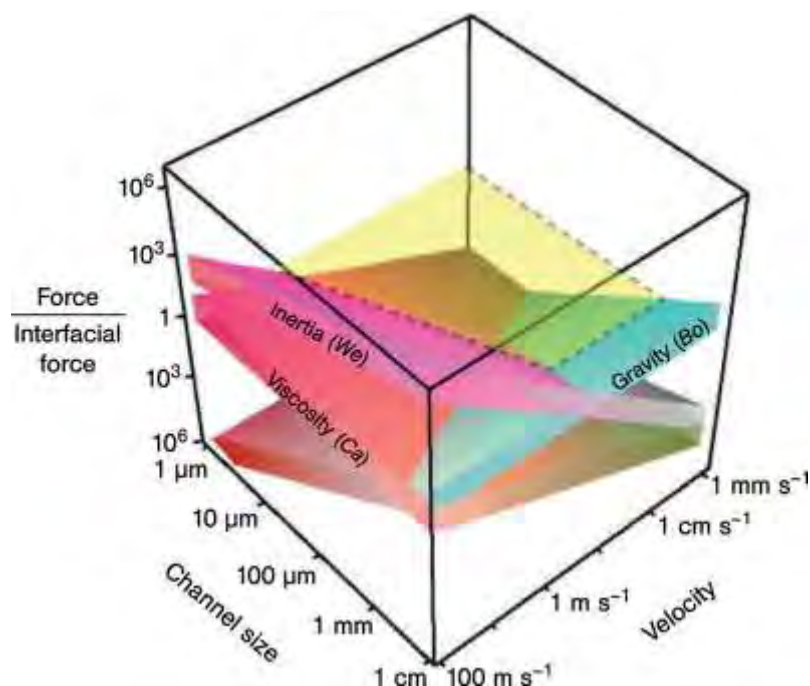


**Figure 2. 9:** Inertial, viscous and gravitational body forces, relative to interfacial forces, as a function of the channel size and characteristic velocity in microfluidic multiphase systems (Gunther and Jensen 2006).

### 2.6.3 Role of flow parameters on bubble size

By varying the flow rates of the continuous and dispersed phases in T-junction microchannels, mainly two types of flow patterns are created (plug flow and droplet/bubbly flow). In plug flows, the length of the plug decreases with the flow rate ratio of the continuous phase to the dispersed phase ( $Q_c/Q_d$ ) and the total flow rate in cross-flowing mode. However, in the perpendicular flowing regime, the plug length is influenced only by  $Q_c/Q_d$ , and is independent of the total flow rate. Furthermore, the plug length is smaller for the cross-flowing rupture technique than using the perpendicular shear force technique (Xu et al., 2006c). However, in the case of droplet flows, droplet formation in the perpendicular shear rupture process is similar to that in the cross-flowing rupture process (Thorsen et al., 2001). The droplet diameter decreases linearly with the flow rate of the continuous phase  $Q_c$ , but is independent of the flow rate of the dispersed phase  $Q_d$ . The droplet size also decreases with the total flow rate. The average droplet size produced by cross-flowing rupture is larger than that produced by the perpendicular shear force technique.

In cross-flowing shear induced droplet formation (Tice et al., 2004), three regimes were observed when varying the flow rate. When the flow rate is low, the interfacial tension force dominates, which enables the sharp breakup of plugs. However, as the relative viscous force and flow rate increase, the interfacial tension force is not sufficient for sharp breakup; therefore, the dispersed-phase flow remains laminar for some distance before the shear-off takes place (Tice et al., 2004). These three regimes have also been revealed in a numerical study of droplet formation in T-junction microchannels, and are named as squeezing, dripping and jetting (De Menech et al., 2008).

### **2.6.4 Role of liquid properties on bubble formation**

#### **2.6.4.1 Interfacial tension**

Due to the large surface area to volume ratio at micrometre scale, the role of surface effects becomes noticeable. Usually surfactants are added to the continuous or dispersed phase to achieve regular droplet/bubble formation. In T-junction microchannels using surfactants in solutions reduces the droplet/bubble diameter compared with those systems without surfactants (van der Graaf et al., 2005). In addition, increasing concentration of surfactant in the continuous phase lead to a decrease in droplet/bubble size. In flow-focusing microchannels, even smaller droplets are formed whilst surfactants are present in the dispersed phase (Wu et al., 2008). Xu et al. (2006d) proposed that surfactants with higher concentrations than the critical micellar concentration (CMC) are required to form ordered droplets. In the microchannel emulsification process, the effect of surfactant concentration varies with the viscosity of the dispersed phase. Below the threshold value, the role of the surfactant concentration in the continuous phase is negligible on the droplet size. While at higher than the threshold value, droplet size is affected by the surfactant concentration (Kobayashi et al., 2005b). Surfactants play an important role in droplet and bubble formation processes. Surfactants not only can reduce the equilibrium interfacial tension, but they can also prompt dynamic effects by changing dynamic interfacial tension, inducing interfacial tension gradients, and by altering interfacial rheology (van der Graaf et al., 2004). These effects on droplet/bubble formation are generally complex and they have been poorly investigated. When droplets are formed,

the dynamic interfacial tension between two liquid phases is neither constant nor uniform. The dynamic interfacial tension effect becomes more dominant at low surfactant concentrations.

#### **2.6.4.2 Surfactant effect**

Surfactants can alter the interfacial stresses in a complicated manner under dynamic conditions. The surfactant mass transfer dynamics and the amount of surfactant adsorption are the key factors that can result in the surfactant to have the ability to either resist or enhance the droplet/bubble formation. Surfactants can also cause droplets/bubbles to break under flow that would otherwise be stable in their absence (Baroud et al., 2012, Eggleton et al., 2001). The gravitational and inertial effects are generally insignificant in comparison to interfacial and viscous forces in microfluidic devices. As well as Capillary number ( $Ca = \mu \frac{u_l}{\sigma}$ ) that describes the ratio between viscous to interfacial forces, fluid wetting plays a central role in determining the flow regime. Wetting behaviour of solid surfaces in the presence of surfactants depends on the physical chemistry, concentration at gas-liquid interfaces and concentration along gas-liquid-solid contact line (Yang et al., 2004). Contact angle affects the movement of the three phase contact line and therefore have an impact in the force balance at the bubble breakup region and as a result have an impact on the size and formation of bubbles (Shao et al., 2008).

When the surfactant molecules are adsorbed at the interfaces (either gas-liquid or liquid-solid), the dynamic surface tension of the liquid as well as the interfacial tension between the liquid and solid is reduced depending on the level of adsorption. Consequently, the dynamic contact angle decreases for the hydrophobic solid-liquid-air systems with low energy. However, in the case of hydrophilic solid-solution-air systems, the adsorption of surfactant molecules at the liquid-solid interface does not always reduce the solid-liquid interfacial tension (Chaudhuri and Paria, 2009, Tostado et al., 2011). Surfactant molecules are adsorbed with their polar heads in the aqueous solution and their tails on the interface (Xu et al., 2006b). Nonionic surfactants, on the other hand, adsorb onto surfaces with either the hydrophilic or hydrophobic group oriented toward the surface, depending upon the nature of the surface (Rosen and

Kunjappu, 2012). Since the surface of microchannel walls is nonpolar, the nonionic surfactants are oriented with their hydrophobic group toward the surface, and therefore make it more hydrophilic.

### 2.6.4.3 Viscosity

Regular plugs or spheres can be formed in T-junction microchannels for both lower viscous ( $\mu_l$  or  $\mu_g \leq 2.0$  mPa s) and higher viscous ( $\mu_l$  or  $\mu_g \geq 18$  mPa s) dispersed and continuous phases. Three regimes of squeezing, dripping and jetting occur depending on the different combinations of low and high viscosity of dispersed and continuous phases (Tice et al., 2004). The viscosities of the continuous and dispersed phases combined with the channel geometrical features and properties influence the droplet/bubble size. However, sometimes even in the same microchannel the behaviour of the flow can be complicated. Several dimensionless parameters are introduced in order to simplify the complex interactions between different properties, as seen in section 2.6. As a result, the effect of viscosities on droplet/bubble formation is generally defined through the Capillary number.

### 2.6.5 Microchannel surface characteristics and wetting

The interfacial properties play a dominant and crucial role in the micrometer scale. Fluid–wall and fluid–fluid are attributed as the interfaces in microfluidic two-phase flows. The wetting properties of the fluid–wall interface are extremely important in determining whether ordered or disordered flow patterns occur (Dreyfus et al., 2003). When the continuous phase completely wets the microchannels, ordered patterns can be obtained. On the other hand, in partial wetting conditions, flow patterns become disordered. Hydrophobic devices are typically used to produce water-in-oil (W/O) droplets. While oil-in-water (O/W) emulsions are formed in hydrophilic channel devices. The hydrophobicity or hydrophilicity property of a solid surface can be expressed quantitatively by contact angles. Xu et al. (2006d) established that at contact angle lower than  $90^\circ$ , disordered flow patterns can only be produced; contrarily, for contact angles higher than  $90^\circ$ , ordered flow of droplets can be observed. By adding

surfactants at different concentrations, the contact angle can be adjusted (Xu et al., 2006b). For instance, when surfactants are added into the water phase, when the concentration of sodium dodecyl sulfate (SDS) is higher than the critical micelle concentration (CMC), the PMMA surface that is characteristically hydrophobic will be totally converted to be hydrophilic (Xu et al., 2006c).

## **2.7 Microfluidic device material and fabrication methods**

Three important aspects in the fabrication of microfluidic devices, including material, tooling and processing methodologies, and measurements must be considered. The choice of materials should be based on the device performance, response to manufacturing methods, device structures, and others. In order to fabricate microfluidic devices there are potentially a variety of abundant materials. Many materials have been previously used to make microfluidic devices, such as silicon, quartz and glass, polydimethylsiloxane (PDMS), poly(methyl methacrylate) (PMMA), polytetrafluoroethylene (PTFE), polyethylene terephthalate (PET) (Yussuf et al., 2007). Due to their good biochemical performance and low cost polymeric materials are used in a wide range of applications in microfluidic devices. Prediction of the behaviour of the material during processing is a critical work for not only the design of the processing equipment but also for process control.

From the simplest mechanical machining to complicated lithography to the nano-imprinting techniques, the conventional tooling and processing methodologies have been the centre of interest for many applications (Fiorini and Chiu, 2005). Sometimes, different techniques are integrated to make one microfluidic device. Generally, the tooling and processing of polymer microfluidic devices are categorised into two types: direct tooling techniques and the mold based processing techniques.

It is necessary to check and measure microfluidic devices for defect detection, bonding quality inspection, and critical dimensional and functionality characterization (Li et al., 2008). The measurement results provide the feedback information for process control and the product quality characterization.

## 2.8 Summary of the literature

A detailed literature survey was presented in this section, and the summary of the key points are as follows:

- Initially, the applications of microbubbles in various industries, especially in biomedical field, have been explained. A thorough literature review of the use of microbubbles as progens for the construction of protein scaffolds, which is of particular relevance to this work, has been presented.
- The requirements for microbubbles to be used in many applications are the stability and uniformity. The factors affecting the stability of bubbles such as the coating material as well as the choice of the gas were all revealed.
- The principles of microbubble formation using different methods of production has been reviewed. Microfluidic devices are established to be reliable techniques in production of uniformly sized microbubbles/droplets.
- Different types of microfluidic geometries as well as the type of flows inside the microchannels were described. Microfluidic pressure driven and electroosmotic flows were looked at in detail.
- In addition, the parameters influencing the formation of bubbles/droplets in microfluidics as well as the governing forces were defined in this chapter. The comparison between the scaling models proposed by researchers on various microfluidic geometries were presented.
- Finally, the methods of manufacturing microfluidic devices from lithography to direct tooling and the materials used to fabricate them were presented.

## Chapter 3

### Experimental details

#### 3.1 Introduction

This chapter describes the materials and procedures used for the experiments subsequently detailed in this Thesis. The materials used, corresponding suppliers and product details are given. The methods used to characterise the materials and solutions are described. A detailed description of the equipment used with the capillary embedded T-junction with and without electrohydrodynamic focusing also given. All experiments were repeated to ensure reproducibility. All equipment was calibrated and measurements were checked against known values quoted by the supplier or in the literature.

#### 3.2 Materials

The main materials used in the experiments conducted for the evaluation of bubble formation and size using the capillary embedded T-junction were aqueous glycerol solutions combined with various surfactants, such as sodium dodecyl sulfate (SDS), cetyltrimethyl ammonium bromide (CTAB), polyoxyethylene (40) sorbitan monopalmitate (Tween 40) and polyoxyethylene glycol 40 stearate (PEG 40S). For the experiments conducted to produce nanoparticle/fibre loaded scaffolds, bovine serum albumin (BSA), L- $\alpha$ -Phosphatidylcholine hydrogenated (phospholipid), poly (lactic-*co*-glycolic acid) (PLGA), polymethylsilsesquioxane (PMSQ) as well as collagen (Type I solution from rat tail), acetone and ethanol were used. A list of all the materials used in the experiments are shown in **Table A.1**.

### 3.2.1 Glycerol

Glycerol with 99% purity ( $C_3H_8O_3$ , density  $1261 \text{ kg m}^{-3}$ , molecular weight 92.09, viscosity  $1.4 \text{ Pa s}$  Sigma Aldrich, U.K.) was diluted with distilled water. Aqueous glycerol solutions are widely used in experimental studies of flow phenomena. Experiments conducted with glycerol solutions facilitate investigation of flows in a wide range of Reynolds numbers (Cheng, 2008).

### 3.2.2 Surfactants

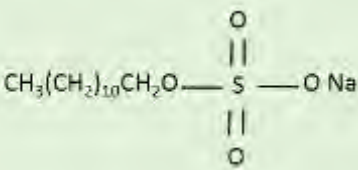
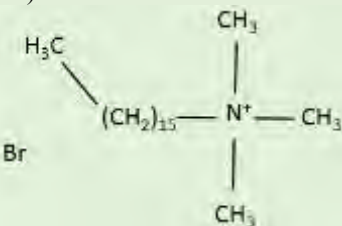
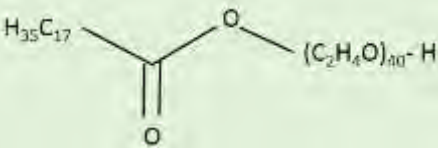
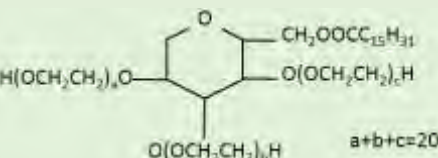
The surfactants used in this study in order to facilitate the formation of bubbles are described as the following:

*SDS*: Sodium dodecyl Sulfate (SDS, Sigma Aldrich, UK) and sodium lauryl sulfate, (SLS, VWR, UK) both from the same family of an anionic surfactant, usually a mixture of sodium alkyl sulfates, mainly the lauryl; lowers surface tension of aqueous solutions; used as fat emulsifier, wetting agent, detergent in cosmetics, pharmaceuticals and toothpastes; also as research tool in protein biochemistry.

*Tween 40*: Polyoxyethylene (40) sorbitan monopalmitate (Tween 40, Sigma Aldrich, UK) is a nonionic detergent used for many pharmaceutical and food applications. They are also used in the cosmetics industry to solubilize essential oils in to water based products. Tweens are considered to be inherently biodegradable.

*PEG 40*: Polyoxyethylene glycol 40 stearate (PEG 40S, Sigma Aldrich) is a nonionic surfactant and has been found to be nontoxic and is approved by the FDA for use as excipients or as a carrier in different pharmaceutical formulations, foods, and cosmetics.

*CTAB*: Cetyltrimethyl ammonium bromide (CTAB, Sigma Aldrich, UK) is a cationic surfactant widely used in the synthesis of gold nanoparticles as well as cosmetics and pharmaceutical industries.

Surfactant	Formula	Molecular weight / g mol <sup>-1</sup>	CMC in water / wt.%
Sodium dodecyl sulfate (SDS) 	Na C <sub>12</sub> H <sub>25</sub> SO <sub>4</sub>	288.4	0.17-0.23
Cetyltrimethyl ammonium bromide (CTAB) 	C <sub>19</sub> H <sub>42</sub> BrN	364.5	0.03
Polyoxyethylene glycol 40 stearate (PEG 40S) 	C <sub>18</sub> H <sub>35</sub> O <sub>2</sub> (C <sub>2</sub> H <sub>4</sub> O) <sub>n</sub> H, n=40	2047	0.01
Polyoxyethylene (40) sorbitan monopalmitate (Tween 40) 	C <sub>22</sub> H <sub>42</sub> O <sub>6</sub> (C <sub>2</sub> H <sub>4</sub> O) <sub>n</sub> , n=20	1277	0.003

**Table 3. 1:** Physico-chemical characteristics of surfactants (data for CMC and Molecular weight were obtained from Prakash (Prakash, 2010) and Sigma Aldrich, UK).

### 3.2.3 Phospholipid

L- $\alpha$ -Phosphatidylcholine from egg yolk, Type XVI-E,  $\geq 99\%$  (TLC), lyophilized powder (Sigma Aldrich, UK). Typical lots of egg yolk phosphatidylcholine have fatty

acid contents of approximately 33% 16:0 (palmitic), 13% 18:0 (stearic), 31% 18:1(oleic), and 15% 18:2 (linoleic) (other fatty acids being minor contributors), which would give an average molecular weight of approximately 768 g/mol. Phosphatidylcholine is the major membrane phospholipid in eukaryotic cells. In addition to being the major structural component of cellular membranes, phosphatidylcholine serves as a reservoir for several lipid messengers. Phosphatidylcholine is used for preparation of vesicle suspensions commonly called liposomes or as monolayers.

### **3.2.4 Bovine serum albumin (BSA)**

Bovine serum albumin (BSA, Sigma Aldrich, UK) is a large protein (66.5 kDa) composed of 582 amino acid residues. The BSA molecule is made up of three homologous domains (I, II, III) which are divided into nine loops (L1-L9) by 17 disulphide bonds. Due to its homology to human serum albumin, low cost and being biologically inert (Waldmann et al., 1977), BSA has been used as a model drug. BSA as a biomaterial has been immobilized in composites to enhance surface properties and cell interactions. Bovine serum albumin (>96.0% lyophilized powder, essentially fatty acid free and globulin free, molecular weight 66,430 Da, Sigma Aldrich, U.K) was used as the main coating material. BSA is used as a model polymeric drug and as a coating material for microbubbles and spheres as contrast agents and in the field of drug delivery.

### **3.2.5 Polymethylsilsesquioxane (PMSQ)**

Polymethylsilsesquioxane (PMSQ) with an average molecular weight of 7465 g mol<sup>-1</sup> was obtained from Wacker Chemie AG, GmbH (Burghausen, Germany). Polymethylsilsesquioxane (PMSQ) is a hybrid polymer with good thermal stability due to its organic–inorganic nature. PMSQ is a chemically stable polymer, which is highly hydrophobic, unreactive and has been used in vivo due to its non-toxicity and biocompatibility for several decades (Gunduz et al., 2012). It has applications in skin care products. It has been previously subjected to electrohydrodynamic and

microfluidics processing for biomedical related applications (Chang et al., 2010, Gunduz et al., 2012).

### **3.2.6 Poly (lactic-co-glycolic acid) (PLGA)**

Poly (lactic-*co*-glycolic acid) is a copolymer of glycolic and lactic acid which has been approved by the Food and Drug Administration (FDA) for uses in therapeutic devices because of its biodegradability and biocompatibility. Depending on the ratio of lactide to glycolide used for the polymerisation, different forms of PLGA can be obtained: these are usually identified in terms of the monomer ratio used. In this research the PLGA copolymer 50:50 Resomer RG503H (Boehringer Ingelheim, Germany) was used with the molecular weight 33000 kDa composed of 50% lactic and 50% glycolic acid.

### **3.2.7 Collagen**

Collagen (Type I solution from rat tail, Sigma Aldrich, UK) is the most abundant long and fibrous protein in mammals and the main component of bone and skin. It has great tensile strength. As a natural material, collagen is biocompatible and doesn't cause any immune response. Due to its role in the extracellular matrix, collagen is mainly used for a bio-mimetic approach to tissue engineering scaffold design. Initially collagen sponges were developed only as wound dressing materials but with the incorporation of other biomolecules (elastin, growth factors, and antibiotics) (Ueda et al., 2008). Collagen has been widely used in all areas needing construction, healing, cell proliferation and drug delivery; not only as scaffolds but also as films and microparticles.

### **3.2.8 Phosphate buffered saline (PBS)**

Dulbecco's phosphate buffered saline (DPBS, Sigma Aldrich, UK) is a balanced salt solution (BSS) used for the handling and culturing of mammalian cells. DPBS is used to irrigate, wash, and dilute mammalian cells. Phosphate buffering maintains the pH in the physiological range. Calcium and magnesium facilitate cell binding and clumping. DPBS without these ions can be used to wash and rinse suspended cells.

### 3.2.9 Ethanol

General purpose research grade ethanol ( $C_2H_5OH$  99%, density  $790 \text{ kg m}^{-3}$ , molecular weight 46, viscosity  $1.3 \text{ mPa s}$ , Sigma Aldrich, Poole, UK) was used in this research. In addition, ethanol was also used for the calibration of the characterisation apparatus and for the cleaning of capillary needles which were essential components of the experimental setup.

### 3.2.10 Acetone

Acetone as a polar solvent ( $CH_3COCH_3$  99.9%, density  $791 \text{ kg m}^{-3}$ , molecular weight  $58.08 \text{ g mol}^{-1}$ , viscosity  $0.3 \text{ mPa s}$ , Sigma Aldrich, Poole, UK) was used in this research for the preparation of PLGA solution for nanoparticle/fibre production.

## 3.3 Characterisation of the solutions

### 3.3.1 Density

The density of the liquids/solutions used was measured using a 25 ml DIN ISO 3507-Gay-Lussac type standard density bottle (VWR International, Lutterworth, UK). The mass of the empty bottle and the mass of the bottle filled with liquid/solution were obtained using an electronic balance (AND HF-1200G A&D Instruments Ltd., Japan). The density ( $\rho$ ) was calculated as follows:

$$\text{The mass of the empty density bottle} = W_1 \text{ g} \quad \text{Eq (3.1)}$$

$$\text{The mass of the density bottle filled with liquid /solution} = W_2 \text{ g} \quad \text{Eq (3.2)}$$

$$\text{Therefore, the mass of liquid/suspension/solution only} = (W_2 - W_1) \text{ g} \quad \text{Eq (3.3)}$$

$$\text{Therefore, the density of liquid /solution} = (W_2 - W_1)/25 \text{ g cm}^{-3} \quad \text{Eq (3.4)}$$

The mean value of five such consecutive calculations was taken as the density of liquid/solution and reported in this thesis. Measurements were taken at the ambient temperature (~22-25 °C) and pressure.

### 3.3.2 Viscosity

The dynamic viscosities of the solutions were determined using a U-tube viscometer (BS/U type, Schott Instruments GmbH, Germany). A calibrated U-tube (size *C*, nominal constant 0.03) was used. The time taken for a standard volume of solution to pass through the capillary of the U-tube was noted for five passes and the mean value of the time was calculated. Then, the kinematic viscosity ( $\nu$ ) was obtained by multiplying the nominal constant (*C*) by the time (*t*):

$$\nu = Ct \quad \text{Eq (3.5)}$$

The dynamic viscosity ( $\mu$ ) was then calculated by multiplying the kinematic viscosity by the density ( $\rho$ ) of the solution:

$$\mu = \nu\rho \quad \text{Eq (3.6)}$$

If equations (3.5) and (3.6) are combined,

$$\mu = C t \rho \quad \text{Eq (3.7)}$$

Ethanol was used to calibrate the viscometer. The mean value of five readings was taken as the dynamic viscosity of the sample. For U-tube viscometers that are not calibrated by manufacturers, use of a calibrating liquid is essential as the viscosity value cannot be calculated without comparing with another liquid.

### 3.3.3 Surface tension and contact angle

#### 3.3.3.1 Wilhely's plate method

The surface tension of the solutions was measured using a Kruss Tensiometer K9 (Standard Wilhelmy's plate method). A platinum plate, fastened to a balance, is immersed deep in the solution and withdrawn to the position shown in **Figure 3.1** where

the buoyancy force is zero. Provided the contact angle is zero between the plate and the solution, the surface tension of the liquid vapour interface,  $\sigma_{lv}$ , is given by the force  $F$  on the plate divided with the perimeter  $L$  of the platinum plate ( $\sigma_{lv} = F/L$ ). In order to minimize errors, the plate was cleaned thoroughly with ethanol or distilled water and dried in a drier before each measurement. The mean values of five readings were taken as the surface tension of the sample.

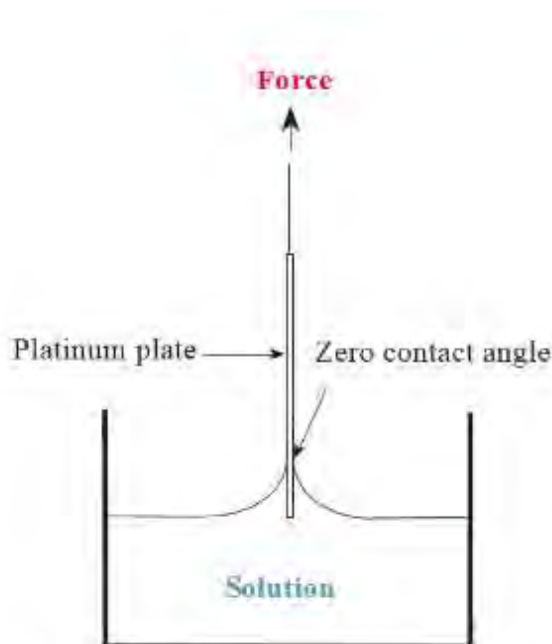


*Figure 3. 1: Submersion of platinum plate for the Wilhelmy balance measurement.*

### 3.3.3.2 Drop shape analysis method

Both static surface tension and contact angle were measured using a Drop Shape Analysis System, Model DSA100 (Kruss GmbH, Hamburg, Germany). Surface tension is determined by fitting the shape of the drop (in a captured video image) to the Young-Laplace equation which relates interfacial tension to drop shape. The software does this automatically.

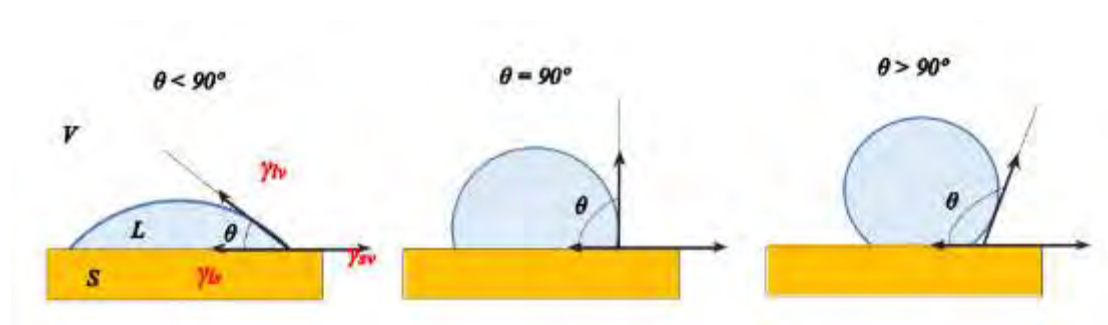


**Figure 3. 2:** Illustration of contact angles formed by sessile liquid drops on a smooth homogeneous solid surface.

The contact angle of a liquid drop on an ideal solid surface as described by Young is defined by the mechanical equilibrium of the drop under the action of three interfacial tensions (**Figure 3.2**):

$$\gamma_{lv} \cos \theta = \gamma_{sv} - \gamma_{sl} \quad (3.8)$$

where  $\gamma_{lv}$ ,  $\gamma_{sv}$ , and  $\gamma_{sl}$  represent the liquid-vapour, solid-vapour, and solid-liquid interfacial tensions, respectively, and  $\theta$  is the contact angle.

### 3.3.4 Electrical Conductivity and pH

The electrical conductivity and pH of the solutions were determined using a Jenway 3540 pH/conductivity meter (Bibby Scientific Limited, Staffordshire, UK). The electrodes were always cleaned and dried before measurements. The electrode was kept immersed in the solution up to the point marked on the electrode for 10 min and the reading shown on the meter was recorded. The mean value of five consecutive readings was taken as the electrical conductivity and pH of the sample.

### 3.4 Preparation of solutions

#### 3.4.1 For the study of the influence of liquid physical parameters on microbubble size study

Glycerol with 99% purity was diluted with distilled water at 5, 10, 20, 30, 35, 50, 60, 65, 70 and 80 wt % concentrations for the study of liquid physical parameters (shown in **Table 3.2**) influence on the bubble production and size in the T-junction device. In order to facilitate bubble formation and reduce the surface tension and stabilize newly created interfaces, an equal amount of 1 wt % of 0.01M SLS solution was added to all the solutions. Compressed air was used as the disperse phase (gas).

Aqueous Solution	Viscosity / mPa s	Surface tension / mN m <sup>-1</sup>
water	0.99	71
100% glycerol	1495	62
5 wt. % glycerol, 1 wt. % SLS	1.2	50
10 wt. % glycerol, 1 wt. % SLS	1.3	52
20 wt. % glycerol, 1 wt. % SLS	1.8	53
30 wt. % glycerol, 1 wt. % SLS	2.5	54
35 wt. % glycerol, 1 wt. % SLS	3	55
50 wt. % glycerol, 1 wt. % SLS	6	56
60 wt. % glycerol, 1 wt. % SLS	10.8	57
65 wt. % glycerol, 1 wt. % SLS	15.2	57
70 wt. % glycerol, 1 wt. % SLS	22.5	58
80 wt. % glycerol, 1 wt. % SLS	60	60

**Table 3. 2:** Measured values of viscosity and surface tension.

### 3.4.2 For the study of the T-junction setup with electrohydrodynamic focusing

Glycerol–water mixtures with viscosities ranging from 1.3 to 36 mPa s were used as the continuous liquid phase. Aqueous glycerol solutions with 5, 50, 65 and 67 wt % concentrations were prepared for this study with the measured properties shown in **Table 3.3**. All measurements were conducted five times and the mean relative value of the error for the measurements is 5%, while the maximum error was recorded for the electrical conductivity measurements at 7%. In order to investigate the effect of liquid electrical conductivity, 1 wt % sodium chloride solution (NaCl, Sigma Aldrich, U.K.) was added to a solution of 50 wt % glycerol concentration to increase the conductivity while keeping the viscosity and surface tension constant. Compressed air was used as the dispersed (gas) phase.

<b>Aqueous Solution</b>	<b>Viscosity / mPa s</b>	<b>Surface tension / mN m<sup>-1</sup></b>	<b>Electrical Conductivity / <math>\mu\text{S m}^{-1}</math></b>	<b>pH</b>
Deionized water	0.99	71	5.4	6.9
100% glycerol	1495	62	0.002	7.4
5 wt. % glycerol, 1 wt. % SLS	1.2	50	12	4.8
50 wt. % glycerol, 1 wt. % SLS	6	56	1.8	8.2
50 wt. % glycerol, 1 wt. % SLS, 1 wt.% NaCl	6	56	150	7.4
65 wt. % glycerol, 1 wt. % SLS	15	57	1.6	8.3
75 wt. % glycerol, 1 wt. % SLS	36	59	1.4	8.4

**Table 3. 3:** *Characteristic properties of solutions used in the experiments.*

### 3.4.3 For the study of the effect of surfactant properties on bubble size and stability

Glycerol with 99% purity (Sigma Aldrich, UK) was diluted with distilled water to achieve 50 wt% concentration to form the basis for the liquid phase. In order to facilitate bubble formation and reduce the surface tension to stabilize newly created interfaces, various concentrations of three different surfactants were added to the aqueous glycerol solution.

To investigate the effect of liquid surface tension and surfactant type on the size and stability of the bubbles produced, 2, 5 and 10 wt % of sodium dodecyl sulfate (SDS), cetyltrimethyl ammonium bromide (CTAB), polyoxyethylene (40) sorbitan monopalmitate (Tween 40) and polyoxyethylene glycol 40 stearate (PEG 40S) were added to the aqueous solution with 50 wt % glycerol concentration (All purchased from Sigma Aldrich, UK). Compressed air was used as the dispersed (gas) phase. The properties of the experimental system are listed in **Table 3.4**. In order to find whether the channel walls are hydrophobic or hydrophilic, static contact angle ( $\theta$ ) of deionized water was measured against the FEP surface and it was shown that  $\theta > 90^\circ$  indicating that the surface is hydrophobic. The mean relative error of the measurements conducted five times was at 6% with the maximum error recorder at 10% for the contact angle measurements.

Aqueous Solution	Density / $\text{mg m}^{-3}$	Viscosity / $\text{mPa s}$	Surface tension / $\text{mN m}^{-1}$	Contact Angle / $^\circ$
Water	0.99	1	72.1	105
50 wt.% glycerol	1.14	5.5	56	80
2 wt. % PEG 40, 50 wt. % glycerol	1.12	5.6	46	58
5 wt. % PEG 40, 50 wt. % glycerol	1.12	7.8	44	49

## Chapter 3: Experimental details

10 wt. % PEG 40, 50 wt. % glycerol	1.13	12.3	44	43
2 wt. % Tween 40, 50 wt. % glycerol	1.12	5.1	41	60
5 wt. % Tween 40, 50 wt. % glycerol	1.12	6	39	54
10 wt. % Tween 40, 50 wt. % glycerol	1.13	10	39	50
2 wt. % SDS, 50 wt. % glycerol	1.12	5.6	40	61
5 wt. % SDS, 50 wt. % glycerol	1.12	7.5	40	59
10 wt. % SDS, 50 wt. % glycerol	1.08	12.4	37	51
2 wt. % CTAB, 50 wt. % glycerol	1.10	5.4	38	42
5 wt. % CTAB, 50 wt. % glycerol	1.04	5.5	37	46
10 wt. % CTAB, 50 wt. % glycerol	1.02	10	36	52

**Table 3. 4:** *Physical properties of the solutions used in the experiment.*

### 3.4.4 For the generation of BSA scaffolds loaded with polymer and collagen nanoparticle/fibres

Poly(lactic-co-glycolic) acid (PLGA co-polymer 50:50, Resomer RG503H, molecular weight: 33000 g mol<sup>-1</sup>) was purchased from Boehringer Ingelheim, (Ingelheim, Germany). Acetone, ethanol, collagen (Type I solution from rat tail), Tween 40, phosphate buffer saline (PBS), L- $\alpha$ -Phosphatidylcholine hydrogenated (phospholipid)

### Chapter 3: Experimental details

and bovine serum albumin (BSA, molecular weight: 66000 g mol<sup>-1</sup>) were purchased from Sigma Aldrich (Poole, UK). Acetone and ethanol were used as solvents to prepare 5% w/w PLGA and 12% w/w PMSQ solutions, respectively, by dissolving them with magnetic stirrers in separate volumetric flasks until a homogenous suspension was formed. The collagen solutions were prepared by adding the viscous solutions into PBS solution and had a concentration of 8% and 15% v/v. Subsequently, the final solutions were vortexed for 120 s. All the instruments were calibrated before use by following the instruments calibration guide and all experiments were performed at the temperature of 25°C, ambient pressure (101.3 kPa), and relative humidity (45-60%). **Table 3.5** shows the measured liquids' physical properties used for the experiments. All measurements were conducted five times and the mean relative value of the error for the measurements is 5%, while the maximum error was recorded for the electrical conductivity measurements at 7%.

Material or polymer solution	Density / kg m <sup>-3</sup>	Viscosity / mPa s	Surface tension / mN m <sup>-1</sup>	Electrical Conductivity / $\mu$ S m <sup>-1</sup>	pH
BSA 15 wt %	1070	1.6	51	6.44	6.7
PLGA 5 wt %	780	0.78	22	339	5.4
PMSQ 12 wt %	810	1.04	22	730	4.1
Collagen 15 % v/v	1060	1.19	51	4.24	6.5
Collagen 8 % v/v	620	0.76	37	3.62	5.6

*Table 3. 5: Physical properties of liquids used in experiments.*

## 3.5 Characterisation of generated microbubbles and scaffolds

### 3.5.1 Optical microscopy

Microbubbles were collected on glass slides for preliminary stability and size study. An optical microscope (Nikon Eclipse ME 600, Nikon, Japan) was extensively used for all the investigations described in **Chapters 4** and **5**. The measurements were carried out by means of 'Image J' digital imaging software as well as Image Tool (Version 2, University of Texas, USA). Bubbles were collected from the tip of the outlet of the device on microscope glass slides and immediately observed under an optical microscope fitted with a camera (JVC KY-F55B). Bubbles were studied at 5x, 10x and 20x magnifications. For each sample, 100 bubbles were chosen to measure the diameter and stability over a fixed collection area of 1.5 mm<sup>2</sup>. The polydispersity index  $\sigma = \delta / D_{avg} \times 100\%$  was calculated from the average bubble size  $D_{avg}$  and standard deviation  $\delta$  (Hettiarachchi et al., 2007), determined by measuring the sizes of at least 100 microbubbles from recorded images.

### 3.5.2 High speed camera images

All measurements of bubble frequency and length were performed on video images of fibre optic illuminated T Junction taken by a Phantom V5 high speed camera. For each flow ratio, three sets of video data were taken, with 5 minutes intervals between changes to any of the flow parameters. The software version 605.2 supplied with the camera could offer image resolutions range of 128, 256, 512 and 1024 pixels in height and width. The measurements were conducted with constant 1024x1024 image area resolution in pixels. While the resolution of 1024x1024 only gives 1000 pictures per second, it has the highest resolution for the V5 camera. In addition to the Phantom V5, bubble formation was recorded using a Phantom V7.10 camera with a maximum resolution of 1280 x 800 pixels at up to 7,500 fps. All data were processed using Cine viewer software (Vision Research, UK).

A Photron Ultima APX high speed camera with a maximum resolution of 1024 x 1024 pixels at up to 2,000 fps giving 3 seconds of recording time (Photron Europe Ltd., U.K.) was also used to obtain real time video images of the bubble formation process. The

data were then processed using PVF image processing tool (version 3392, Photron Europe Ltd., U.K.). All the high speed cameras were provided by the Engineering and Physical Science Research Council through their Instrument Loan Pool system.

### **3.5.3 Scanning electron microscopy (SEM)**

The bubbles/scaffolds, particles, fibres and the combined structures were analysed for their diameter and surface morphology by optical microscopy (Micropublisher 3.3 RTV, 3.3 megapixel CCD Color-Bayer Mosaic, Real Time Viewing camera, Media Cybernetics, Marlow, UK) and scanning electron microscopy (Hitachi S-3400N and JEOL JSM-6301F field emission scanning electron microscopes, SEM). JEOL JSM-6301F field emission scanning electron microscope was equipped with an emitter that can achieve a resolution of  $\sim 1.5$  nm. The accelerating voltage was set at 6 kV and the working distance between the emitter and the sample was 20 mm. The bubbles, bubble/particle and bubble/fibre structures were collected and studied by optical microscopy immediately and after 15 and 30 minutes of production to detect any changes in their size and morphology. Then they were left to dry for 12 hours and they were studied by scanning electron microscopy at an acceleration voltage of 3-5kV. All the samples were vacuum-coated with gold for 120s before obtaining SEM images. Since the materials used for the preparation of scaffolds and nanoparticle/fibres are nonconductive, the SEM sample was gold coated for 2 min using a sputtering machine (Edwards sputter coater S 1 50B) to enable conduction of the sample surface and avoid charging which can cause damage when gold is used to make the surface conductive. The samples were then placed on an aluminium stub with a carbon sticker and were placed in the SEM chamber. Analysis of the products was carried out using the Image-Pro Insight software (Media Cybernetics Ltd., Marlow, UK) and the image-processing program UTHSCSA Image Tool (Image Tool Version 2, University of Texas, USA).

## 3.6 Experimental Setup

### 3.6.1 Standard capillary embedded T-junction device

A schematic of the T-junction set up and the junction geometry is shown in **Figure 3.3**. This device consists of two Teflon FEP (Fluorinated Ethylene Polypropylene, Upchurch, USA) capillaries with fixed internal diameters of 150  $\mu\text{m}$  (for the set of the experiments conducted to investigate the effect of the variation of viscosity and flow ratio) inserted in a polymer block with the ends 200  $\mu\text{m}$  apart and the third Teflon FEP capillary inserted perpendicular to these two capillaries. In addition, the influence of channel geometry was studied by using three different capillary sizes with inner diameters of 100, 150 and 200  $\mu\text{m}$ . In all these experiments the gap in the junction, shown in **Figure 3.4 a,b** was set to be 200  $\mu\text{m}$ . The top capillary was connected to a gas regulator fitted to a pressurized air tank via a 6 mm diameter tubing, where the gas was supplied to the junction at constant pressure  $P_g$ . A digital manometer was connected to the pipe to measure the in-line gas pressure. Also a gas regulator was used to vary the pressure supplied to the T- junction. The capillary perpendicular to the capillary supplying air was connected to a 20ml stainless steel syringe (KD Scientific, Holliston, MA, USA).

In order to investigate the effect of variation in the size of the gap between the vertically aligned channels (in the case of our T-junction, the gap between the gas inlet capillary and the main channel), a fixed size capillary inner diameter of 200  $\mu\text{m}$  was chosen. The experiments were conducted for the gap size of 50, 200, and 220  $\mu\text{m}$ . **Figure 3.5** depicts 3D and 2D schematic of the junction geometry when the gap size is smaller than the capillary inner diameter at 50  $\mu\text{m}$  (a), similar to the size of the capillary inner diameter at 200  $\mu\text{m}$  (b) and larger than the capillary inner diameter at 220  $\mu\text{m}$  (c). For all these experiments, the liquid viscosity and flow rate was kept constant at 60 mPa s and 0.01 ml/min respectively.

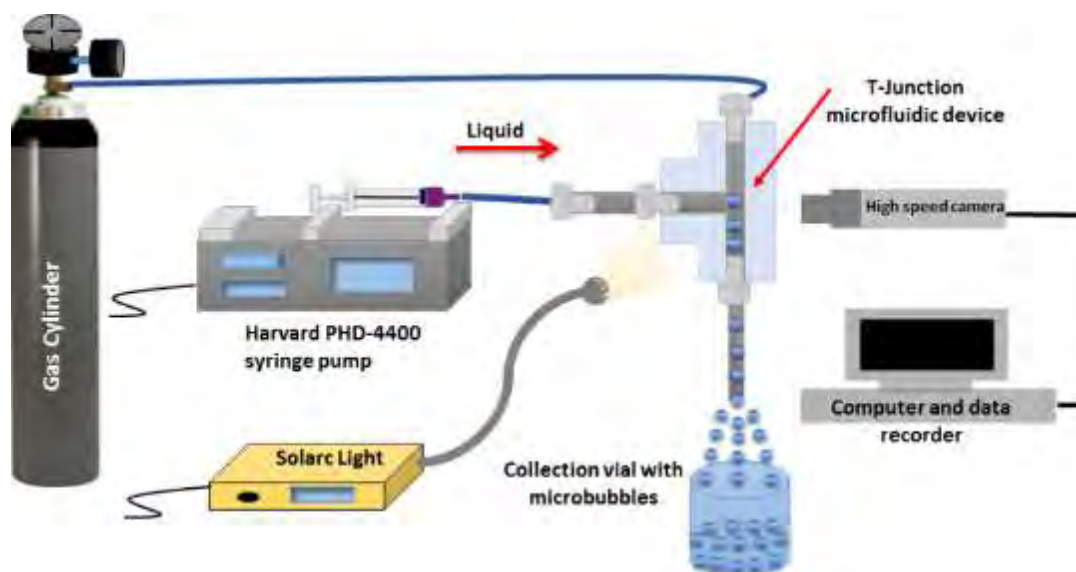


*Figure 3. 3: Schematic of the T-junction device (system apparatus)*

A Harvard syringe pump PHD-4400 (Harvard Apparatus Ltd., Edenbridge, UK) was used to force liquid through the capillaries at a constant flow rate. The geometry of the junction which consists of circular cross-section capillary tubing is different from that of a conventional rectangular T-junction device. The gas inlet capillary is placed on the main channel and the liquid inlet capillary is on the perpendicular channel. The length of the junction is larger than the capillaries inner diameter. This creates a cylindrical cavity at the junction where the two phases meet. Bubble formation was monitored at the junction in the 200  $\mu\text{m}$  gap between the main capillaries, where the liquid and gas phases meet to start bubble formation. Each capillary was secured mechanically to the block via a standard HPLC (high-performance liquid chromatography) connector to prevent any slippage at the junction during operation at high pressure. All connections were checked for leakages and blockages prior to experiments.

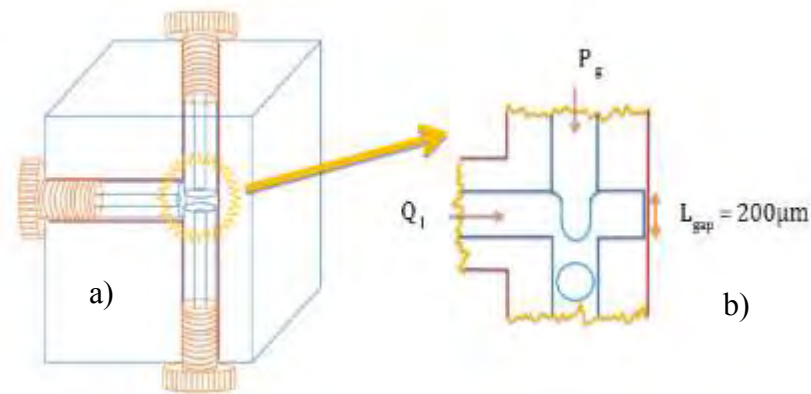


**Figure 3. 4:** (a) 3D and (b) 2D representation of junction diagram, where  $P_g$  and  $Q_l$  are gas pressure and liquid flow rate, respectively, and  $L_{gap}$  is the distance between the capillaries in the junction.

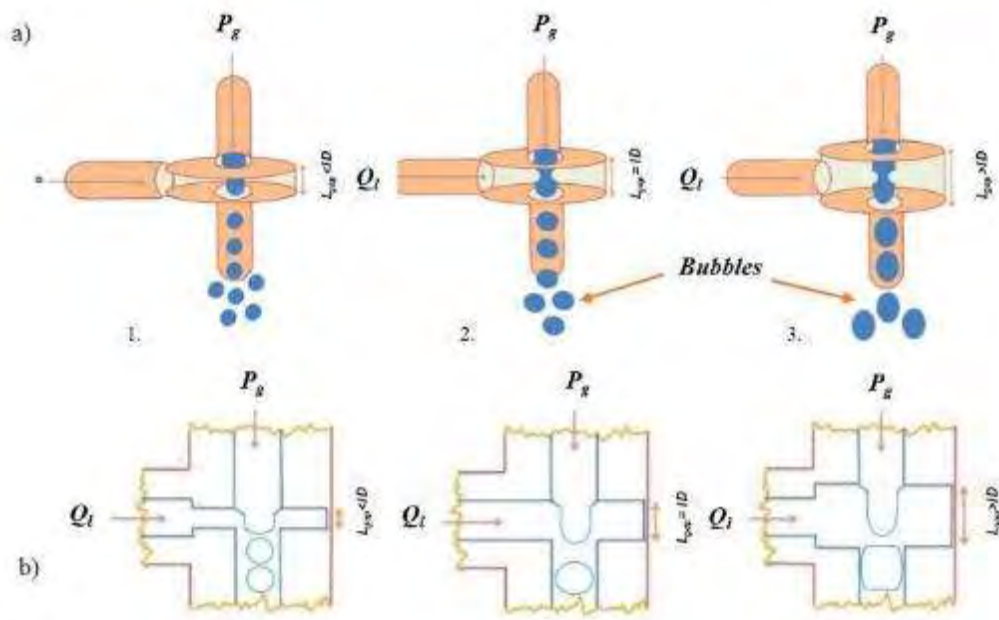


**Figure 3. 5:** (a) 3D and (b) 2D illustration of the junction geometry for 3 cases of 1. Gap size < Capillary inner diameter ( $50\mu\text{m}$ ), 2. Gap size = Capillary inner diameter ( $200\mu\text{m}$ ) and 3. Gap size > Capillary inner diameter ( $220\mu\text{m}$ ).

### **3.6.1.1 Specific experimental details for the effect of parameters on bubble size**

The microbubble samples were collected from the end of the third capillary. For each solution of a given viscosity, the effect of varying the gas pressure ( $P_g$ ) from 30 to 300 kPa was determined for different liquid flow rates ( $Q_l$ ) from 0.07 to 0.4 ml/min ( $1.15 \times 10^{-9}$  to  $6.6 \times 10^{-9}$  m<sup>3</sup>/s). Between the experiments the junction was cleaned with ethanol and any liquid inside the capillaries was flushed by applying air at 40 kPa pressure. A Phantom V5.1 high speed camera (Vision Research Ltd. Bedford, U.K.) was used to obtain real time video images of the bubble formation process. Values for the Reynolds numbers for the liquid ( $Re_l$ ) were determined and  $7 \times 10^{-4} \leq Re_l \leq 9.3 \times 10^{-3}$ .

It was found that  $Re_l < 2300$ , which indicates that the flow should be laminar in the lead capillary and dominated by viscous forces rather than interfacial tension. Any change in the liquid flow rate or gas pressure causes a variation in bubble size due to the fact that the generation of bubbles in the T-junction depends on the pressure balance of liquid and gas at the junction. Therefore, the results here are analyzed in terms of a dimensionless flow ratio, to take into account the combined effect of the gas and liquid flow rates. Since the pressure drop along the gas capillary is very small and the Mach number ( $M = u_g/a$ ) of the gas flow  $\leq 0.3$ , the gas flow inside the capillary was considered as incompressible and the gas pressure drop was converted into volume flow rate using Poiseuille's law for the length of capillary used in this experiment (Pancholi et al., 2008).

### **3.6.1.2 Specific details of experiments for the effect of surfactants on bubbles**

The channel wall surface was created by inserting two Teflon FEP (Fluorinated Ethylene Polypropylene) capillaries perpendicularly into a rigid Polydimethylsiloxane (PDMS) block as inlet channels for the gas and liquid flows. A third FEP capillary was embedded in the polymer block aligned with the gas inlet channel with a 200  $\mu\text{m}$  distance to create the junction where the two phases meet. The internal diameter for all of the channels was fixed at 200  $\mu\text{m}$ .

Experimental conditions	Liquid flow rate / ml min <sup>-1</sup>	Channel diameter / $\mu\text{m}$	Gap between capillaries / $\mu\text{m}$	Gas pressure / kPa	Capillary Number
2wt% PEG 40	0.2	200	200	45-95	0.0013
5wt% PEG 40	0.2	200	200	80-150	0.0019
10wt% PEG 40	0.2	200	200	140-200	0.0029
2wt% Tween 40	0.2	200	200	30-120	0.0013
5wt% Tween 40	0.2	200	200	45-155	0.0016
10wt% Tween 40	0.2	200	200	70-135	0.0027
10wt% Tween 40	0.25	200	200	80-140	0.0034
2wt% SDS	0.2	200	200	35-100	0.0014
5wt% SDS	0.2	200	200	65-120	0.0019
10wt% SDS	0.2	200	200	110-190	0.0034
2wt% CTAB	0.2	200	200	50-100	0.0015
5wt% CTAB	0.2	200	200	75-125	0.0016
10wt% CTAB	0.2	200	200	115-195	0.0029

**Table 3.6:** Conditions tested in the experiments (at 22 ° C)

The conditions tested in the experiments are shown in **Table 3.6**. Each experiment was conducted 10 times to provide an indication of the experimental uncertainty for the

measured mean bubble diameter that was calculated to be approximately between 2-5%.

### 3.6.2 Capillary embedded T-junction device with electrohydrodynamic focusing

The experimental setup consisted of two Teflon FEP (Fluorinated Ethylene polypropylene) capillaries with outer diameter of 1.58 mm were inserted perpendicularly into a Polydimethylsiloxane (PDMS) block (100x100x10 mm<sup>3</sup>) as inlet channels for the gas and liquid flows. A third stainless steel capillary was embedded in the polymer block aligned with the gas inlet channel with a 200  $\mu\text{m}$  distance to create the junction where the two phases meet. The internal diameter for all of the channels was fixed at  $D_{ch} = 100 \mu\text{m}$ . A schematic of the T-junction set up is shown in **Figure 3.6**. The top capillary was connected to a gas regulator fitted to a pressurized air tank via a 6 mm diameter pipe, where the gas was supplied to the junction at constant pressure  $P_g$ . A digital manometer was connected to the pipe to measure the in-line gas pressure. Also a gas regulator was used to vary the pressure supplied to the T-junction. The liquid capillary perpendicular to the capillary supplying air was connected to a 20 ml stainless steel syringe (KD Scientific, Holliston, MA, USA). A Harvard syringe pump PHD-4400 (Harvard Apparatus Ltd., Edenbridge, UK) was used to force liquid through the capillaries at a constant flow rate.

The advantages that this setup has over conventional lithographically manufactured microfluidic chips are: that it can be easily constructed, blocked capillaries can be easily replaced, and microbubbles smaller than the channel width can be produced. To apply an electrical potential difference to the device, the steel capillary tube was connected to a high voltage power supply (Glassman Europe Ltd. Tadley, UK) while the ground electrode was placed 100 mm below the tip of the outlet channel. Once the gas pressure and liquid flow rates were set and conditions for stable bubble formation in the T-junction determined, the applied voltage across the outer steel tube was varied between 6 and 21 kV.

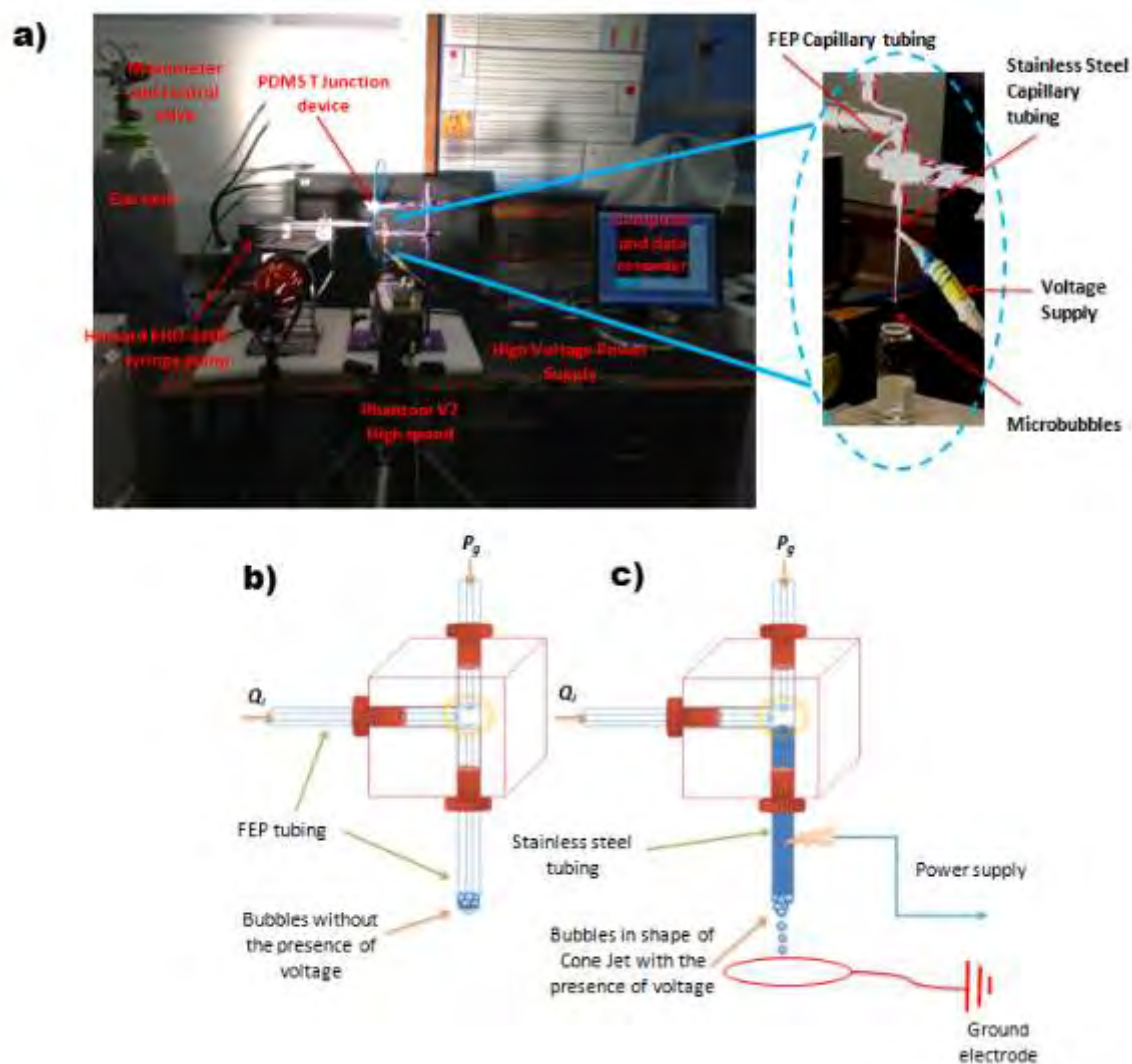


**Figure 3. 6:** *T- Junction setup a) and schematic of the T-junction setup and bubble formation with b) and without c) an applied electric field.*

For a solution with a given viscosity and liquid flow rate, bubble formation occurs for a range of gas pressures with the smallest bubble size obtained at the lowest gas pressure and largest bubble size at the highest gas pressure. Outside this range, monodisperse microbubble formation is not achievable. This is prior to applying voltage. In this experimental investigation, the smallest gas pressure at which bubble formation was achievable, were chosen for each solution.

### 3.6.3 Combined T-junction and single needle EHD setup

The experimental setup for producing the bubble/particle and bubble/fibre products is shown in **Figure 3.7**. It consists of a single brass EHD needle device (inner diameter: 1.35mm, outer diameter: 1.82mm), a microfluidic T-junction device (two entry ports and an exit port), two ‘PHD 4400’ high precision syringe pumps (Harvard Apparatus Limited, Edenbridge, UK) to control the flow rate of the solutions to one of the entry ports of the T-junction device and to the EHD needle, a high precision voltage generator connected to the EHD needle (Glassman Europe Limited, Bramley, UK) and a gas supply cylinder, which transports air through high pressure into the secondary T-junction entry port. A 10ml volume capacity Becton-Dickinson (Becton and Dickinson Company, Oxford, UK) syringe containing the 15% w/w BSA solutions was loaded to one of the syringe pumps and a silicone tube was used to transfer it to one of the T-junction entry ports. The other syringe pump was loaded with a 10 ml syringe filled with a different solution at each time (PLGA, PMSQ and collagen) and a silicone tube was used to transfer these to the EHD needle. The air cylinder is connected to the secondary T-junction entry port. A 10ml volume capacity Becton-Dickinson (Becton and Dickinson Company, Oxford, UK) syringe containing the 15% w/w BSA solutions was loaded to one of the syringe pumps and a silicone tube was used to transfer it to one of the T-junction entry ports. The other syringe pump was loaded with a 10 ml syringe filled with a different solution at each time (PLGA, PMSQ and collagen) and a silicone tube was used to transfer these to the EHD needle.

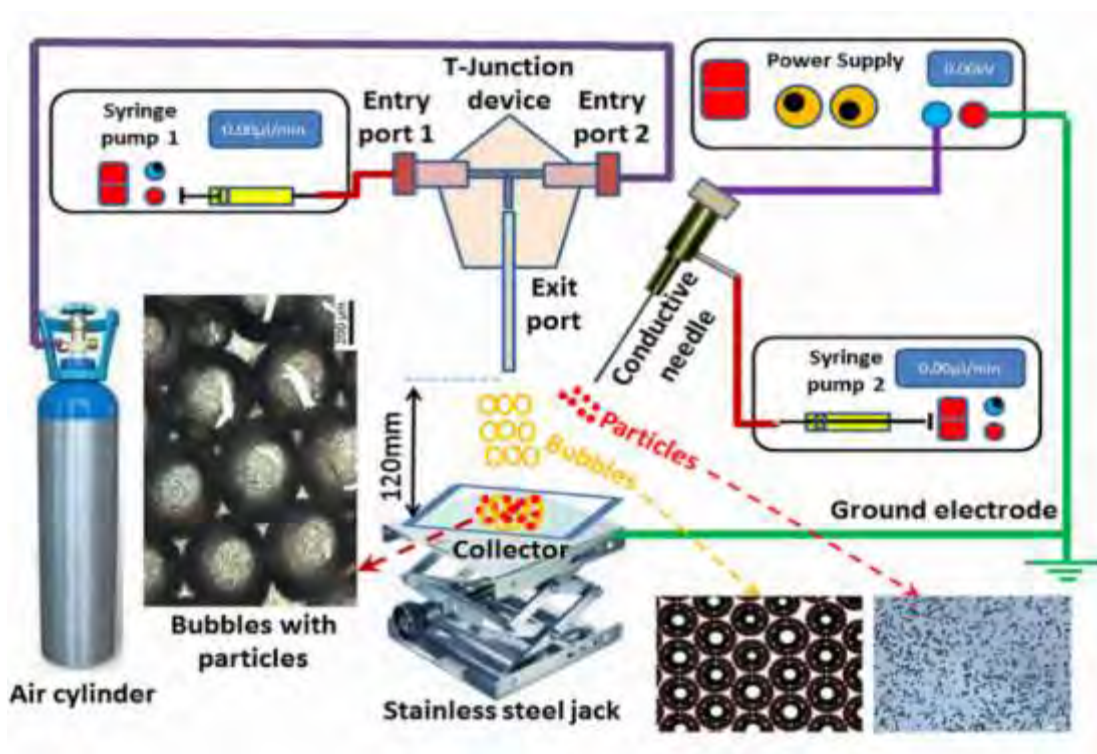


*Figure 3. 7: Schematic illustration of the T-Junction/EHD setup used for the experiments.*

## **Chapter 4**

### **Results and Discussion**

#### **Production of Microbubbles using a capillary embedded T-junction device**

##### **4.1 Overview**

Production of stable microbubbles with uniform size has been the subject of many researchers. In order to facilitate bubble formation, microfluidic techniques have been widely used. To understand the mechanism of bubble formation various studies suggested scaling models with a number of variables affecting the size of bubbles formed through this technique. In this part of the research, a detailed investigation of parameters such as viscosity, surface tension, flow parameters and channel geometry were conducted. Principles of bubble formation for a range of viscosities and mapping of the size and size distribution were presented. Capillary tubing with channel diameters much larger than lithography manufactured microfluidic chips were embedded in a T-junction block in order to enable the possibility of replacing the tubing if blocked as well as creating different gap sizes in the mixing area. In addition, pressure drop associated with the smaller channel diameter was reduced by using larger capillaries and therefore higher liquid and gas flow rates can be used that lead to higher rate of production than conventional microfluidic devices. In this study, the role of surfactant concentrations and types on the formation and stability of bubbles in this device was also investigated. Lastly, the T-junction device was optimised with electrohydrodynamic focusing to further decrease the bubble size and the role of voltage and electrical conductivity in conjunction with viscosity was studied.

## **4.2 Effect of operating conditions and liquid physical properties on the size of microbubbles in the T-junction device**

### **4.2.1 Introduction**

The main goal of this work was to characterize the bubble formation process in a capillary embedded T-junction and determine the factors that affect the bubble size; in particular the parameters that reduce it. In the past decade there has been intense interest in microfluidic systems with the evolution of inexpensive and simple methods for fabrication of the devices, such as lithography and wet etching (Garstecki et al. 2005; Zhang and Wang 2009). One of the challenges that the users of these devices face is the regular blockage and clogging of the flow channels and the consequent need for expensive cleaning processes and/or replacement of the devices (Mustin and Stoeber, 2008). Compared with conventional methods, the set-up used in this work provides a robust and low-maintenance system for fabricating bubbles/droplets. Any blocked channel can be easily replaced by inserting a new section of capillary tubing whilst control over bubble/droplet size can be achieved through appropriate selection not only of the flow rate ratio, solution viscosity, and surface tension but also capillary inner diameter and/or separation.

In order to investigate the bubble formation process and compare this system with previously reported methods, a detailed study was made of the relationship between bubble size and uniformity and the operating parameters. The effect of the channel inner diameter was investigated by varying all the inlet and outlet capillary sizes. In addition, the effect of changes in the continuous-phase viscosity and flow rate ( $Q_l$ ) as well as the gas pressure ( $P_g$ ) on the resulting bubble size was studied. Aqueous glycerol solutions were chosen for the liquid phase, as they are widely used in experimental studies of flow phenomena, including the majority of the studies referred to above since viscosity can be varied easily and in a repeatable manner through dilution, and without significantly changing the surface tension and density of the solutions (Cheng, 2008). The experimental data were then compared with published data derived from scaling models proposed by Garstecki et al. (2006), which are widely used and accepted as a

basis of comparison among investigators. While the role of liquid viscosity was investigated by these authors, it was not directly incorporated in the scaling models proposed and therefore the effect of viscosity was also studied experimentally in this work.

#### 4.2.2 Bubble formation

As the gas inlet pressure was gradually increased under constant liquid flow rate, it was found that bubble formation occurred only within a certain range of gas pressures, where  $P_{gmin}$  and  $P_{gmax}$  are represented as minimum and maximum gas inlet pressure, respectively. For any gas pressure below  $P_{gmin}$ , the liquid phase would push the gas stream back to the gas channel due to the capillary force of the liquid phase and cause leakage in the capillaries.

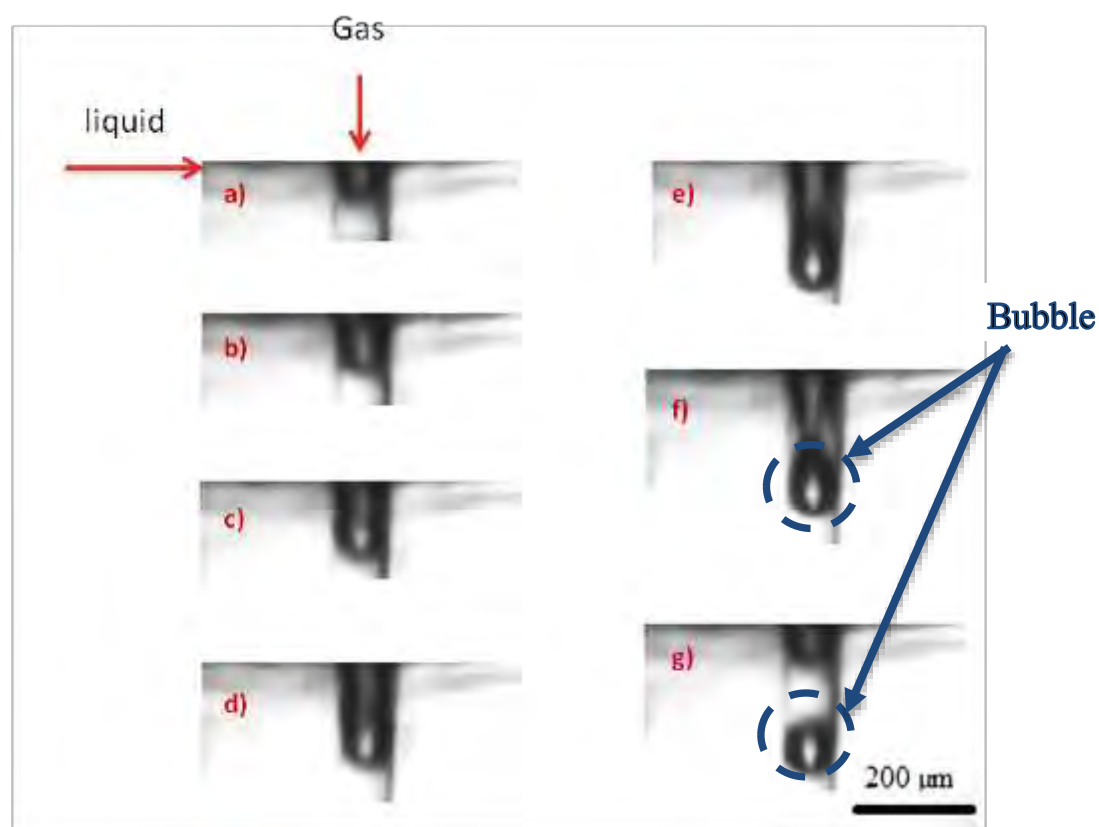


**Figure 4. 1:** Bubble formation process as a function of time for liquid solution viscosity of 10.8 mPa s and flow rate of 0.01 ml/min at (a)  $t=0$  ms, (b)  $t=1.62$  ms, (c)  $t=3.82$  ms, (d)  $t=4.95$  ms, (e)  $t=6.62$  ms, (f)  $t=7.45$  ms, (g)  $t=8.28$  ms.

On the other hand, gas pressures larger than  $P_{gmax}$  would disturb the layered laminar flow of both gas and liquid phases in the outlet channel. The bubble generation process can be seen in the video images taken by the high speed camera, presented in **Figure 4.1**, where the time evolution of a bubble is captured. Initially, the gas column enters the junction and liquid and gas phases meet. The gas column expands until a neck appears and propagates downstream while its diameter decreases and it finally breaks. The bubble formation process can be considered in three stages: 1) growth stage (**Figure 4.1a, b, c, d**), 2) necking stage (**Figure 4.1e, f**) and 3) pinch off (**Figure 4.1g**).

### 4.2.3 Effect of gas inlet pressure on bubble size

**Figure 4.2** illustrates the effect of gas flow rate on the average bubble size whilst the gas inlet pressure was varied at a constant liquid flow rate. The continuous phase viscosities ranged from 1.15 to 60 mPa s. The average bubble size increased with increasing gas flow rate/gas inlet pressure. From **Figure 4.3a, b** it was found that at a fixed liquid flow rate of 0.01 ml/min and viscosity of 10.8 mPa s, the bubble diameter increased with the gas inlet pressure. The increase in gas pressure led to the expansion time increasing and a longer bubble /slug was produced (**Figure 4.3a, b**).

It is also shown that for a constant flow rate of 0.1 ml/min, bubble formation occurs within a larger range of gas pressures for the most viscous solution. This can be seen from the curve corresponding to  $\mu_l = 60$  mPa s in the graph shown in Figure 4, where the difference in pressures to obtain the largest and the smallest bubbles is approximately 100 kPa. Whereas for the lowest liquid viscosity of  $\mu_l = 1.8$  mPa s, the difference between  $P_{gmin}$  and  $P_{gmax}$  is approximately 30 kPa. In addition, at constant liquid flow rate, for the more viscous solutions, higher gas pressure is required to produce bubbles. All the microbubbles produced in this study were highly monodisperse with a polydispersity index of  $< 1\%$ .

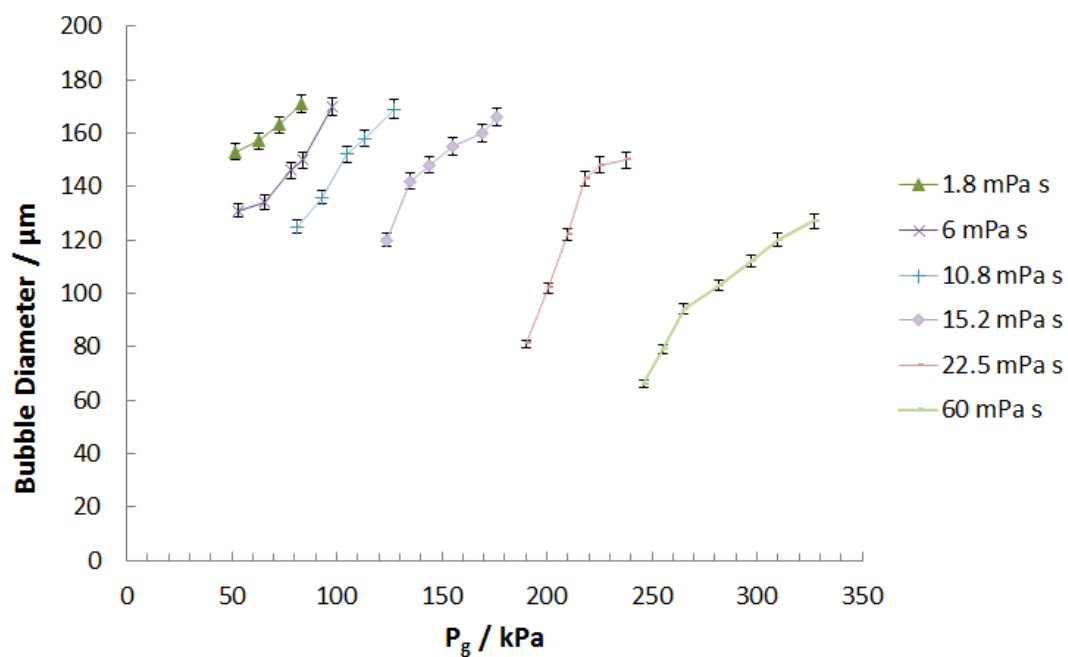


**Figure 4. 2:** The variation of bubble size with gas inlet pressure for liquid with different viscosities at a constant liquid flow rate of 0.1 ml/min.

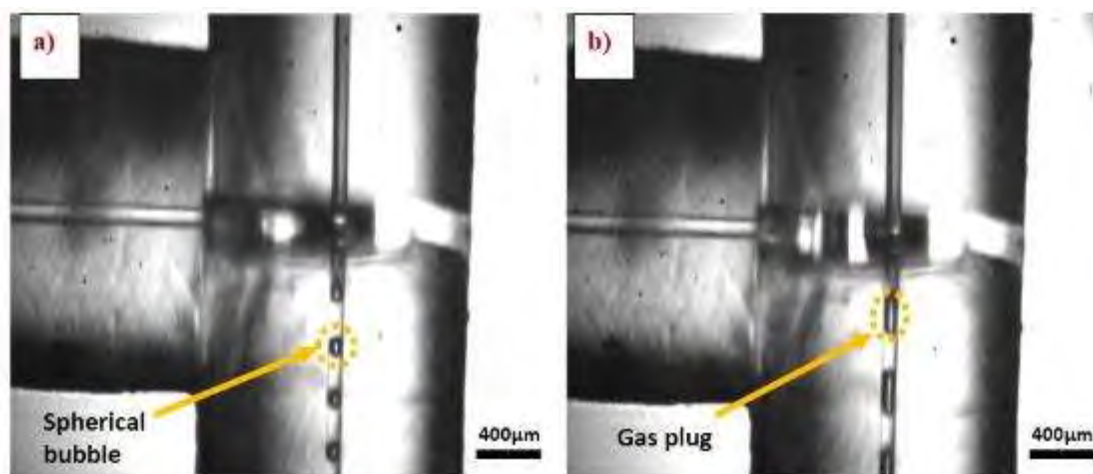


**Figure 4. 3:** High speed camera images of bubble formation for liquid solution viscosity of 10.8 mPa s at constant flow rate of 0.01ml/min varying gas inlet pressure a) 150 kPa, b) 170 kPa.

#### 4.2.4 Effect of flow ratio and liquid viscosity on bubble size

Micrographs in **Figure 4.4** show that by increasing the viscosity, the bubble size decreases. For a given value of continuous phase flow rate ( $Q_i$ ), smaller bubble sizes were created at higher values of viscosity due to the relative increase in the cross-flow shear force over the capillary force at the channel junction. Optical images of bubbles shown in **Figure 4.4** correspond to the smallest bubble size presented in each curve of constant viscosity in the graph presented in **Figure 4.5**. By increasing the gas inlet pressure, an increase in bubble size is observed in each curve. Image (a) in **Figure 4.4** shows the largest bubbles (163  $\mu\text{m}$ ) with the lowest solution viscosity (1.8 mPa s), while image (c) has the smallest bubbles (66  $\mu\text{m}$ ) with the highest solution viscosity (60 mPa s).

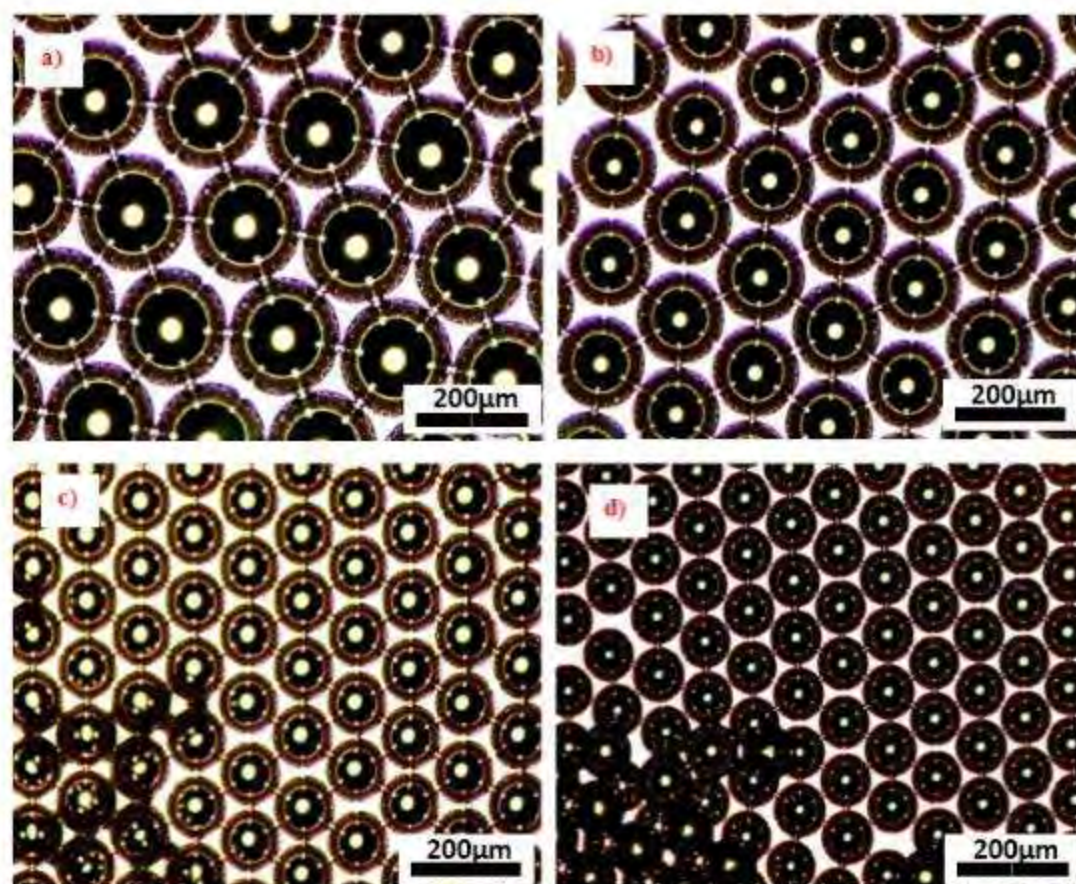


**Figure 4. 4:** Microscopic images of bubbles with constant liquid flow rate of 0.1 ml/min and viscosities of: a)  $\mu = 1.76 \text{ mPa s}$  @  $P_{g_{\min}} = 52 \text{ kPa}$ , b)  $\mu = 10.8 \text{ mPa s}$  @  $P_{g_{\min}} = 81 \text{ kPa}$  c)  $\mu = 22.5 \text{ mPa s}$  @  $P_{g_{\min}} = 190 \text{ kPa}$  d)  $\mu = 60 \text{ mPa s}$  @  $P_{g_{\min}} = 246 \text{ kPa}$ .

**Figure 4.5** shows how the diameter of the bubble varied with flow rate ratio ( $Q_l/Q_g$ ) for different viscosities. As anticipated, increasing the flow rate ratio was found to reduce bubble size. The bubble size decreased with increasing continuous phase flow rate ( $Q_l$ ) under a given gas flow rate ( $Q_g$ ), and the bubble size increased as the gas-phase flow rate increased. It is also shown that as the viscosity of the solution increases, bubble formation occurs within a lower range of ratio of liquid to gas flow rate. The results were compared to the previous work carried out by Pancholi et al. (2008a, b). In particular, in figure 7a of the paper by Pancholi *et al.*, the slug height curves for lower viscosities of 4.85 and 48.5 mPa s coincide within the curves presented in **Figure 4.5** of this study.

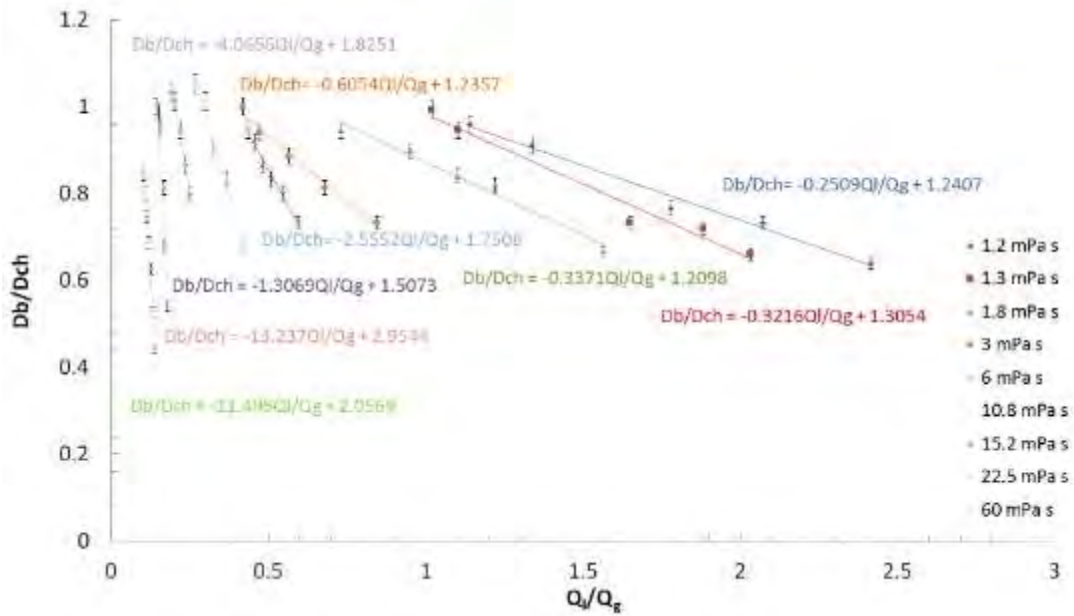


**Figure 4. 5:** The variation of bubble size with viscosity and flow ratio.

From the graphs shown in **Figure 4.5**, a predictive model (**Eq 4.1**) is obtained for the range of viscosities and flow ratios investigated in this study. The model shows that there is a good correlation for viscosities from 1.2 to 10.8 mPa s, with the mean relative error being 4.8%. For the range of viscosities higher than 10.8 mPa s, the correlation does not predict the experimental results with the same accuracy (22% error) due to the very small range of  $Q_l/Q_g$  for higher viscosities.

$$D_b/D_{ch} = (-0.25\mu + 0.09) Q_l/Q_g + (0.058\mu + 1.14) \quad \text{Eq (4.1)}$$

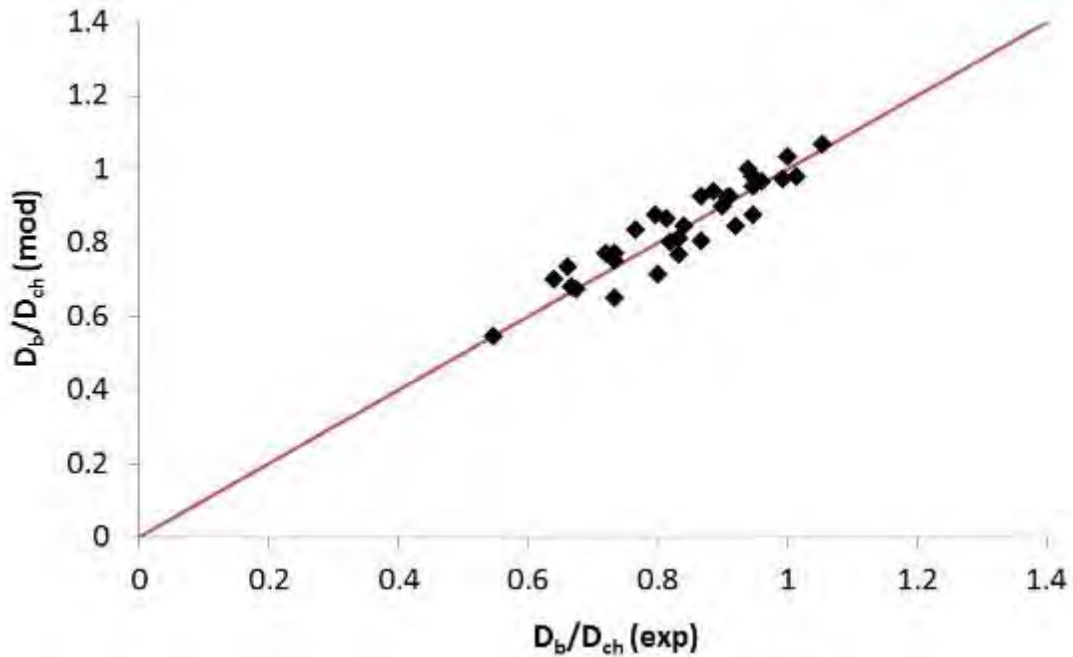


*Figure 4. 6: Comparison between the experimental data and predictive values.*

In **Figure 4.6**, the experimental values for  $D_b/D_{ch}$  are plotted against the predictive values for  $1.3 \leq \mu \leq 10.8$  mPa s, and the proximity of the experimental data to the parity line suggests that the experimental data and the predictive model are in agreement.

#### 4.2.5 Effect of capillary size on bubble diameter

Previous studies of droplet and bubble formation have been conducted mainly in rectangular cross-section T-junctions (Garstecki et al. 2006; Thorsen et al. 2001). In this study, the T-junction was created with circular cross-section capillary tubing. Computational and theoretical studies favour round channels in which only two-dimensional, i.e. axisymmetric, solutions are required. The dominance of surface tension ensures that fluid–fluid interfaces maintain smooth curvatures and conform poorly to the sharp microchannel corners. In conventional T-junction devices, bubble and droplet formation is highly influenced by the geometry of the channels.

Unlike co flowing and flow focusing devices where it is possible to obtain bubbles/droplets whose size is significantly smaller than the characteristic geometric length, bubble size produced by cross flowing techniques (T-junction device) is in the

order of the characteristic width of the channel. This is due to the fact that the emerging bubble/droplet has to fill the junction in order for the breakup to occur. In this study, the geometrical shape of the junction is different from that in rectangular cross section T-junction devices. The scaling model proposed by Garstecki et al. (2006) suggested that the bubble size is dependent on the width of the junction. In this study, the geometrical shape of the junction is different from that in rectangular cross-section T-junction devices.

Therefore the study was conducted to investigate whether the capillary diameter has any effect on the bubble size by varying all the three capillary tubing inner diameter sizes of 100, 150, and 200  $\mu\text{m}$ . Each set of the experiment was performed twice; initially with constant liquid viscosity of 15.2 mPa s and later with solution viscosity of 60 mPa s. **Figure 4.7** a) and b) displays how the bubble size varied with respect to flow ratio, with curves corresponding to each capillary size and all experiments were conducted at constant liquid viscosity. **Figure 4.7** a) and b) fits the results for the experiments at constant liquid viscosities of 15.2 and 60 mPa s respectively. It can be observed that by increasing the capillary diameter, the bubble size increased and bubble formation occurs within a larger range of flow ratio.

This was evident in both graphs and it confirms that capillary size, i.e. the geometrical effects of the junction is another crucial factor to consider in bubble formation process. As the capillary size decreases, it becomes more difficult to find a stable regime to produce microbubbles. The liquid volume flow rates were chosen within a smaller range for smaller capillary tubing, while the gas pressure range increases, leading to formation of bubbles within a smaller ratio of liquid to gas flow rate. For highly viscous solutions the process of bubble formation in smaller capillaries is a challenge, as the flow of the liquid phase in smaller capillaries has to overcome capillary forces.

The scaling model proposed by Garstecki et al. (2006) suggested that the bubble size is dependent on the width of the junction. The experimental data strongly support the hypothesis that the junction geometry also influences the gas column breakup to form bubbles.

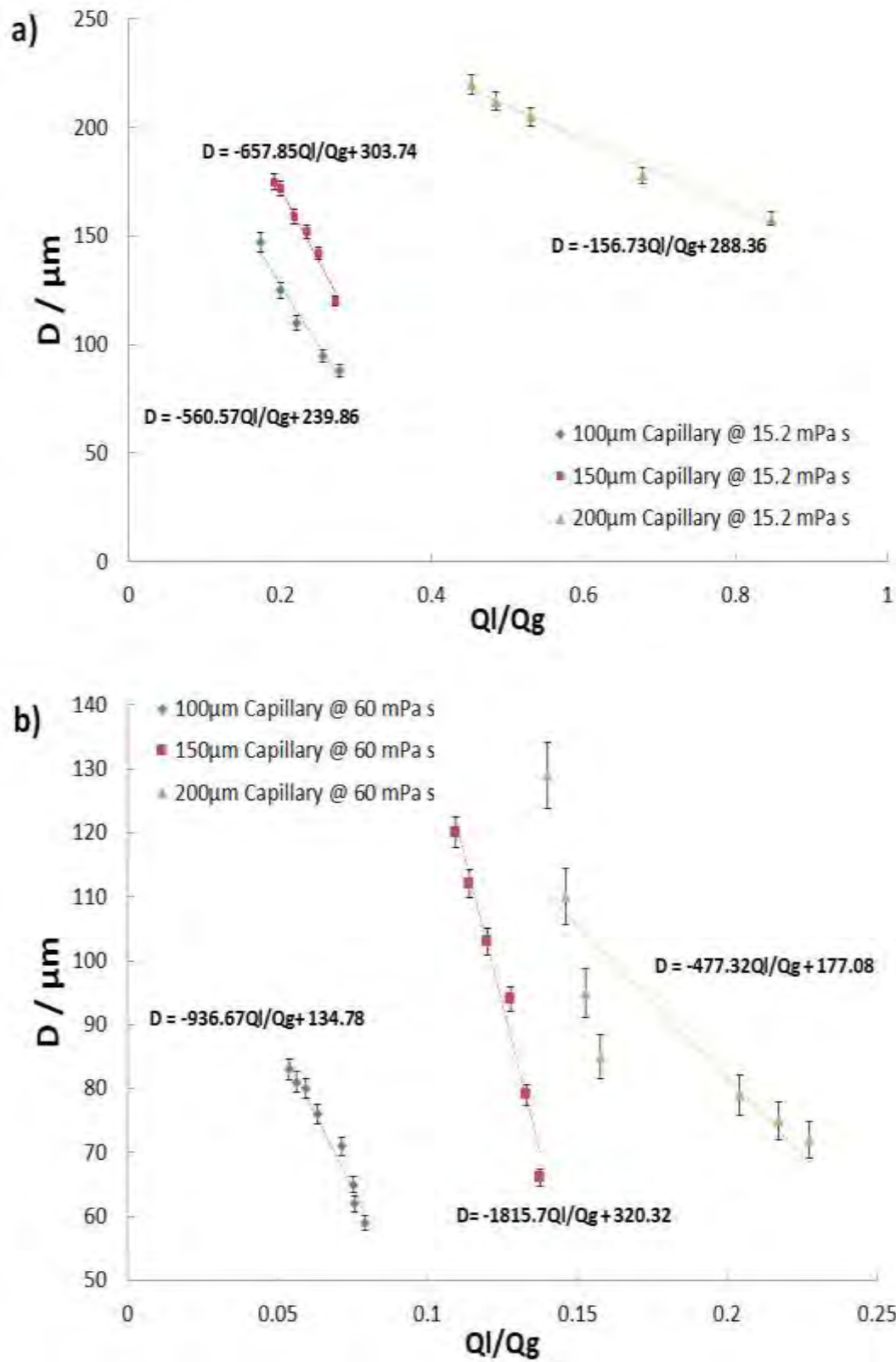


**Figure 4. 7:** Dependence of bubble diameter on the flow ratio for different capillary diameter at liquid viscosity of a) 15.2 mPa s and b) 60 mPa s.

#### 4.2.6 Comparison of experimental data with scaling model

Garstecki et al. (2006) assumed that the detachment of the neck begins when the emerging bubble fills the junction and the resulting bubble size is governed by rate of thinning the neck and filling the bubble during detachment. This assumption is consistent with observations of slug like bubbles. However in our experiments, *squeezing* is clearly not the only mechanism for breakup of the gas column and subsequently formation of bubbles. In some cases, the bubbles are smaller than the channel width, and therefore the detachment begins before the bubble has completely filled the gap. We suggest, similar to Christopher et al. (Christopher et al., 2008), that the bubble size is determined by the balance of three primary forces that govern the breakup process: the capillary force resisting deformation of the interface, the viscous stress acting on the emerging bubble, and the *squeezing* pressure.

The capillary force arises from the difference in Laplace pressures at the upstream and downstream of the emerging bubble multiplied by the surface area of the emerging interface, where the viscous force acting to deform the interface is driven from the product of viscous stress acting on the emerging bubble and the projected area of the emerging interface. In addition, the emerging bubble obstructs the junction as it grows, leading to a dramatic increase in the upstream pressure, also known as *squeezing* pressure.

Once the sum of viscous stress and the *squeezing* pressure exceed the capillary pressure, detachment begins. During detachment, the rate of thinning of the neck and the rate of filling of the bubble increases and additional growth of the bubble occurs. Christopher et al. (2008) described the size of droplets at the onset detachment in dimensionless terms, where the sum of all the forces is equal zero.

$$(1-\bar{b})^3 = \bar{b} \times Ca \quad \text{Eq (4.2)}$$

Where  $\bar{b} = b/w_c$ ,  $b$  is the length of the emerging droplet/bubble measured downstream of the junction and  $w_c$  is the width of the continuous phase capillary. Hence the capillary number becomes the controlling parameter in the initial size of the droplet before detachment.

In **Figure 4.8**, the bubble diameter is plotted as a function of capillary number for three different liquid viscosities. The results have similarities to Figure 3 in the paper by Garstecki et al. (2006), where the shape and magnitude of the curves are similar and support the scaling model presented in Christopher et al. (2008) which shows that the bubble diameter depends on both capillary number and the flow ratio. At low capillary number both models are identical. As capillary number increases, the bubble volume decreases. Bubble formation in the capillary embedded T-junction, described in this work, mainly occurs when the capillary number is higher than the critical capillary number  $Ca \sim 0.015$  previously mentioned by De Menech et al. (2008) and therefore the effect of viscosity on the size of microbubbles is evident. In addition, viscosity plays a major role in the range of operating flow ratios under which bubble formation occurs. As shown in **Figure 4.8**, for each solution viscosity the bubbles in this T-junction device are being produced at different ranges of liquid to gas flow ratio. It was observed that the viscosity of solution plays a major role in determination of the region of liquid to gas flow ratio that bubble formation occurs for a given solution viscosity. In contrast with previous studies that either focus on the squeezing regime (where bubble size is dependent on flow rate ratio) or the dripping regime (where bubble size depends on capillary number), this experimental study shows that bubble size depends on both capillary number and flow ratio. On the other hand, due to the different geometry of the system, where bubble formation occurs in a cylindrical cavity as oppose to the confined geometry of the junction investigated by previous studies, bubble size is majorly influenced by the geometrical effects of the junction. Additionally, it appears that factors such as liquid viscosity and the microchannel geometry have not been adequately accounted for in the scaling laws reported to date and therefore a modified scaling law is required to describe the behaviour of the process and predict bubble size taking all these parameters in to account.

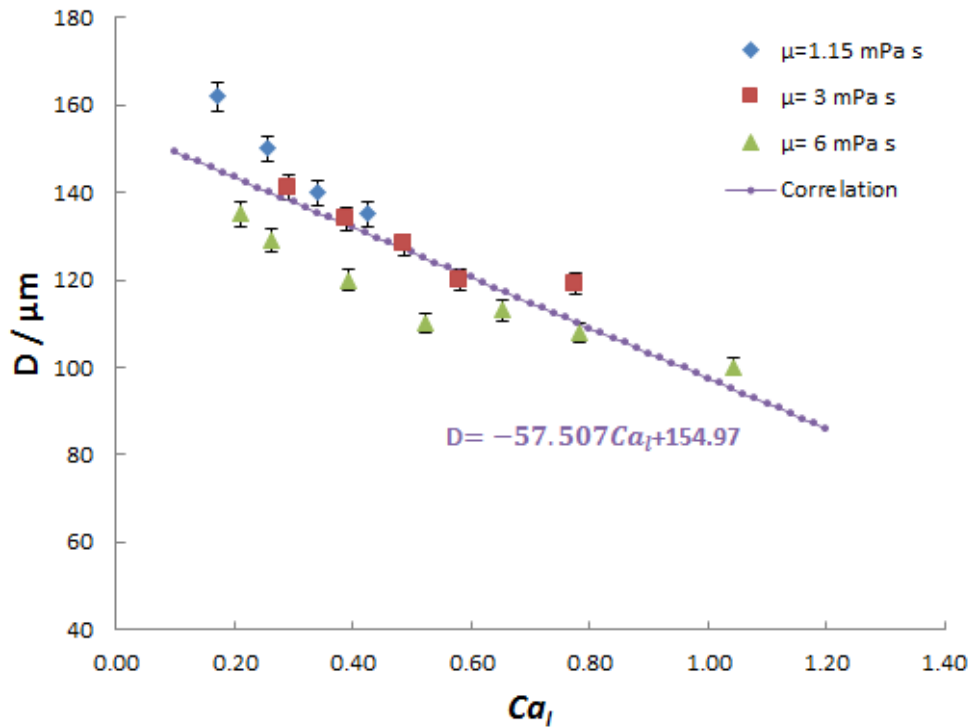


**Figure 4. 8:** Diameter of bubbles produced in the T-junction as a function of liquid capillary number for three different viscosities (see legend in the figure) and constant gas pressure of 60 kPa.

#### 4.2.7 Effect of the vertical gap size (Cavity) on bubble size

In order to investigate the effect of the change of the gap size (shown in **Figure 3.5**) on the bubble formation, three different gap sizes were chosen for the experiments. The effect of increasing the gap size on bubble formation and eventually bubble size was studied. As illustrated in micrographs in **Figure 4.9**, bubble size increases by increasing the gap size from 50 to 220  $\mu$ m. In this set of images, a1 and a2 are images corresponding to a 50  $\mu$ m gap size shown in **Figure 4.10**. In addition b1 and b2 correspond to 220  $\mu$ m gap size. It is evident in both images and the graphs that bubble size for the smallest and largest bubbles produced for a given flow rate and viscosity increases significantly by increasing the gap size. Also it is clear that for the same liquid flow rate and viscosity, bubble formation occurs within a higher range of gas pressure for the larger gap size.

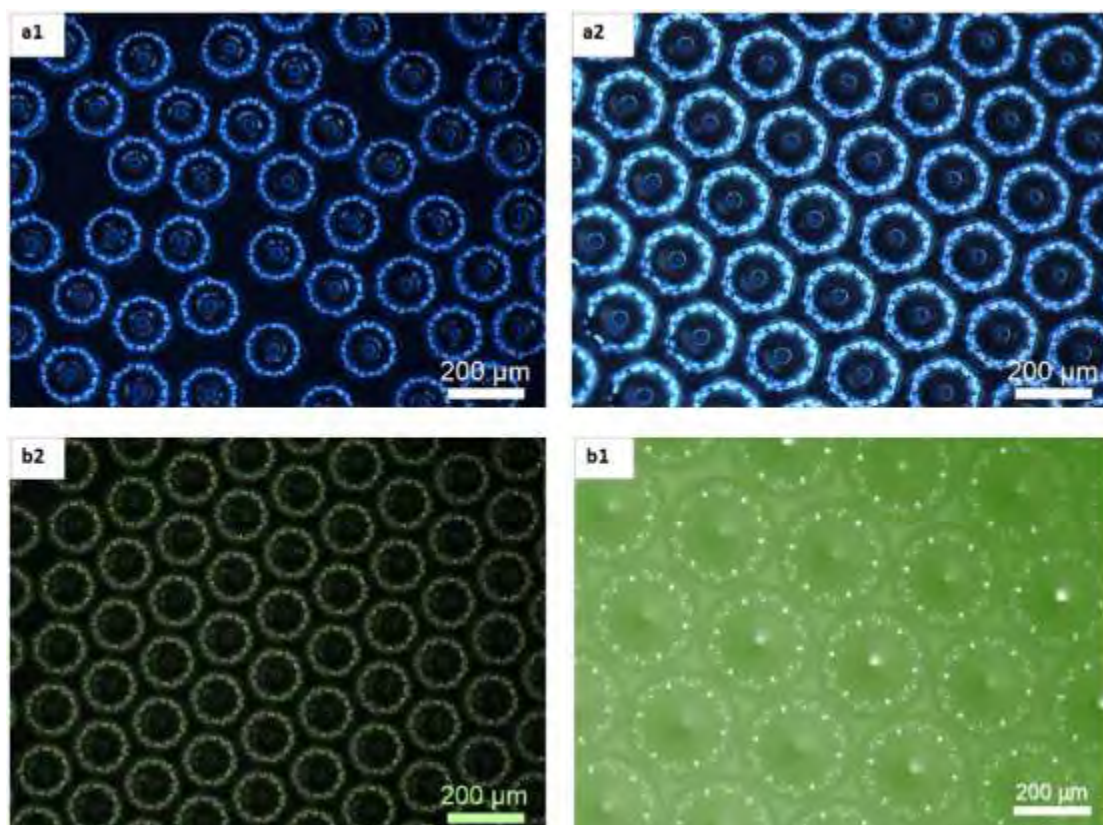


*Figure 4. 9: Micrograph images of bubbles produced with two different junction gap sizes of a) 50 $\mu$ m and b) 220 $\mu$ m.*

However in a region where bubbles are formed at a constant gas pressure, bubbles formed are smaller for the larger gap size, indicated by boxes drawn on the graphs in **Figure 4.10**.

As well as images and graphs that show bubble formation is influenced by the variation in size of the gap between the aligned capillaries, **Figure 4.11** illustrates the time evolution of bubble formation with the gap sizes of a) 50 and b) 220  $\mu$ m. Images in **Figure 4.11** reveal that at a fixed liquid flow rate of 0.04 ml/min and viscosity of 60 mPa s, the increase in the gap size increases in the bubble size while it leads to the expansion time decreasing and a longer bubble /slug being produced. As shown in **Figure 4.11a, b**, the time taken for the bubble to form from growth to pinch off is lower (0.165 s) for the smaller gap size (50  $\mu$ m), whereas, for the larger gap size (200  $\mu$ m) the overall time for bubble formation is  $t = 0.024$  s.

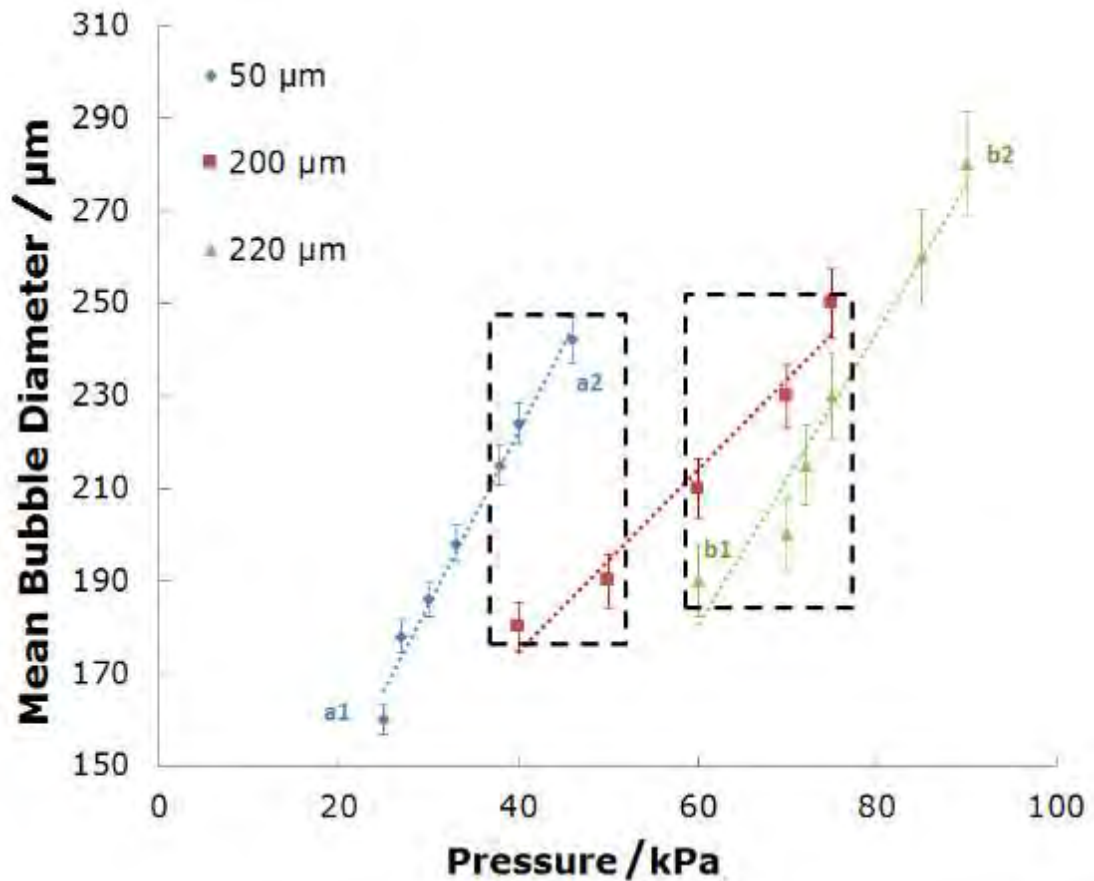


Figure 4. 10: Graph representing variation of bubble size with gas inlet pressure at three different gap sizes of 50, 200 and 220 $\mu\text{m}$ .

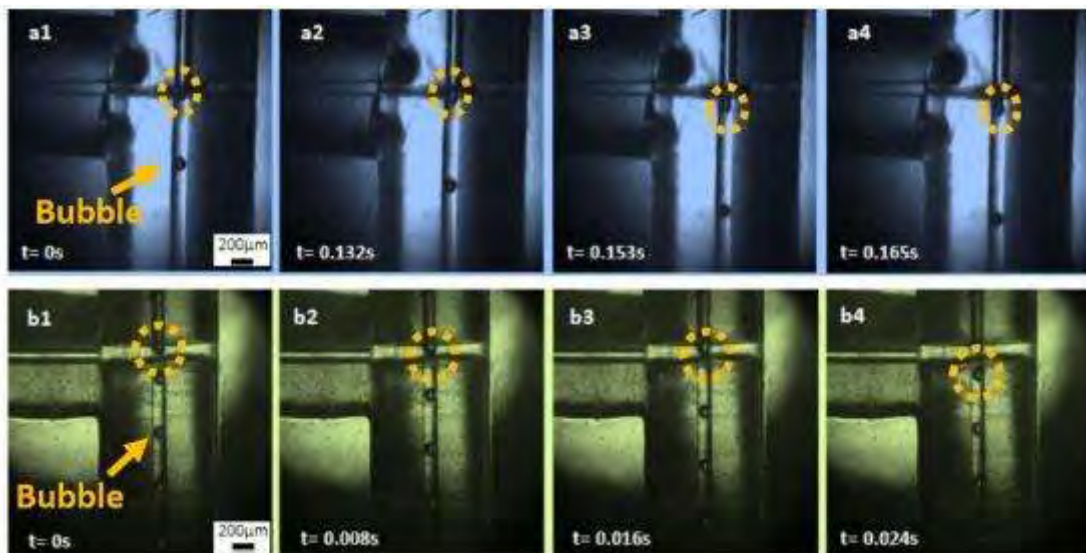


Figure 4. 11: High speed camera images of time evolution of the bubble formation in the capillary embedded T-junction, for two different junction gap sizes of a) 50 and b) 220 $\mu\text{m}$  at constant liquid flow rate (0.04 ml/min) and viscosity(60 mPa s).

#### 4.2.8 Bubble entrapment inside channels

In the process of bubble formation in the capillary embedded T-junction, it has been noted that bubbles become trapped in the junction, where the two phases meet, and influence the flow inside the capillaries and further affect the size of bubbles produced (**Figure 4.12**). This could be caused by a number of issues.



*Figure 4. 12: Existence of trapped bubbles in the junction cavity.*

First, the capillary tubing inserted in the T-junction block does not fit perfectly within the walls and small gaps appear either to be filled with gas or excess liquid. In addition, the geometrical irregularities in the transversal cut of the tubes or the presence of some debris in the gap are believed to have led to the occurrence of trapped bubbles in the junction. Finally, a sudden rise in gas pressure due to restrictions of the gas regulator could cause this effect. In order to ensure that the measurements taken are accurate, every time any reading is done, one has to check there are no bubbles trapped in the junction by using the real time images from the high speed camera.

#### Summary

The mechanism of bubble formation in a capillary embedded T-junction was investigated in detail and the influence of different variables, in particular flow rate ratio and viscosity on the bubble size was determined. While the bubble size decreases with increasing liquid flow rate and viscosity, the increase in gas inlet pressure proportionally increases the bubble size. Furthermore, there is a limit to the extent to

which bubble size can be reduced by increasing viscosity and/or flow ratio for a given capillary diameter and gap size. Therefore, a fixed size capillary diameter was chosen for all sets of experiments that involved the investigation of the effect of parameters other than the capillary size. Further experiments were carried out to investigate the effect of capillary size in conjunction with the solution viscosity and liquid/gas flow ratio, to further reduce the bubble size. The results presented in this study facilitate the selection of solutions based on their physical properties and flow parameters as well as the capillary size for the controlled formation of highly monodisperse bubbles in the capillary embedded T-junction device. Factors such as liquid viscosity and the microchannel geometry have not been adequately accounted for in the scaling laws reported to date and therefore a modified scaling law is required to describe the behaviour of the process and predict bubble size taking all these parameters in to account. In addition, there is a possibility of presence of swirl effect on the junction where the two phases meet. From the findings in this work, it can be concluded that, in the bubble formation regime, by increasing the viscosity and decreasing the capillary size, producing smaller bubble size could eventually become achievable; bearing in mind the restrictions of the experimental setup (i.e. range of liquid flow rate and gas pressure and geometry).

### **4.3 Preparation of microbubbles with T-junction integrated with electrohydrodynamic focusing**

#### **4.3.1 Introduction**

While previously the two standard techniques (microfluidics and EHD) have been separately used to produce microbubbles, to the best of author's knowledge, the combination of these two methods to form bubbles has not been reported in the literature. The capillary embedded T-junction device described in this work is different from the conventional microfluidic chips manufactured through much more expensive methods (i. e. lithography). This device provides a simple but yet robust production of highly monodisperse microbubbles without the need of continuous cleaning and replacement due to the blockage of channels caused by the material residue.

Another advantage of this setup is that the channel diameter is generally larger and therefore pressure drop in the channel is much lower than smaller diameter channels. However, because the channel diameters are large the production of bubbles much smaller than the channel diameter is not viable with only the T-junction device with mechanically driven flows. In this work by introducing the electric field directly into the bubble breakup region, the flow of the continuous phase is assisted with electrohydrodynamic flow and bubbles with almost an order of magnitude smaller than the channel diameter were generated. In this work, a microfluidic system with integrated electrohydrodynamic focusing with the aim of both reducing bubble size and maintaining monodispersity is presented. In addition, the effect of applied voltage, solution viscosity and electrical conductivity on the production of microbubbles and their characteristics are investigated.

#### **4.3.2 Influence of electric field on bubble formation**

Reynolds number for the liquid phase was calculated as  $7 \times 10^{-5} \leq Re_l \leq 9.3 \times 10^{-3}$ , for the constant liquid flow rate of 0.01 ml/min and range of solution viscosities from 1.3 to 60 mPa s. When  $Re_l < 1$  creeping motion or stokes flow occurs and as a result the flow is dominated by viscous stresses and pressure gradients and therefore inertial effects are negligible. This is due to the fact that the fluid velocities are slow, while the liquid

viscosity is reasonably high and the length scale of the flow is very small. Once the flows of the two phases in the junction reach equilibrium, bubbles are formed whose size depends upon the balance of capillary force, Laplace pressure and liquid shear stress force (Christopher et al., 2008). For these experiments the solution viscosity was fixed and the flow rate and the minimum gas pressure required to produce the smallest bubble size, for a fixed polydispersity index was determined.

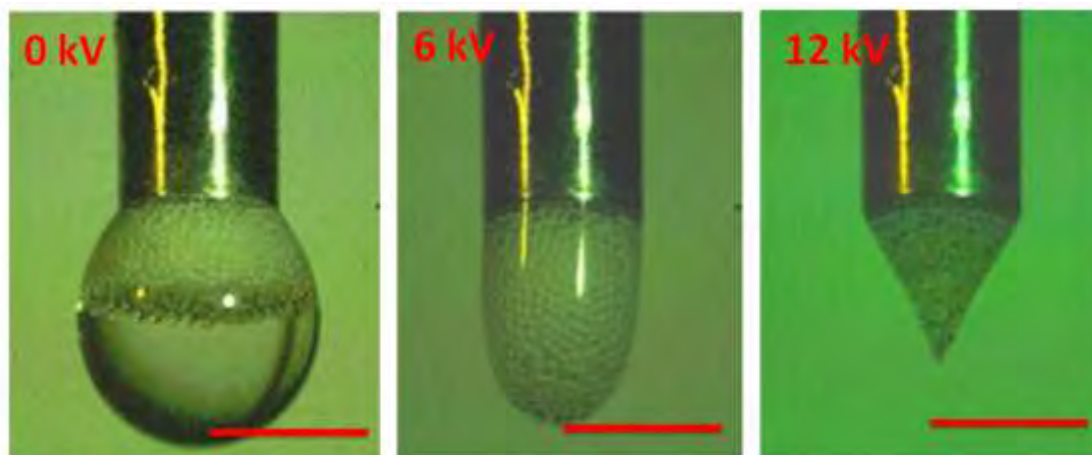


*Figure 4. 13: High speed camera images of microbubbles at the tip of the outlet at applied voltages of 0, 6 and 12 kV. Scale bar is 1.6 mm.*

In the absence of an electric field a hemispherical droplet containing microbubbles was observed emerging from the tip of the outlet capillary (**Figure 4.13a**). This shape is due to liquid surface tension exceeding the weight of the droplet. With the application of an electrical potential, the air/liquid interface became polarized causing deformation of the meniscus containing bubbles (**Figure 4.13b**). With increasing voltage the droplet adopted a conical shape (**Figure 4.13c**), referred to as a Taylor cone (Taylor, 1964). With increasing voltage, the surface tension cannot maintain the liquid inside the meniscus, thus a thin jet at the tip of the cone appears, which subsequently breaks up into a spray containing smaller microbubbles. In this set up the formation of a Taylor cone and stable jet was initiated at 9 kV.

As well as the aforementioned effect at the tip of the outlet channel, a tangential electrical force is created that leads to faster breakup of the gas column at the junction, therefore reducing the detachment time hence leading to the formation of smaller bubbles at a faster rate (Jayasinghe and Edirisinghe, 2005).

### 4.3.3 Effect of voltage increment on microbubble size

Bubble formation under the influence of an electric field was observed in the experiments using aqueous glycerol solution with 5, 50, 65 and 75 wt% glycerol concentrations in order to determine the effect of viscosity. The liquid flow rate was set for all the experiments as 0.01 ml/min, while the gas pressure was adjusted to generate monodisperse bubbles for each solution. Once the bubbles were formed at the minimum gas pressure ( $P_{gmin}$ ) for each solution, the applied voltage was increased to 6 kV, where the meniscus at the tip of the outlet channel became thinner while the jet diameter was reduced and therefore microbubble size decreased. For instance, for the lowest solution viscosity (1.3 mPa s) the diameter of microbubbles produced without an electric field was 170  $\mu\text{m}$ , which reduced to 120  $\mu\text{m}$  at 6 kV (**Figure 4.14**).

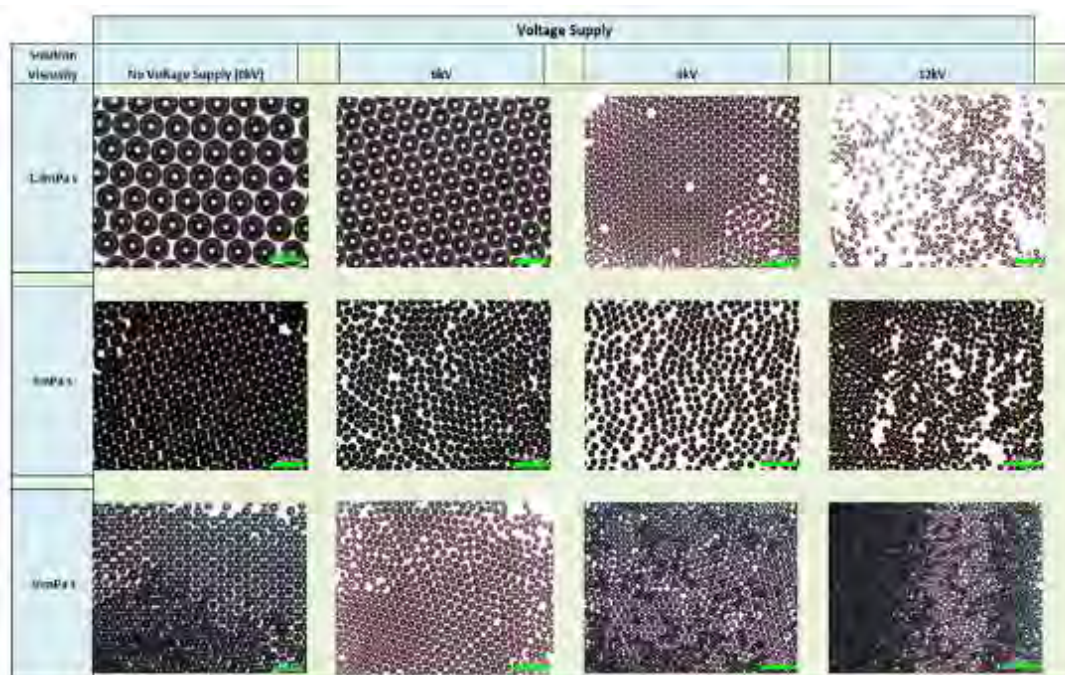


**Figure 4. 14:** Optical micrographs of bubbles formed in aqueous glycerol with 5, 50 and 75 % concentration at applied voltages of 0, 6,9 to 12 kV and a constant liquid flow rate of 0.01ml/min. Scale bar is 200  $\mu\text{m}$ .

By increasing the voltage to 9 kV, a cone jet was created at the tip of the outlet channel and the size of bubbles reduced further, to 40  $\mu\text{m}$  with polydispersity index (PDI, defined as the ratio between the standard deviation and mean diameter in percentage (Hettiarachchi et al., 2007)) of  $\sim 1\%$ . At 12 kV voltage, the cone jet broke up into a spray of fine liquid threads and bubbles with even smaller diameters ( 30 $\pm$ 0.95  $\mu\text{m}$ )

were produced. This process was repeated for solutions with higher glycerol concentration and viscosities of 6, 15 and 36 mPa s and it was shown that increasing the voltage also affected bubble size for the highest viscosity solution while the smallest microbubble diameter of 25  $\mu\text{m}$  was produced for the solution with 36 mPa s viscosity at 12 kV.

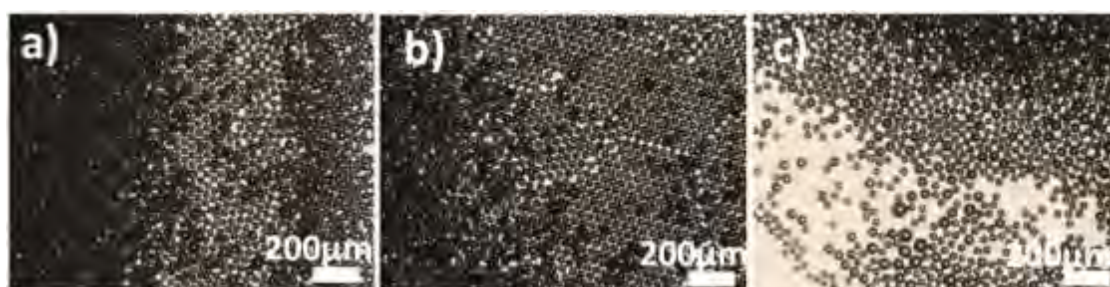


**Figure 4.15:** Optical micrographs of microbubbles from a solution with 75% glycerol concentration at constant liquid flow rate of 0.01 ml/min at applied voltages of a) 12, b) 15 and c) 21 kV.

Increasing the applied voltage to 15 kV, did not change the bubble size significantly at any of the glycerol concentrations. However bubble stability decreased, most likely as a result of coalescence due to the higher surface charge. **Figure 4.15** shows microscopic images of microbubbles produced from 75% glycerol solution at constant liquid flow rate and applied voltages of 12-21 kV. It is evident from the images that at 12 and 15 kV the bubble size was the same (25  $\mu\text{m}$ ) and they were near monodisperse. However, increasing the voltage supply to 21 kV led to a much broader size distribution. This suggests that the optimum voltage for this system is 12 kV and increasing the voltage above this rate only reduces microbubble stability and monodispersity.

A series of graphs were plotted (**Figure 4.16**) to show the variation in microbubble size with increasing voltage. In all cases, as the voltage increased, bubble diameter decreased; however a dramatic decrease in bubble diameter was observed between 6-9 kV for the solution with lowest viscosity that was not seen in the other solutions. This is most likely to be due to the fact that the solution with 5% glycerol concentration has a much higher dielectric constant (Behrends et al., 2006) and therefore the effect of applied voltage on bubble diameter is greater. The scaling law proposed by Pantano et al. (Pantano et al., 1994) predicts that the diameter of droplets produced by

electrospraying is inversely proportional to the liquid dielectric constant.

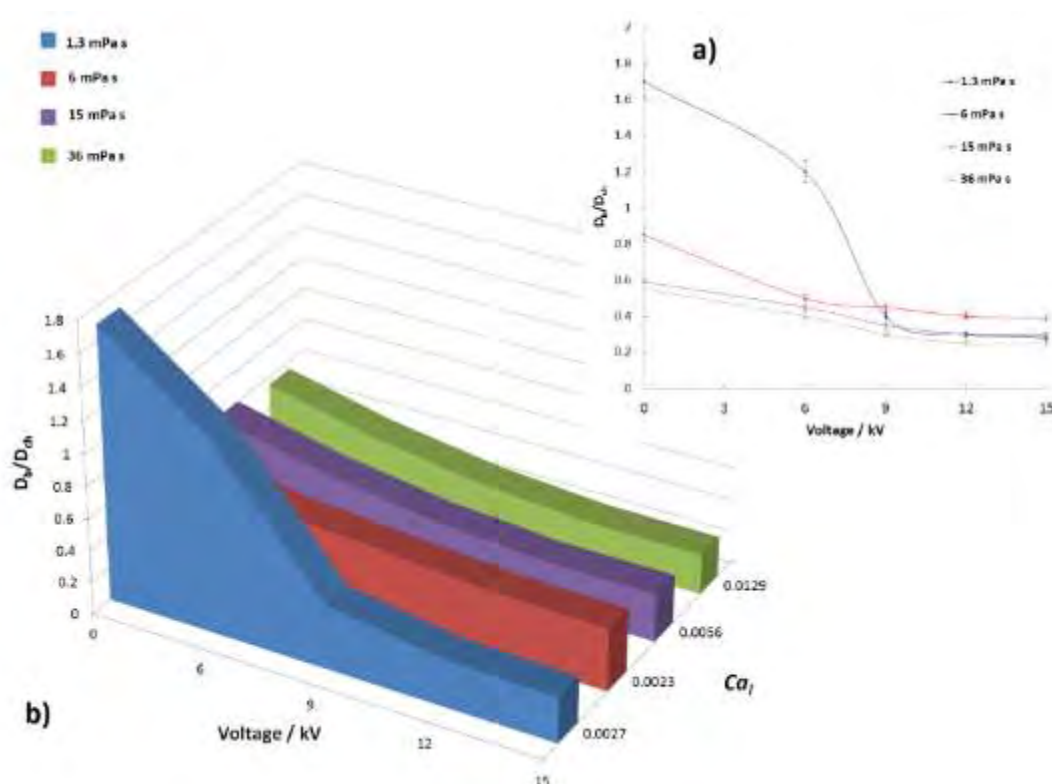


**Figure 4. 16:** a) Graph showing variation of bubble diameter with applied voltage for solution viscosities of 1.3, 6, 15 and 36 mPa s, and b) 3D plot of dimensionless bubble diameter with respect to voltage and capillary number increment.

In order to investigate the effect of viscosity, surface tension, flow rate ratio and applied voltage supply in parallel, a 3D plot of the variation of ratio of bubble diameter to channel width was plotted as shown in **Figure 4.16b**. It can be observed that for each value of the capillary number, with increasing voltage the bubble to channel diameter ratio decreased dramatically between 0 and 9 kV. The reduction in this value is less significant, however at larger voltages. According to Ku and Kim (Ku and Kim, 2002) for highly conducting and viscous liquids, the size of droplets electrospayed from a Taylor cone are found to be relatively insensitive to the applied voltage and as long as the corona discharge density is not too high, monodisperse droplets are produced. Corona discharge is caused by the ionization of the surrounding medium that occurs once the electric field strength exceeds a certain level (the corona threshold voltage)

while conditions are inadequate for a complete electrical breakdown. Above this voltage, there is a limited region, in which current increases proportionately with voltage according to Ohm's law. After this region, the current increases more rapidly, leading to complete breakdown and arcing or sparking at a point called the breakdown potential.

It is also shown in **Figure 4.16 b** that with increasing capillary number, there is a smaller reduction in bubble size for the same increase in applied voltage. This suggested that there other parameters such as solution electrical conductivity and relative permittivity as mentioned previously influence the bubble formation process.

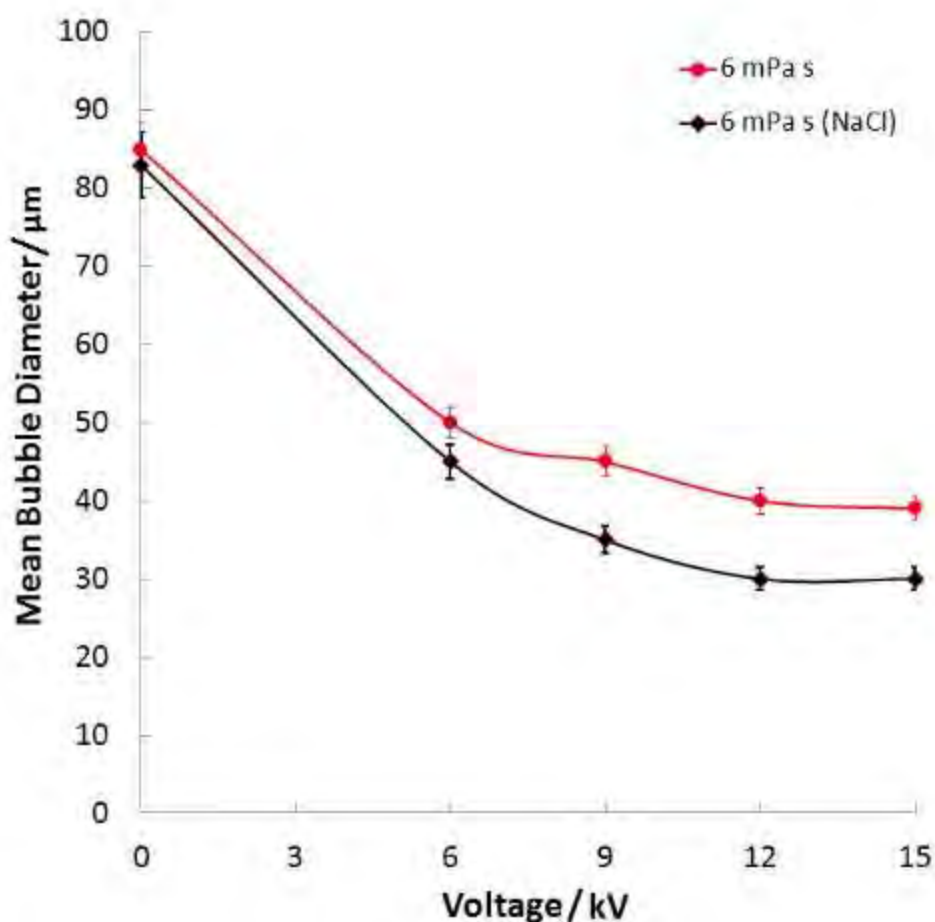


**Figure 4. 17:** Graph showing variation of bubble diameter with applied voltage for solution with constant viscosity of 6 mPa s with and without NaCl solution added. (PDI < 1%, Error bars indicating the experimental errors.)

To investigate this further, NaCl was added to the solution keeping the concentration of glycerol constant at 50% in order to increase the electrical conductivity while keeping the other solution parameters constant. The results are plotted in **Figure 4.17** and as predicted, by increasing the electrical conductivity of the solution while keeping the viscosity and flow ratio constant, the influence of the voltage supply on microbubble size increases. This explains the dramatic decrease in bubble diameter in the graph representing the solution with lowest concentration of glycerol compared with the other graphs in **Figure 4.16**. The electrical conductivity of the liquid phase is one of the key parameters in determining and predicting the bubble diameter.

### **4.3.4 Mapping of the dimensionless bubble diameter with applied voltage and liquid physical parameters**

In **Figure 4.18**, the non-dimensional bubble diameter ( $D_b/D_{ch}$ ) is plotted as a function of the applied voltage for four solutions of different concentration of glycerol. As mentioned previously, the results are in agreement with the theory of electrohydrodynamic instability in microchannels. It can be seen that in all cases the non-dimensional bubble diameter decreases by increasing voltage, while it reaches a plateau at voltages higher than 12 kV. When low voltage is applied, the electric field assists with the compression of the neck of the dispersed phase, resulting approximately linear decrease in bubble size for voltages  $\leq 12$  kV. By further increasing the applied voltage, the width of the neck during the breakup reduces. However, similar to observations by Kim et al. (Kim et al., 2007) and Link et al. (Link et al., 2006) jetting appears at high voltage and electric field barely has any effect on the bubble size. While at low voltage supplies, hydrodynamic effect is the dominant factor in bubble size, formation of Taylor cone is disrupted at high voltages due to the larger electric field from the electrospraying regime. Hence, the production of monodispersed bubbles is aborted at voltages more than 20 kV. For each case, a correlation that represents this asymptotical decrease is also plotted. According to the curves obtained, it can be observed that the solutions of higher concentration of glycerol (i.e. higher viscosity) follow a similar trend, whilst in the case for the solution with the lowest viscosity the trend is slightly changed due to the fact that the electrical conductivity is higher than the other solutions with higher concentration of glycerol and analogous values for

electrical conductivity. For the range of  $Ca$  numbers investigated, a general predictive model is obtained where the normalized bubble diameter can be estimated as the following:

$$\frac{D_b}{D_{ch}} = (-11.8 Ca + 0.37) + (-0.98Ca + 0.5)e^{(6.8Ca-0.2)V} \quad \text{Eq (4.3)}$$

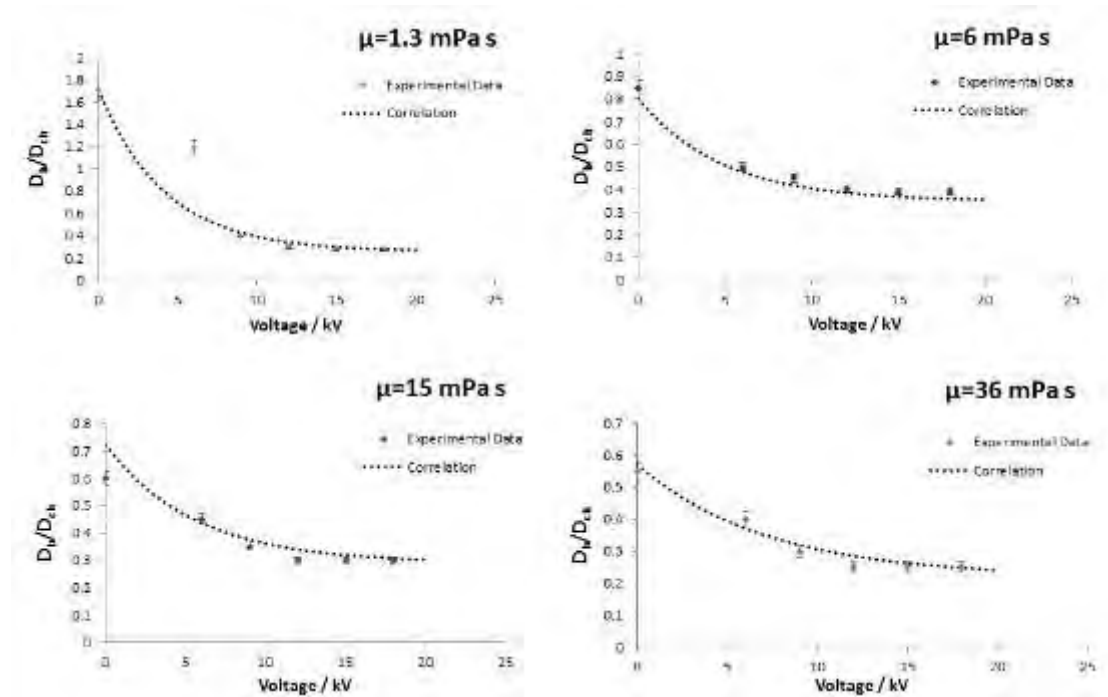


**Fig. 4. 18:** Experimental results versus correlations and predictive model for bubble dimensionless diameter for solution with viscosity of a) 1.3, b) 6, c) 15 and d) 36 mPa s. (PDI < 1% , Error bars indicating the experimental errors.)

This model can predict the dimensionless bubble size for a range of capillary numbers  $0.001 \leq Ca \leq 0.04$ , with approximately 8% error. In **Figure 4.19**, the experimental values for  $D_b/D_{ch}$  are plotted against the predictive values and the proximity of the experimental data to the parity line suggests that the predictive model is in agreement with the experimental data especially for the obtained values of  $D_b/D_{ch} < 0.6$ . This model does not take into account the geometrical aspects of the channel (i.e. the gap between the capillaries), as these parameters also affect the bubble size.

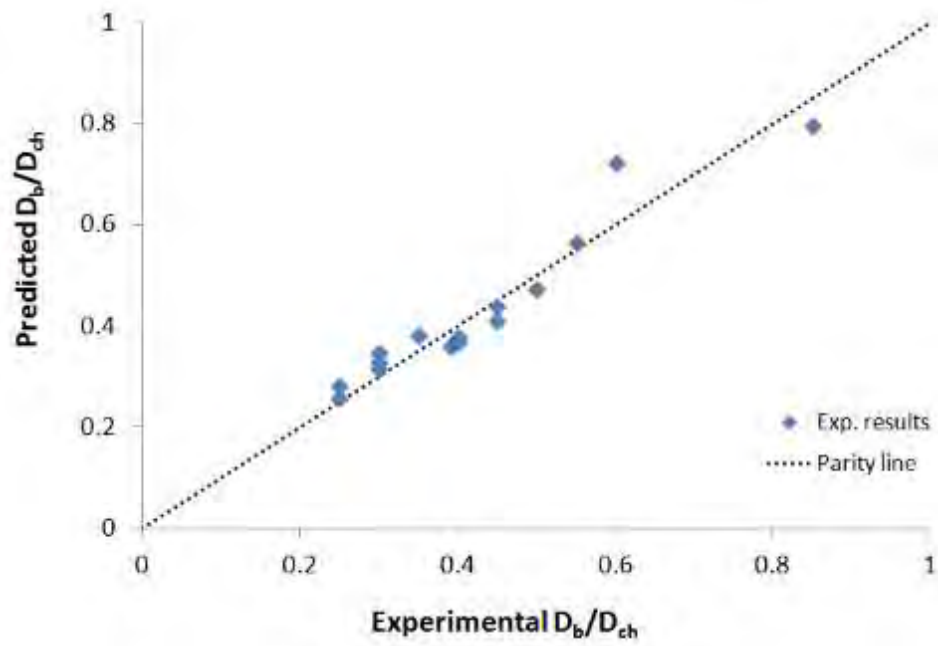


*Figure 4. 19: Graph representing experimental data for dimensionless bubble diameter against predictive values.*

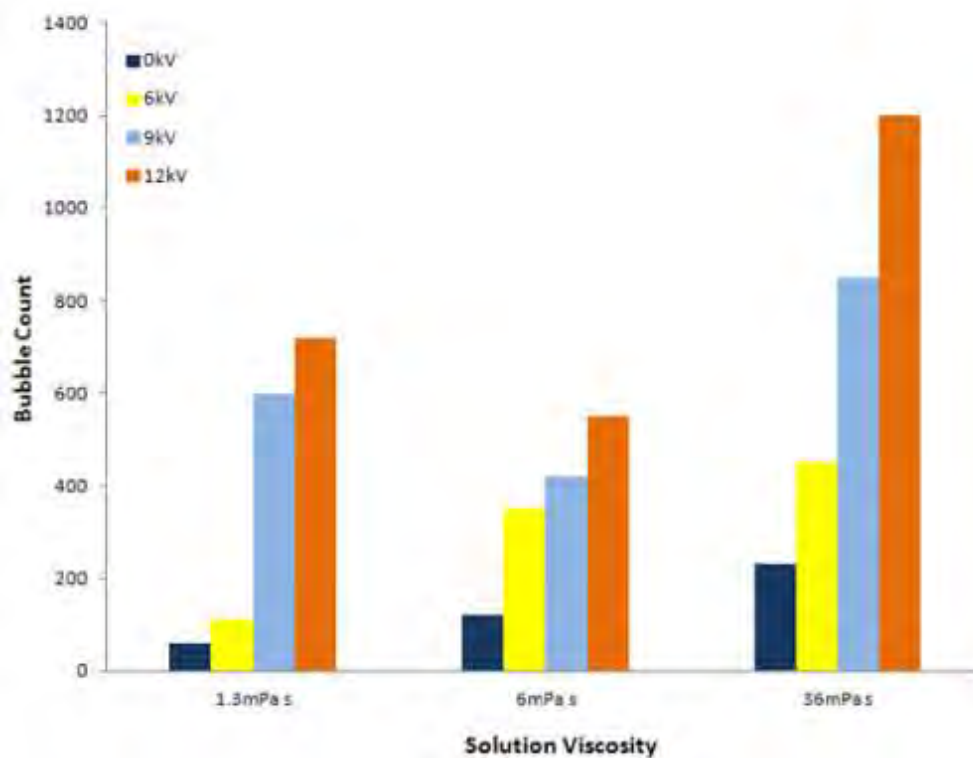


*Figure 4. 20: Chart showing variation in the number of bubbles generated with applied voltage for three different solution viscosities of 1.3, 6 and 36 mPa s over a fixed time period of 5 seconds and collection area of 1.5 mm<sup>2</sup>.*

#### 4.3.5 Influence of electric field on bubble uniformity and production yield

Microbubbles produced with voltage supply  $\leq 15$  kV were highly monodispersed with polydispersity index of  $\leq 1\%$ . It was shown that electrohydrodynamic instability caused by the applied electric field only increased the velocity of the suspension flow due to an increase in the exerted body force and had little effect on the uniformity of the bubbles produced. **Figure 4.20** depicts the number of bubbles produced with and without the presences of an electric field for variation of solutions viscosities over a fixed time period of 5s and collection area of  $1.5 \text{ mm}^2$ . It is shown that by increasing the voltage not only the bubbles become smaller but also the production rate increases. In addition, from the data obtained from the high speed camera images, for a given liquid flow rate of  $0.01 \text{ ml/min}$ , the number of bubbles in every 1 ml of the collected sample is between  $1.9 \times 10^6$  and  $5.98 \times 10^6$  depending on the bubble size. While this work is demonstrating the principle of reduction in bubble size with the electrically assisted microfluidic flow, the scaling up in the production of monodisperse bubble was not the main focus in this study.

#### 4.3.6 Comparison with other bubble formation techniques

The three common methods of producing microbubbles are sonication, Electrohydrodynamic (EHD) bubbling and microfluidics. Amongst these techniques, CEHD and sonication produce microbubbles with diameters smaller than  $10 \mu\text{m}$  with a very wide size distribution of  $\sim 30\text{-}40\%$ . While the production rate is very high with the sonication method, the number of microbubble formed using the EHD technique proposed by Farook et al. (Farook et al., 2007) is smaller than that obtained using the sonication method. Microfluidics, on the other hand have the potential to produce uniformly size microbubbles with  $\text{PDI} < 2\%$ . In order to produce microbubbles suitable for biomedical applications, it is required to use microchannels with smaller diameter  $< 20 \mu\text{m}$ , hence these small channels can easily get blocked by the material residue. Also it is very difficult to pump highly viscous liquid through these channels due to the higher pressure drop. Hettiarachchi et al. (Hettiarachchi et al., 2007) have used a rather complicated flow focusing geometry and bubbles were generated through jetting mode rather than bubble dripping mode that is harder to control as the increase in the flow rate leads to decrease in the distance of the bubbles formed and therefore causes the

bubbles to coalesce inside the channels prior to collection. Whilst they used high flow rates and gas pressures (e. i.  $Q_l > 1 \mu\text{l/s}$   $P_g > 10 \text{ psi}$ ) to increase the production rate, the polydispersity of microbubbles were  $> 50 \%$ . Furthermore, Kendall et al. (Kendall et al., 2012) used multi array microfluidic flow focusing geometry containing up to eight channels to scale up the production of bubbles. They have reported the highest production at  $1.34 \times 10^5 \text{ Hz}$  (bubbles/second) with bubble size ranging between  $18.6\text{-}22.3 \mu\text{m}$  and polydispersity index  $< 9\%$ . In this T-junction set-up bubbles were produced with  $1000 \text{ Hz}$  to achieve the highest production rate of a much lower liquid flow rate compared to the studies mentioned above. A method has been proposed to use a simple T-junction setup with larger channels and the bubble size was successfully reduced within the same channels by using an external electric field while the polydispersity index is  $< 1\%$  as well as increasing the production rate.

### **4.3.7 Applications impacted on by the reduction of microbubble size using electric field**

Size of microbubbles is an important parameter governing the interfacial area between the gas and liquid phases; smaller microbubble size generally implies a larger interfacial area. The size of microbubbles also influences many important properties of microbubbles (e.g., shrinkage and floatation). There are various applications from biomedical to food to water treatment that require microbubbles with smaller size range. For instance, microbubble destruction has been proposed as an innovative method for non-invasive delivering of drugs and genes to different tissues. Conventional flotation assisted with microbubbles ( $30\text{-}100 \mu\text{m}$ ) finds application in the recovery of fine mineral particles and flotation with these fine bubbles is being used as a solid/liquid separation to remove pollutants. Recent bench studies of flotation of different minerals; with injection of microbubbles ( $40 \mu\text{m}$ , mean diameter) to lab cells (in addition to the cell generated coarse bubbles) have improved separation parameters when compared to the mill standard (Yalcin et al., 2002). Microbubble having boost utilization in formation of biofuel. Thus microbubbles having various applications in various fields. Mixture of ozone nanobubbles with oxygen microbubbles can be used as a water sterilizer. Water in which ozone bubbles are combined with oxygen microbubbles is more effective in fighting bacteria than conventional ozone water (Kukizaki and Goto, 2006). In this work by introducing the external electric field, a wider range of

microbubble size can be produced with this modification which enables a larger control over the generation of bubbles for a variety of applications mentioned above.

### **Summary**

Monodisperse microbubbles were successfully produced using an integrated microfluidic and electrohydrodynamic device. A systematic investigation of bubble formation at different applied voltages and with different liquid properties was performed. It was shown that bubbles of much smaller diameter than that of the microchannel (for the smallest bubble size that was produced with almost an order of magnitude smaller than the channel diameter) could be produced with a polydispersity index close to 1%. A critical voltage of 12 kV was determined above which no further reduction in bubble size was achieved, and this limit was not affected by increasing the solution viscosity or electrical conductivity within the ranges used in this study. The observed dependence of bubble size on applied voltage is consistent with electrohydrodynamic theory. In addition to reducing the bubble size, applying an electrical potential difference increased the rate at which bubbles were produced.

## **4.4 The effect of surfactant type and concentration on the Size and stability of microbubbles in the T-junction device**

### **4.4.1 Introduction**

The composition and physiochemical properties of the surfactant used can greatly affect the formation and stabilization of microbubbles. One of the most important factors to consider with respect to surfactant-containing solutions is the critical micelle concentration (CMC) (Xu et al., 2009), at which the surfactant aggregates and form micelles while the properties of the solution dramatically change at this concentration. It is generally known that in order to achieve the maximum effect of the surfactant, higher concentrations than the CMC are required. Therefore, in this study experimental investigations on the influence of three different types of commonly used surfactants (cationic, anionic and nonionic surfactants) at concentrations much higher than CMC for the effect of the chain lengths and molecular structure of surfactants on the properties of the liquid phase, mainly the contact angle and capillary number, are presented. In this work a detailed analysis of variation of the concentration and type of surfactants on bubble formation and size in a capillary embedded T-junction device was carried out. Moreover, the stability of microbubbles produced for each type and concentration are examined. This study was conducted to select a surfactant type and concentration to achieve the best results in terms of bubble size and stability.

### **4.4.2 Effect of surfactant concentration on the properties of the liquid phase**

Three types of differently charged surfactants with three different concentrations of 2, 5 and 10 wt % were chosen for this study. Both PEG 40 and Tween 40 were chosen as nonionic type. The molecular structure of these two surfactants contain polyoxyethylene units that decrease the hydrophobic character of the surfactant, and as a results they appear to adsorb more efficiently onto hydrophobic surfaces than onto hydrophilic ones. SDS was selected as the anionic surfactant and CTAB for the cationic category (Rosen and Kunjappu, 2012) . All surfactants have both hydrophilic and hydrophobic chains. Both nonionic surfactants Tween 40 and PEG 40 have relatively large hydrophilic groups, while CTAB has the larger hydrophobic chain (Tong et al., 2000). On the other hand, for higher concentrations of CTAB and SDS the preparation

of the solutions required heating the solutions at 70 °C for approximately 120 s prior to the experiments. From the data in **Table 3.4**, it is clear that the concentration and type of the surfactant have an impact on the surface tension and contact angle of the aqueous glycerol solution. All the surfactants selected for this study are water soluble. The surfactants have different abilities in lowering the surface tension of the aqueous phase. The interfacial tension of the solutions containing nonionic surfactants Tween 40 and PEG 40 decreased dramatically to 41.6 and 46.3 mN/m, respectively, at 2 wt % concentration. However, increasing the concentration of these surfactants further to 5 and 10 wt % had a little effect on the surface tension but increased the viscosity of the solutions. This suggests that the concentrations used in this study were higher than the critical micelle concentration (CMC). This trend also occurred for the case of SDS and CTAB, although the surface tension of the solution decreased more with the addition of the latter. As demonstrated in **Table 3.4**, the surface tension for 2 wt % PEG 40 has the largest value, while the solution with 10 wt % CTAB concentration has the lowest interfacial tension. For the case of nonionic surfactants, by increasing the concentration, the contact angle decreased. Otherwise, the increase in concentration of cationic surfactant CTAB and anionic SDS led to increase in the contact angle. In polyoxyethylene nonionic surfactants, increasing the number of oxyethylene groups ( $C_2H_4O$ )<sub>n</sub> reduces the efficiency of adsorption of the surfactant on the surface of most materials because the cross sectional area of the molecule at the interface increases (Rosen and Kunjappu, 2012). Since the number of oxyethylene groups in PEG 40 is higher than Tween 40 (**Table 3.1**), the hydrophobic character of the surfactant is decreased, leading to higher adsorption of surfactant molecules on the channel hydrophobic surface and therefore at all concentrations of surfactants the contact angle is lower compared with PEG 40. At a constant 2 wt % concentration, solutions with both nonionic surfactants (Tween 40 and PEG 40) and SDS have similar contact angles which were all higher than CTAB. Lower contact angle of CTAB results in the reduction of the liquid film thickness at the three phase contact line and therefore formation of bubbles with larger diameter is anticipated for these surfactants. While at 10 wt % concentration, the solution containing PEG 40 has the lowest contact angle, while the other three surfactants have similar contact angles. At higher concentrations of well above the CMC (5 and 10 wt %), the surfactant molecules aggregate and form micelles in the bulk (Xu et al., 2006b).

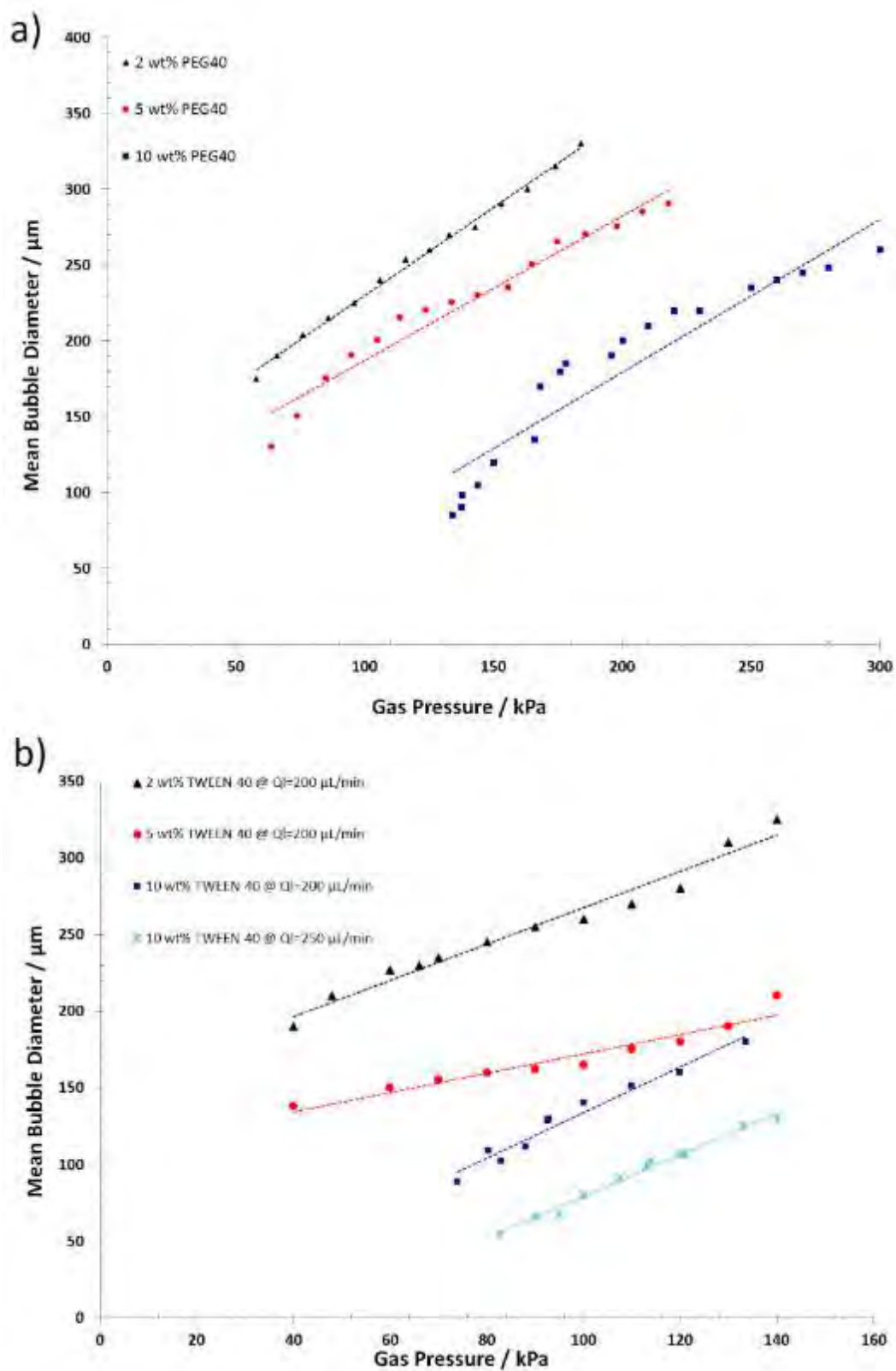


**Figure 4. 21:** The effect of surfactant concentration on bubble size and gas pressure range where bubble formation is achievable for a) PEG 40 and b) Tween 40, all of the microbubbles produced with this setup were highly monodispersed with polydispersity index < 2 %.

#### 4.4.3 Effect of surfactant concentration on bubble size

To investigate the effect of surfactant concentration on microbubble size, three concentrations of the solutions with nonionic surfactants PEG 40 and Tween 40 were chosen. The liquid flow rate was kept constant at 200  $\mu\text{l}/\text{min}$  for all experiments to study the effect of capillary number in conjunction with gas pressure on the given concentration of surfactant in the solution, except for the experiment with 10 wt% Tween 40 where this parameter was increased to 250  $\mu\text{l}/\text{min}$ . As indicated in **Figure 4.21**, bubble formation occurred within a larger range of gas pressures for the highest concentrations for both cases of PEG 40 and Tween 40. In order to produce the same size bubble with diameter of 250  $\mu\text{m}$  (**Figure 4.21a**), larger gas pressure was required for the solution with the highest concentration of PEG 40 (10 wt %). From the measured capillary numbers shown in **Table 3.6**, it can be suggested that by increasing the capillary number, higher gas pressure is required to produce bubbles. On the other hand, for a given gas pressure of 100 kPa (**Figure 4.21b**), where bubble formation occurred for all cases of Tween 40 concentrations, the solution with the lowest concentration generated larger bubble size. As anticipated, the decrease in the bubble size due to increase in capillary number is mainly related to the increase in viscosity of the solution rather than the small variation in the surface tension as a result of the increase in surfactant concentration. It was shown that by increasing the concentration of both surfactants at values higher than the CMC, the bubble size is generally affected by the viscosity changes in the solutions.

#### 4.4.4 Influence of surfactant type on the bubble formation time

In this section, the time taken from the gas column entering the exit channel and the reduction of the neck until the breakup of the formed bubble as well as the effect of the surfactant type on the formation time were studied. In order to study the effect of surfactant type on the formation of microbubbles in the capillary embedded T-junction device, gas column breakup and bubble formation was visualized through a Photron Ultima APX camera with 2000 fps and 3 s recording time. The behaviour of the two phase flow was recorded for the solutions containing 2 wt % of the surfactants, as well as keeping the liquid flow rate constant at 200  $\mu\text{l}/\text{min}$ .

The gas pressure of  $\sim 60$  kPa chosen for this study was within the range of bubble production for all solutions, and therefore the only parameters that changed by varying the surfactant type were the capillary number and the contact angle. Once the bubbles were produced, their diameters were measured with an optical microscope. **Figure 4.22** shows the high speed camera frames illustrating the time evolution of bubble breakup for each surfactant. From the images obtained, it is clear that whilst the operating conditions of the T-junction set-up were kept constant throughout the experiments, the solution containing CTAB produced the largest bubble size ( $290 \mu\text{m}$ ) and the solution with PEG 40 formed the smallest bubbles with  $170 \mu\text{m}$  diameter. The images show that bubbles produced with Tween 40 had a spherical shape and the time taken for the neck to decrease and finally pinch off was longer ( $8.5$  ms) compared to the other surfactants. The bubble size increased with the other nonionic surfactant Tween 40. It is interesting to notice that for both cases of anionic and cationic surfactants, SDS and CTAB respectively, the bubble size increased into a plug like shape while the pinch off time was reduced. Bubble breakup occurred in a quicker rate of  $2.5$  ms for the solution containing CTAB, indicating that for the set operating parameters of liquid flow rate of  $200 \mu\text{l}/\text{min}$  and gas pressure of  $60$  kPa, the number of monodisperse bubbles produced were  $1.2 \times 10^5$  in every  $1$  ml of the collected sample. Since the microchannel walls are made from FEP material, their surface is hydrophobic. The interaction between the solution containing surfactant molecules and the microchannel walls is the key factor that can affect the hydrophilicity of the surface (Kukizaki and Baba, 2008). Both nonionic surfactants PEG 40 and Tween 40 have relatively large hydrophilic chain compared to the large hydrophobic groups in SDS and CTAB. Due to the larger hydrophilic chain of the nonionic surfactants, the adsorption of the surfactant molecules at the contact line between the three phases increase and therefore the thickness of the liquid film at this point increases, which consequently increases the time of the bubble formation. The measured surface tension of  $38$  mN/m for the solution containing CTAB was lower than the SDS, PEG 40 and Tween 40 solution, as listed in **Table 3.4**. This leads to larger surface activity of CTAB compared with other surfactants. On the other hand, the positive CTAB molecules (cations) are attracted to the negatively charged microchannel surface that causes the adsorption of the surfactant molecules to the channel surface and therefore decreases the hydrophilicity of the channel walls. These effects consequently lead to change in dynamic contact angle and wettability of the channel surface that are also important factors to consider in bubble formation process.

Dynamic contact angle would affect the movement of the three phase contact line at the bubble breakup point and therefore it influences the shape of the gas-liquid interface as well as the amount of gas entering the mixing channel. While measuring the dynamic contact angle in the microfluidic channel is challenging, the measured values for the static contact angle can give an indication of the effect that each surfactant has on the wettability of the channel wall surface. The presence of surfactants also creates interfacial gradients (Tong et al., 2000). The interfacial gradients can cause interruption in the flow regime and therefore influence the formation of bubbles.

### 4.4.5 Effect of surfactant type on bubble size

For this study, all surfactants were investigated with concentrations of 2 and 5 wt %. Bubble size was measured for each surfactant and concentration and plots of bubble diameter for the range of gas pressures that bubble formation was possible are presented in **Figure 4.23**. For a given gas pressure at both concentrations, the bubbles produced with the PEG 40 solution were generally the smallest, followed by the solution containing Tween 40. It was shown that for a given gas pressure and surfactant concentration smaller microbubbles were produced at higher capillary numbers for nonionic surfactants followed by anionic surfactant SDS, while cationic surfactant CTAB produced the largest bubbles due to lower capillary numbers. At 2 wt % concentration of Tween 40 and PEG 40, the static contact angles with respect to the channel wall surface were approximately similar ( $58^\circ$  and  $60^\circ$ ), however bubble size as shown in **Figure 4.23 a**) is smaller for PEG 40 and this is due to the effect of the lower capillary number of 2 wt % PEG 40 solution. On the other hand, the values of the contact angle for 5 wt% concentration of Tween 40 and PEG 40 are different but smaller bubbles were produced when the capillary number was smaller for Tween 40, as shown in **Figure 4.23 b**). In addition, at 5 wt % concentration of PEG 40 and SDS where the capillary numbers were the same (0.0019), while the viscosity is approximately similar, PEG 40 produced smaller bubbles. The measured contact angle for PEG 40 ( $49^\circ$ ) is larger than SDS ( $59^\circ$ ). This indicates that the factor affecting the bubble formation and size is the wettability of the channel by the surfactant molecules.

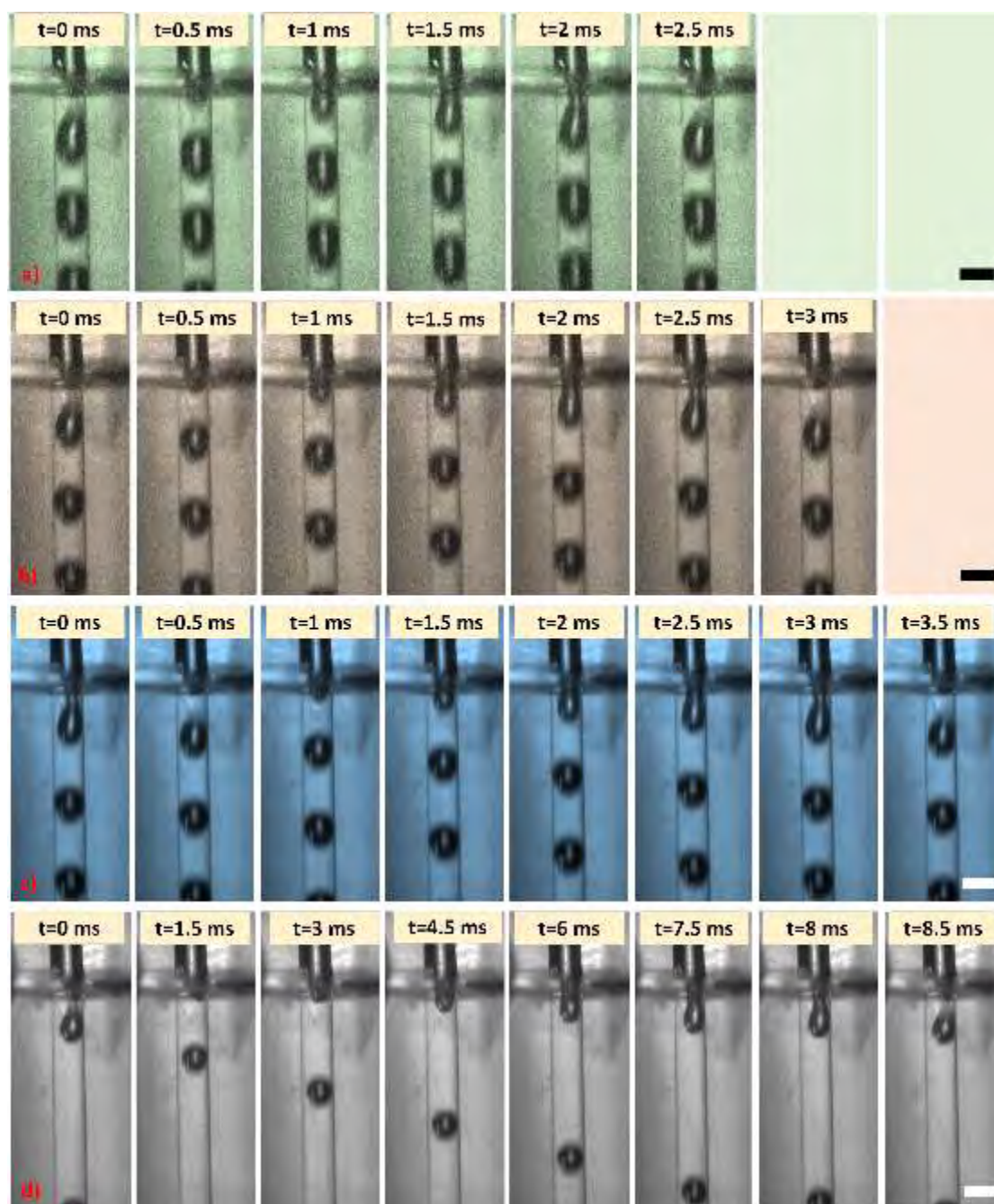
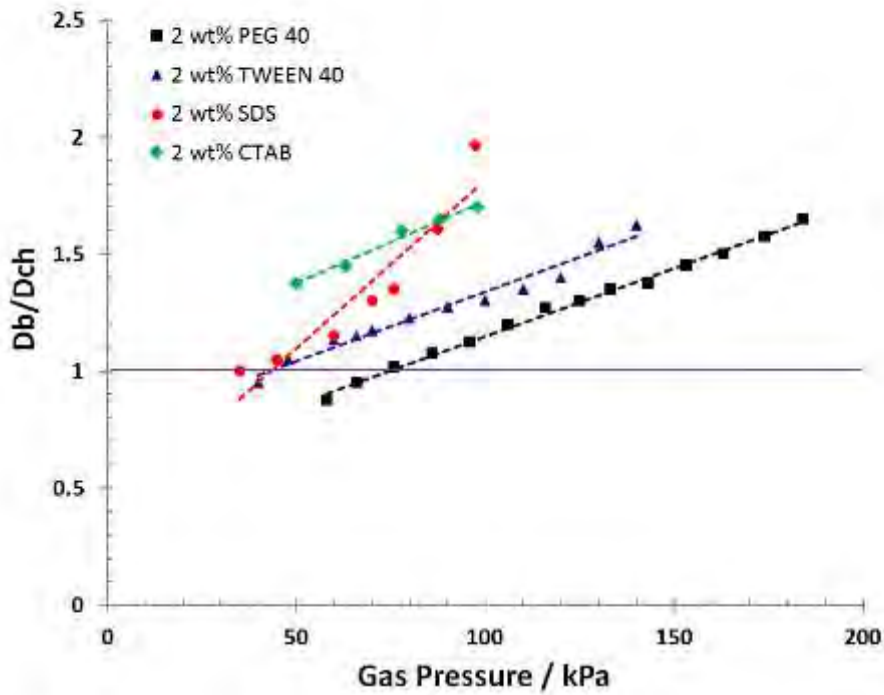


**Figure 4. 22:** High speed camera images of the bubble formation time for a) CTAB, b) SDS, c) Tween 40 and d) PEG 40, scale bar is 200  $\mu\text{m}$ .

a)



b)

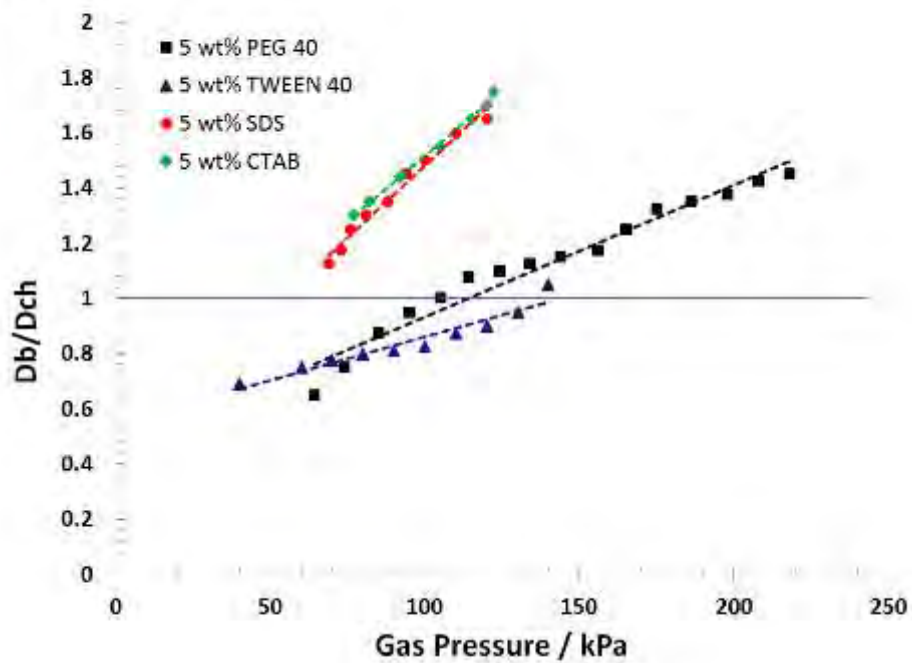


*Figure 4. 23: The effect of surfactant type on microbubble size for a) 2wt % concentration and b) 5wt % concentration, all bubbles were monodispersed with polydispersity index < 2 %.*

#### 4.4.6 Stability of microbubbles

The stability of bubbles/foams is governed by the balance between the roles of surface tension, surface activity and adsorption kinetics (Beneventi et al., 2001). The shorter the length of the hydrophobic chain of the surfactant molecule, the adsorption rate becomes faster. On the other hand, larger hydrophobic chains are slower in reaching the fresh surface and therefore the decrease in surface tension may not necessarily be sufficient for bubble stability.

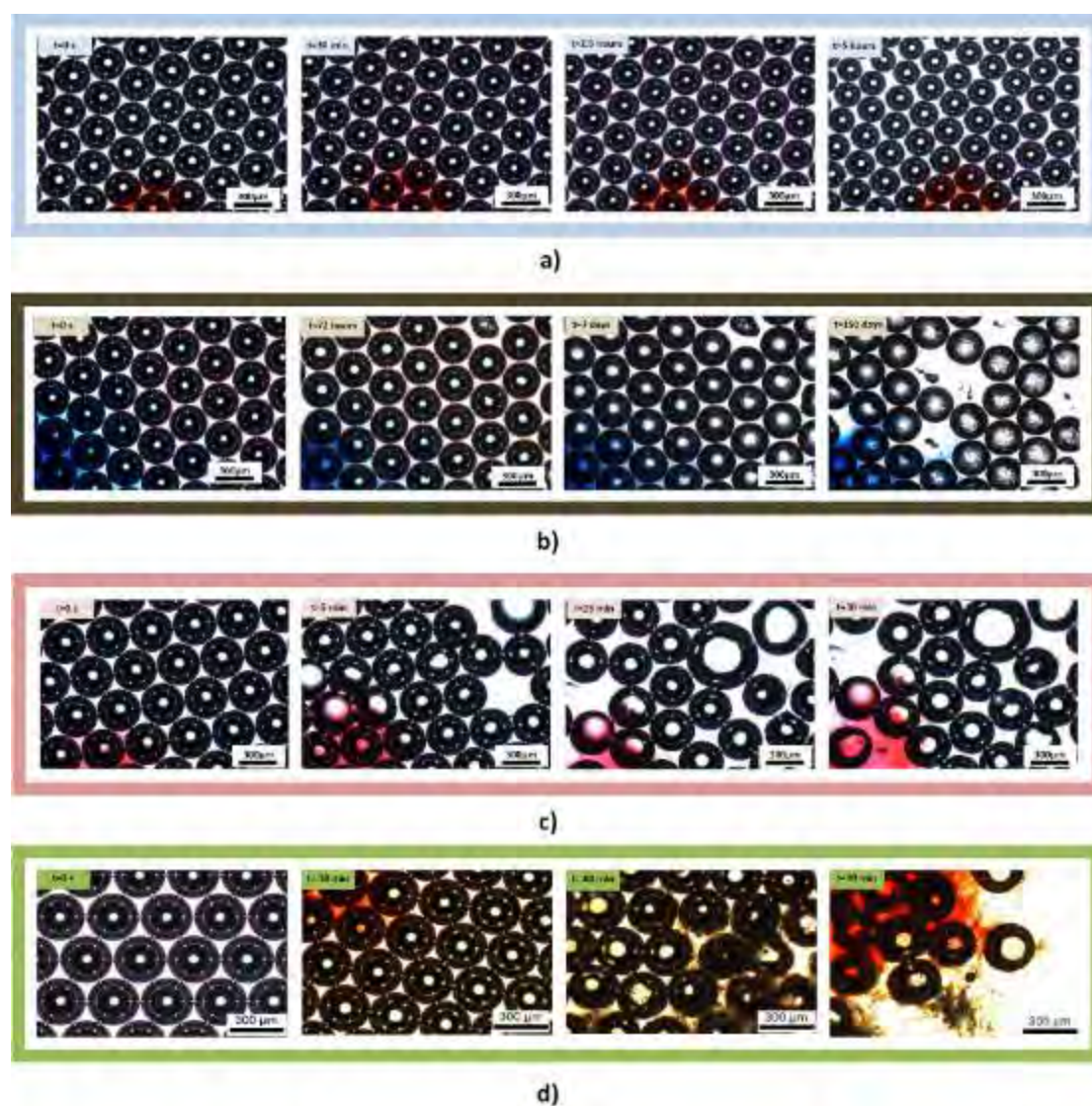


**Figure 4. 24:** Micrographic images showing the stability of 5 wt % concentration of  
a) Tween 40, b) PEG 40, c) SDS and d) CTAB.

Also Microbubble size distribution was measured as a function of time via optical microscopy. 100 microbubbles from each sample collected on the glass slides ( 2 samples for each surfactant) were studied and measured every 5 mins for 2 h and additionally every hour to 5 h and consequently 24, 48 and 72 h and 7 to 150 days. Generally, microbubbles produced with both nonionic surfactants PEG 40 and Tween 40 were the most stable for all concentrations studied in this report. For the purpose of comparison, 5 wt % concentration of all surfactants were selected. As shown in **Figure 4.24**, microbubbles produced with SDS were the least stable, where over the course of 30 minutes at the ambient temperature and pressure, the size distribution of the bubbles broaden greatly and bubble coalescence occurred until they burst and disappeared. This is due to significant Ostwald ripening affected by the surfactant molecule adsorption on the bubble surface. The dynamic interfacial behaviour is an important factor to consider if the rate of the transport of surfactant molecules between the bulk liquid and the interface by way of convective flow and diffusion is slower than surface expansion and breakup of bubbles. Furthermore, when the surface monolayer at the interface is closely packed, the diffusion of the encapsulated gas into the surrounding is limited and therefore bubbles become more stable (Atta et al., 2004, Stride, 2008).

Although, SDS and CTAB solutions have lower surface tension than the other surfactants, but they both produced the least stable bubbles in this study, with bubbles produced lasting for only 30 and 90 mins, for SDS and CTAB, respectively. The electrostatic repulsion between the ions of both cationic and anionic surfactants head group on the surface of adjacent bubbles lead to instability of bubbles produced with these surfactants. While CTAB has a longer hydrophobic chain, bubbles were more stable than SDS, which implies that, in this particular case, the higher surface activity and surface modulus of the CTAB were more important in the stability of CTAB bubbles rather than the slower diffusion rate.

On the other hand, the most stable bubbles were produced with the solution containing PEG 40, due to steric stabilization by the nonionic surfactant (Napper, 1977) at the adjacent bubbles. For the case of both PEG 40 and Tween 40, the bubbles had undergone a reduction in the radius under the influence of interfacial tension and the gas concentration gradient with respect to the surroundings. Bubbles produced with PEG 40 surfactant were the most stable in this study, surviving 150 days of this experimental study.

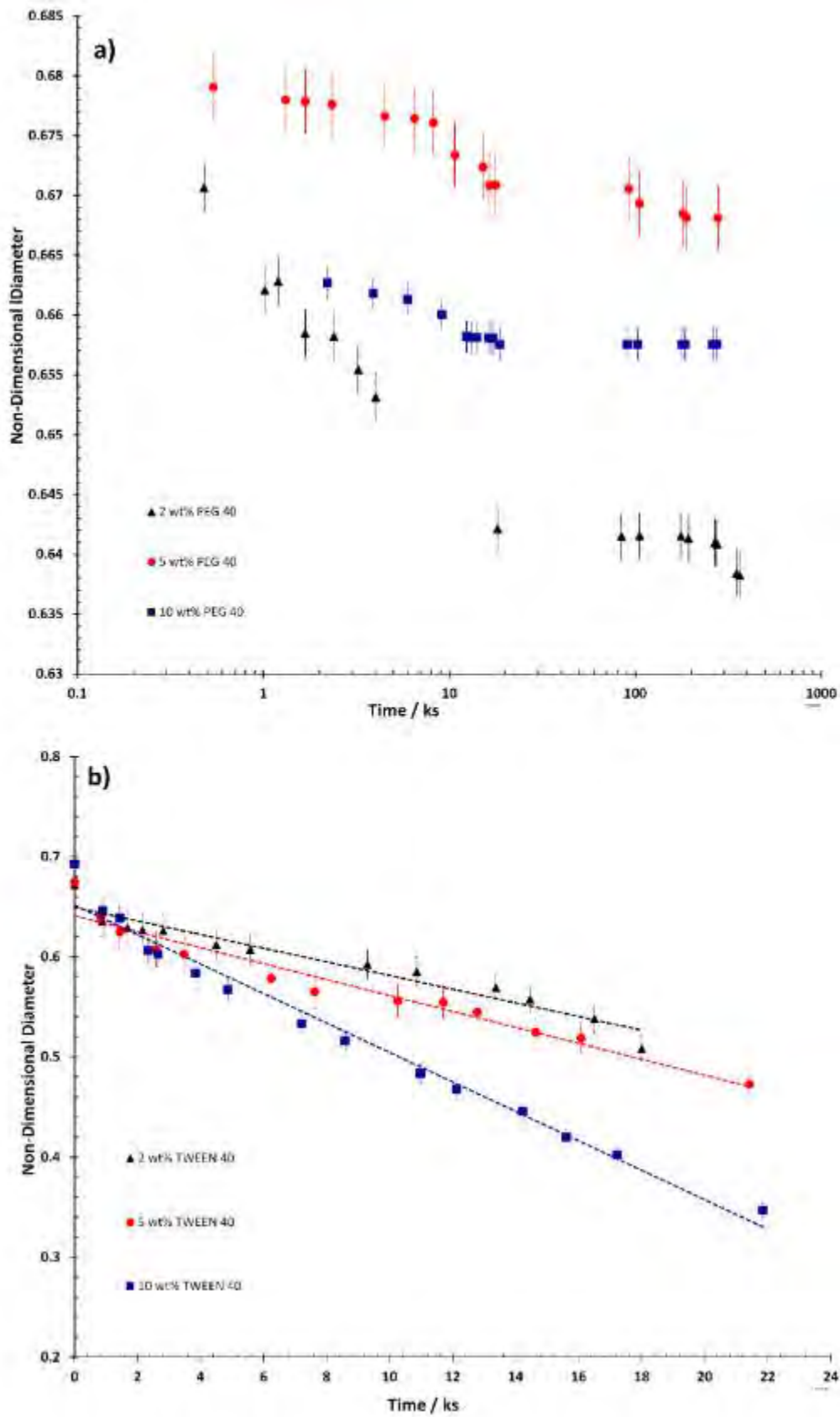


*Figure 4. 25: Bubble dimensionless diameter stability profile for a) PEG 40 b) Tween 40.*

Having confirmed that microbubbles are produced with PEG 40 and Tween 40 surfactants were the most stable, the variation of the mean diameter and standard deviation of bubbles with time for sample of 100 bubbles collected were studied. As shown in **Figure 4.25**, the diameter of bubbles produced with Tween 40 decreased linearly at the same rate for a period of 72 hours from the collection time until they all disappeared. However, for the case of PEG 40, after a certain period of time (7 days) the rate of bubble shrinkage became negligible. Since the diameter of all bubbles decreased at the same rate, they were still monodispersed. Monodispersed microbubbles can greatly reduce Ostwald ripening by reducing the effective Laplace pressure difference due to the uniformity in bubble size. During the measurements it was noted that the area where the measurement is taken is crucial. As shown in **Figure 4.26**, if the sample taken is from the centre of the collection sample, where the bubbles are closely packed, remained more stable. In comparison, the microbubbles in close proximity of the edge were affected by the constant flux of gas from the bubbles to the liquid and to the surrounding air. The diffusion of gas is influenced by the amount of surfactant molecules adsorbed on the bubble surface as well as the amount of solution around the microbubbles. The more surfactant molecules are adsorbed, the less mass transfer from the bubble surface would occur.

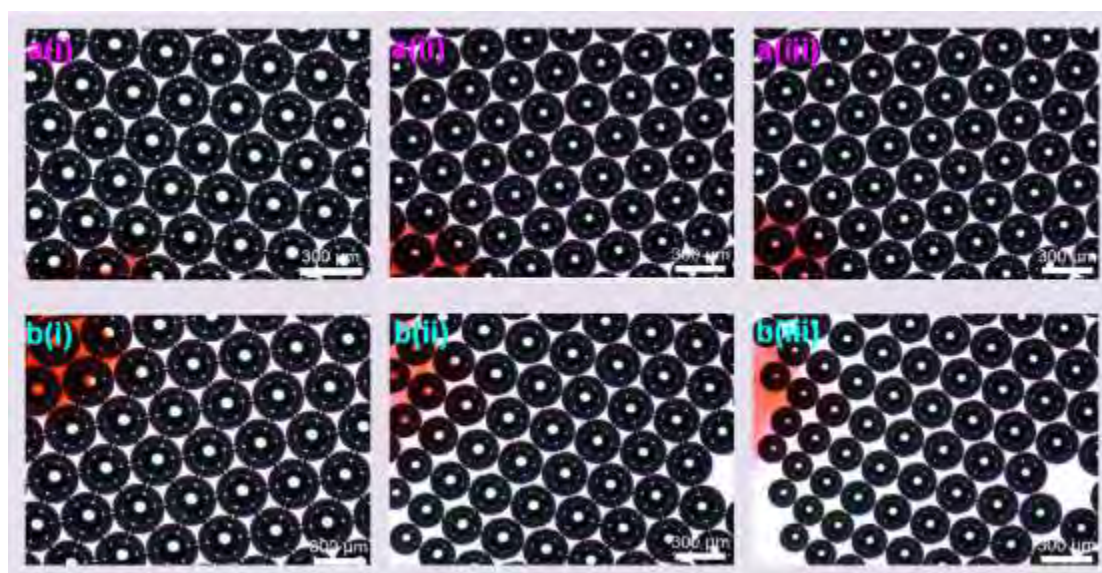


**Figure 4. 26:** Micrograph images of microbubbles with 2 wt % Tween 40 surfactant from a) centre of the collection sample b) edge of the collected sample at i) time of collection ii) 2.5 hours and iii) 5 hours after collection.

### Summary

In this work, an experimental study of the effect of the type and concentration of three differently charged surfactants on the formation and stability of microbubbles was conducted. For all surfactant types, significant changes in the bubble formation, size and stability were observed by increasing the concentration of the surfactant. This can be explained by the effect that surfactants have on the dynamics of bubble formation by influencing factors such as the channel surface character (i.e. hydrophilicity of channel walls) and the dynamic adsorption of surfactant molecules on the liquid-solid and liquid-gas interfaces in the microchannels. Both Capillary number and the wetting characteristics of the channel wall surface are proven to be the key factors in determining the size of microbubbles. Bubble size produced by a T-junction device is generally dependent on capillary number but it is shown in this study that for the solutions containing different surfactants but same physical properties, at approximately similar capillary numbers, the wetting characteristic of the solution is the key factor in determining the bubble size. It was noted that microbubbles produced with solutions containing nonionic surfactants PEG 40 and Tween 40 were generally smaller with 10 wt % Tween 40 producing the smallest bubble size of  $\sim 50 \mu\text{m}$  for the set operating parameters of the T-junction microfluidics device. This is due to the fact that these two surfactants have a larger hydrophilic chain and therefore the wettability of the channel wall surface is affected in a different manner. The wettability of the channels wall surface consequently effects the dynamic interfacial tension and therefore the bubble formation leading to production of smaller bubbles.

Analysis of the microbubble stability was performed and it was shown that the solution containing 5 and 10 wt % PEG produced microbubbles that were highly stable as they lasted for 150 days on the collection glass slides within this study's time frame. On the other hand, the microbubbles produced with SDS were the largest and least stable amongst all. All the microbubbles produced in this study were highly monodisperse with a polydispersity index  $< 2 \%$ . From the findings in this study, it is suggested that for the conditions tested (i. e. in this case hydrophobic FEP channel surface) generally nonionic surfactants and particularly PEG 40, that is much cheaper compared to the other surfactants studied in this report, produced microbubbles with superior monodispersity and stability, while increasing the surfactant concentration did not considerably change the microbubble stability.

## **Chapter 5**

### **Production of scaffolds and foams from microbubbles**

#### **5.1 Overview**

Methods for producing scaffolds and foams with a predictable narrow size distribution are in high demand for a wide range of biomedical and food applications. In this part of the work, a microfluidic technique was used to scale up the production of microbubbles into formation of foams and consequently by drying the formed foams and bubbles into highly uniform pore scaffold structures. The study later advances into incorporation of polymeric particles and collagen nanoparticle/fibres on to the porous protein structures. In order to achieve these novel structures, a combination of microfluidic and EHD techniques were used to initially produce scaffolds from microbubbles through the capillary embedded T-junction microfluidic device and then either electrospray the nanoparticles or electrospin the nanofibres via the EHD technique onto the uniform structures.

## 5.2 BSA Foams and scaffolds from microbubbles

### 5.2.1 Introduction

In addition to the methods mentioned in **Chapter 2** of this thesis, the microfluidic technique has been used to produce uniformly sized scaffolds. Chiu et al. (2013) applied a microfluidic technique to generate gelatine microbubbles and incorporated them into scaffold structures in the microchannel. Colosi et al. (2013) used a microfluidic foaming technique for the generation of highly monodisperse gas-in-liquid poly(vinyl alcohol) (PVA) bubbles as a template for scaffold characterized by an ordered and homogeneous porous texture. This part of the work investigates the generation of foam and scaffold structures produced in a T-junction device with highly uniform pores compared to the methods described previously.

### 5.2.2 Formation of foams from bubbles

In this part of the study, T-junction microfluidic device was used as a tool to produce foams from microbubbles. In order to achieve this, 15 wt % BSA in PBS was used to investigate the mechanism of formation of foams from microbubbles via this method. As previously mentioned in **Chapter 4**, bubble formation and size is affected by the gas pressure for a given liquid flow rate. Therefore for a set liquid flow rate of 0.2 ml/min, gas pressure was varied from 30-200 kPa. As shown in **Figure 5.1 a**), microbubbles were produced initially at a slower rate while there was also an amount of excess liquid at the tip of the channel prior to collection. The excess liquid increased the surface activity at the interface of bubbles and reduced the stability, leading to decreased production rate and bubbles being unstable before the drying period which therefore hindered the process of scaffold formation. This process only occurred at lower gas pressures below 90 kPa. Nonetheless, the bubbles produced within this region of gas pressures were highly monodisperse.

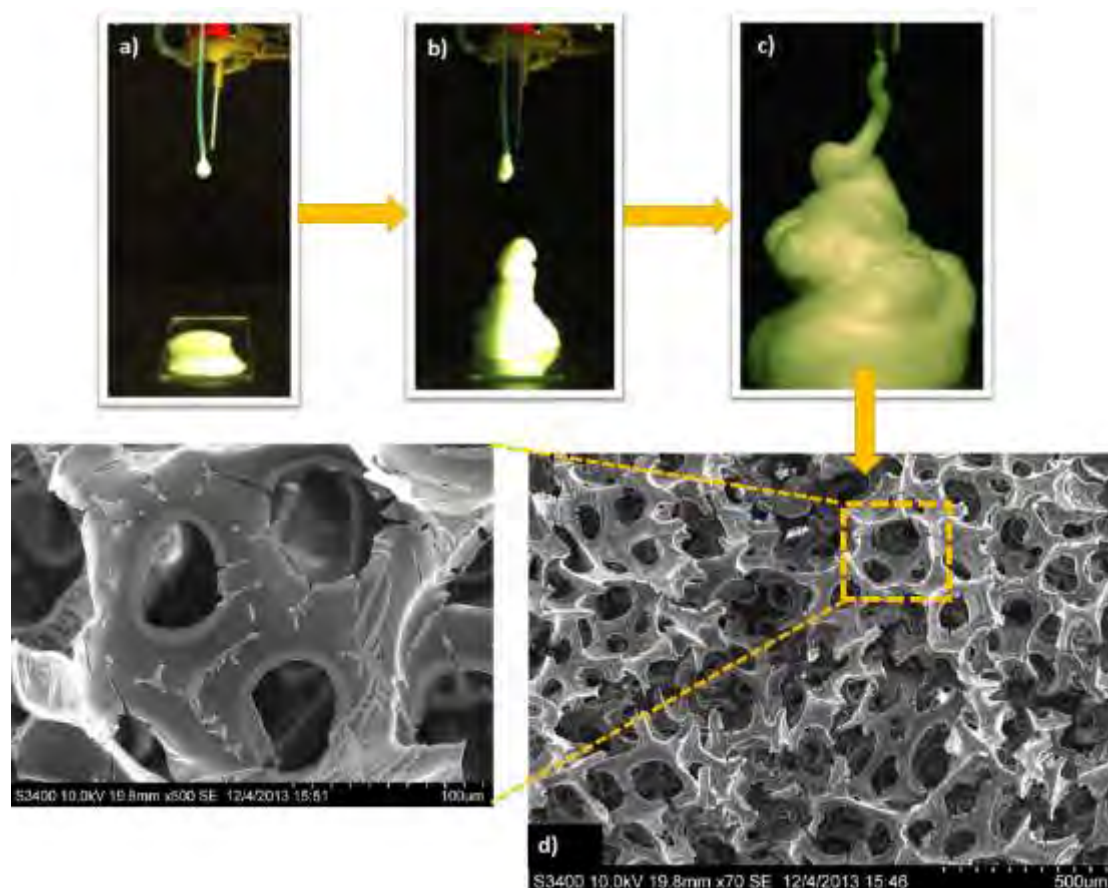


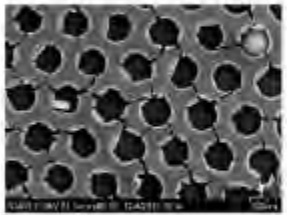
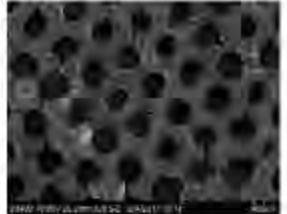
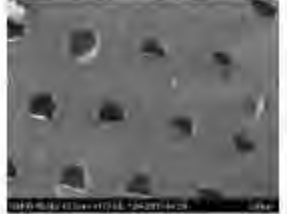
**Figure 5. 1:** Preparation of BSA scaffolds through a) microbubble formation, b) and c) foams from bubbles and d) dried BSA scaffolds.

Increasing the gas pressure led to a change in the mode of bubble formation in the T-junction from bubble dripping mode to jetting mode, where the amount of gas pressure overcome the liquid shear force. In this mode, foams containing microbubbles with narrow size distribution are produced (**Figure 5.1 b, c**), however the polydispersity increases when the pressure is higher than 90 kPa. Once the foams were produced, they were left to dry at room temperature for 30 mins to form highly porous scaffolds. The SEM image in **Figure 5.1 d** shows that a scaffold structure with uniform pore size of 80 μm was produced.

### 5.2.3 Effect of concentration of BSA on foam stability and scaffold structure

In order to investigate the effect of protein concentration on the stability of foams and the structure of scaffolds generated from these foams, BSA was added to PBS at

concentrations shown in **Table 5.1**. BSA bubbles were produced with the T-junction device for a constant liquid flow rate of 0.2 ml/min. Gas pressure was varied between 80-100 kPa in order to achieve the same bubble size for this part of the study. The stability of bubbles was monitored until the protein degenerated and the bubbles were dried into a scaffold structure.

BSA Concentration	Solution surface tension / $\text{mN m}^{-1}$	Solution viscosity / $\text{mPa s}$	foam stability-drying time / mins	Scaffold structure
15 wt. %	51	1.6	most stable foam before drying- 30	
20 wt. %	56	3	Average foam stability- 20	
25 wt. %	60	5	Least stable foams, bubbles diffuse and shrink- 25	

**Table 5. 1:** Properties of BSA foams and scaffolds produced via T-junction microfluidics.

Microbubbles produced with the lowest concentration of BSA were the most stable before drying and this is due to the lower surface tension of 15 wt % solution compared to the other two concentrations. The stability of foams and bubbles is highly dependent on the interfacial tension at the interface of the gas and liquid. As shown in **Table 5.1** microbubbles produced with the 20 wt % concentration demonstrated a rather

interesting trend of bubbles diffusing uniformly in every other rows and therefore leaving a pattern of small and large pores in the subsequent scaffold structure.

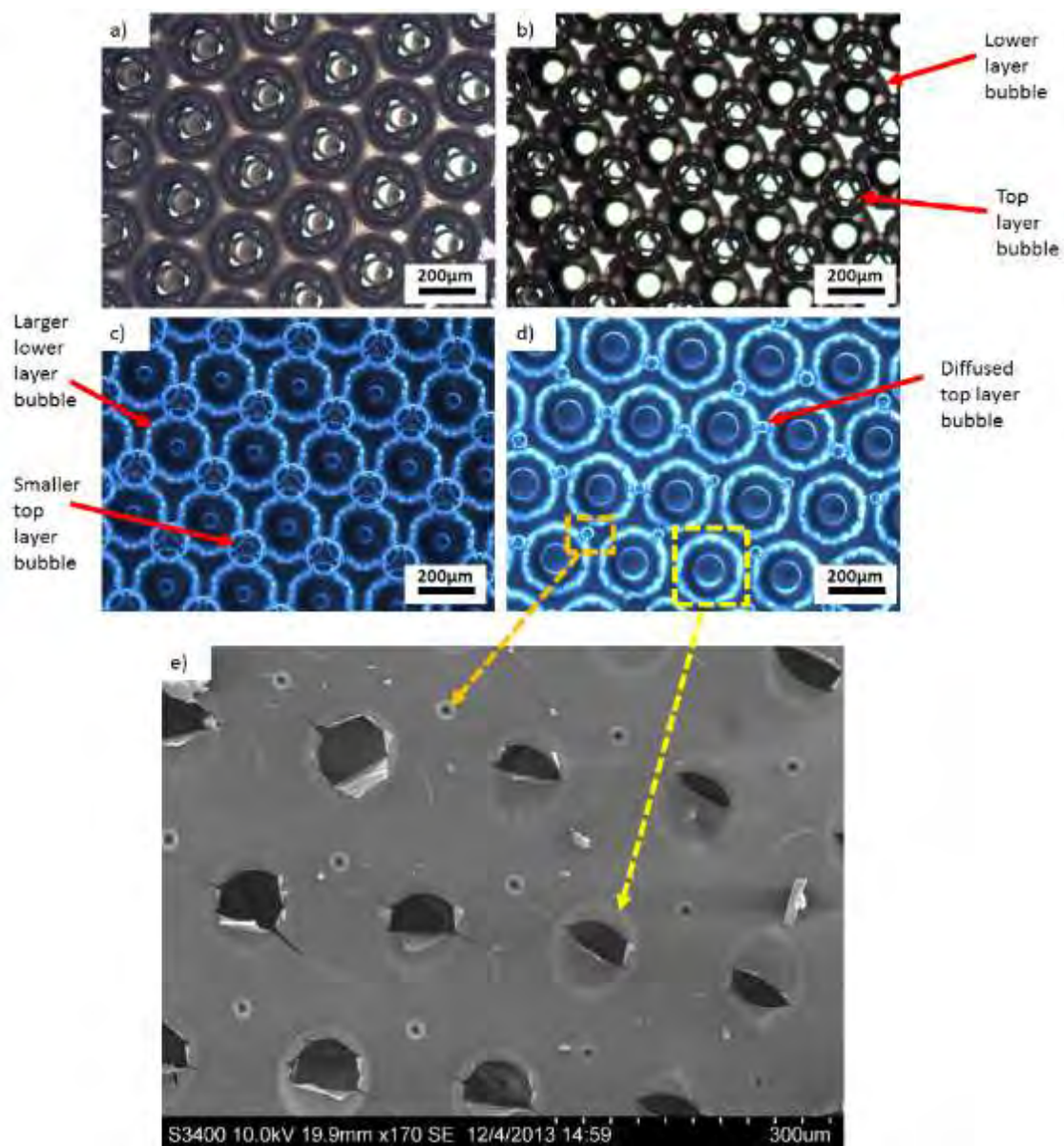


**Figure 5.2:** Micrograph images showing the diffusion and change in bubble size in a multi-layer bubble structure of the solution containing 25 wt % BSA at a)  $t= 0$  s, b) 10 mins, c) 15 mins and d) 20 mins, and e) SEM image of scaffold with both small and large shrinkage voids.

Ostwald ripening is driven by differences in the pressure inside larger and smaller bubbles as described by the Young–Laplace equation described in **Chapter 2**. Therefore, the solubility of the gas in the liquid just around the bubble is higher than in the bulk liquid (Henry's law). This excess of gas will diffuse to areas where the

dissolved gas concentration is lower, i.e. to larger bubbles, or to the atmosphere. In a multilayer foam structure, the very top layer of closely packed uniform bubbles is in contact with the atmosphere. As a result, at the initial stage, the gas inside the microbubbles in this layer diffuses to the surrounding air at a faster rate, leading to the shrinkage of the top layer microbubbles.

**Figure 5.2** shows a remarkable trend in gas diffusion and shrinkage of bubbles on the top layer of a double-layered foam structure for the solution containing 25 wt % BSA. At the initial stage microbubbles in both layers were uniform in size (220  $\mu\text{m}$ ). Since the bubbles in the lower layer of the structure were in contact with the excess liquid, therefore the mass transfer at the interface of the bubbles only occurred between the gas and the liquid. However, for the case of bubbles on the top layer of the structure, the gas inside the bubbles not only diffused to the surrounding air, but also into the lower layer bubbles. This process led to the simultaneous shrinkage of the top layer bubbles and expansion of the lower layer bubbles. After 20 mins, the bubbles on the top layer were decreased to 30  $\mu\text{m}$  as they moved towards the gaps between adjacent bubbles (grown to 250  $\mu\text{m}$ ) in the lower layer. At this time the protein in the solution is denatured and the scaffold structure is formed. The initial rate of adsorption of the protein molecules at the air-water interface is an important factor affecting the stability of the gas bubbles. The adsorption rate of protein molecules is influenced by the concentration, type and pH of the protein used. Therefore a further detailed study is required to investigate the effect of the concentration of protein in microbubble stability and the resulting scaffold structure.

Generally, the increase in the concentration of BSA did not favour either the foam stability or the scaffold structure. At 20 wt % concentration, cracks appear on the structure of the scaffolds, making them fragile and mechanically unstable for many biomedical and tissue engineering applications. Therefore, for the following part of this work, 15 wt % was chosen for the experimental investigations.

### **5.3 Preparation of controlled porosity particle/ fibre loaded scaffolds using a hybrid micro-fluidic and electrohydrodynamic technique**

#### **5.3.1 Introduction**

In this study a novel method is presented that combines microfluidics with EHD processing to produce porous BSA scaffolds from microbubble templates with functional particles and/or fibres incorporated into the scaffolds' structure. The porosity and the size of the scaffolds' were controlled by adjusting the processing parameters of the microfluidic device. PLGA, PMSQ and collagen particles/fibres were then sprayed on them using the EHD technique. These secondary elements in the assembly of scaffolds can assist with the mechanical strength of the structure as well as providing a suitable route to deliver drugs and growth factors.

#### **5.3.2 Formation of Bio-products**

The processing conditions were optimised to form uniform and reproducible products in micro and nano scale dimensions, as described below:

##### **5.3.2.1 Bubbles**

The T-junction device was used to obtain the bubbles providing the scaffold template. Three different solutions of BSA 15% w/w were used to produce the bubbles: BSA, BSA + Tween 40 (90 wt.% / 10 wt.%) and BSA + phospholipid solution (50 wt.% / 50 wt.%). Air was used in all cases as the gas phase. Following bubble production, the most stable ones (assessing them by the number of bubbles bursting in time) before and after drying were chosen for the experiments. The bubble diameter was controlled by changing the air pressure and liquid flow infused to the T-junction device. The processing conditions were optimised to generate monodispersed bubbles for each experiment. The working distance between the T-junction needle tip and the collector (glass slide) was set to 120 mm. Once the bubbles were collected on glass slides, they were left to dry at ambient temperature and pressure.

### 5.3.2.2 Particles

The EHD process was used to produce polymeric particles. The processing conditions (flow rate, voltage) were optimised to form particles in nano and sub-micro scale in order to increase their density per mm<sup>2</sup> on the bubbles' surfaces. To achieve this, EHD parameters were optimised in order for a stable cone-jet at the EHD needle tip (Xie and Wang, 2007, Yarin et al., 2001).

*PLGA*: To produce the PLGA particles the voltage was set to 11kV and the flow rate of the PLGA solution was fixed at 20 µl/min. The working distance between the needle tip and the collector (glass slide) was set to 120 mm and the distance between the EHD needle and the T-junction metallic needle tip was set at a distance of 50 mm. The EHD needle was set at an angle of 45° (Reference Angle (RA): At 0° if the EHD needle was set at a vertical position with its nozzle facing the ground) in order to spray directly onto the bubbles that were produced from the T-junction process.

*PMSQ*: To produce the PMSQ particles the voltage was set to 9 kV and the flow rate of the PLGA solution was fixed at 10 µl/min. All the other parameters remained the same as in the PLGA particles production experiment.

*Collagen*: Collagen solution 8% v/v was used to form the particles. The voltage was set to 14 kV and the flow rate of the collagen solution was fixed at 5 µl/min. All the other parameters remained the same as in the previous experiments.

### 5.3.2.3 Collagen beaded Nanofibres

To form collagen fibres, a solution of 15% v/v collagen was used and the applied voltage was set to 21 kV. The flow rate of the collagen solution was fixed at 3 µl/min. All the other parameters remained the same as the previous experiments.

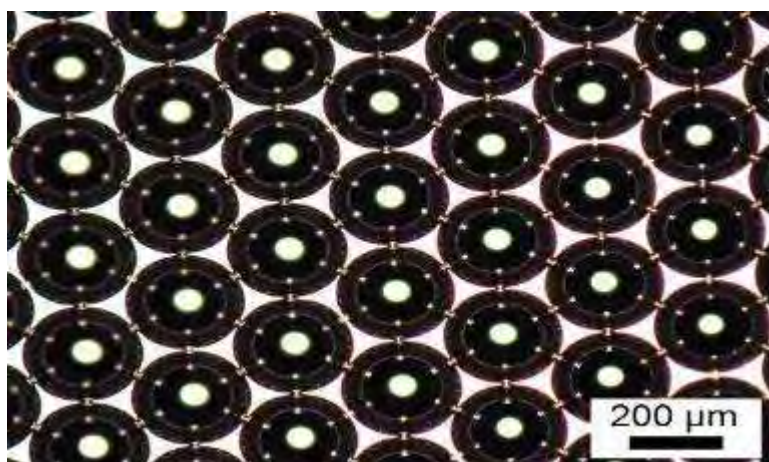
### 5.3.2.4 Combination of bio-products

After the production of the BSA bubbles two different experimental approaches were followed to spray the secondary bio-products onto the bubbles: a) when the bubbles were produced by the T-junction process, the secondary bio-products formed by the

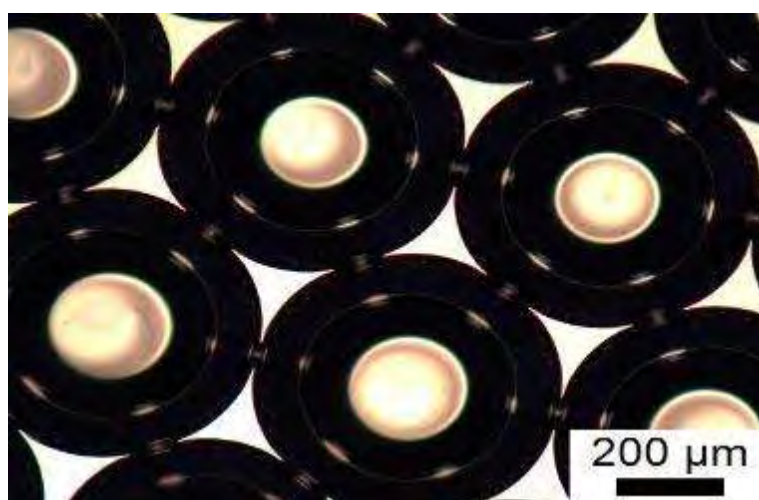
EHD process were simultaneously sprayed directly on them (**Figure 5.3**) and b) the bubbles/scaffolds were left to dry after their production and then the secondary bio-products were sprayed on them.

### 5.3.3 Bubble formation

After the bubbles were produced they were monitored for their stability (number of bubbles bursting as time progressed and how long they need to dry in order to obtain a solid scaffold). The most stable bubbles were the BSA bubbles obtained without the addition of any surfactants or phospholipids. Hence the experiments were continued with the BSA solution only.



(a)



(b)

*Figure 5. 3: BSA bubbles produced from the T-junction.*

<b>Solution</b>	<b>Air Pressure / kPa</b>	<b>Bubble Diameter / <math>\mu\text{m}</math></b>	<b>Stability</b>
BSA	32.3	81 $\pm$ 2	Stable until dried
	34.9	95 $\pm$ 2	
	41.2	141 $\pm$ 3	
	42.7	152 $\pm$ 4	
	44.3	162 $\pm$ 3	
	45	164 $\pm$ 3	
	46.1	174 $\pm$ 4	
	48.3	190 $\pm$ 4	
	51.6	208 $\pm$ 4	
	57.3	251 $\pm$ 2	
	75	302 $\pm$ 2	
	81	418 $\pm$ 4	
	92	478 $\pm$ 2	
	103.5	555 $\pm$ 3	
BSA + Phospholipid	53	245 $\pm$ 5	Unstable, burst prior to drying
	75	285 $\pm$ 5	
BSA + Tween 40	1100	82 $\pm$ 4	Unstable, burst prior to drying
	1200	95 $\pm$ 4	

**Table 5. 2:** Parameters used to generate bubbles and their stability at a liquid flow rate of 200  $\mu\text{l min}^{-1}$ . The bubbles diameter value is the mean diameter of 50 bubbles.

It is well known that by adjusting the T-junction processing parameters (solution concentration, gas pressure, liquid flow and capillary diameter size) bubbles of different size can be generated (Parhizkar et al., 2013). In this study, BSA bubbles ranging from  $\sim 80 \mu\text{m}$  to  $\sim 550 \mu\text{m}$  were produced by keeping the liquid flow rate constant at  $200 \mu\text{l}\cdot\text{min}^{-1}$ , while increasing the gas pressure from 30 to 100 kPa. Examples of the bubbles produced are shown in **Figure 5.3** with images (a) and (b) showing bubbles having an average size of  $251 \pm 2 \mu\text{m}$  and  $418 \pm 4 \mu\text{m}$ , respectively. **Table 5.2** shows the parameters used to obtain the different bubble diameters.

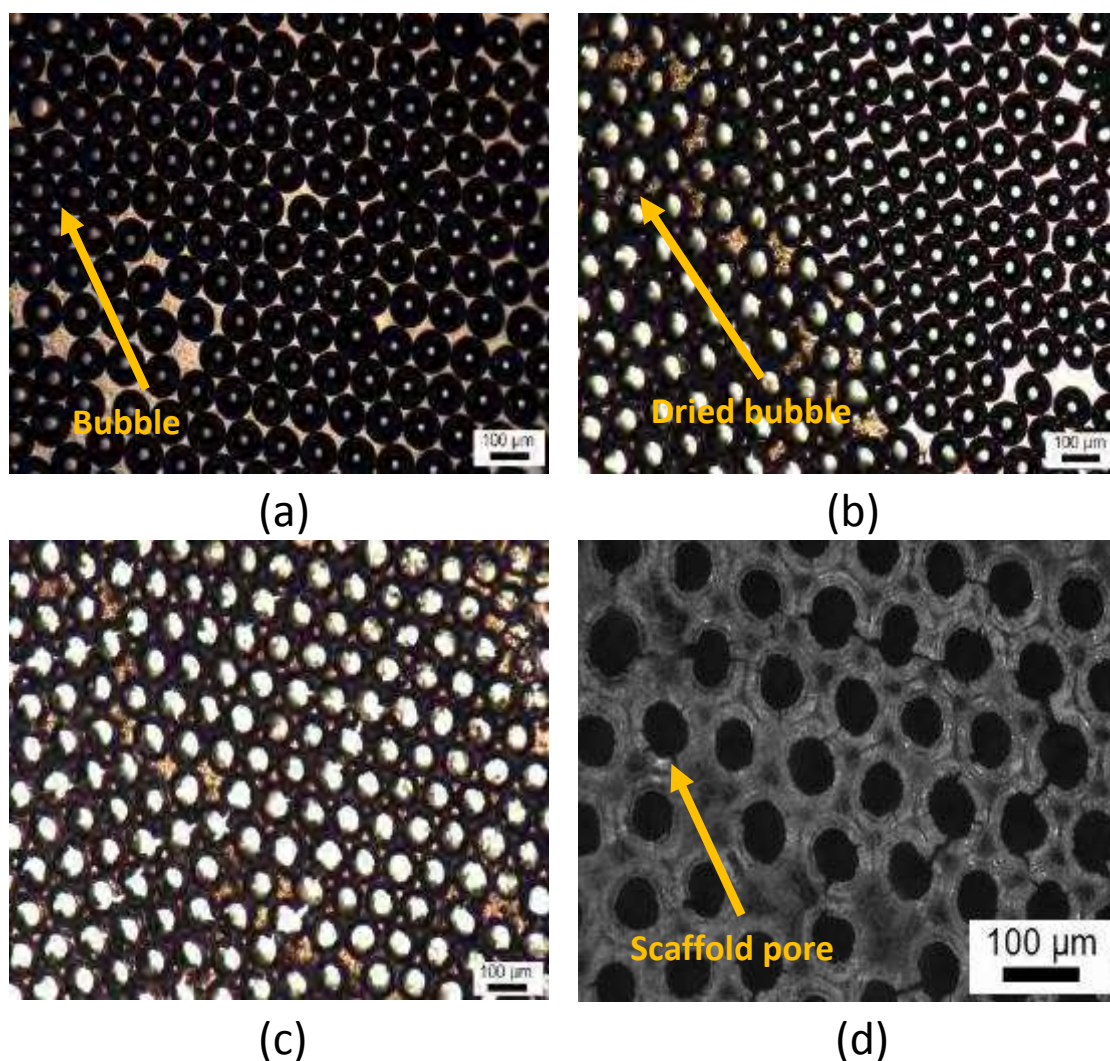


*Figure 5. 4: Optical microscope images of BSA bubbles after: a) 1min, b) 10min, c) 15min and d) 20min after generation.*

### 5.3.4 Scaffold structure

The bubbles produced from the T-junction process had a foam-like texture, hence to produce the multi-layered BSA scaffolds, the bubbles were left to dry for a short period of time (20 min-60 min) before spraying onto them. **Figure 5.4** shows the BSA bubbles immediately after generation and at different time intervals while drying. The bubbles in this case had an average size of  $(81\pm 2)\ \mu\text{m}$ .

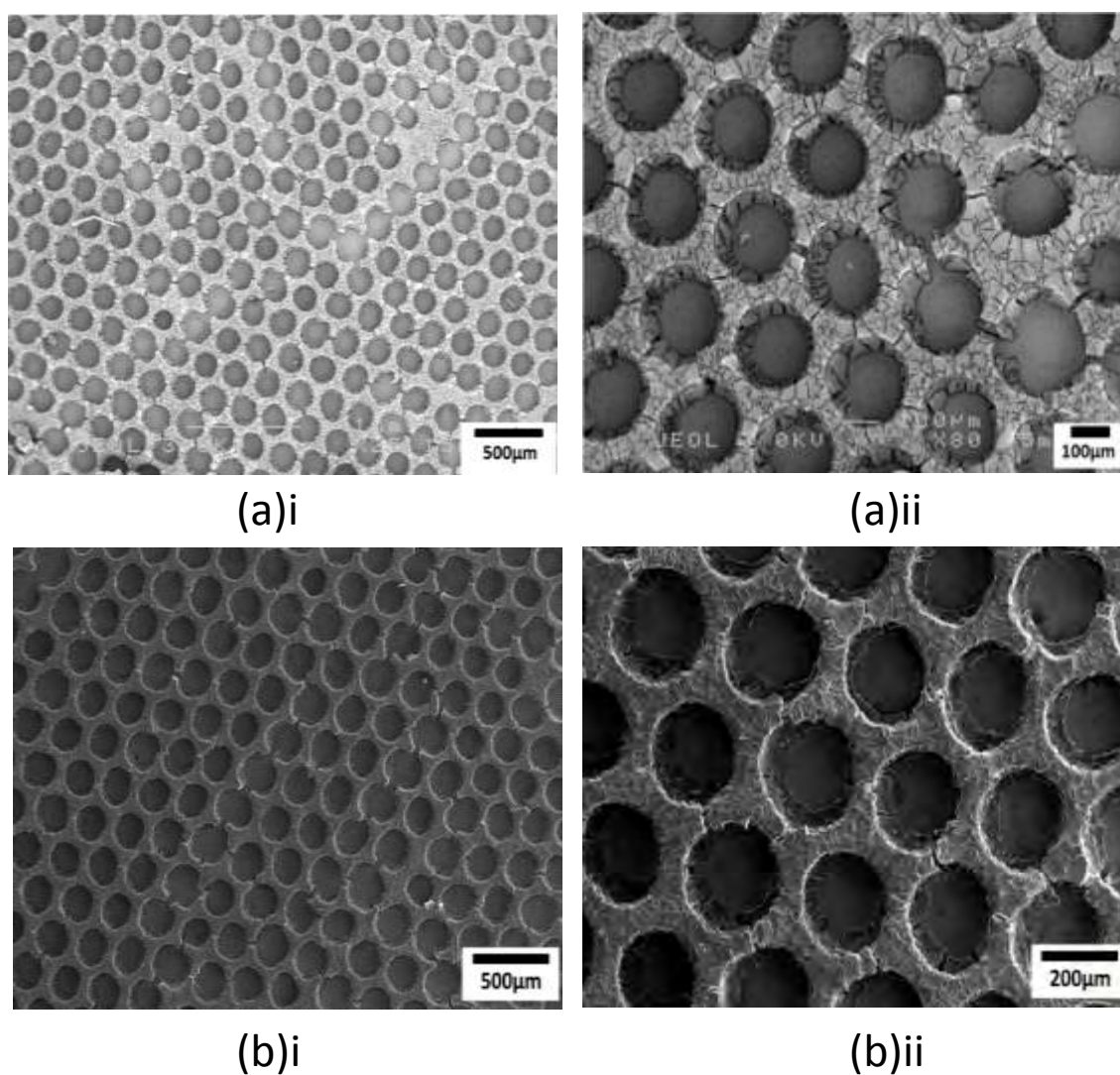


**Figure 5. 5:** SEM images of a single layer of dried BSA bubbles formed on a glass slide with [(a,b)i] showing structures with two different windows controlled by changing the T-junction parameters according to Table5.2 and [(a,b)ii] showing the images in [(a,b)i] at higher magnification.

*Single layer structure:* By collecting a single layer of BSA bubbles on a glass slide and leaving it to dry for 20 min a single layer honeycomb arrangement with the same diameter scaffold window was obtained. **Figure 5.5** shows these structures with [a(i)] and [b(i)] having average gap diameter size of  $(152\pm 7)$   $\mu\text{m}$  and  $(208\pm 8)$   $\mu\text{m}$ , respectively and the images [(a,b)ii] showing the same structures at higher magnification. The depth of the windows was found to be  $(100\pm 9)$   $\mu\text{m}$  almost half the pore diameter and the interconnected regions of the dried bubbles had an average thickness of  $(30\pm 9)$   $\mu\text{m}$ .

*Double layer structure:* By changing the T-junction parameters, the bubbles' size was increased and a two-layered structure was obtained by adding another layer at the top of a single layer of bubbles instantly after collection on the glass slide. The structure was also left to dry for 20 min and after analysis it was found that the windows formed had an average diameter of  $(190\pm 8)$   $\mu\text{m}$ . **Figure 5.6** shows images of the two layered structure taken by optical microscope and SEM with **Figure 5.6 a** clearly showing the double layered arrangement. The thickness of the two layer structure formed had an average value of  $(342\pm 11)$   $\mu\text{m}$ .

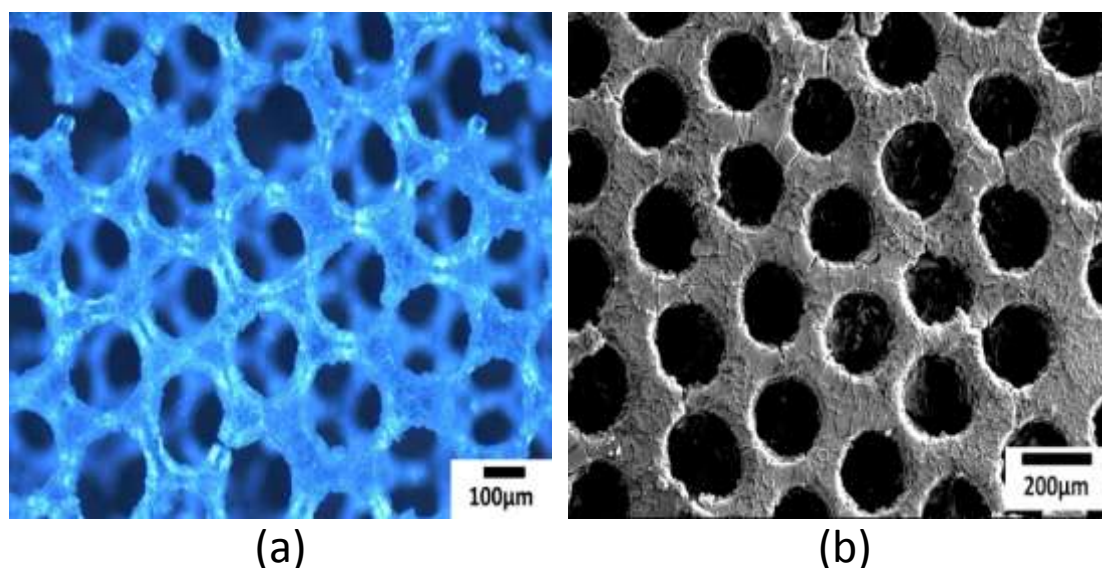


**Figure 5. 6:** Double layer dried BSA scaffold structure (a) optical and (b) SEM micrographs.

*Multilayer scaffold:* After experimenting with the single and double layered structures, scaffolds were formed by accumulating many layers of bubbles. By adjusting the T-

junction processing parameters, mainly increasing the gas pressure to control the bubble size and collecting multiple layers of bubbles on a glass slide or a glass vial, 3-D scaffolds with different window sizes and hence porosity, were produced. The BSA bubbles spontaneously self-assembled into liquid foam structures, which were solidified after leaving to dry for up to 60 min.

During the drying process, the pressure difference between the bubbles and the ambient atmosphere ruptured the film between the bubbles and only the plateau borders were left (Chung et al., 2009). The dried foam formed 3-D scaffolds and by adjusting the T-junction processing parameters four different structures were obtained with window diameters of  $(162\pm 17)$   $\mu\text{m}$ ,  $(327\pm 24)$   $\mu\text{m}$ ,  $(478\pm 28)$   $\mu\text{m}$  and  $(543\pm 33)$   $\mu\text{m}$  at various gas pressures of 44, 67, 93 and 102 kPa, respectively. **Figure 5.7** shows these scaffolds with **Figure 5.7(a)** having the biggest pore size and **Figure 5.7(d)** the smallest. The figures indicate the ordered and interconnected pores of the 3-D scaffolds.

It was noticed that despite the monodispersity of the bubbles formed during the process, the diameter size distribution of the scaffold pores was broader in the multi-layered scaffolds than in the single and double layered structures obtained at the previous experiments. This can also be confirmed from the relatively large standard deviation values measured (17, 24, 28 and 33) during the scaffold pore size analysis. This was probably caused by the increased pressure due to the weight of the bubbles located on the top layers acting on the bubbles in the lower layers. However, the pore size of the scaffolds produced in this study by T-junction process still had a narrower size distribution than other techniques used to fabricate scaffolds (Lima et al., 2012, Liu et al., 2011). It was also noticed in some cases that when the BSA bubbles were bursting during the drying process a thin cracked layer of protein coating was left at the sides of the scaffolds gaps. According to Neir *et al.* (Nair et al., 2007) this thin protein coating may serve as a biocompatible layer to upsurge cell seeding and growth.

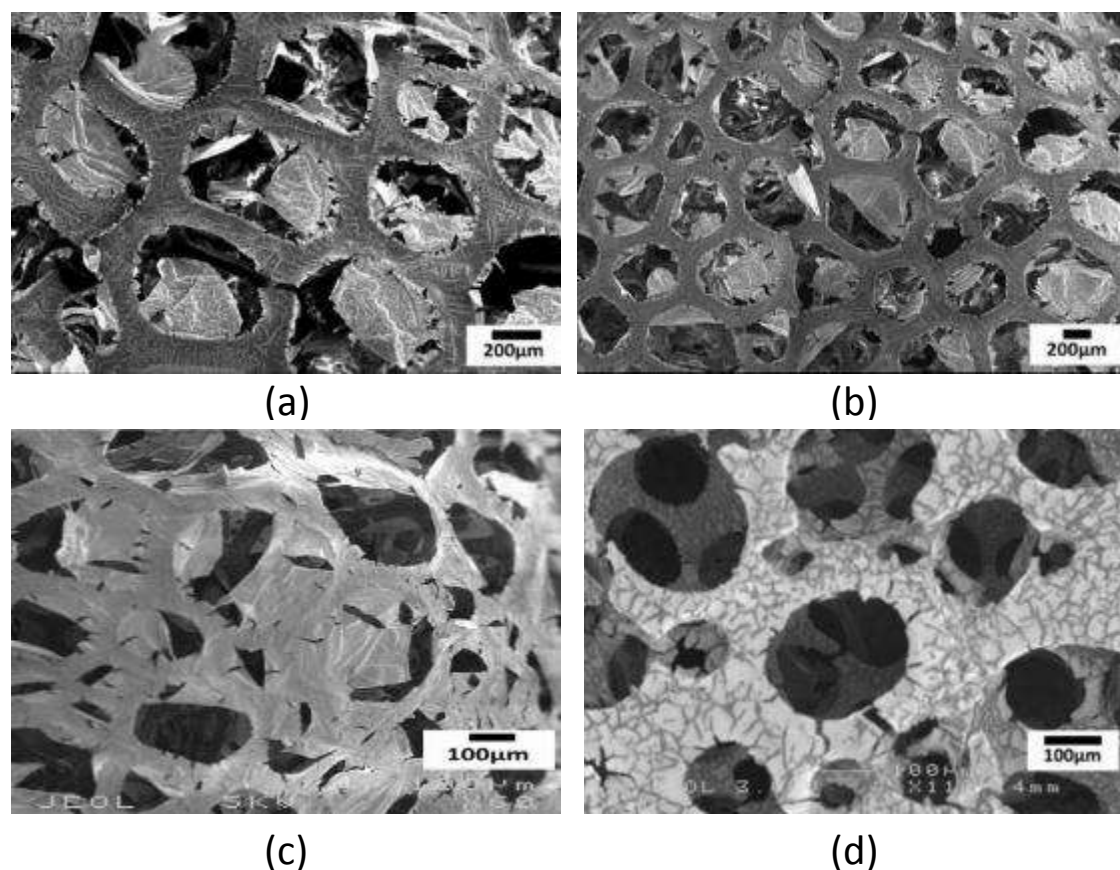


**Figure 5. 7:** Scanning electron micrographs of multi-layer scaffold made using dried BSA bubbles showing the different diameter window sizes obtained by changing the T-junction processing parameters (a) having the biggest gap diameter ( $543\pm 33\mu\text{m}$ ) and (d) the smallest one ( $162\pm 17\mu\text{m}$ ).

### 5.3.5 Particles sprayed on bubbles

The first experimental approach was to spray the bio-particles formed by the EHD process simultaneously onto the BSA bubbles generated via the T-junction process. In this procedure the stability of bubbles was affected by the particles accelerated due to the electric potential difference induced by the EHD process hence rupturing the bubbles shell and causing them to burst. Approximately 30% of the bubbles produced were bursting due to this effect. Although many steps were attempted to resolve this, such as adjusting the liquid flow rate into the EHD needle, increasing the BSA concentration and the distance between the EHD needle tip and the collection area, none had a significant effect on the bubbles stability. An advantage of this approach,

however, was that the particles were distributed equally in the inner and outer surfaces of the scaffold while it was formed.

The second experimental approach was to leave the scaffold to dry and then spray the particles onto it. The advantage of this method was that the bubbles were left to dry without any external disturbance and thus the percentage of bubbles bursting decreased to less than 5%. Also the particles were still able to infiltrate into the scaffolds' structure very easily because of their small size, and hence were distributed on the scaffolds' inner surfaces. As expected, however the outer surface of the final scaffold had a higher density of particles than the inner ones.

*PLGA Particles:* The bubbles and particles size used for this experiment were  $(141\pm 3)$   $\mu\text{m}$  and  $(130\pm 23)$  nm (mean diameter of 100 particles), respectively. Firstly, PLGA particles were sprayed onto wet (not dried) bubbles (**Figure 5.8 a and b**) and then PLGA particles were sprayed onto a single layered (**Figure 5.8 c**), two layered (**Figure 5.8c**) and multi layered (**Figure 5.8f**) BSA scaffolds.

In order to check if the particles had infiltrated into the inner layers of the BSA scaffold, the surface of the structure was removed by a surgical blade. **Figure 5.8 (c)** confirms that the particles were present on the bottom layer of the scaffold. **Figure 5.8 (d)** shows the PLGA particles aggregating into different shapes while they were sprayed into the inner cavities of the scaffold. This is caused by the difference in the hydrophobic and hydrophilic nature of the PLGA and BSA, respectively (Danhier et al., 2012, Yoon and Garrell, 2008).

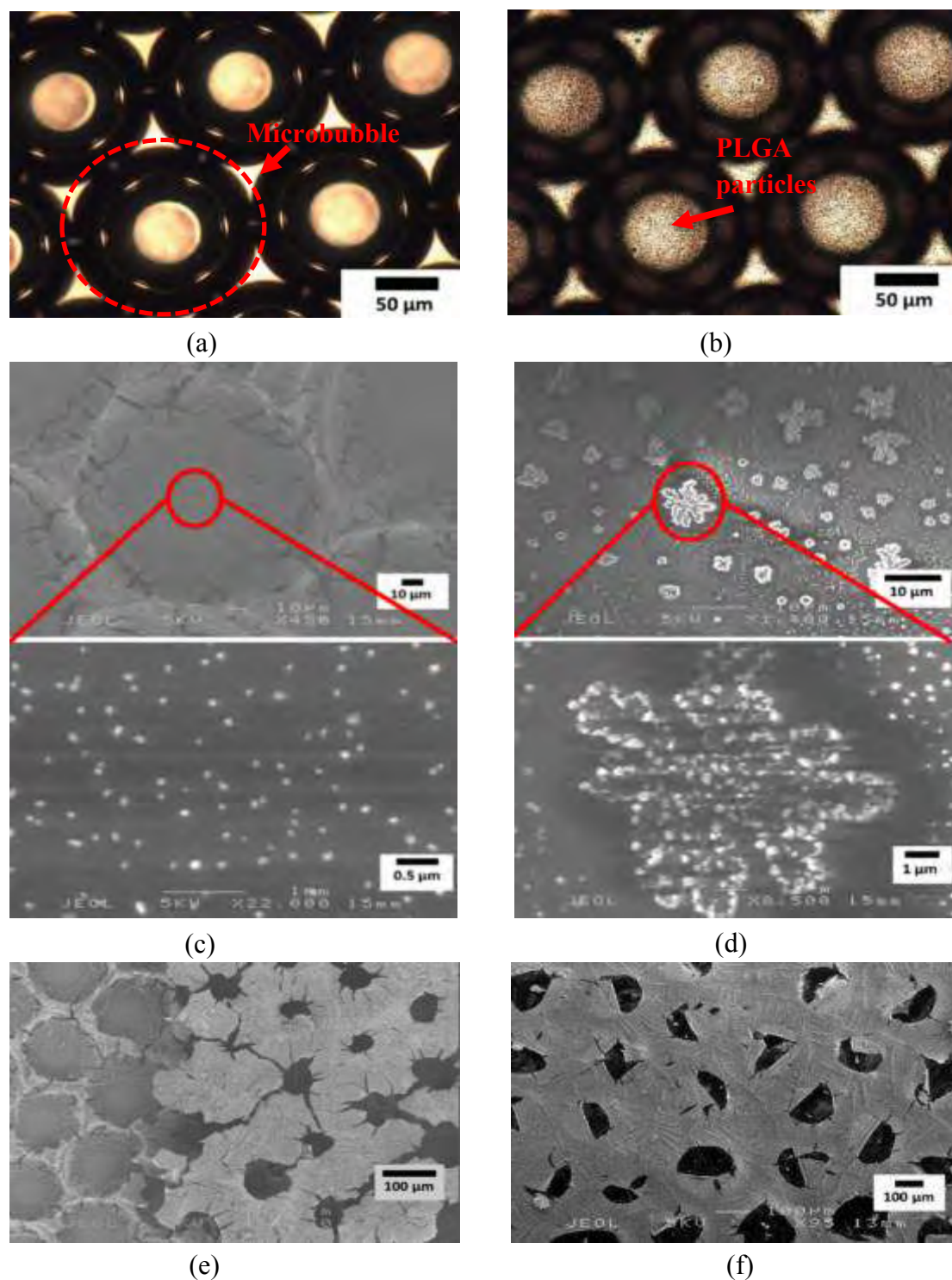


**Figure 5. 8:** Images showing (a) dried BSA bubbles, (b) dried BSA bubbles with PLGA nanoparticles, (c) a single layer BSA scaffold with PLGA nanoparticles in its cavities after spraying for 1min (see arrows), (d) PLGA nanoparticles aggregating into different shapes in a BSA scaffold cavity after spraying for 5min (e) a two layer BSA scaffold with PLGA nanoparticles and (f) a multilayer BSA scaffold with PLGA nanoparticles.

*PMSQ Particles:* The average window diameter of the multilayered scaffold was measured and found to be  $(95\pm 41)$   $\mu\text{m}$ . The PMSQ particles sprayed had an average size of  $(1.94\pm 0.4)$   $\mu\text{m}$  (mean diameter of 100 particles). **Figure 5.9** shows SEM images of the same BSA scaffold at different magnifications after being sprayed with PMSQ microparticles. It can be seen clearly that the particles infiltrated onto the inner surfaces of the scaffold and were distributed homogeneously.

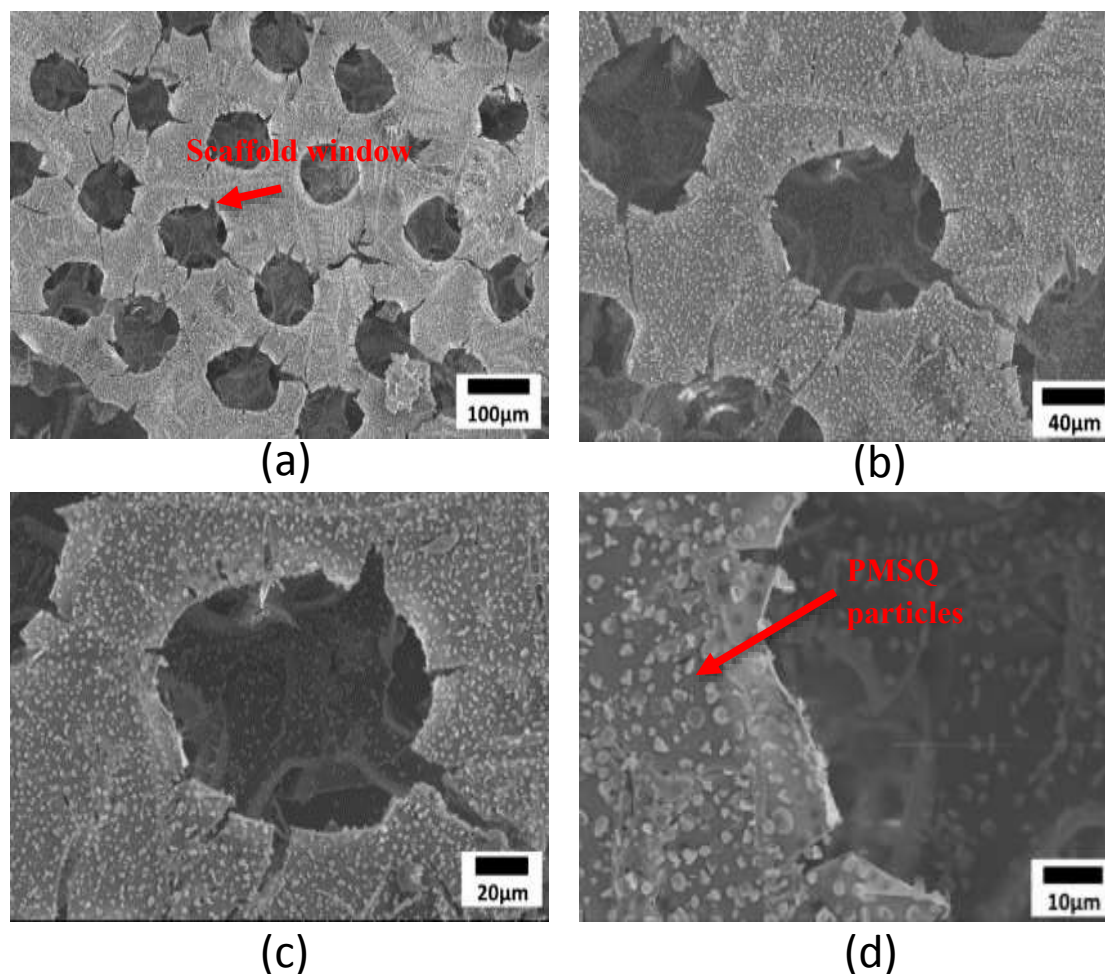


**Figure 5. 9:** SEM images at different magnifications showing the same multilayered BSA scaffold after sprayed with PMSQ micro-particles with images (a) and (d) having the lowest and the highest magnification, respectively.

*Collagen Particles:* In these experiments the pores of the scaffold prepared had an average diameter of  $(174\pm 8)$   $\mu\text{m}$  and the collagen particles sprayed on it had a size of  $(1.35\pm 0.3)$   $\mu\text{m}$  (mean diameter of 100 particles). **Figure 5.10** shows SEM images at

different magnifications of the same BSA scaffold sprayed with collagen micro-particles. It was observed that the scaffold surface (see **Figure 5.10f**) appeared degraded due to spraying of the collagen particles. This was caused by the low concentration of acidic acid found in the collagen type I solution used for the experiments. When the collagen solution was sprayed onto the scaffold, it is assumed that the acid did not fully evaporate during the flight from the EHD needle tip to the collection area (probably due to its high boiling point of 118°C), hence causing the protein based surface of the scaffold to locally dissolve and the collagen particles to embed into the BSA scaffold.

### 5.3.6 Spraying of collagen beaded fibres

Collagen beaded fibres with average fibres and beads size of (257±25) nm (mean diameter of 100 fibres) and (685±67) nm (mean diameter of 100 beads), respectively, were spun successfully onto the outer surface of the dried BSA scaffold, which had an average pore size of (164±11) µm. **Figure 5.11 (b)** shows SEM images at different magnifications of the same BSA scaffold after being sprayed with collagen beaded nanofibres for 5 min and **Figure 5.11 (b)** shows the same scaffold after spraying on it for 15 min. In this experiment it was not possible for the fibres to infiltrate into the inner structure of the scaffold due the fibres' "large" length. Although an attempt was made to spin the fibres simultaneously while the bubbles were produced from the T-junction device, the bubble stability and self-assembly properties were affected thus causing the scaffold formation to fail.

### 5.3.7 Possible applications

The BSA scaffolds with secondary bio-products attached on them have potential applications in tissue and bone regeneration engineering, wound care and cosmetics. BSA is a biocompatible and biodegradable FDA approved material that has no toxicity and can provide high cell affinity when the scaffold pores size are around 100-150 µm (Nair et al., 2007, Nair et al., 2010). In this study it was shown that the porosity of the scaffolds can be very easily controlled thus providing the necessary structure for different types of cell to achieve infiltration into the scaffold.

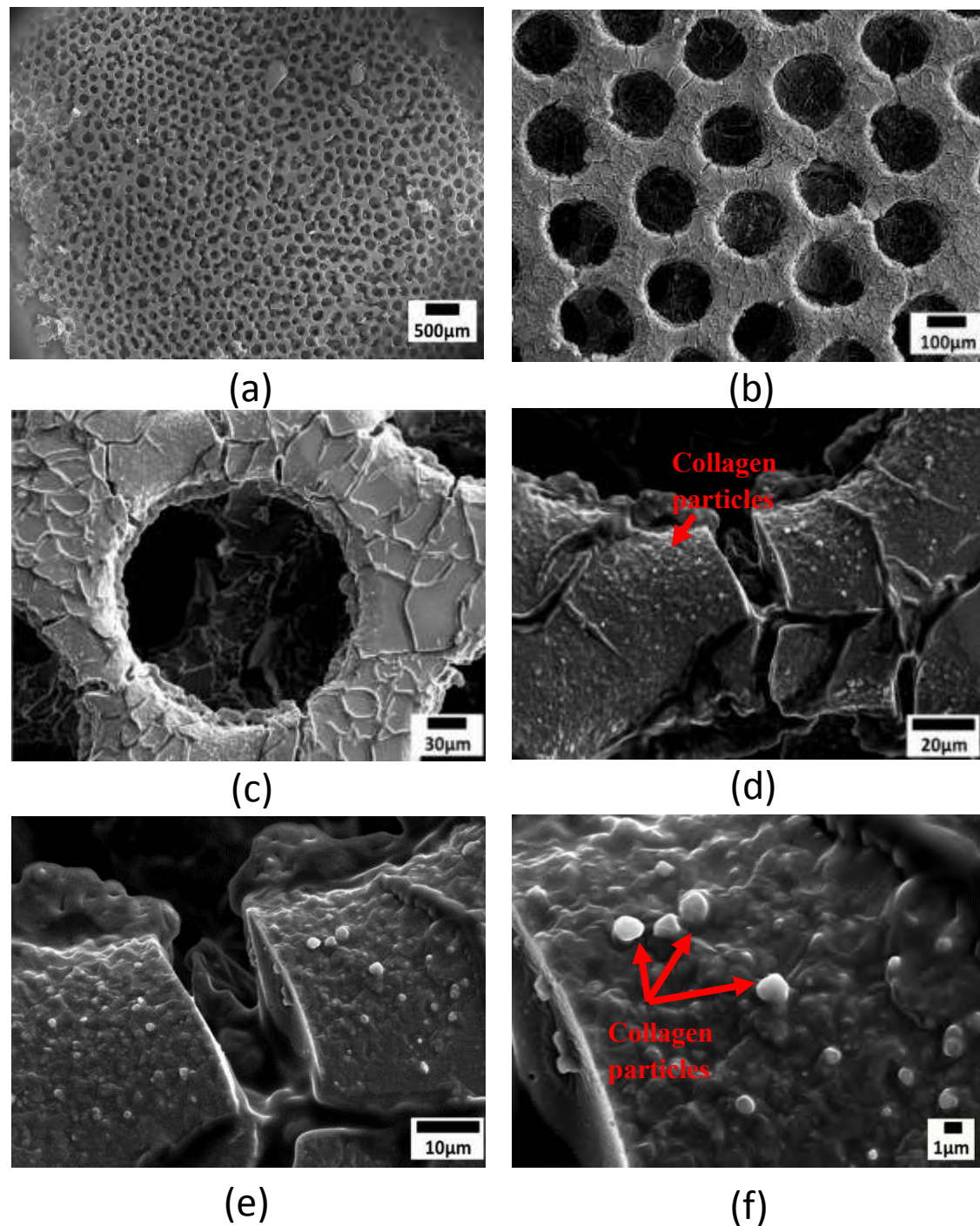


*Figure 5. 10: SEM images at different magnifications showing the same multilayered BSA scaffold after spraying with collagen micro-particles with images (a) and (f) having the lowest and the highest magnification, respectively.*

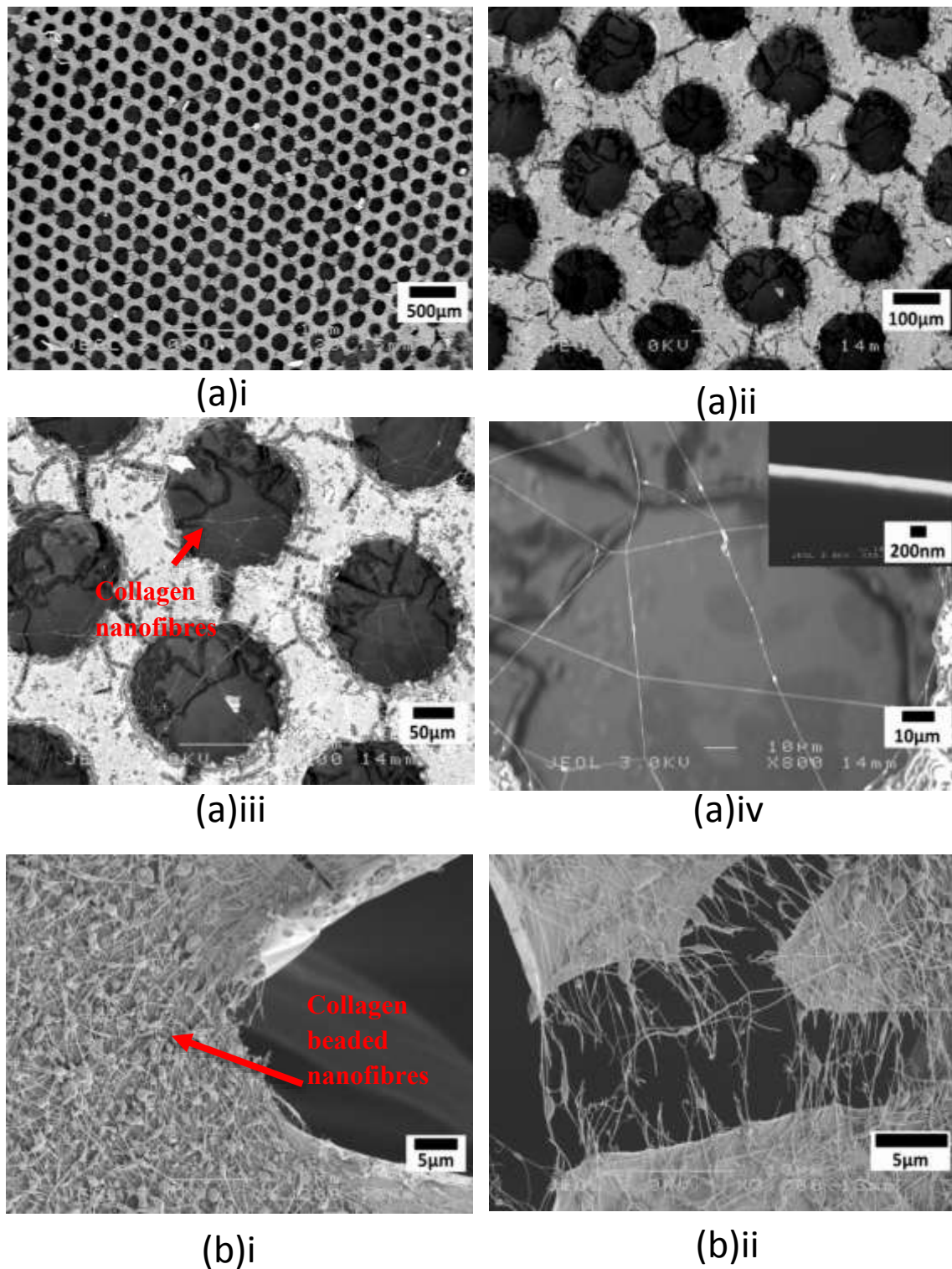


*Figure 5. 11: Scanning electron micrographs of multilayered BSA scaffolds sprayed with collagen beaded nanofibres for (a) 5min and (b) 15min at different magnifications.*

The BSA solution can be replaced or combined with other materials such as hydroxyapatite that can be used for bone regeneration (Ishaug et al., 1997, Rathbone et al., 2013). The PLGA, PMSQ and collagen particles/fibres sprayed onto the scaffolds (which can also have a foam like texture) can be loaded with drugs, growth factors and other bioactive agents in order to achieve controlled release into locations such as wounds, thus accelerating the healing process and prevent infections (Pereira et al., 2013, Boateng et al., 2008). They can also be used in the cosmetic industry in the form of cream lathers and facial scrubbing creams to deliver vitamins, proteins and other substances into the skin (Friess, 1998). The main advantage of using these biodegradable and biocompatible products produced in this work in cosmetics applications are that they are generally non-reactive when in contact with the human skin and by encapsulating them with the polymeric particles/fibres their biological stability can be increased (Ammala, 2013).

### **Summary**

In this study T-junction microfluidic and EHD techniques were combined and used together successfully to engineer advanced biocompatible scaffolds containing secondary bio-products on their structure. BSA protein scaffolds with controlled porosity varying from  $(81\pm 2)$   $\mu\text{m}$  to  $(543\pm 33)$   $\mu\text{m}$  were produced from microbubbles generated with the T-junction technique by adjusting the operating parameters and solution properties. Once the microbubbles were dried, the 3D protein scaffold structures were obtained. The microbubbles produced with the T-junction technique were highly monodispersed and hence led to the uniformity of the scaffold structure. Further by using the EHD process, biocompatible PLGA, PMSQ and collagen particles were produced and sprayed onto the scaffolds having an average size of  $(130\pm 23)$  nm,  $(1.94\pm 0.4)$   $\mu\text{m}$  and  $(1.35\pm 0.5)$   $\mu\text{m}$ , respectively. Furthermore, beaded collagen nanofibres (fibre size:  $257\pm 25$  nm and beads size:  $685\pm 67$  nm) were spun on the BSA scaffolds. The BSA protein scaffolds with attached secondary bio-products formed in this work have the potential to be used as medical and tissue engineering scaffolds, as well as delivery devices containing multiple bioactive agents. It is also believed that introducing these secondary elements in the scaffolds' assembly can assist with the mechanical strength of the structure.

## **Chapter 6**

### **Conclusions and Future Work**

#### **6.1 Conclusions**

The main contribution of the research described in this thesis is the demonstration of the capillary embedded T-unction microfluidic processing as an alternative and viable technique for preparing microbubbles with narrow size distributions, and which satisfy the requirements for many applications including biomedical applications and food industries. The ultimate objective in this study was to investigate the parameters that affect the microbubble formation in the T-junction device that eventually enables users to be able to have a great amount of control over the size and uniformity of bubbles produced with this technique. This objective was fulfilled via two sets of investigations; firstly the influence of liquid physical properties were studied by varying the surface tension and viscosity of the solutions; secondly, the operating conditions were tested by varying the liquid flow rate and gas pressures. From the experimental data, the size and polydispersity of the bubbles produced is highly dependent on all these parameters. The experiments were then focused on the effect of various surfactant type on the formation and stability of bubbles produced via this set-up and it was concluded that due to different adsorption rate and wetting characteristics of the surfactants bubble formation and stability can be altered by changing the surfactant type and concentrations. Microbubbles produced in the standard T-junction device had a diameter range of 50 -300 $\mu$ m. In order to reduce the microbubble size even further, an external field was introduced to the outlet capillary to optimise the microfluidic device with electrohydrodynamic focusing and bubble size was successfully reduced by approximately an order of magnitude. Finally, the device was used to produce foams and scaffolds from protein coated microbubbles and consequently novel scaffolds

loaded with nanoparticles/fibres were generated with a combination of microfluidic and EHD techniques. The following conclusions are drawn from the extensive investigations carried out to achieve this objective:

### **6.1.1 T-junction and parameters influencing bubble formation and size**

The mechanism of bubble formation in a capillary embedded T- Junction was investigated in detail and the influence of variables, mainly flow rate ratio and viscosity on the bubble size were determined. While the bubble size decreases with increasing liquid flow rate and viscosity, the increase in gas inlet pressure proportionally increases the bubble size as anticipated.

Furthermore, there is a limit to the extent to which bubble size can be reduced by increasing viscosity and/or flow ratio for a given capillary diameter and gap size. Therefore, a fixed size capillary diameter was chosen for all sets of experiments that involved the investigation of the effect of parameters other than the capillary size. With the increase in liquid viscosity, the radial pressure around the air jet is the major factor for bubble pinch off, whereas with the decrease in viscosity the deceleration of the air jet surrounded by liquid becomes dominant for the pinch off.

Further experiments were carried out to investigate the effect of capillary size in conjunction with the solution viscosity and liquid/gas flow ratio, to further reduce the bubble size. In addition, the influence of the junction gap width was also investigated. An increase in the gap width resulted in an increase in the size of bubbles for a fixed capillary number and liquid viscosity, flow rates of both gas and liquid.

The microbubbling process described in this work can be used to generate bubbles in the diameter range of 50 -300 $\mu\text{m}$ . However, producing smaller bubbles in highly viscous liquids is still a challenge using the current T-junction set-up. This is because formation of bubbles smaller than 20 $\mu\text{m}$  is only achievable by using smaller capillary

tubing than the current setup. Moreover, forcing high viscous liquid through such small capillary tubing is nearly unfeasible.

The results presented in this study facilitate the selection of solutions based on their physical properties and flow parameters as well as the capillary size for the controlled formation of highly monodisperse bubbles in the capillary embedded T Junction device. From the findings, it can be concluded that, in the bubble formation regime, by increasing the viscosity and decreasing the capillary size, producing smaller bubble size could eventually become achievable; bearing in mind the restrictions of the experimental setup (i.e. range of liquid flow rate and gas pressure and geometry).

### **6.1.2 Surfactant type and concentration on microbubble formation and stability**

The effects of various surfactants on microbubble formation, size and stability in a capillary embedded T-junction microfluidic device were investigated in this study. Four differently charged surfactants were chosen. An anionic surfactant, sodium dodecyl sulfate (SDS), two non-ionic surfactants, polyoxyethylene sorbitan monopalmitate (Tween 40) and polyoxyethylene glycol 40 stearate (PEG 40), and a cationic surfactant, cetyltrimethyl ammonium bromide (CTAB). Each surfactant was added to 50 wt% aqueous glycerol solution at high concentration (above the critical micelle concentration) varying from 2 to 5 and 10 wt%.

Static surface tension and contact angle were measured, as well as the viscosity of the solutions. While the value of surface tension did not significantly change with increasing surfactant concentration, other properties of the solutions (i.e. viscosity and contact angle) were affected.

Microbubbles with size varying from 50 to 360  $\mu\text{m}$  and polydispersity index values of  $< 2\%$  were produced with this technique. The nonionic surfactants produced smaller

bubbles. This is likely to have been due to their higher adsorption on to the hydrophobic channel surface and hence increase in the thickness of the liquid film at the contact line between the three phases for approximately similar capillary numbers and viscosities.

Bubble stability for all cases was evaluated by monitoring the change in average diameter with time. Microbubbles coated with PEG 40 were found to be the most stable, lasting for 150 days with a uniform size reduction of  $\sim 1.5\%$  as compared with SDS microbubbles lasting only for 30 mins after collection.

### **6.1.3 Optimization of T-junction with electrohydrodynamic focusing and reduction of bubble size**

While in a standard capillary embedded T-junction device bubble diameter ranged between 50-300  $\mu\text{m}$ . In order to reduce the bubble size to uncover more applications including biomedical, an external electric field was introduced to the junction. In this part of study generation of monodisperse microbubbles using a microfluidic setup combined with electrohydrodynamic processing were investigated. A basic T-junction microfluidic device was modified by applying an electrical potential difference across the outlet channel.

In order to investigate the influence of the electric field strength on bubble formation, the applied voltage was increased systematically up to 21 kV. The effect of solution viscosity and electrical conductivity was also investigated. It was found that with increasing electrical potential difference, the size of the microbubbles reduced to  $\sim 25\%$  of the capillary diameter whilst their size distribution remained narrow ( polydispersity index  $\sim 1\%$  ).

A critical value of 12 kV was found above which no further significant reduction in the size of the microbubbles was observed. The findings suggest that the size of the bubbles formed in the T-junction (i.e. in the absence of the electric field) is strongly influenced by the viscosity of the solution. The eventual size of bubbles produced by the composite

device, however, was only weakly dependent upon viscosity. Further experiments, in which the solution electrical conductivity was varied by the addition of a conductive salt indicated that this had a much stronger influence upon bubble size.

In order to produce microbubbles suitable for biomedical applications, flow focusing geometries with channel geometries much smaller were previously used by researchers. The number of bubbles produced however are not comparable to methods such as sonication. In order to scale up the production rate as well as avoiding the pressure build up that occurs in smaller channels, larger capillary diameters were used to produce bubbles. Producing bubbles much smaller than the channel diameter is very difficult, therefore by introducing an external force (electric field) bubbles much smaller than the channel geometrical features were produced.

### **6.1.4 Production of foams and scaffolds from bubbles and loading with nanoparticle/fibres**

This part of the research was aimed at the production of scaffolds and foams potentially suitable for tissue engineering and cosmetics applications. This piece of work provided an insight into the production of novel nanoparticle/fibre loaded scaffold structures using a combination of two well established techniques. Scaffolds with uniform pore size were developed from protein microbubbles formed via capillary embedded T-junction microfluidic cross flowing device. Polymer nanoparticles were electrosprayed on the structure; while collagen beaded nanofibres were electrospun via the EHD setup. This method of synthesis of highly uniform structures as well as embedding them with polymeric bio products delivers a new route to the development of the biomedical and cosmetics industries.

Valuable understanding of the concepts of microfluidics and EHD techniques and the combination of two simple but highly reliable methods in order to construct advanced multi-dimensional structures is presented. This experimental study produced highly uniform protein scaffolds from microbubbles generated with our state of the art

capillary embedded T-junction device with a high level of control over the size of microbubbles. In addition, the attachment of nanoparticles/fibres on the multi-layered structures through the EHD method improved the functionality of the scaffolds for possible future applications.

## 6.2 Future Work

Ideally, microbubbles should possess the following features: high stability and uniform size. The processing technique should be able to generate these features, be efficient in terms of time and material usage, convenient and easily scalable. T-junction microfluidic processing techniques have shown great promise in terms of these criteria offering a versatile tool for the generation of uniform bubbles and encapsulated structures. As it was shown in this thesis, microfluidic technique can achieve highly monodisperse bubbles and eventually products such as scaffolds with uniform pores size can be generated with this device. However there are still several aspects of future work recommended as the following:

- I. The T-junction can be adjusted to form smaller bubbles by using a capillary of internal diameter smaller than  $20\mu\text{m}$ . A right combination of capillary length and diameter can yield smaller monodispersed bubbles with the T-junction set-up. A reduction in capillary diameter will increase the liquid velocity in the capillary which will increase the bubble production rate without losing monodispersity. However, it should be noted that producing smaller bubbles in highly viscous liquids is a challenge using the current T-junction setup and therefore for this set of experiments, less viscous solutions should be chosen. The gap between the aligned capillaries can be precisely set by using a micromanipulator which will enable distances of a few micrometres upwards to be accurately maintained.
- II. Liquid can be supplied to the junction at different angles to decrease the air jet radius after focusing. The study of dynamics suggests that if liquid is supplied at a different angle than  $90^\circ$ , it will increase strain rate around the air jet at a

lower flow rate. This will enable the system to generate smaller bubbles, without requiring higher flow rates.

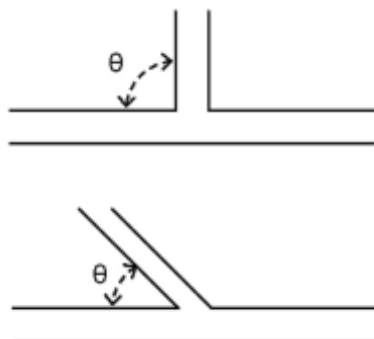


**Figure 6. 1:** *T-junction device with different angles.*

- III. The effect of channel geometry shall be further studied by several different aspect ratios including the ratio of the widths of channels. This shall be done systematically, by varying the capillary inner diameter of inlet channels as well as the outlet channel. If the gas inlet channel width is chosen to be smaller than the liquid inlet channel width (combined with the reduced vertical gap size between the gas inlet channel and the outlet channel), there is a possibility of reducing the air jet diameter further.
- IV. The biomedical applications of microbubbles require them to be highly stable and uniform in size. In order to meet such requirements, bubbles coated with a shell of polymer or lipid are emerging as vehicles for drug delivery and ultrasound imaging, where the stability is much higher than uncoated microbubbles. If a polymeric solution or a solution containing lipid can be added with a material to boost the viscosity of the solution to such viscosity or higher, the desired small bubble size with a high stability profile can be produced.
- V. Another factor that affects the bubble size and stability is the collection method. So far, the bubbles produced in the microfluidic device have been collected on an empty vial or a glass slide. Bubbles produced can be collected in a material that can manipulate the size and shape of the bubbles while preserving their

stability. This could be one of the cheapest methods to form bubbles in a very controlled way.

- VI. It would be beneficial to investigate the effect of applied voltage for a range of channel diameters, as it is suggested that by decreasing the channel diameter bubble size reduces. An optimised system can be achieved by understanding the variety of factors that can influence the size of bubbles produced.
- VII. In order to have more control over the applied voltage through the DC electric field supply, a frequency (signal) generator can be introduced into the setup to assist with the control of the flow even further.
- VIII. For the purpose of increasing the production rate of bubbles/droplets, blocks of multi channels can be replaced with the single T-junction setup investigated in this work. Also, it is possible to run a number of T-junction devices in parallel and study the different techniques to increase the production rate without affecting the stability and size.
- IX. The stability of microbubbles can be further increased by using higher molecular weight gases with low solubility such as FCs as mentioned in the literature review. The effect of these gases can be investigated in comparison with the bubbles with regular gases like nitrogen.
- X. Further experimental and modelling analysis can be conducted to study the effect of channel surface characteristics and dynamic interfacial tension and dynamic contact angle on the formation of bubbles/droplets.
- XI. The study of the effect of surfactants with the same hydrophobic chain and type, where all surfactants are from the same type (i.e. anionic, cationic or nonionic) can provide a better insight into how the surfactant molecules change the properties of the solution and further influence the formation process in microchannels.
- XII. Microchannel walls surface characteristics can be altered by inserting a variety of capillary tubes of different material. This can provide a better control on the

wetting ability of the wall surface. Depending on the application of the setup changing the material enables either a hydrophobic or hydrophilic surface and therefore the interfacial forces governing the formation can be affected.

- XIII. Further work is required to reduce the size of microbubbles to a biomedically acceptable diameter range (as ideally these vesicles would be approximately 15  $\mu\text{m}$  smaller than our system is currently optimized for) while maintaining the clinical-scale production and monodispersity achieved here. In order to achieve smaller microbubbles the reduction in capillary diameter is one solution to consider, however this can come at the cost of the rate of production. The primary goal of this work was to reduce the bubble size while maintaining the monodispersity and the rate of production. Relatively straightforward modifications in the design as well as the operating conditions are required in order to optimise the setup to produce smaller bubbles for biomedical applications at higher production rates.
- XIV. With regards to production of scaffolds from protein bubbles, it would be beneficial to incorporate materials that increase the strength of the 3D structure, such as hydroxyapatite (which is the main ingredient in bone regeneration applications) or biocompatible polymers.
- XV. Further analysis and testing is required to optimise the scaffolds produced in this work. These include: study on the variation of protein structures, the collection and drying method, and incorporation of growth factors instead of polymeric particles.

### **6.2.1 Commercial viability**

A full assessment of commercial and clinical viability of the techniques used in this study is an important issue which should be addressed in future. The T-junction microfluidic technique has some clear advantages in terms of simplicity, efficiency, cleanliness and ambient operation. However there is the issue of scaling up and associated cost to address. For the biomedically suitable microbubble production, the cost is one of the important issues. In contrast to the traditional method such as

## Chapter 6: Conclusions and future work

sonication and agitation, microfluidic method with a single T-junction unit still has some limitations such as low concentration and high consumption of material. It should be noted that microfluidic T- Junction with a single unit is a low-volume throughput process and it is not suitable or efficient for traditional industrial microbubbling processes. Approaches that address this problem are to use multi-channel (Kendall et al., 2012, Jiang et al., 2010). Therefore, more investigation can be conducted on scaling up and commercialising this technique via two methods: first, scaling up for mass production through the use of multiple T-junction devices, second, fabrication of miniaturised portable devices for in situ production of microbubbles.

**References**

- AGO, K., NAGASAWA, K., TAKITA, J., ITANO, R., MORII, N., MATSUDA, K. & TAKAHASHI, K. 2005. Development of an aerobic cultivation system by using a microbubble aeration technology. *Journal of Chemical Engineering of Japan*, 38, 757-762.
- AHMAD, B., GUNDUZ, O., STOYANOV, S., PELAN, E., STRIDE, E. & EDIRISINGHE, M. 2012. A novel hybrid system for the fabrication of a fibrous mesh with micro-inclusions. *Carbohydrate Polymers*, 89(1), 222-229.
- AHMADI, A., HOLZMAN, J. F., NAJJARAN, H. & HOORFAR, M. 2011. Electrohydrodynamic modeling of microdroplet transient dynamics in electrocapillary-based digital microfluidic devices. *Microfluidics and Nanofluidics*, 10, 1019-1035.
- AHMED, N. & JAMESON, G. J. 1985. The effect of bubble-size on the rate of flotation of fine particles. *International Journal of Mineral Processing*, 14, 195-215.
- AMMALA, A. 2013. Biodegradable polymers as encapsulation materials for cosmetics and personal care markets. *Int J Cosmet Sci*, 35, 113-24.
- ATTA, K. R., GAVRIL, D., LOUKOPOULOS, V. & KARAIKAKIS, G. 2004. Study of the influence of surfactants on the transfer of gases into liquids by inverse gas chromatography. *Journal of Chromatography A*, 1023, 287-296.
- BAROUD, C. N., GALLAIRE, F. & DANGLA, R. 2010. Dynamics of microfluidic droplets. *Lab on a Chip*, 10, 2032-2045.
- BAYRAKTAR, T. & PIDUGU, S. B. 2006. Characterization of liquid flows in microfluidic systems. *International Journal of Heat and Mass Transfer*, 49 (5), 815-824.
- BEHRENDTS, R., FUCHS, K., KAATZE, U., HAYASHI, Y. & FELDMAN, Y. 2006. Dielectric properties of glycerol/water mixtures at temperatures between 10 and 50 degrees C. *Journal of Chemical Physics*, 124, 1445121-8.
- BENEVENTI, D., CARRE, B. & GANDINI, A. 2001. Role of surfactant structure on surface and foaming properties. *Colloids and Surfaces A: Physicochemical and Engineering Aspects*, 189, 65-73.
- BHARDWAJ, N. & KUNDU, S. C. 2010. Electrospinning: A fascinating fiber fabrication technique. *Biotechnology Advances*, 28, 325-347.
- BLANCHARD, D. C. 1975. Bubble scavenging and water-to-air transfer of organic material in sea. *Advances in Chemistry Series*, 360-387.

## References

- BLOMLEY, M. J., COOKE, J. C., UNGER, E. C., MONAGHAN, M. J. & COSGROVE, D. O. 2001. Science, medicine, and the future: Microbubble contrast agents: a new era in ultrasound. *BMJ: British Medical Journal*, 322, 1222-1225.
- BOATENG, J. S., MATTHEWS, K. H., STEVENS, H. N. & ECCLESTON, G. M. 2008. Wound healing dressings and drug delivery systems: a review. *J Pharm Sci*, 97, 2892-923.
- BORDEN, M. 2009. Nanostructural features on stable microbubbles. *Soft Matter*, 5, 716-720.
- BORDEN, M. A. & LONGO, M. L. 2002. Dissolution Behavior of Lipid Monolayer-Coated, Air-Filled Microbubbles: Effect of Lipid Hydrophobic Chain Length. *Langmuir*, 18, 9225-9233.
- BURNS, S. E., YIACOUMI, S. & TSOURIS, C. 1997. Microbubble generation for environmental and industrial separations. *Separation and Purification Technology*, 11, 221-232.
- CAMPBELL, G. M. & MOUGEOT, E. 1999. Creation and characterisation of aerated food products. *Trends in Food Science & Technology*, 10, 283-296.
- CARLETTI, E., ENDOGAN, T., HASIRCI, N., HASIRCI, V., MANIGLIO, D., MOTTA, A. & MIGLIARESI, C. 2011. Microfabrication of PDLA scaffolds. *Journal of Tissue Engineering and Regenerative Medicine*, 5, 569-577.
- CASSELL, E. A., KAUFMAN, K. M. & MATIJEVIC, E. 1975. EFFECTS OF BUBBLE SIZE ON MICROFLOTATION. *Water Research*, 9, 1017-1024.
- CASTRO-HERNANDEZ, E., VAN HOEVE, W., LOHSE, D. & GORDILLO, J. M. 2011. Microbubble generation in a co-flow device operated in a new regime. *Lab on a Chip*, 11, 2023-2029.
- CHAKRABORTY, J., RAY, S. & CHAKRABORTY, S. 2012. Role of streaming potential on pulsating mass flow rate control in combined electroosmotic and pressure-driven microfluidic devices. *Electrophoresis*, 33, 419-425.
- CHAN, B. P. & LEONG, K. W. 2008. Scaffolding in tissue engineering: general approaches and tissue-specific considerations. *European Spine Journal*, 17 Suppl 4, 467-79.
- CHANG, M.-W., STRIDE, E. & EDIRISINGHE, M. 2010. Controlling the thickness of hollow polymeric microspheres prepared by electrohydrodynamic atomization. *Journal of The Royal Society Interface*, 7, S451-S460.
- CHAUDHURI, R. G. & PARIJA, S. 2009. Dynamic contact angles on PTFE surface by aqueous surfactant solution in the absence and presence of electrolytes. *Journal of Colloid and Interface Science*, 337, 555-562.

## References

- CHEN, C., ZHU, Y., LEECH, P. W. & MANASSEH, R. 2009. Production of monodispersed micron-sized bubbles at high rates in a microfluidic device. *Applied Physics Letters*, 95, 1441011-3.
- CHEN, F., PENG, Y., SONG, Y. Z. & CHEN, M. 2007. EHD behavior of nitrogen bubbles in DC electric fields. *Experimental Thermal and Fluid Science*, 32, 174-181.
- CHEN, G. H. 2004. Electrochemical technologies in wastewater treatment. *Separation and Purification Technology*, 38, 11-41.
- CHENG, N.-S. 2008. Formula for the viscosity of a glycerol-water mixture. *Industrial & Engineering Chemistry Research*, 47, 3285-3288.
- CHIU, P.-J., MEI, J.-C., HUANG, Y.-C. & YU, J. 2013. Monolayer microbubbles fabricated by microfluidic device for keratocytes observation. *Microelectronic Engineering*, 111, 277-284.
- CHRISTOPHER, G. F., NOHARUDDIN, N. N., TAYLOR, J. A. & ANNA, S. L. 2008. Experimental observations of the squeezing-to-dripping transition in T-shaped microfluidic junctions. *Physical Review E*, 78, 0363171-12.
- CHU, L.-B., XING, X.-H., YU, A.-F., ZHOU, Y.-N., SUN, X.-L. & JURCIK, B. 2007. Enhanced ozonation of simulated dyestuff wastewater by microbubbles. *Chemosphere*, 68, 1854-1860.
- CHUNG, K.-Y., MISHRA, N. C., WANG, C.-C., LIN, F.-H. & LIN, K.-H. 2009. Fabricating scaffolds by microfluidics. *Biomicrofluidics*, 3, 022403-8.
- COLOSI, C., COSTANTINI, M., BARBETTA, A., PECCI, R., BEDINI, R. & DENTINI, M. 2013. Morphological Comparison of PVA Scaffolds Obtained by Gas Foaming and Microfluidic Foaming Techniques. *Langmuir*, 29, 82-91.
- COOLEY, J. F. 4<sup>th</sup> Feb 1902. Apparatus for electrically dispersing fluids. U.S. Patent No. 692,631.
- CUBAUD, T. & HO, C. M. 2004. Transport of bubbles in square microchannels. *Physics of Fluids*, 16, 4575-4585.
- CUI, W. J., BEI, J. Z., WANG, S. G., ZHI, G., ZHAO, Y. Y., ZHOU, X. S., ZHANG, H. W. & XU, Y. 2005. Preparation and evaluation of poly(L-lactide-co-glycolide) (PLGA) microbubbles as a contrast agent for myocardial contrast echocardiography. *Journal of Biomedical Materials Research Part B-Applied Biomaterials*, 73B, 171-178.
- CUI, Y., CAMPBELL, P. A. & IEEE 2008. Towards Monodisperse Microbubble Populations via Microfluidic Chip Flow-Focusing. *2008 IEEE Ultrasonics Symposium, Vols 1-4 and Appendix*, 1663-1666.

## References

- CUTRONEO, K. R. 2003. Gene therapy for tissue regeneration. *Journal of Cellular Biochemistry*, 88, 418-425.
- DANHIER, F., ANSORENA, E., SILVA, J. M., COCO, R., LE BRETON, A. & PREAT, V. 2012. PLGA-based nanoparticles: an overview of biomedical applications. *J Controlled Release*, 161, 505-22.
- DE MENECH, M., GARSTECKI, P., JOUSSE, F. & STONE, H. A. 2008. Transition from squeezing to dripping in a microfluidic T-shaped junction. *Journal of Fluid Mechanics*, 595, 141-161.
- DHANDAYUTHAPANI, B., YOSHIDA, Y., MAEKAWA, T. & KUMAR, D. S. 2011. Polymeric Scaffolds in Tissue Engineering Application: A Review. *International Journal of Polymer Science*. 2011, 1-19.
- DIJKMANS, P. A., JUFFERMANS, L. J. M., MUSTERS, R. J. P., VAN WAMEL, A., TEN CATE, F. J., VAN GILST, W., VISSER, C. A., DE JONG, N. & KAMP, O. 2004. Microbubbles and ultrasound: from diagnosis to therapy. *European Journal of Echocardiography*, 5, 245-56.
- ECKMANN, D. M. & DIAMOND, S. L. 2004. Surfactants attenuate gas embolism-induced thrombin production. *Anesthesiology*, 100, 77-84.
- EGGLETON, C. D., TSAI, T. M. & STEBE, K. J. 2001. Tip streaming from a drop in the presence of surfactants. *Physical Review Letters*, 87.
- EKEMEN, Z., CHANG, H., AHMAD, Z., BAYRAM, C., RONG, Z., DENKBAS, E. B., STRIDE, E., VADGAMA, P. & EDIRISINGHE, M. 2011. Fabrication of Biomaterials via Controlled Protein Bubble Generation and Manipulation. *Biomacromolecules*, 12, 4291-4300.
- ENAYATI, M., AHMAD, Z., STRIDE, E. & EDIRISINGHE, M. 2009. Preparation of Polymeric Carriers for Drug Delivery with Different Shape and Size Using an Electric Jet. *Current Pharmaceutical Biotechnology*, 10, 600-608.
- EPSTEIN, P. S. & PLESSET, M. S. 1950. On the Stability of Gas Bubbles in Liquid-Gas Solutions. *The Journal of Chemical Physics*, 18, 1505-1509.
- FAROOK, U., STRIDE, E. & EDIRISINGHE, M. J. 2009. Preparation of suspensions of phospholipid-coated microbubbles by coaxial electrohydrodynamic atomization. *Journal of the Royal Society Interface*, 6, 271-277.
- FAROOK, U., STRIDE, E., EDIRISINGHE, M. J. & MOALEJI, R. 2007. Microbubbling by co-axial electrohydrodynamic atomization. *Medical & Biological Engineering & Computing*, 45, 781-789.
- FERRARA, K., POLLARD, R. & BORDEN, M. 2007. Ultrasound microbubble contrast agents: Fundamentals and application to gene and drug delivery. *Annual Review of Biomedical Engineering*, 9, 415-447.

## References

- FIORINI, G. S. & CHIU, D. T. 2005. Disposable microfluidic devices: fabrication, function, and application. *BioTechniques*, 38, 429-446.
- FRIESS, W. 1998. Collagen--biomaterial for drug delivery. *Eur J Pharm Biopharm*, 45, 113-36.
- FU, T., MA, Y., FUNFSCHILLING, D. & LI, H. Z. 2009. Bubble formation and breakup mechanism in a microfluidic flow-focusing device. *Chemical Engineering Science*, 64, 2392-2400.
- GAÑÁN-CALVO, A. M. & GORDILLO, J. M. 2001. Perfectly monodisperse microbubbling by capillary flow focusing. *Physical Review Letters*, 87, 274501.
- GARSTECKI, P., FUERSTMAN, M. J., STONE, H. A. & WHITESIDES, G. M. 2006. Formation of droplets and bubbles in a microfluidic T-junction-scaling and mechanism of break-up. *Lab Chip*, 6, 437-46.
- GARSTECKI, P., FUERSTMAN, M. J. & WHITESIDES, G. M. 2005a. Nonlinear dynamics of a flow-focusing bubble generator: An inverted dripping faucet. *Physical Review Letters*, 94, 2345021-4.
- GARSTECKI, P., FUERSTMAN, M. J. & WHITESIDES, G. M. 2005b. Oscillations with uniquely long periods in a microfluidic bubble generator. *Nature Physics*, 1, 168-171.
- GARSTECKI, P., GANAN-CALVO, A. & WHITESIDES, G. 2005c. Formation of bubbles and droplets in microfluidic systems. *Technical Sciences*, 53, 361-372.
- GARSTECKI, P., GITLIN, I., DILUZIO, W., WHITESIDES, G. M., KUMACHEVA, E. & STONE, H. A. 2004. Formation of monodisperse bubbles in a microfluidic flow-focusing device. *Applied Physics Letters*, 85, 2649-2651.
- GERBER, F., KRAFFT, M. P., WATON, G. & VANDAMME, T. F. 2006. Microbubbles with exceptionally long life—synergy between shell and internal phase components. *New Journal of Chemistry*, 30, 524-527.
- GLASGOW, I., BATTON, J. & AUBRY, N. 2004. Electroosmotic mixing in microchannels. *Lab on a Chip*, 4, 558-562.
- GORDILLO, J. M., CHENG, Z., GANAN-CALVO, A. M., MARQUEZ, M. & WEITZ, D. 2004. A new device for the generation of microbubbles. *Physics of Fluids*, 16, 2828-2834.
- GUNDUZ, O., AHMAD, Z., STRIDE, E. & EDIRISINGHE, M. 2012. A device for the fabrication of multifunctional particles from microbubble suspensions. *Materials Science and Engineering: C*, 32, 1005-1010.
- GUNTHER, A. & JENSEN, K. F. 2006. Multiphase microfluidics: from flow characteristics to chemical and materials synthesis. *Lab Chip*, 6, 1487-503.

## References

- HANWRIGHT, J., ZHOU, J., EVANS, G. M. & GALVIN, K. P. 2005. Influence of Surfactant on Gas Bubble Stability. *Langmuir*, 21, 4912-4920.
- HAYNESWORTH, S. E., REUBEN, D. & CAPLAN, A. I. 1998. Cell-based tissue engineering therapies: the influence of whole body physiology. *Advanced Drug Delivery Reviews*, 33, 3-14.
- HERNOT, S. & KLIBANOV, A. L. 2008. Microbubbles in ultrasound-triggered drug and gene delivery. *Advanced Drug Delivery Reviews*, 60, 1153-1166.
- HETTIARACHCHI, K., TALU, E., LONGO, M. L., DAYTON, P. A. & LEE, A. P. 2007. On-chip generation of microbubbles as a practical technology for manufacturing contrast agents for ultrasonic imaging. *Lab on a Chip*, 7, 463-468.
- HOLLISTER, S. J. 2005. Porous scaffold design for tissue engineering. *Nature materials*, 4, 518-524.
- HU, Y., HOLLINGER, J. O. & MARRA, K. G. 2001. Controlled release from coated polymer microparticles embedded in tissue-engineered scaffolds. *Journal of Drug Targeting*, 9, 431-438.
- HUA, J., ZHANG, B. & LOU, J. 2007. Numerical simulation of microdroplet formation in coflowing immiscible liquids. *AIChE Journal*, 53, 2534-2548.
- HUANG, Z.-M., ZHANG, Y. Z., KOTAKI, M. & RAMAKRISHNA, S. 2003. A review on polymer nanofibers by electrospinning and their applications in nanocomposites. *Composites Science and Technology*, 63, 2223-2253.
- ISHAUG, S. L., CRANE, G. M., MILLER, M. J., YASKO, A. W., YASZEMSKI, M. J. & MIKOS, A. G. 1997. Bone formation by three-dimensional stromal osteoblast culture in biodegradable polymer scaffolds. *J Biomed Mater Res*, 36, 17-28.
- JAWOREK, A. 2007. Micro- and nanoparticle production by electrospraying. *Powder Technology*, 176, 18-35.
- JAYASINGHE, S. N. & EDIRISINGHE, M. J. 2005. Jet break-up in nano-suspensions during electrohydrodynamic atomization in the stable cone-jet mode. *Journal of Nanoscience and Nanotechnology*, 5, 923-926.
- JIANG, C., LI, X., JIN, Q., CHEN, T., WANG, Z. & ZHENG, H. Mass Production of Monodisperse Ultrasound Contrast Microbubbles in Integrated Microfluidic Devices. *Bioinformatics and Biomedical Engineering (iCBBE)*, 2010 4th International Conference on, 2010. IEEE, 1-4.
- JIMENEZ, C., TALAVERA, B., SAEZ, C., CANIZARES, P. & RODRIGO, M. A. 2010. Study of the production of hydrogen bubbles at low current densities for electroflotation processes. *Journal of Chemical Technology and Biotechnology*, 85, 1368-1373.

## References

- JOHNSON, B. D. & COOKE, R. C. 1980. Organic particle and aggregate formation resulting from the dissolution of bubbles in seawater. *Limnology and Oceanography*, 25, 653-661.
- KANG, S.-T. & YEH, C.-K. 2012. Ultrasound microbubble contrast agents for diagnostic and therapeutic applications: current status and future design. *Chang Gung Medical Journal*, 35, 125-39.
- KENDALL, M. R., BARDIN, D., SHIH, R., DAYTON, P. A. & LEE, A. P. 2012. Scaled-up production of monodisperse, dual layer microbubbles using multi-array microfluidic module for medical imaging and drug delivery. *Bubble Science, Engineering and Technology*, 4, 12-20.
- KETKAR, D. R., MALLIKARJUNAN, R. & VENKATACHALAM, S. 1991. Electroflotation of quartz fines. *International Journal of Mineral Processing*, 31, 127-138.
- KIESSLING, F., FOKONG, S., KOCZERA, P., LEDERLE, W. & LAMMERS, T. 2012. Ultrasound Microbubbles for Molecular Diagnosis, Therapy, and Theranostics. *Journal of Nuclear Medicine*, 53, 345-348.
- KIM, H., LUO, D., LINK, D., WEITZ, D. A., MARQUEZ, M. & CHENG, Z. 2007. Controlled production of emulsion drops using an electric field in a flow-focusing microfluidic device. *Applied Physics Letters*, 91, 133106-3.
- KIM, H. J., KIM, U. J., VUNJAK-NOVAKOVIC, G., MIN, B. H. & KAPLAN, D. L. 2005. Influence of macroporous protein scaffolds on bone tissue engineering from bone marrow stem cells. *Biomaterials*, 26, 4442-4452.
- KIM, N., EVANS, E. T., PARK, D. S., SOPER, S. A., MURPHY, M. C. & NIKITPOULOS, D. E. 2011a. Gas-liquid two-phase flows in rectangular polymer micro-channels. *Experiments in Fluids*, 51, 373-393.
- KIM, S. J., SONG, Y.-A., SKIPPER, P. L. & HAN, J. 2006. Electrohydrodynamic generation and delivery of monodisperse picoliter droplets using a poly(dimethylsiloxane) microchip. *Analytical Chemistry*, 78, 8011-8019.
- KIM, W., RYU, J. C., SUH, Y. K. & KANG, K. H. 2011b. Pumping of dielectric liquids using non-uniform-field induced electrohydrodynamic flow. *Applied Physics Letters*, 99, 2241021-3.
- KLIBANOV, A. L. 1999. Targeted delivery of gas-filled microspheres, contrast agents for ultrasound imaging. *Advanced Drug Delivery Reviews*, 37, 139-157.
- KRAUS, T., GUNTHER, A., DE MAS, N., SCHMIDT, M. A. & JENSEN, K. F. 2004. An integrated multiphase flow sensor for microchannels. *Experiments in Fluids*, 36, 819-832.

## References

- KREMKAU, F. W., GRAMIAK, R., CARSTENS, EL, SHAH, P. M. & KRAMER, D. H. 1970. Ultrasonic detection of cavitation at catheter tips. *American Journal of Roentgenology Radium Therapy and Nuclear Medicine*, 110, 177-&.
- KU, B. K. & KIM, S. S. 2002. Electrospray characteristics of highly viscous liquids. *Journal of Aerosol Science*, 33, 1361-1378.
- KUKIZAKI, M. & BABA, Y. 2008. Effect of surfactant type on microbubble formation behavior using Shirasu porous glass (SPG) membranes. *Colloids and Surfaces A: Physicochemical and Engineering Aspects*, 326, 129-137.
- KUKIZAKI, M. & GOTO, M. 2006. Size control of nanobubbles generated from Shirasu-porous-glass (SPG) membranes. *Journal of Membrane Science*, 281, 386-396.
- LAU, C. K. & DICKINSON, E. 2005. Instability and structural change in an aerated system containing egg albumen and invert sugar. *Food Hydrocolloids*, 19, 111-121.
- LEE, J. S. H. & LI, D. 2006. Electroosmotic flow at a liquid-air interface. *Microfluidics and Nanofluidics*, 2, 361-365.
- LEE, K., SILVA, E. A. & MOONEY, D. J. 2011. Growth factor delivery-based tissue engineering: general approaches and a review of recent developments. *Journal of The Royal Society Interface*, 8, 153-170.
- LI, M. Y., MONDRINOS, M. J., GANDHI, M. R., KO, F. K., WEISS, A. S. & LELKES, P. I. 2005. Electrospun protein fibers as matrices for tissue engineering. *Biomaterials*, 26, 5999-6008.
- LI, S., XU, Z., MAZZEO, A., BURNS, D. J., FU, G., DIRCKX, M., SHILPIEKANDULA, V., CHEN, X., NAYAK, N. C. & WONG, E. Review of production of microfluidic devices: material, manufacturing and metrology. Photonics Europe, 2008. International Society for Optics and Photonics, 69930F-69930F-12.
- LIMA, E. G., DURNEY, K. M., SIRSI, S. R., NOVER, A. B., ATESHIAN, G. A., BORDEN, M. A. & HUNG, C. T. 2012. Microbubbles as biocompatible porogens for hydrogel scaffolds. *Acta Biomaterialia*, 8, 4334-4341.
- LINDNER, J. R. 2004. Microbubbles in medical imaging: current applications and future directions. *Nature Reviews Drug Discovery*, 3, 527-532.
- LINK, D. R., GRASLAND-MONGRAIN, E., DURU, A., SARRAZIN, F., CHENG, Z., CRISTOBAL, G., MARQUEZ, M. & WEITZ, D. A. 2006. Electric Control of Droplets in Microfluidic Devices. *Angewandte Chemie International Edition*, 45, 2556-2560.
- LIU, J., MORYKWA, M. J., ARGENTA, L. C. & WAGNER, W. D. 2011. Development of a biodegradable foam for use in negative pressure wound

## References

- therapy. *Journal of Biomedical Materials Research Part B: Applied Biomaterials*, 98B, 316-322.
- LIU, X. & MA, P. X. 2004. Polymeric scaffolds for bone tissue engineering. *Annals of Biomedical Engineering*, 32, 477-486.
- MA, P. X. & CHOI, J.-W. 2001. Biodegradable polymer scaffolds with well-defined interconnected spherical pore network. *Tissue Engineering*, 7, 23-33.
- MA, P. X. & ZHANG, R. 1999. Synthetic nano-scale fibrous extracellular matrix. *Journal of Biomedical Materials Research*, 46, 60-72.
- MA, P. X. & ZHANG, R. 2001. Microtubular architecture of biodegradable polymer scaffolds. *Journal of Biomedical Materials Research*, 56, 469-477.
- MAAS, M., BODNAR, P. M., HESS, U., TRECCANI, L. & REZWAN, K. 2013. Towards the synthesis of hydroxyapatite/protein scaffolds with controlled porosities: Bulk and interfacial shear rheology of a hydroxyapatite suspension with protein additives. *Journal of Colloid and Interface Science*, 407, 529-535.
- MALLICK, K. K. 2009. Freeze Casting of Porous Bioactive Glass and Bioceramics. *Journal of the American Ceramic Society*, 92, S85-S94.
- MARTINEZ, C. 2009. Bubble generation in microfluidic devices. *Bubble Science, Engineering & Technology*, 1, 40-52.
- MIKOS, A. G., THORSEN, A. J., CZERWONKA, L. A., BAO, Y., LANGER, R., WINSLOW, D. N. & VACANTI, J. P. 1994. Preparation and characterization of poly(l-lactic acid) foams. *Polymer*, 35, 1068-1077.
- MOHAMEDI, G., AZMIN, M., PASTORIZA-SANTOS, I., HUANG, V., PEREZ-JUSTE, J., LIZ-MARZAN, L. M., EDIRISINGHE, M. & STRIDE, E. 2012. Effects of Gold Nanoparticles on the Stability of Microbubbles. *Langmuir*, 28, 13808-13815.
- MOLHO, J. I., HERR, A. E., DESPHANDE, M., GILBERT, J., GARGUILO, M. G., PAUL, P. H., JOHN, P., WOUDEBERG, T. & CONNELL, C. 1998. Fluid transport mechanisms in microfluidic devices. *Proc. ASME Micro-Electro-Mechanical-Systems (MEMS)*, 66, 69-76.
- MUSTIN, B. & STOEBER, B. Design considerations for robust suspension-based microfluidic systems for biomedical applications. Mixed-Signals, Sensors, and Systems Test Workshop, 2008. IMS3TW 2008. IEEE 14th International, 2008. IEEE, 1-6.
- NAIR, A., JIAN, Y. & LIPING, T. A Novel Preparation of Degradable Scaffolds Using BSA Microbubbles as Porogen. Engineering in Medicine and Biology Workshop, 2007 IEEE Dallas, 11-12 Nov. 2007. 31-34.

## References

- NAIR, A., THEVENOT, P., DEY, J., SHEN, J., SUN, M.-W., YANG, J. & TANG, L. 2009. Novel polymeric scaffolds using protein microbubbles as porogen and growth factor carriers. *Tissue Engineering Part C: Methods*, 16, 23-32.
- NAPPER, D. H. 1977. Steric stabilization. *Journal of Colloid and Interface Science*, 58, 390-407.
- NIE, Z., SEO, M., XU, S., LEWIS, P. C., MOK, M., KUMACHEVA, E., WHITESIDES, G. M., GARSTECKI, P. & STONE, H. A. 2008. Emulsification in a microfluidic flow-focusing device: effect of the viscosities of the liquids. *Microfluidics and Nanofluidics*, 5, 585-594.
- OH, S. D. & KWAK, H. Y. 2000. A study of bubble behavior and boiling heat transfer enhancement under electric field. *Heat Transfer Engineering*, 21, 33-45.
- PANCHOLI, K., STRIDE, E. & EDIRISINGHE, M. 2008. Dynamics of bubble formation in highly viscous liquids. *Langmuir*, 24, 4388-4393.
- PANTANO, C., GAÑÁN-CALVO, A. M. & BARRERO, A. 1994. Zeroth-order, electrohydrostatic solution for electrospraying in cone-jet mode. *Journal of Aerosol Science*, 25, 1065-1077.
- PARHIZKAR, M., EDIRISINGHE, M. & STRIDE, E. 2013. Effect of operating conditions and liquid physical properties on the size of monodisperse microbubbles produced in a capillary embedded T-junction device. *Microfluidics and Nanofluidics*, 14, 797-808.
- PARK, J. I., TUMARKIN, E. & KUMACHEVA, E. 2010. Small, Stable, and Monodispersed Bubbles Encapsulated with Biopolymers. *Macromolecular Rapid Communications*, 31, 222-227.
- PEREIRA, R. F., BARRIAS, C. C., GRANJA, P. L. & BARTOLO, P. J. 2013. Advanced biofabrication strategies for skin regeneration and repair. *Nanomedicine*, 8, 603-621.
- PRAJAPATI, J. & AGRAWAL, Y. 2012. Synthesis, characterization and application of microbubbles: a review. *International Journal of Pharmaceutical Sciences & Research*, 3, 1532-1543.
- PRAKASH, A. S. 2010. Selecting surfactants for the maximum inhibition of the activity of the multidrug resistance efflux pump transporter, P-glycoprotein: conceptual development. *Journal of Excipients & Food Chemicals*, 1, 51-59.
- QUAN, X., CHEN, G. & CHENG, P. 2011. Effects of electric field on microbubble growth in a microchannel under pulse heating. *International Journal of Heat and Mass Transfer*, 54, 2110-2115.
- RALLISON, J. M. 1984. The deformation of small viscous drops and bubbles in shear flows. *Annual Review of Fluid Mechanics*, 16, 45-66.

## References

- RAMAKRISHNA, S., FUJIHARA, K., TEO, W.-E., LIM, T.-C. & MA, Z. 2005. An introduction to electrospinning and nanofibers, Vol 90. Singapore, World Scientific.
- RATHBONE, C. R., GUDA, T., SINGLETON, B. M., OH, D. S., APPLEFORD, M. R., ONG, J. L. & WENKE, J. C. 2014. Effect of cell-seeded hydroxyapatite scaffolds on rabbit radius bone regeneration. *J Biomed Mater Res A*, 102, 1458-1466.
- READEY, D. W. & COPPER JR, A. R. 1966. Molecular diffusion with a moving boundary and spherical symmetry. *Chemical Engineering Science*, 21, 917-922.
- REDDY, V., ZAHN, J. D. & ASME 2005. Two phase electrohydrodynamic instability micromixing. *Proceedings of the ASME Fluids Engineering Division*, 267-271.
- RODRIGUES, R. T. & RUBIO, J. 2007. DAF-dissolved air flotation: Potential applications in the mining and mineral processing industry. *International Journal of Mineral Processing*, 82, 1-13.
- ROSEN, M. J. & KUNJAPPU, J. T. 2012. *Surfactants and interfacial phenomena*, John Wiley & Sons.
- ROSSI, S., WATON, G. & KRAFFT, M. P. 2009. Phospholipid-coated gas bubble engineering: Key parameters for size and stability control, as determined by an acoustical method. *Langmuir*, 26, 1649-1655.
- SALAGER, J.-L. 2002. Surfactant's types and uses. *FIRP booklet-E300-A teaching aid in surfactant science and engineering in English. Merida Venezuela*, 3.
- SEN, A. K., DARABI, J. & KNAPP, D. R. 2011. Analysis of Droplet Generation in Electrospray Using a Carbon Fiber Based Microfluidic Emitter. *Journal of Fluids Engineering-Transactions of the Asme*, 133,0713011-8.
- SENGUPTA, D. & HEILSHORN, S. C. 2010. Protein-Engineered Biomaterials: Highly Tunable Tissue Engineering Scaffolds. *Tissue Engineering Part B-Reviews*, 16, 285-293.
- SERIZAWA, A., FENG, Z. P. & KAWARA, Z. 2002. Two-phase flow in microchannels. *Experimental Thermal and Fluid Science*, 26, 703-714.
- SHAO, N., SALMAN, W., GAVRIILIDIS, A. & ANGELI, P. 2008. CFD simulations of the effect of inlet conditions on Taylor flow formation. *International Journal of Heat and Fluid Flow*, 29, 1603-1611.
- SHEN, Y. Y., LONGO, M. L. & POWELL, R. L. 2008. Stability and rheological behavior of concentrated monodisperse food emulsifier coated microbubble suspensions. *Journal of Colloid and Interface Science*, 327, 204-210.
- SHERWOOD, J. D. 1984. Tip streaming from slender drops in a nonlinear extensional flow. *Journal of Fluid Mechanics*, 144, 281-295.

## References

- SIRSI, S. & BORDEN, M. 2009. Microbubble compositions, properties and biomedical applications. *Bubble Science, Engineering & Technology*, 1, 3-17.
- SOFOKLEOUS, P., STRIDE, E., BONFIELD, W. & EDIRISINGHE, M. 2013a. Design, construction and performance of a portable handheld electrohydrodynamic multi-needle spray gun for biomedical applications. *Materials Science & Engineering C-Materials for Biological Applications*, 33, 213-223.
- SOFOKLEOUS, P., STRIDE, E. & EDIRISINGHE, M. 2013b. Preparation, Characterization, and Release of Amoxicillin from Electrospun Fibrous Wound Dressing Patches. *Pharmaceutical Research*, 30, 1926-1938.
- SRIVASTAVA, Y., LOSCERTALES, I., MARQUEZ, M. & THORSEN, T. 2008. Electrospinning of hollow and core/sheath nanofibers using a microfluidic manifold. *Microfluidics and Nanofluidics*, 4, 245-250.
- STONE, H. A. 1994. DYNAMICS OF DROP DEFORMATION AND BREAKUP IN VISCOUS FLUIDS. *Annual Review of Fluid Mechanics*, 26, 65-102.
- STONE, H. A., STROOCK, A. D. & AJDARI, A. 2004. Engineering flows in small devices: Microfluidics toward a lab-on-a-chip. *Annual Review of Fluid Mechanics*, 36, 381-411.
- STRIDE, E. 2008. The influence of surface adsorption on microbubble dynamics. *Philosophical Transactions of the Royal Society a-Mathematical Physical and Engineering Sciences*, 366, 2103-2115.
- STRIDE, E. 2009. Physical principles of microbubbles for ultrasound imaging and therapy. *Cerebrovascular diseases (Basel, Switzerland)*, 27 Suppl 2, 1-13.
- STRIDE, E. & EDIRISINGHE, M. 2008. Novel microbubble preparation technologies. *Soft Matter*, 4, 2350-2359.
- STRIDE, E. & EDIRISINGHE, M. 2009. Novel preparation techniques for controlling microbubble uniformity: a comparison. *Medical & Biological Engineering & Computing*, 47, 883-892.
- STRIDE, E., PORTER, C., PRIETO, A. G. & PANKHURST, Q. 2009. Enhancement of microbubble mediated gene delivery by simultaneous exposure to ultrasonic and magnetic fields. *Ultrasound in Medicine and Biology*, 35, 861-868.
- STRIDE, E. & SAFFARI, N. 2003. Microbubble ultrasound contrast agents: a review. *Proceedings of the Institution of Mechanical Engineers Part H-Journal of Engineering in Medicine*, 217, 429-447.
- SULLIVAN, A. C. & JAYASINGHE, S. N. 2007. Development of a direct three-dimensional biomicrofabrication concept based on electro spraying a custom made siloxane sol. *Biomicrofluidics*, 1, 034103-10.

## References

- SUSLICK, K. S., DIDENKO, Y., FANG, M. M., HYEON, T., KOLBECK, K. J., MCNAMARA, W. B., MDLELENI, M. M. & WONG, M. 1999. Acoustic cavitation and its chemical consequences. *Philosophical Transactions of the Royal Society of London Series a-Mathematical Physical and Engineering Sciences*, 357 (1751), 335-353.
- SZÍJJÁRTÓ, C., ROSSI, S., WATON, G. & KRAFFT, M. P. 2012. Effects of perfluorocarbon gases on the size and stability characteristics of phospholipid-coated microbubbles: osmotic effect versus interfacial film stabilization. *Langmuir*, 28, 1182-1189.
- TAKAGI, S. & MATSUMOTO, Y. 2011. Surfactant Effects on Bubble Motion and Bubbly Flows. *Annual Review of Fluid Mechanics*, 43, 615-636.
- TANG, K. & GOMEZ, A. 1994. On the structure of an electrostatic spray of monodisperse droplets. *Physics of Fluids*, 6, 2317-2332.
- TAVERNA, G., GIUSTI, G., SEVESO, M., BENETTI, A., MINUTI, F., GRIZZI, F. & GRAZIOTTI, P. 2012. Colour doppler combined with microbubble contrast agent ultrasonography and the cancer detection rate in transrectal systematic prostate biopsy sampling. *Journal of Urology*, 187, E820-E820.
- TAYLOR, G. 1964. DISINTEGRATION OF WATER DROPS IN ELECTRIC FIELD. *Proceedings of the Royal Society of London Series a-Mathematical and Physical Sciences*, 280, 383-397.
- TEH, S.-Y., LIN, R., HUNG, L.-H. & LEE, A. P. 2008. Droplet microfluidics. *Lab on a Chip*, 8, 198-220.
- THORSEN, T., ROBERTS, R. W., ARNOLD, F. H. & QUAKE, S. R. 2001. Dynamic pattern formation in a vesicle-generating microfluidic device. *Physical Review Letters*, 86, 4163-4166.
- TICE, J. D., LYON, A. D. & ISMAGILOV, R. F. 2004. Effects of viscosity on droplet formation and mixing in microfluidic channels. *Analytica Chimica Acta*, 507, 73-77.
- TONG, J. H., NAKAJIMA, M., NABETANI, H. & KIKUCHI, Y. 2000. Surfactant effect on production of monodispersed microspheres by microchannel emulsification method. *Journal of Surfactants and Detergents*, 3, 285-293.
- TOSTADO, C. P., XU, J. & LUO, G. 2011. The effects of hydrophilic surfactant concentration and flow ratio on dynamic wetting in a T-junction microfluidic device. *Chemical Engineering Journal*, 171, 1340-1347.
- UEDA, H., MEGURI, N., MINAGUCHI, J., WATANABE, T., NAGAYASU, A., HOSAKA, Y., TANGKAWATTANA, P., KOKAI, Y. & TAKEHANA, K. 2008. Effect of collagen oligopeptide injection on rabbit tenositis, *J Veterinary Medical Science*, 70 (12):1295-1300.

## References

- UNGER, E. C., HERSH, E., VANNAN, M., MATSUNAGA, T. O. & MCCREERY, T. 2001. Local drug and gene delivery through microbubbles. *Progress in Cardiovascular Diseases*, 44, 45-54.
- VAN DER GRAAF, S., NISISAKO, T., SCHROEN, C., VAN DER SMAN, R. & BOOM, R. 2006. Lattice Boltzmann simulations of droplet formation in a T-shaped microchannel. *Langmuir*, 22, 4144-4152.
- VAN STEIJN, V., KREUTZER, M. T. & KLEIJN, C. R. 2007.  $\mu$ -PIV study of the formation of segmented flow in microfluidic T-junctions. *Chemical Engineering Science*, 62, 7505-7514.
- VATS, A., TOLLEY, N., POLAK, J. & GOUGH, J. 2003. Scaffolds and biomaterials for tissue engineering: a review of clinical applications. *Clinical Otolaryngology & Allied Sciences*, 28, 165-172.
- WALDMANN, T., ROSENOER, V., ORATZ, M. & ROTHSCILD, M. 1977. Albumin structure, function and uses. Pergamon Press, 255-273.
- WANG, C.-C., YANG, K.-C., LIN, K.-H., LIU, H.-C. & LIN, F.-H. 2011. A highly organized three-dimensional alginate scaffold for cartilage tissue engineering prepared by microfluidic technology. *Biomaterials*, 32, 7118-7126.
- WANG, F., GUO, G., MA, Q., GU, M., WU, X., SHENG, S. & WANG, X. 2013. Investigation on the thermo-mechanical properties and thermal stability of polylactic acid tissue engineering scaffold material. *Journal of Thermal Analysis and Calorimetry*, 113, 1113-1121.
- WANG, H.-J., DI, L., REN, Q.-S. & WANG, J.-Y. 2009. Applications and degradation of proteins used as tissue engineering materials. *Materials*, 2(2), 613-635.
- WANG, W., MOSER, C. C. & WHEATLEY, M. A. 1996. Langmuir Trough Study of Surfactant Mixtures Used in the Production of a New Ultrasound Contrast Agent Consisting of Stabilized Microbubbles. *The Journal of Physical Chemistry*, 100, 13815-13821.
- WONGSASULAK, S., PUTTIPAIBOON, N. & YOOVIDHYA, T. 2013. Fabrication, Gastromucoadhesivity, Swelling, and Degradation of Zein–Chitosan Composite Ultrafine Fibers. *Journal of Food Science*, 78, N926-N935.
- XIE, J. & WANG, C.-H. 2007. Encapsulation of proteins in biodegradable polymeric microparticles using electrospray in the Taylor cone-jet mode. *Biotechnology and Bioengineering*, 97, 1278-1290.
- XIONG, R., BAI, M. & CHUNG, J. N. 2007. Formation of bubbles in a simple co-flowing micro-channel. *Journal of Micromechanics and Microengineering*, 17, 1002-1011.

## References

- XU, J., LI, S., CHEN, G. & LUO, G. 2006a. Formation of monodisperse microbubbles in a microfluidic device. *AIChE journal*, 52, 2254-2259.
- XU, J., LI, S., WANG, Y. & LUO, G. 2006b. Controllable gas-liquid phase flow patterns and monodisperse microbubbles in a microfluidic T-junction device. *Applied Physics Letters*, 88, 133506.
- XU, J. H., LI, S. W., TAN, J., WANG, Y. J. & LUO, G. S. 2006c. Preparation of highly monodisperse droplet in a T-junction microfluidic device. *AIChE Journal*, 52, 3005-3010.
- XU, Q., NAKAJIMA, M., ICHIKAWA, S., NAKAMURA, N., ROY, P., OKADOME, H. & SHIINA, T. 2009. Effects of surfactant and electrolyte concentrations on bubble formation and stabilization. *Journal of Colloid and Interface Science*, 332, 208-214.
- XU, Q., NAKAJIMA, M., ICHIKAWA, S., NAKAMURA, N. & SHIINA, T. 2008. A comparative study of microbubble generation by mechanical agitation and sonication. *Innovative Food Science & Emerging Technologies*, 9(4), 489-494.
- XU, Q. Y. & NAKAJIMA, M. 2004. The generation of highly monodisperse droplets through the breakup of hydrodynamically focused microthread in a microfluidic device. *Applied Physics Letters*, 85, 3726-3728.
- YALCIN, T., BYERS, A. & UGHADPAGA, K. 2002. Dissolved gas method of generating bubbles for potential use in ore flotation. *Mineral Processing and Extractive Metallurgy Review*, 23, 181-197.
- YANG, L. J., YAO, T. J. & TAI, Y. C. 2004. The marching velocity of the capillary meniscus in a microchannel. *Journal of Micromechanics and Microengineering*, 14, 220-225.
- YARIN, A. L., KOOMBHONGSE, S. & RENEKER, D. H. 2001. Taylor cone and jetting from liquid droplets in electrospinning of nanofibers. *Journal of Applied Physics*, 90, 4836-4846.
- YASUNO, M., SUGIURA, S., IWAMOTO, S., NAKAJIMA, M., SHONO, A. & SATOH, K. 2004. Monodispersed microbubble formation using microchannel technique. *AIChE Journal*, 50, 3227-3233.
- YOBAS, L., MARTENS, S., ONG, W. L. & RANGANATHAN, N. 2006. High-performance flow-focusing geometry for spontaneous generation of monodispersed droplets. *Lab on a Chip*, 6, 1073-1079.
- YOON, H. & KIM, G. 2011. A Three-Dimensional Polycaprolactone Scaffold Combined with a Drug Delivery System Consisting of Electrospun Nanofibers. *Journal of Pharmaceutical Sciences*, 100, 424-430.

## References

- YOON, J.-Y. & GARRELL, R. 2008. Biomolecular Adsorption in Microfluidics. *In*: LI, D. (ed.) *Encyclopedia of Microfluidics and Nanofluidics*. Springer US, 68-76.
- YUSSUF, A., SBARSKI, I., SOLOMON, M., TRAN, N. & HAYES, J. 2007. Sealing of polymeric-microfluidic devices by using high frequency electromagnetic field and screen printing technique. *Journal of materials Processing Technology*, 189, 401-408.
- ZENG, J. 2011. Non-Linear Electrohydrodynamics in Microfluidic Devices. *International Journal of Molecular Sciences*, 12, 1633-1649.
- ZHANG, Y. & WANG, L. 2009. Experimental investigation of bubble formation in a microfluidic t-shaped junction. *Nanoscale and Microscale Thermophysical Engineering*, 13, 228-242.
- ZHAO, C.-X. & MIDDELBERG, A. P. J. 2011. Two-phase microfluidic flows. *Chemical Engineering Science*, 66, 1394-1411.
- ZHENG, H. 2012. Ultrasonic microbubbles: vehicles for molecular imaging and localized drug delivery. *The Journal of the Acoustical Society of America*, 131, 3245.
- ZHOU, C. F., YUE, P. T. & FENG, J. J. 2006. Formation of simple and compound drops in microfluidic devices. *Physics of Fluids*, 18, 0921051-14.
- ZIMMERMAN, W. B., TESAR, V., BUTLER, S. & BANDULASENA, H. C. 2008. Microbubble generation. *Recent Patents on Engineering*, 2, 1-8.

## Appendix

Type	Chemicals used in experiments	Molecular weight / g mol <sup>-1</sup>	Density / g m <sup>-3</sup>
Solvents	Acetone	58.08	0.79
	Ethanol	46	0.78
Proteins	BSA	66500	1.32
	Collagen	–	–
Lipids	Phospholipid	768	0.99
Polymers	PLGA	33000	1.34
	PMSQ	7465	1.24
Surfactants	CTAB	364.5	no data available
	PEG 40	2047	no data available
	SLS, SDS	288.4	1.01
	Tween 40	1277	1.09
Other	Deionized water	18.01	0.99
	Glycerol	92.09	1.26
	PBS	–	–

**Table A.1:** List of chemicals used in the experiments and their properties.